ISBN 978-82-326-2576-5 (printed ver.)
ISBN 978-82-326-2577-2 (electronic ver.)
ISSN 1503-8181

NTNU
Norwegian University of
Science and Technology

Sandra Helen Skjærvø

Doctoral theses at NTNU, 2017:252

NTNU

Doctoral thesis

Doctoral theses at NTNU, 2017:252

Sandra Helen Skjærvø

Structural and chemical stability of the hexagonal manganites

NTNU
Norwegian University of Science and Technology
Thesis for the Degree of
Philosophiae Doctor
Faculty of Natural Sciences
Department of Materials
Science and Engineering

NTNU
Norwegian University of
Science and Technology

Sandra Helen Skjærvø

Structural and chemical stability of the hexagonal manganites

Thesis for the Degree of Philosophiae Doctor

Trondheim, August 2017

Norwegian University of Science and Technology
Faculty of Natural Sciences
Department of Materials Science and Engineering

NTNU
Norwegian University of
Science and Technology

NTNU
Norwegian University of Science and Technology

Thesis for the Degree of Philosophiae Doctor

Faculty of Natural Sciences
Department of Materials Science and Engineering

ISBN 978-82-326-2576-5 (printed ver.)
ISBN 978-82-326-2577-2 (electronic ver.)
ISSN 1503-8181

Doctoral theses at NTNU, 2017:252

Printed by NTNU Grafisk senter

Preface

This dissertation has been submitted to Norwegian University of Science and Technology (NTNU) in partial fulfilment of the requirements for the academic degree Philosophiae Doctor.

The doctoral studies were mainly performed in the Inorganic Materials and Ceramics group, Department of Materials Science and Engineering (IMA), NTNU, Trondheim, under the supervision and guidance of Associate Professor Sverre M. Selbach (IMA) and Professor Thomas Tybell from Department of Electronic Systems. The project was supported by the The Research Council of Norway through project 231430 and by NTNU. Part of the studies were performed in the Materials Theory group at ETH Zürich under the guidance of Professor Nicola A. Spaldin and supported by the European Research Council through Advanced Grant N.A.S. no. 291151. Computational resources were provided through the supercomputers ABEL and STALLO by The Norwegian Metacentre for Computational Science (UNINETT Sigma AS) through project NN9264K, and on the EULER supercomputer provided by ETH Zürich.

The present work consists of eight chapters. Chapters 1-3 present the motivation, introduction, and methods. Chapters 4-6 address three research topics used to prepare publications. Chapters 7-8 connect the topics, conclude the work, and discuss the outlook on future research.

Parts of this thesis have been published, or prepared for publication and these papers and manuscripts are included in Appendix A.

All computational work has been performed by the author with the exception of the structural relaxations for Chapter 4, to investigate sublattice behaviour, which were done by Quintin Noel Meier at ETH, Materials Theory. Gerhard H. Olsen helped with transition state calculations. The spallation neutron scattering measurements at Spallation Neutron Source (SNS), Oak Ridge National Lab (ORNL) were performed jointly by the author, Sverre M. Selbach, Simon J. L. Billinge (Brookhaven National Laboratory, USA, and Columbia University, Department of Applied Physics and Applied Mathematics, USA), Emil S. Bozin (Brookhaven National Laboratory, USA), Mikhail Feygenson (Forschungszentrum Jülich, Germany), Marshall McDonnel (Adv. Diffr. Gr., Chem. Eng. Mater. Div., ORNL) and Matt Tucker (Adv. Diffr. Gr., Chem. Eng. Mater. Div., ORNL). Post-processing of the scattering data was performed mainly by the author, with supervision from Sverre M. Selbach, Emil S. Bozin and Simon J. L. Billinge. The ceramic processing of bulk and nano-crystalline samples was performed by Sverre M. Selbach, Silje K. Nesdal and Nikolai H. Gaukås. The thermoelectric measurements were performed by Espen T. Wefring. The AC impedance measurements were performed jointly by the author and Julia Glaum (Department of Materials Science, NTNU). Thermogravimetric measurements were performed by Sverre M. Selbach. In-house high-temperature X-ray diffraction was performed by Sverre M. Selbach and Nikolai H. Gaukås. Quintin N. Meier prepared Fig. 2.15 and parts of Fig. 7.1 and Fig. C.1.

Papers and manuscripts included in this thesis

1. **S. H. Skjærvø***, E. T. Wefring, S. K. Nesdal, N. H. Gaukås, G. H. Olsen, J. Glaum, T. Tybell and S. M. Selbach, Interstitial oxygen as a source of p-type conductivity in hexagonal manganites. *Nature Communications* **7**, 13745 (2016).
   *Contributions: Acquiring, analysis and interpretation of the computational data, collecting AC impedance spectroscopy data, designing the work, preparing the figures and drafting of the manuscript.

2. **S. H. Skjærvø***, Q. N. Meier, E. S. Bozin, S. J. L. Billinge, M. Feygenson, N. A. Spaldin, and S. M. Selbach, Unconventional order-disorder phase transition in improper ferroelectric hexagonal manganites, *Submitted* (2017).
   *Contributions: Acquiring, analysis and interpretation of the neutron scattering data, designing the work, preparing the figures and drafting of the manuscript.

3. **S. H. Skjærvø***, D. R. Småbråten, N. A. Spaldin, T. Tybell, and S. M. Selbach, Oxygen vacancy ordering and the interplay with neutral domain walls in h-$YMnO_3$. *In preparation.*
   *Contributions: Acquiring, analysis and interpretation of the computational data, designing the work, preparing the figures and drafting of the manuscript.

Manuscripts omitted from this thesis

1. J. Schaab, **S. H. Skjærvø***, S. Krohns, X. Dai, M. Holtz, M. Lilienblum, Z. Yan, E. Bourret, D. A. Muller, M. Fiebig, S. M. Selbach and D. Meier, Electrical half-wave rectification at improper ferroelectric domain walls. *In preparation.*
   *Contributions: Acquiring, analysis, interpretation and presentation of the computational data and reviewing the manuscript.
2. J. Schaab, **S. H. Skjærvø***, D. R. Småbråten, Z. Yan, E. Bourret, M. Fiebig, A. Cano, S. M. Selbach, and D. Meier, Adjustable hole- or electron-dominated transport at semiconducting ferroelectric domain walls. *In preparation*
   *Contributions: Acquiring and discussion of the Seebeck measurements.
3. D. R. Småbråten, Q. N. Meier, **S. H. Skjærvø***, T. Miyazaki, D. Meier, N. A. Spaldin, and S. M. Selbach. A first principles study of charged domain walls in improper ferroelectric hexagonal $YMnO_3$, $InMnO_3$ and $YGaO_3$. *In preparation.*
   *Contributions: Acquiring and discussing parts of the computational results.
4. D. R. Småbråten, N. H. Gaukås, **S. H. Skjærvø***, S. P. Singh, D. Meier and S. M. Selbach. Tailoring n- and p-type conductivity in donor and acceptor doped $YMnO_3$. *In preparation.*
   *Contributions: Discussing the computational results.

Trondheim, 24th of August 2017
Sandra Helen Skjærvø

Acknowledgements

Looking back on my time as a PhD student, I remember both challenges and victories, but most of all the support from the people around me. This PhD would not have been possible without the continuous encouragement and inspiration from the people in my life.

First, I want to thank my main supervisor, Sverre M. Selbach, in whose office I have both laughed and cried. I told you the day I started my PhD that I like being outside of my comfort zone. Thank you for giving me the opportunity to work on this varied and challenging project. Being your *padawan*[1] has taught me a lot and I am now truly an hexagonal manganite enthusiast. My co-supervisor Thomas Tybell at Department of Electronic Systems also deserves acknowledgement for his great knowledge and positive attitude. Discussions with you have always given me a better perspective of the project and taught me how to better present my stories. Although not a co-supervisor on paper, I have much gratitude for Nicola A. Spaldin for taking me under her wing when visiting the Materials Theory group at ETH Zürich. Working with you has been truly inspiring both regarding the fascinating science and for pursuing an academic career as a woman.

Someone told me once that science consists of two parts: the first is observation of nature and the second is hard thinking. For me, the thinking part has been made so much easier through collaboration and discussion with fellow researchers. A big thank you goes to all the Master students working with me on hexagonal manganites or related materials during my PhD, Tormod Østmoe, Madelen Mørk Frydenlund, Christine Blom, Mari Reidulff, Elise Ramleth Østlie, Nikolai Helth Gaukås and Mohammed Mostafa Adnan, and everyone in my closest hexagonal manganite family, especially Didrik René Småbråten, Theodor Secanell Holstad, Donald Malcolm Evans and Quintin Noel Meier. The discussions and collaboration with all of you have led to many brilliant ideas and new

---

[1] That is what the Jedi in Star Wars call their trainees. It means that she is not yet a Jedi.

insight!

A big part of my scientific training has been teaching and outreach activities. Thanks to all my former laboratory students in the Chemical Engineering and Biotechnology study program. Your questions and enthusiasm for chemistry have inspired me to stay curious. Also, thanks to NRK for giving me the opportunity to do outreach to the general public.

Thanks to all my former office mates, both in Trondheim and in Zürich, for all the scientific and non-scientific conversations, and for bearing with my occasional outbursts of frustration. Further, to all my friends and colleagues at the Department of Materials Science and Engineering at NTNU and in the Materials Theory group at ETH. You have made everyday work fun and dynamic.

The warmest gratitude goes to all my friends, both on and off the climbing wall, and to my family. You have made it possible for me to reach new heights. Finally, a special thanks to Quintin. Together we have made bridges both between countries and scientific fields, and I would never have been where I am without you.

Summary

The hexagonal manganites h-RMnO$_3$ (R = Y, In, Sc, Ho,...,Lu) are interesting for both fundamental studies – i.e. formation of cosmic strings – and technological purposes, e.g. nano-sized conducting domain walls, and oxygen carrier materials for chemical looping combustion. This thesis investigates the microscopic mechanisms determining for the oxygen defect chemistry and the domain wall conduction, revealing the critical importance of the yttrium-oxygen interactions.

The thesis is divided into three main topics, investigating the ferroelectric phase transition, accommodation of oxygen vacancies, and accommodation of oxygen interstitials. It further discusses the intimate connection between the three topics and the implications.

The improper mechanism for ferroelectricity is well established. However, there has been controversy about why the observable ferroelectric polarization is not seen until several hundred degrees below the Curie temperature, where the non-centrosymmetric distortions, often called *trimerization*, occur. This controversy is addressed in the thesis by using high-energy neutron total scattering. The measurements probed the local structure across the ferroelectric transition in hexagonal YMnO$_3$. Upon heating, the average structure shows signatures of becoming paraelectric – with trimerization decreasing to zero – whereas the local structure partially retains its trimerization amplitude. It is shown that this trimerization averages to zero when fluctuations lower the local symmetry to a continuum of structures. This unconventional phase transition reconciles previously reported anomalies related to the phase transition, and is expected to apply to all hexagonal manganites.

Functional properties at ferroelectric domain walls, e.g., domain wall conductivity, are often attributed to oxygen vacancies. Despite no electric driving force for charge accumulation at neutral domain walls, also these walls have been shown to have higher conductivity than the bulk. This implies an elastic driving force for point defect segregation to these walls. This thesis discusses the accommodation of oxygen vacancies in h-$YMnO_3$, through first principles calculations. The vacancies are accommodated in the manganese-oxygen layers, reducing the manganese. Moreover, the oxygen vacancies *do not* accumulate at the neutral domain walls. The distance to the closest yttrium and the structural flexibility are inferred to be important for the defect accommodation. The yttrium-oxygen bonds are shorter at the domain walls, and the structure is less flexible with respect to structural distortions. Hence, breaking the bonds at the domain walls cost more energy than breaking these bonds in the bulk.

It has been ubiquitously observed that undoped hexagonal manganites are p-type semiconductors. This has often been attributed to cation vacancies. However, observations of large oxygen excess, tunable by oxygen partial pressure at low temperatures, imply that cation vacancies may not be the only point defects accommodating the p-type conductivity. The measured excess of oxygen can also be due to additional oxygen at interstitial lattice sites. These interstitial oxygens have not previously been investigated by first principles calculations in h-$R\text{MnO}_3$, possibly because this type of point defect can not be accommodated in more close-packed ABO_3 structures. This thesis presents the electronic and structural effects of interstitial oxygen in h-$YMnO_3$ by first principles calculations and experiments on samples with different thermo-atmospheric history. The interstitial oxygen is found to form in the manganese-oxygen layers of the structure, oxidizing manganese to give rise to the observed p-type conductivity. The calculations also show that the migration barrier for the defect is low in bulk, and explains the microscopic origin of the reversible excess oxygen at low temperatures. Further, the interstitial oxygen is shown to accumulate at neutral ferroelectric domain walls where it can bond stronger to nearby yttrium. The results hence provide an explanation for the previously reported conducting neutral domain walls.

Connecting the topics reveal that although the multivalent nature of manganese is the reason why oxygen point defects form in the manganese-oxygen layers, the electropositivity of yttrium and the structural flexibility – determined by the cost of changing the trimerization – determines the defect positions within these layers. The bonds between yttrium and oxygen are thus important for the structural and chemical stability of the hexagonal manganites, and constitute the key entities coupling the cation sublattices. Oxygen vacancies breaking these bonds will be accommodated by structural distortions that counteract the bond breaking. Introduction of additional oxygen interstitials forms new structurally stabilizing yttrium-oxygen bonds. Understanding this coupling between the defect chemistry and the functional properties arising from the trimerization is important if the hexagonal manganites are to be used in electrochemical applications at the nano-meter range or in bulk.

Contents

Part I

Background

Chapter 1

Motivation

Many modern technologies are based on materials in which electric, magnetic or elastic properties can be induced or manipulated by applying electrical, magnetic or elastic fields. Of special interest are materials that show a coupling between electric, magnetic or elastic properties, illustrated in Fig. 1.1. In particular, *piezoelectric*[1,2] materials have coupled electric polarization and elastic strain such that an electric field can change the shape and size of the material, and mechanical stress can induce an electric polarization. Piezoelectrics are the cornerstones of sensor and actuator technology as they enable the conversion of mechanical to electrical energy. *Magnetoelectrics*[3–5], with coupled magnetization and electric polarization hold great promise for future technologies. Particularly, magnetoelectric *multiferroics*, where the coupled properties form spontaneously, are interesting for the development of e.g. multiferroic data storage devices where the information can be written with an electric field, while the coupled magnetization is read out[6–8].

The functional properties at the bottom of the diagram in Fig. 1.1 are also inevitably coupled to the chemical composition of the materials through the chemical potential of atomic species[9–11]. Introduction of relatively immobile and irreversible cation point defects has been the way of tuning and optimizing properties in materials for a long time, for example in doped semiconductors. Reversible defect concentrations from exchange with the surroundings are intentionally exploited in electrochemical devices such as solid oxide fuel cells[12] and batteries[13], but high temperatures of several hundred degrees are often required. As the size of technological devices and their components become progressively smaller and enter the nano-meter range, the temperatures required

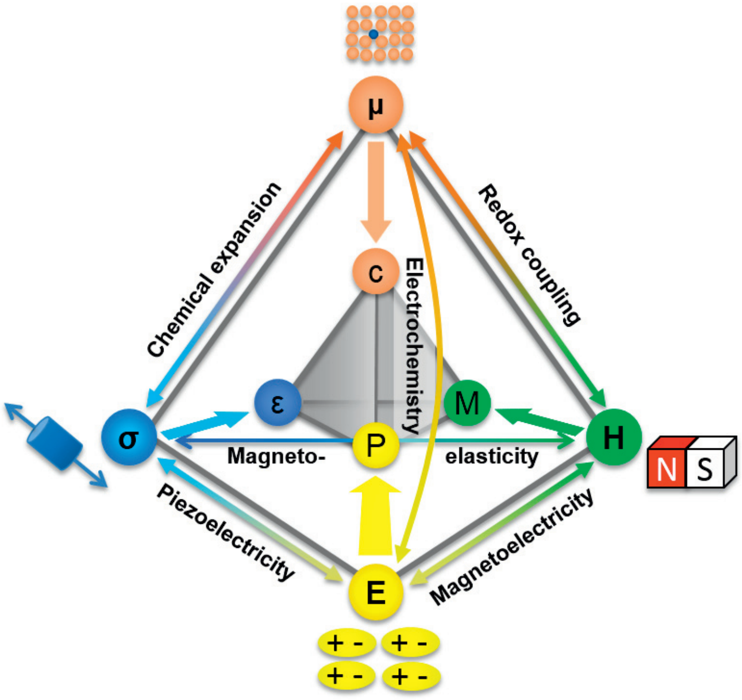

Figure 1.1: Coupling between electric, magnetic and elastic properties. Schematic presentation of interaction between the control parameters electric field E, magnetic field H, stress σ and chemical potential μ, and the functional response in a material through polarization P, magnetization M, strain ϵ and concentration c of defects. *Based on Fiebig, Kalinin and Spaldin*[6,10,18].

for exchanging reversible species between the material and the atmosphere decreases[14]. Moreover, the chemical potential of species become comparable to the elastic and electric fields at more static objects at the nano-scale, such as domain walls separating regions of ferroelectric polarization[15]. Controlling the chemical potentials of the relevant species thus becomes imperative. Ferroelectric domain walls have shown several orders of magnitude different electrical conductivity, which is likely connected with the defect chemistry of the materials[16,17]. However, the mechanism that govern defect accommodation, mobility, and their elastic and electrostatic effects at the nanoscale, are not fully understood.

The hexagonal manganites were discovered as a new class of material with coupled ferroelectricity and antiferromagnetism in the late 1950's and early

1960's[19–22]. The ferroelectricity emerges from an improper mechanism[23,24], giving intricate domain structures[25,26]. The combination of these domain structures with the material's ability to accommodate large concentrations of oxygen point defects makes the materials interesting for possible nano-scale electronics[17]. However, the short range structural changes across the ferroelectric phase transition are not understood, and thereby neither the structural flexibility in the bulk nor at the domain walls.

Advances in computational first principles methods, and increased computational power, now allow the study of these complex material systems at the atomic and electronic scale, exceeding the energetic and structural resolution of any known experimental technique. The flexibility in modelling the materials and in separating the effects of many variables, makes computational methods ideal for studying functional properties and defect chemistry on the atomic level. Further, total scattering measurements are becoming more recognized for their strength in revealing the local structure and structural coherence across phase transitions. The method distinguishes between structural symmetry which extends over the length scale of the whole material and symmetry that only emerges in small regions.

1.1 Aim of work

The aim of this work was twofold. Firstly, the aim was to investigate the local structure and structural coherence across the ferroelectric transition of the hexagonal manganites, and thereby understand the emergence of their ferroelectric polarization and structural flexibility. The bulk structure was measured by high energy neutron scattering and analysed in real space as pair distribution functions (PDFs) across the ferroelectric transition.

The second goal was to understand the oxygen defect chemistry of the hexagonal manganites and its effect of the structural, electronic and functional properties. First principles calculations and experimental measurements of structural and electrical properties were used to study both oxygen vacancies and oxygen interstitials, in bulk and at neutral 180° domain walls.

Chapter 2

Introduction

2.1 Ferroelectrics and multiferroics

Ferroelectricity

Ferroelectricity is the establishment of a spontaneous electric polarization in a material, exemplified by ordering of electric dipoles. The spontaneous polarization can point in two or more allowed directions in the material, and the direction can be switched by an external electric field. Ferroelectric materials become polar below the *Curie temperature*, T_{C}, when inversion symmetry is broken by small displacements of the atoms and anisotropic distribution of the electron density. The polarization varies with temperature and strain, and ferroelectric materials are therefore also pyroelectric and piezoelectric[1,2].

The spontaneous polarization can emerge by several mechanisms[27,28]. A common mechanism for polarization is partial covalency between empty d-states and O $2p$-states[29]. This type of ferroelectricity is commonly found in d^0 transition metal perovskite oxides, such as $BaTiO_3$. This mechanism cannot accommodate multiferroicity of magnetic and electric orders, as magnetic order requires unpaired valence electrons, d^n.

Another driving force for ferroelectricity occurs in materials with *electron lone-pairs*. These electrons create local dipoles by anisotropic distribution of the electron density in the structure, and partial covalency might order these dipoles such that a long range ferroelectric polarization emerges. Two examples of materials with lone-pair ferroelectricity are $BiFeO_3$[30] and $PbTiO_3$[29,31].

In materials with less covalent character, ferroelectricity can occur due to a *geometric* mechanism where entire sublattices shift with respect to each other. The driving force for the shift can be pure steric effects, optimizing the packing of hard atoms of different size, or electrostatic optimization through ionic bonds. This mechanism is found in the hexagonal manganites, $R\mathrm{MnO}_3$[23,24,32].

A different mechanism is found in materials with *charge ordering*[33]. The spinel $\mathrm{LuFe_2O_4}$ with alternating order of Fe^{2+} and Fe^{3+} is believed to be ferroelectric due to this mechanism[34,35].

Yet another mechanism is *spin-driven ferroelectricity*, which can occur in materials where the magnetic spin order breaks the inversion symmetry and induces an electric polarization[36].

Proper and improper ferroelectrics

It it common to separate ferroelectrics into two classes. In *proper* ferroelectrics, the structural changes are proportional to the resulting polar distortion below the transition temperature, and can thus be taken as the *order parameter* driving the phase transition. For *improper* ferroelectrics the spontaneous polarization emerges as a secondary effect to a non-polar distortion driving the phase transition[37]. The order parameter thereby expresses the non-polar distortions below the transition temperature, while the polarization is not proportional to the primary order parameter. The large magnitudes of polarization in many proper ferroelectrics, often combined with strong coupling to strain, make them technologically interesting for applications such as sensors, ferroelectric bypass capacitors, actuators, ferroelectric memory and electrocaloric cooling devices[38,39]. Improper ferroelectrics usually have much weaker spontaneous polarization, but have gained more interest the last two decades due to the physical phenomena related to their special *domain structures*[17].

Ferroelectric domain structures

Upon cooling through the phase transition, the microscopic *domain* structure of a ferroelectric is mainly determined by the electrostatic boundary conditions[15,40]. If the polarization is pointing in the same direction in the whole material, the surfaces perpendicular to the polarization will have a charge density equal to the dipole moment per unit volume. This creates an electric field of opposite sign and equal magnitude as the polarization. The larger the magnitude of this *depolarization field*, the larger electric energy it stores, and charge compensation is hence favourable. Application of an external field can partially screen the depolarization field, such that ferroelectricity can be stabilized for thin films up to a few unit cells thick[41].

If the material cools without the presence of an external field, the material divides the polar ground state into smaller regions, called domains, collaboratively minimizing the depolarization field. The number of allowed polarization directions determines the polarization change across the domain walls. A ferroelectric material with two allowed polarization directions, will consist of domains with polarization alternating by 180°. An example of this is the hexagonal manganites, as shown in Fig. 2.1. The domain structure of these materials are discussed in more detail in Section 2.3.

The size of the domains is dependent on the magnitude of the polarization and the elastic and electrostatic energy cost of forming the domain walls separating the domains. Large polarization will favour the formation of domains, counteracted by the cost of creating the domain walls. Neutral domain walls, as in Fig. 2.1**a**, are associated with an elastic energy arising from structural distortions across the wall. Charged walls, as in Fig. 2.1**b-c**, are in addition associated with electric energy due to polarization contributions perpendicular to the wall. This results in a bound electric charge at the wall which can be accommodated by free charges, i.e. ionic and electronic defects, screening the electric field.

Domain formation in improper ferroelectrics is not mainly driven by electrostatics, but by the critical dynamics of the primary order parameter when crossing T_{C}. For the hexagonal manganites, this means that the domain walls are formed before the coupling to the polarization becomes significant. Hence, charged walls are equally likely to form as neutral walls[16,17,26,42].

The technological applications of ferroelectric domains include actuators, high-frequency resonators, focused acoustic transducers, sensors and capacitors for electric memory devices[38,43,44]. The domain walls are becoming more recognized for their potential use in nano-sized electronic components. The interest was sparked by the discovery of domain walls with orders of magnitude higher electrical conductivity than the domains[15–17].

Multiferroics

Analogously to ferroelectric materials, long range magnetic or elastic orders exist in *ferromagnets* and *ferroelastics*. These orders are switchable by magnetic or elastic fields. Data is often stored in ferromagnetic domains, of opposite magne-

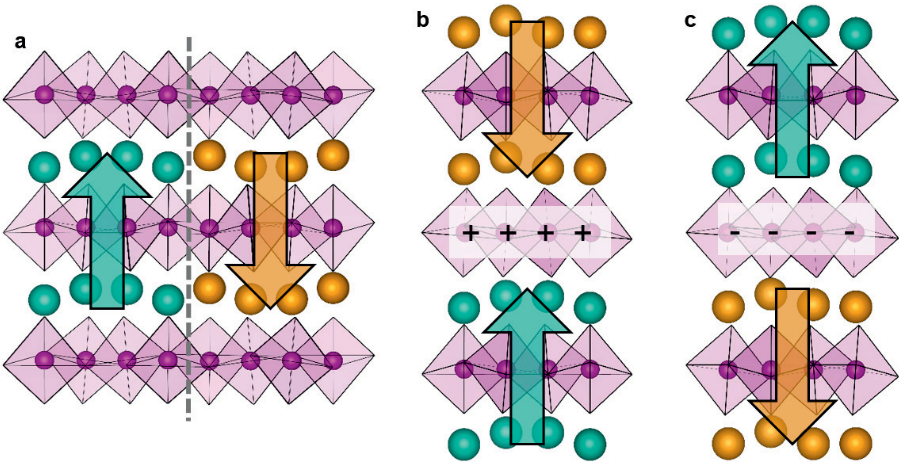

Figure 2.1: Electrostatics at 180° domain walls. The three types of domain walls that emerge in the hexagonal manganites upon cooling. **(a)** Electrostatically neutral domain wall. **(b)** Head-to-head domain wall with positive electrostatic charge. **(c)** Tail-to-tail domain wall with negative electrostatic charge.

tization. Ferroelastics can be applied in mechanical switches[45]. The long range ordering of these functional properties, in some cases also including long range antiferroic orders, are referred to as *ferroic* properties.

Multiferroics are materials that combine two or more ferroic orders[46]. From a technological perspective, the focus has been on finding materials which combine ferro- or antiferromagnetism with ferroelectricity[6,47]. The first discoveries of multiferroic oxide perovskite materials, were pioneered by Smolenskii and co-workers from the late 50's[48], including the discovery that hexagonal manganites were both ferroelectric and antiferroelectric. However, the field progressed slowly in the beginning, as these first reports of including magnetic ions in ferroelectric crystals often impeded the ferroelectric polarization. It would take almost half a century after Smolenskii's discoveries before Hill (now Spaldin) could explain why the ferroic orders were competitive and multiferroic oxides were so rare[49–51]. She showed that in these materials, atoms which were good for ferroelectricity did not carry d electrons, as discussed in the previous section. This mechanism thus did not comply with magnetism, as magnetic atoms need unpaired d electrons. The discovery initiated the search for materials with other ferroelectric mechanisms that could accommodate a simultaneous magnetic order, such as geometric ferroelectricity[6]. There are many reviews on multiferroics, e.g. 7, 28, 47, 52–57.

Multiferroics with electric and magnetic orders are often categorized in two classes depending on whether the orders arise independently or not[57], see Fig. 2.2. In type I multiferroics, the ferroelectric order arises at typically much higher temperatures than the magnetic order, and have only weak *magnetoelectric coupling*[58] between the magnetization and electric orders, discussed below. Such materials have potential use in four-state data storage elements[59] and multifunctional photonic devices[60,61]. Materials where the appearance of a magnetic order causes the inversion symmetry to break, by inducing atomic distortions, belong to type II of the multiferroics. The simultaneous breaking of both inversion and time symmetry originates in the relatively strong magnetoelectric coupling in these materials.

Coupled properties and magnetoelectricity

The couplings between electric polarization, magnetization, strain and their external fields were illustrated in Fig 1.1. The chemical potential of relevant species is included at the top of the diagram, as the chemical flexibility of materials has great impact on functional properties, especially as the component sizes become decreasingly smaller[9,10,18]. This electrochemical coupling is the main motivation for this work on hexagonal manganites, as the interplay between their chemical flexibility and domain structures hold potential for future technological advances, as is discussed in Section 2.3.

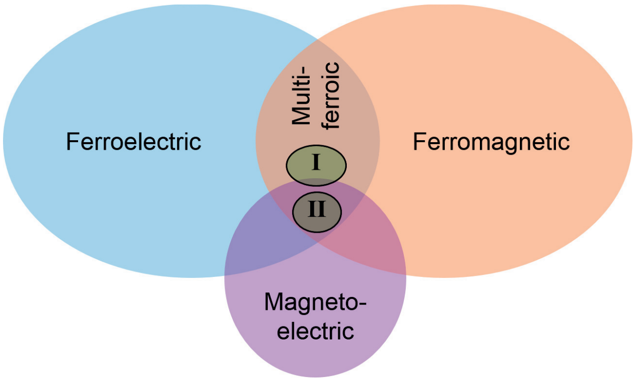

Figure 2.2: Types of multiferroics with magnetic and electric orders. Coexistence of ferroelectricity and ferromagnetism can give either non-magnetoelectric or magnetoelectric multiferroics. Type I multiferroicity have coexisting orders which arise at different temperature and are not or only weakly coupled. Type II multiferroics have strongly coupled orders that arise at the same temperature. *Inspired by Eerenstein*[57].

Magnetoelectric coupling also motivates much of the research done on hexagonal manganites. The first report on magnetically induced ferroelectricity was published in the 70's on Cr_2BeO_4[62]. In such *magnetoelectric* materials[3,4,63,64] an electric field can control the magnetization, and a magnetic field can control the electrical polarization. Magnetoelectric multiferroics[5] can host novel functionalities not present in either ferroic state alone. One example of this is a two-memory element where a magnetic bit is coupled to an electric bit[8], such that information can be written efficiently by an electric voltage, whereas the induced magnetic dipole is read out.

Despite the vast amount of multiferroic materials known today, there are still many challenges to be resolved before they can be used in applications[5,28,65,66]. Strong magnetoelectric coupling is necessary if they are to be used in e.g. spin-based devices with ultra-low power consumption[67–70], or in two-state multiferroic memory-devices[8].

2.2 Thermodynamics

General topics in this thesis are defect chemistry reactions and structural phase transitions, both which are studied from the perspective of thermodynamics.

If a system is in equilibrium, the *Gibbs' free energy* (Eq. 2.1) is in a *global* minimum.

$$G = U - TS + PV \tag{2.1}$$

Gibbs' free energy is comprised of the enthalpy ($H = U + PV$) and the temperature-scaled entropy (TS). The internal energy, U, is primarily associated with the bond energy stored in the lattice vibrations and electronic energy. G also depends on the properties pressure P and volume V. If the difference in Gibbs' free energy between two states is negative, a spontaneous transition or reaction can occur. Although such a spontaneous process would be energetically favourable, many chemical reactions and physical phase changes have to overcome a certain energy barrier, or activation energy, before the process can occur, see illustration in Fig. 2.3. Diamond, the strongest material we know, is also a famous example of a material which is not in its most stable form. Diamond is a *metastable* polymorph of the element carbon, while graphite is the true *stable ground state*. However, the structural transition from diamond to graphite requires tremendous amounts of energy, so that diamond – if it has already been created – will stay that way if kept at ambient conditions. Such transitions, sep-

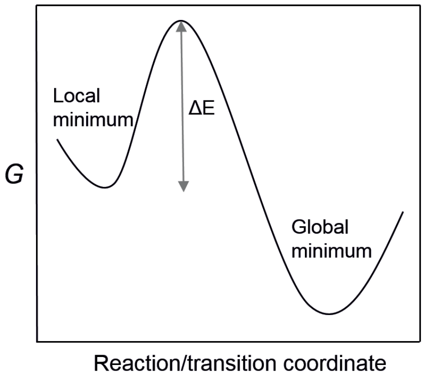

Figure 2.3: Stability and metastability. Schematic illustration of the Gibbs' free energy in a system with a metastable phase in a local minimum and a stable phase in a global minimum separated by an energy barrier of ΔE.

arating a stable and a metastable phase, are observed to have discontinuities in measurable variables, such as heat flow as a function of temperature or volume as a function of pressure, upon the phase transition. Paul Ehrenfest developed the order classification of transitions by relating these physical observables to the differentiated Gibbs' free energy[71,72]. Transitions are classified *first order* if the discontinuous physical property, such as heat flow or volume, is proportional to the first differentiation of G. First order transitions require coexistence of phases, with one phase nucleating in the other, such as melting of water or precipitation. *Second order* transitions, or *continuous* phase transitions, have no discontinuities in the first differentiations of G. They are however characterized by other *critical phenomena*, such as discontinuous heat capacity and divergent susceptibility and correlation length near the phase transition, proportional to the second differentiation of G. Examples of phase transitions that behave as second-order are magnetic transitions, type II superconducting transitions and some ferroelectric transitions. Weakly first order transitions are sometimes also referred to as continuous transitions, as the discontinuity in the first differentiation of G is small.

A material can also be metastable with respect to chemical changes. As will be shown in Section 2.3, the hexagonal manganites are metastable below 1062 K, which means that it would be energetically favourable for the material to decompose into the Mn-rich YMn_2O_5 and the Y-rich Y_2O_3. Nevertheless, the hexagonal manganites do not automatically decompose, since it would require overcoming a large activation energy barrier. However, this metastability is central to the formation energy of the enthalpy stabilized interstitial oxygen defects which will be addressed in Chapter 6.

2.2.1 Structural stability: phase transtitions and Landau Free energy

Phase transitions are not only interesting on a technological level, but also fundamentally as they combine many topics: crystal structure and symmetry, bonding, thermodynamics, kinetics and lattice dynamics. The microscopics and dynamics of a phase transition determine to a large extent the physical properties that arise at and below the phase transition. Knowing the mechanisms and how the symmetry evolves on average and at the local scale, thus makes it possible to tune the properties.

In second order transitions and first order transitions with group-subgroup relationship between the high- and low-temperature phases, the low-symmetric structure can be described as a perturbed version of the high-symmetric structure[73]. Landau acknowledged that for these phase transitions, he could express the Gibbs' free energy of the system as a Taylor expansion of these changes[74]. He treated the small structural or electronic changes by introducing the simple concept of the *order parameter*, φ, which expressed the *relative difference* between the phases, with $\varphi = 0$ for the high symmetry structure and $\varphi \neq 0$ for the low symmetry structure. It naturally follows that for second order phase transitions, the order parameter should go continuously to zero at the phase transition temperature, but discontinuously for first order transitions, as illustrated in Fig. 2.4. Since the order parameter has to be defined for each specific system, expressing it is not always straight-forward. In magnetic materials, the order parameter can be magnetization, in proper ferroelectrics it can be polarization, and for superconductors it can be the square of the Cooper pair wavefunction. The theory was developed further for ferroelectric materials by Devonshire, known as *Landau-Devonshire theory*[75].

The free energy G as a function of temperature T, pressure P and the order parameter φ is as follows:

$$G(P,T,\varphi) = G_0(P,T) + a\varphi^2 + b\varphi^4 + c\varphi^6 ... \tag{2.2}$$

Here, G_0 is the free energy for the high symmetry structure, while $a, b, c, ...$ are material dependent coefficients varying with the reduced temperature, $\tau =$

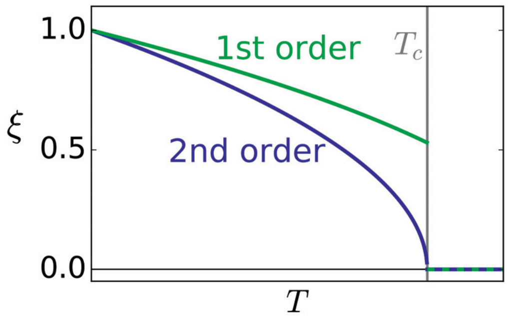

Figure 2.4: The order parameter. Order parameter evolution with temperature for first and second order transitions.

$(T\text{-}T_\mathrm{C})/T_\mathrm{C}$. Minimizing the energy with respect to φ, gives the φ for which the system is at a global minimum. The solutions to the differentiated G express how the order parameter depends on external parameters and material properties. These can be inserted into Eq. 2.2 such that G is only expressed in terms of the reduced temperature and coefficients.

Differentiating G with respect to T or an external field E gives the measurable observables heat capacity C_p and susceptibility χ[76]:

$$C_p = \frac{\partial^2 G}{\partial T^2} \propto \tau^{-\alpha} \tag{2.3}$$

$$\chi = \frac{\partial^2 G}{\partial E^2} \propto \tau^{-\gamma} \tag{2.4}$$

where α and γ are called *critical exponents*. Critical exponents are believed, although not proven, to be universal and only depending on the dimensions of the system, the range of interactions, and the symmetry of the order parameter. This means that the critical behaviour of very different systems can be described by the same critical exponents if they belong to the same universality class[77].

It should be noted that Landau theory cannot predict if or under what conditions a transition occurs, as it takes the existence of the phase transition as a premise. The Landau free energy describes the energy landscape for changing the material as a function of the order parameter. For a proper uniaxial ferroelectric with two possible polarization directions, the free energy landscape as a function of polarization will look like a double well below the phase transition, as illustrated in Fig. 2.5.

The Landau-Ginzburg theory[79] was formulated already in late 1950's. This

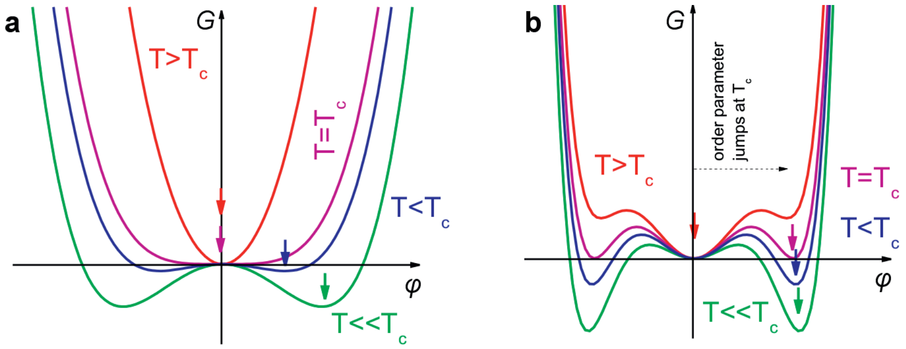

Figure 2.5: Landau Free energy G as a function of the order parameter φ for various temperatures for a system with two degenerate ground states undergoing **(a)** a second-order continuous phase transition and **(b)** a first-order discontinuous transition. Note how a new equilibrium state suddenly appears at a non-zero value of φ in panel **b**. *Modified from ref. 78.*

extension to Landau theory includes additional gradient terms $(\nabla\varphi)$ to Eq. 2.2 which makes the order parameter a local property. In this way, the expansion can describe spatial inhomogeneities of the order parameter. This expansion can be used to describe domain structures as long as the mean field approximation is valid[80], as discussed below. From the Ginzburg extension to Landau theory it is also possible to calculate the *correlation length* of fluctuations, ξ. This parameter describes the how far-reaching the effects of a spatial fluctuation of the order parameter are, and it is related to the stiffness of the order parameter. It is calculated by considering a two-point correlation function of the order parameter. When approaching T_{C}, ξ diverges with the critical exponent ν.

Where fluctuations matter

The universality of critical exponents originates in the diverging correlation length of fluctuations, such that any intrinsic length scale vanishes. This leads to a scalability of the system in the critical regime such that the critical behaviour can be described by the same parameters at any length scale. All critical exponents can be calculated analytically within the framework of the *Mean-field approximation*[80]. This framework assumes that fluctuations of the order parameter are entirely uncorrelated in space so that they will have no qualitative influence on the transition. It is therefore expected to predict well the behaviour of materials far away from T_{C}, where correlation lengths are short compared to the long range order in the structure. However, since the susceptibility of a continuous phase transition is expected to diverge close to T_C, as seen in Eq. 2.4, fluctuations of the order parameter will be strongly correlated and influence the qualitative behaviour of the transition. In most systems, fluctuations do not become strongly correlated until very close to the transition and they can therefore be neglected. However, in a few cases, including the hexagonal manganites[81], Landau theory in its simplest form fails quite far away from the transition, according to the Ginzburg criterion. The Ginzburg criterion formulates at which amount of fluctuations the energy stored in fluctuations, $\langle \nabla\varphi \rangle$, become significantly smaller than the energy stored in the expectation value of the order parameter, $\bar{\varphi}$, per volume of the correlation length ξ in a system with dimensionality d[79]:

$$\left\langle (\nabla\varphi)^2 \right\rangle_{\xi^d} << \bar{\varphi}^2 \tag{2.5}$$

As long as this criterion holds, mean-field theories apply. However, close to T_C, the critical exponents of the system need to be *renormalized* to include fluctuation corrections. This is done by using the scalability of the system and constructing a renormalization group transformation that transforms the Hamiltonian appropriate to one length scale into one describing the system on a larger length scale[82,83]. This approach works because of the assumption that the energy will be dominated by long-range fluctuations close to T_C, and hence the correlation length will be the only relevant length scale. The temperature interval around T_C where the renormalized exponents apply is called the fluctuation regime, or the *Ginzburg regime*.

To explain the link between the Ginzburg regime and phase transition in real systems, one should start by considering the structural changes that occur at the local scale upon the transitions.

Local and average structure across phase transitions

Phase transitions are at the most general level divided into the mutually exclusive categories *reconstructive* and *displacive*. Reconstructive transitions require breaking of bonds and are always of first order. Displacive transitions involve continuous distortions of the high-symmetry phase to the low-symmetry phase and can be both of first and second order. *Order-disorder* transitions, of both first and second order, constitute a third category. In this mechanism, the material goes from being ordered at low temperature and disordered at high temperature such that variations of the structure on a local scale average out to a higher symmetry. The order-disorder and displacive transitions are often considered two limiting cases for ferroelectric phase transitions. The driving force for either order-disorder or displacive symmetry breaking is determined by competition between short range and long range forces, as illustrated in Fig. 2.6**a**. This competition decides how coherently the unit cells of the material distorts, quantified by a *structural coherence length*.

A. Strictly displacive transitions

In the limiting case of infinitely strong long range forces, all the unit cells will distort coherently throughout the whole material, as illustrated in Fig. 2.6**b**. For such displacive transitions, the structural coherence length spans the whole sample both well below and well above T_C. The order parameter describes equally well the local atomic displacements and the average, macroscopic polarization, going to zero when heating to T_C. This means that all the entropy in the system comes only from phonons. No configurational disorder can be allowed since this would give local variations from the average picture. A simple free-energy model from Landau theory therefore gives a good approximation of the transition. The classic proper ferroelectric $\mathrm{PbTiO_3}$ is an example of a material which becomes polar through a predominantly displacive mechanism. The Pb^{2+} atoms each carry a $6s^2$ electron lone-pair which bonds covalently with neighbouring oxygens. The lone pairs order in the same direction below T_C, creating strong long-range forces for the other ions. In addition, covalent Ti^{4+} $3d^0$ and O $2p$ stabilize the polar structure through covalent bonds[85].

Strictly displacive phase transitions are expected to have small Ginzburg regimes[84,86]. The energy stored in fluctuation becomes negligible compared to the expectation value of the order parameter when the expectation value decreases.

B. Strictly order-disorder transitions

Ferroelectric transitions with strong order-disorder character combine weak long-range forces with strong short range forces. For such transitions, the coherence length becomes progressively shorter upon heating towards T_C, and remains small above T_C. In the high-temperature structure, short range forces are still present, driving the structure to be locally polar. However, the long range forces are too weak to order the dipoles, such that they cancel out when averaging over a volume larger than the coherence length. The polarization emerges

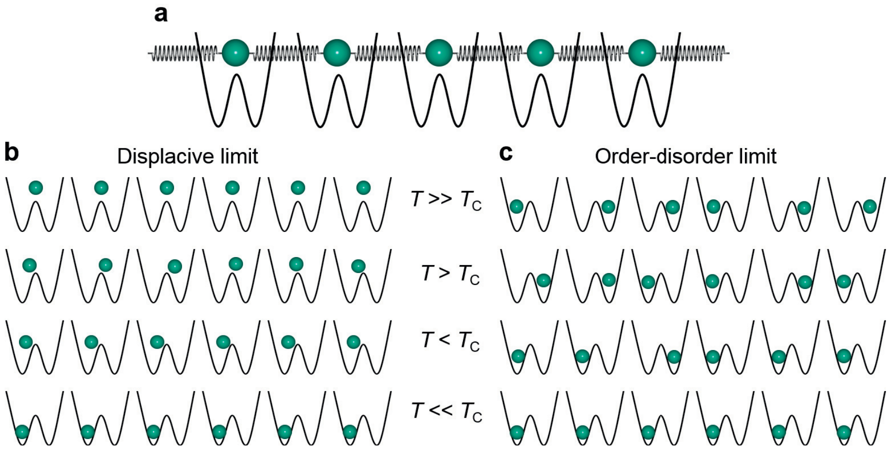

Figure 2.6: Spring-and-well model for phase transition mechanisms. **(a)** One-dimensional model of neighbouring unit cells in a material to illustrate different phase transition mechanisms. The spheres represent the occupied polar ground state of the unit cell, exemplified by off-centring of the cations. The double well beneath each sphere represents the *ground state* local environment felt by the unit cell from the rest of the crystal, and is the short range driving force for off-centring. The springs between the unit cells represent the harmonic energy from interaction between neighbouring atoms. Stiff springs will give long range vibrations and favour all the unit cells to do the same, while soft springs will give local vibrations. **(b)** Displacive limit where stiff springs give long range vibrational effects that are stronger than the local double-wells. Above T_C all the unit cells have atoms vibrating around centrosymmetric positions, while below they all coherently displace to the same off-centred positions. **(c)** Order-disorder limit where the local double-well potentials are dominating over long-range vibrational effects. At any temperature, all unit cells have off-centered atoms. Above T_C the distribution between the minima is random, while below they order in the same minimum. *Inspired by Dove*[84].

under T_C when neighbouring unit cells eventually start ”communicating” with each other and small regions in the material start ordering in the same direction, as illustrated in Fig. 2.6**c**. Landau theory can describe the average distortion in order-disorder ferroelectric transitions, but it cannot describe the local structure as the coherence length decreases when approaching T_C.

$BaTiO_3$ used to be considered an archetypal displacive ferroelectric where the Ti atoms were displaced in the direction of the polarization vectors[87], as illustrated in Fig. 2.7. At high temperatures $BaTiO_3$ has cubic symmetry ($Pm\bar{3}m$). The structure becomes tetragonal ($P4mm$) below 393 K giving a macroscopic polarization vector along [001], and orthorhombic ($Amm2$) below 278 K with a polarization direction of [011]. Finally, the structure distorts to a rhombohedral ($R3m$) structure with a macroscopic polarization direction along [111]. The displacive picture of the transition was questioned when total scattering measurements showed that the Ti atoms were displaced in the [111] directions in all four space groups[88], corresponding to the eight faces of the TiO_6 octahedra. This controversial result indicated that the polarization directions, in fact, resulted from averaging over relative occupancies of the eight displaced sites[89–91]. The order-disorder mechanism is a result of strong short range forces. Ba^{2+} has an ionic radii of 1.36 Å, and is larger than Pb^{2+} of 1.20 Å. This expands the lattice of $BaTiO_3$ such that the tetragonality decreases compared to $PbTiO_3$[89], giving room for and driving the Ti^{4+} to distort along all the [111] directions. Also, Ba^{2+} does not have a lone-pair as Pb^{2+} in $PbTiO_3$, such that long range ordering is weaker than in $PbTiO_3$, as discussed in the previous paragraph.

For strictly order-disorder phase transitions, the Ginzburg regime is expected to be broad. The energy stored in fluctuations remains significant across the phase transition since the expectation value of the local order parameter decreases only slightly.

Real materials

The displacive and order-disorder mechanisms are limiting cases for ferroelectric phase transitions. Phase transitions in all real ferroelectric materials have contributions from both, including the example systems $BaTiO_3$ and $PbTiO_3$. Another example is the ferroelectric perovskite $LiNbO_3$ where Nb^{5+} atoms are off-centered at low temperature[92]. Upon heating, the Nb^{5+} ions move displacively closer to their centrosymmetric positions. At roughly 400-500 K below the phase transition, the Nb^{5+} ions disorder between two possible configurations, causing

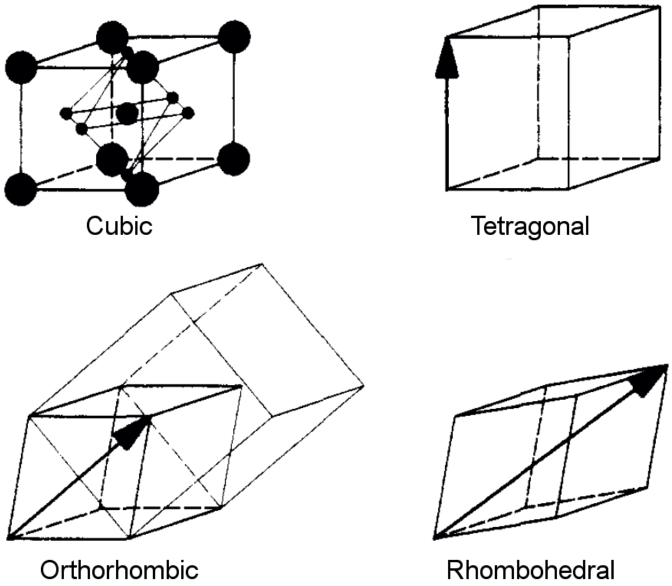

Figure 2.7: Symmetry breaking in proper ferroelectric $BaTiO_3$. Schematic diagrams of the crystal symmetries in $BaTiO_3$ upon the structural phase transitions on decreasing temperature. The arrow indicates the direction of the macroscopic polarization and distortion of the cubic unit cell. The larger unit-cell superimposed in the orthorhombic case shows the relationship of the crystallographic orthorhombic unit cell to the distorted pseudo-cubic cell. Reprinted from Kwei *et al.*[87].

electric dipoles in the material to cancel and macroscopic polarization to decrease faster as temperature rises. An example of a non-ferroelectric with mixed order-disorder and displacive character is the perovskite $SrSnO_3$. This material goes through an octahedral tilting transition[93]. In the low-temperature structure of this perovskite, the octahedra are rotated in-phase, with two symmetry allowed directions of the tilt, see Fig. 2.8. Upon heating, this tilt angle first decreases displacively as the lattice expands. At around 200 K below the phase transition, the structural tilt disorders between the two allowed tilt directions, such that the average tilt goes to zero, while the local tilt is conserved.

Continuous disorder

At the phase transitions of $BaTiO_3$, $LiNbO_3$ and $SrSnO_3$, the local structure disorders upon heating between *discrete* minima in the energy landscape. The minima exist because of short range forces favouring specific atomic configura-

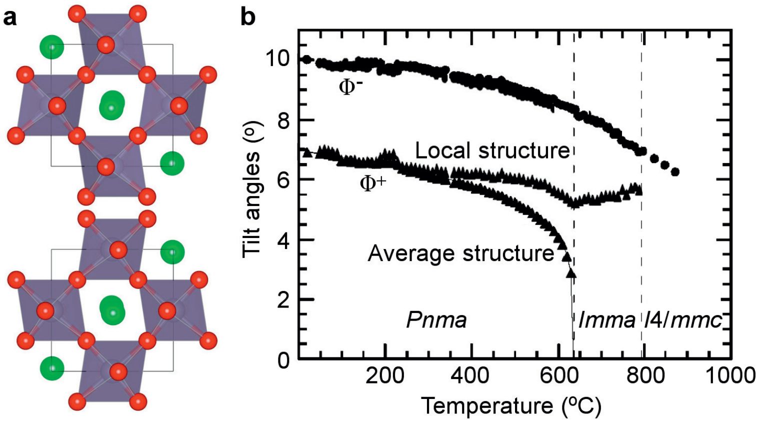

Figure 2.8: Order parameter evolution in perovskite $\mathrm{SrSnO_3}$. (a) Structures showing the two symmetry allowed tilt directions (Φ^+) of the rotational perovskite $\mathrm{SrSnO_3}$ in the $Pnma$ space group. **(b)** Refined tilting angles from diffraction showing that the structure becomes disordered between the two tilt directions ∼200°C before the structural phase transition at 630°C. Locally the Φ^+ tilt is conserved although the two tilt directions cancel out on average, to give an $Imma$ symmetry. *Modified from Mountstevens et al.*[93].

tions. If the short range forces do not favour a discrete number of states, the structure could disorder between a continuum of states. For e.g. $\mathrm{SrSnO_3}$, this would result in a continuum of tilting directions. This type of disorder is difficult to imagine for an crystalline material. The combination of a lattice with restricted rotational degree of freedom and short range forces locks atoms in more or less discrete positions. In Chapter 4, this special form of disorder is shown to exist on heating to T_C in the hexagonal manganites, as fluctuations of a two-dimensional order parameter lowers the symmetry. Structural refinement of scattering data of such continuous disorder includes an additional level of complexity. Materials with discrete disorder is often successfully refined to the ground state symmetry. However, continuous disorder with lower symmetry can no longer be refined to the ground state symmetry, and other approaches are needed.

2.2.2 Chemical stability: non-stoichiometry and point defects

No real material is perfect at finite temperatures, as entropy will always favour changes in composition or structure. When investigating *physical* ground state properties of materials at very low temperatures, one can often assume low defect concentrations. The properties of materials at elevated temperatures are often determined by exchange of atoms with the surroundings. Therefore one needs to consider high concentrations of impurities and structural defects, such as ionic or electronic conductivity. This conceptual separation between physical ground state research at low temperatures and electrochemical studies at high-temperature becomes blurred as the dimensionality of materials enter the nano range[10,11]. Defects are known to change e.g. conductivity, colour, luminescence and magnetic susceptibility of materials. Understanding how defects affect the material properties and how they are implemented not only provides the ability to control their existence, it also opens up new ways for tailoring material properties[94].

Point defects and compensation mechanisms

The dimensionality and spatial extent of defects vary. Pores and voids are considered three-dimensional, grain boundaries are examples of two-dimensional *interfacial defects*, while twin boundaries and line dislocations are considered one-dimensional *line defects*. *Point defects* are zero-dimensional atomic deviations from an otherwise perfect crystal lattice. They can be substitutional atoms, vacant atomic positions, or additional atoms between lattice sites, called interstitials, as illustrated in Fig. 2.9. Common defects in materials with atoms of similar sizes and charges are anti-site defects in which two atoms have interchanged lattice sites.

Any point defect has to be accommodated by the material such that charge balance is preserved. Compensation can be done either by another defect, or by electrons. Removing a neutral oxygen atom from an oxide will leave two electrons behind in the material. These electrons can be accommodated by one or more cations, which become formally reduced. The electrons can also be removed from the material along with a positively charged cation, ionically compensating the oxygen vacancy with a cation vacancy. Such combined charged-balanced cation and anion vacancies are called *Schottky defects*, and are common in ionic mate-

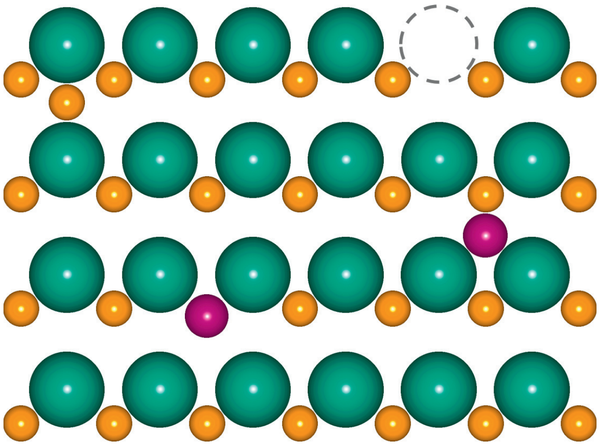

Figure 2.9: Illustration of defect types. *Top left*: an orange interstitial atom, *top right*: a vacant lattice site, *bottom left*: purple substitutional impurity atom, *middle right*: interstitial impurity atom.

rials where the ions have similar sizes and large coordination numbers, such as NaCl or MgO (Eq. 2.6). A vacancy can also be charge compensated by a charge-balancing interstitial, simply viewed as an atom displacing from its lattice site and into an interstitial site. Such defects are called *Frenkel defects*, and are common in ionic materials where the cations and anions have very different ionic radii, such as AgI (Eq. 2.7). Substitutional defects can be charge compensated similarly (Eq. 2.8).

Defect accommodation in materials is usually expressed with *Kröger-Vink* notation[95]. The difference from normal reaction equations is that they express the *site balanced relative* charge of the defects with respect to the host lattice instead of absolute, or formal, charge of the atoms. The notation follows the scheme M_s^c, where M is the defect atom, s is the site it is occupying and c is the relative charge of the defect compared to the original charge of the site. The site can be a lattice site, noted by the name of the element, or an interstitial site, noted i. Positive charge is noted as $^{\bullet}$, negative charge by a $'$, and the use of an $^{\mathrm{x}}$ means that the relative site charge is neutral. One should keep in mind that a Kröger-Vink equation always presents the charge compensating electrons or holes as localized on specific atoms which will be misrepresented in cases where the charge carriers are delocalized.

Schottky defect in MgO:

$$\mathrm{Mg_{Mg}^{x} + O_{O}^{x} \rightleftharpoons v_{Mg}'' + v_{O}^{\bullet\bullet} + Mg_{surface}^{x} + {}^{1}\!/\!{}_{2}O_2(\mathit{g})} \tag{2.6}$$

Frenkel defect in AgI:

$$\mathrm{Ag_{Ag}^{x} \rightleftharpoons v_{Ag}' + Ag_{i}^{\bullet}} \tag{2.7}$$

Substitutional cation from $\mathrm{TiO_2}$ in $\mathrm{YMnO_3}$:

$$\mathrm{TiO_2 + Mn_2O_3 \xrightleftharpoons{YMnO_3} Ti_{Mn}^{\bullet} + Mn_{Mn}' + 5\,O_{O}^{x}} \tag{2.8}$$

Structural effects of point defects

The illustration of defect types in Fig. 2.9 does not consider the structural changes associated with defects, although point defects can cause both local and global distortions of the structure. The structural effect of the defects are mainly determined by three factors: i) how they are charge compensated, ii) how strain is mediated in the structure, and iii) the concentration of the defects. Fig. 2.10 shows how charge compensating electrons, for oxygen vacancies, and electron holes, for cation vacancies, cause structural expansion or contraction in transition metal oxides depending on whether the charge carriers are fully localized or fully delocalized in the lattice. For fully localized charge carriers, the structural changes will be mainly local. The rigidity of the bonds and the rotational flexibility of the polyhedra determines how far away from the defect the structural changes are negligible. If the concentration of defects is so high that the defect-defect distance is shorter than the range of structural distortions, the material contracts or expands globally. In most materials, the charge carriers are neither fully localized nor delocalized, giving an intermediate situation. In bulk perovskite transition metal oxides it is well established that oxygen vacancies cause an expansion of the crystal lattice due to the localized charge compensating electrons. As the oxygen site becomes vacant, the two neighbouring cations are no longer screened by the oxygen. Additionally, they accommodate the charge compensating electrons and increase in ionic radius. This creates a strong repulsion between the cations, known as *chemical expansion*[96,97]. It is most pronounced in perovskites containing multivalent transition-metal ions which can readily accommodate the associated change in formal charge as localized electrons[14,94,98–101]. In materials with no multivalent species, localized charge compensation is not possible and can lead to opposite trends for the chemical expansion[102].

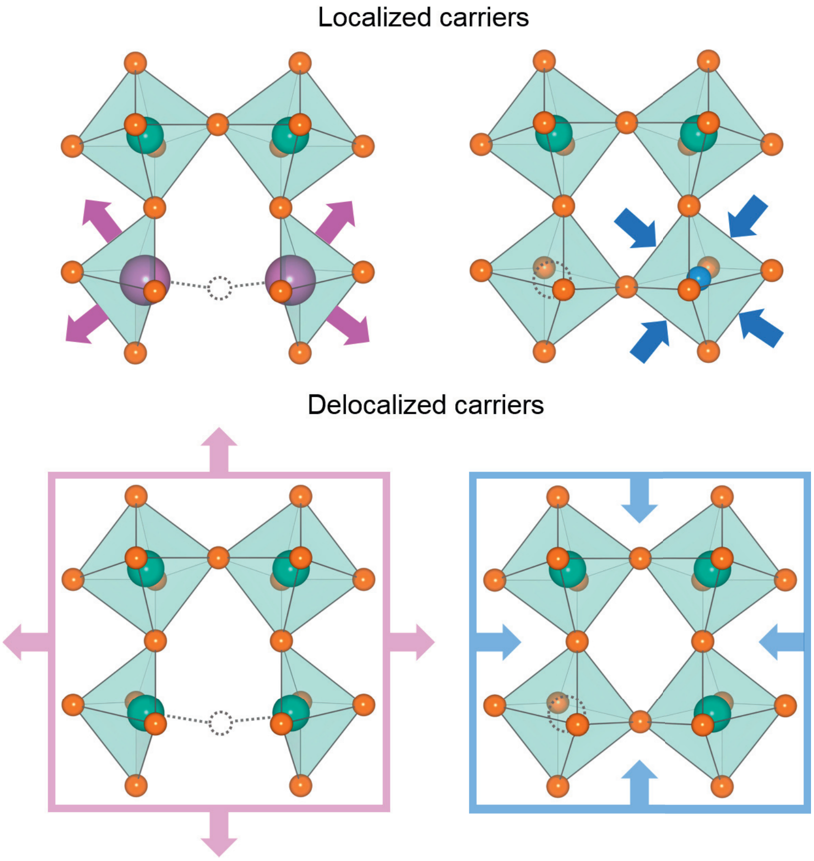

Figure 2.10: Charge compensation and chemical expansion and contraction. Structural changes due to charge compensation of vacancies in a perovskite with and without redox active transition metal. Dotted lines represent vacancies. *Top left*: Oxygen vacancy with fully localized charge compensating electrons on redox active transition metal leading to *local expansion* of the lattice. *Bottom left*: Oxygen vacancy with fully *de*localized charge compensating electrons leading to *global weak* expansion. *Top right*: Cation vacancy with fully localized charge compensating holes on redox active transition metal leading to *local contraction* of the lattice. *Bottom right*: Cation vacancy with fully *de*localized charge compensating holes leading to *global weak* contraction.

Defect formation energy

For the formation of defects in a crystal lattice to be spontaneous, the change in the free energy for the reaction must be negative:

$$\Delta G = n(\Delta H - T\Delta S_{\mathrm{vibr}}) - T\Delta S_{\mathrm{config}} < 0, \tag{2.9}$$

where ΔH is the enthalpy of formation for one defect, ΔS_{vibr} is the vibrational entropy associated with one defect, and $\Delta S_{\mathrm{config}}$ is the configurational entropy for n defects accommodated in a lattice of N atoms. In enthalpy stabilized materials, defects are created when the contribution from the entropy terms becomes negative. In first principles calculations, the materials are modelled at 0 K, such that only enthalpy is calculated. Entropy can be calculated only if more advanced schemes are employed to account for finite temperatures. The defect formation enthalpy for a defect in a charge state q is defined as[103–105]

$$E^f = \Delta H = E_{\mathrm{tot}}^{\mathrm{w/def}} - E_{\mathrm{tot}}^{\mathrm{wo/def}} - \mu_{\mathrm{def}} + qE_{\mathrm{F}} + E_{\mathrm{corr}} \tag{2.10}$$

The total energies $E_{\mathrm{tot}}^{\mathrm{w/def}}$ and $E_{\mathrm{tot}}^{\mathrm{wo/def}}$ are calculated for supercells with and without the defect. The chemical potential of the defect species represent the energy of the reservoirs with which atoms are being exchanged. If the total charge of the system changes upon inclusion of the defect, the charge has to be multiplied with the Fermi energy. E_{corr} is a correction term that accounts for errors originating in the limitations of first principles calculations, and will be addressed in Section 3.1.

Point defects and functional properties

The formation energy and transport properties of point defects are often coupled to the electrostatic and elastic properties of the host. Controlling the amount of reversible oxygen defects and their effects on macroscopic and atomic level is not only important in order to avoid their detrimental effects on physical properties, such as for example ferroelectric fatigue[106–108] and domain wall pinning[109]. It is also well known that point defects are crucial for some functional properties of oxides used in electrochemical devices like solid oxide fuel cells[12], batteries[13] and memristors[110–112]. Using point defects as a design parameter to tailor and create new properties in multiferroics, especially on the atomic level, is imperative to reach the goal of making new multiferroics for devices[10,18,113]. As components are made smaller, the available length for point defects in materials to diffuse is made shorter. This reduces the time required for the point defect to diffuse through the samples compared with bulk materials[14]. Controlling the electrochemical properties that arise in small components has potential for future applications. Engineering the point defect populations at domain walls and harvesting the the electrochemical phenomena that arise, motivates the study of hexagonal manganites[10,15,17,18,25,114–117].

2.3 The hexagonal manganites

2.3.1 Crystal structure and electronic structure

The hexagonal manganites consitute a series of $R\mathrm{MnO}_3$ oxides where the rare-earth cation R is Y, In, Sc, Ho,..,Lu. The hexagonal structure can also be stabilized in reducing atmosphere for R = Dy[119], and with epitaxial strain for R = Dy, Ga, Eu[120] and Tb[121], although the orthorhombic *Pnma* structure is the ground state in bulk for these compositions. The hexagonal manganite structure consists of layers of corner-sharing Mn^{3+}-O_5 trigonal bipyramids separated by layers of rare-earth cations, presented in Fig. 2.11**a**. Most of the hexagonal manganites have space group symmetry $P6_3cm$, which is ferroelectric due to an improper mechanism where the rare-earth layers are shifted slightly with respect to the Mn-O layers. This leads to a small polarization of about ∼5.6 μC cm^{-2} at room temperature. The rare-earth cations are alternatingly shifted in an up-down-down pattern. The total off-centring of the R cations is described by the R corrugation, shown in panel **b**. The R corrugation is strongly coupled to the Mn-O bipyramids tilting in trimers as seen in panel **c**. The bipyramids are slightly distorted, giving rise to two distinct tilt angles, as defined in panel **d**. These tilt angles, and the Y corrugation, are direct measures of the *structural trimerization*. This trimerization is described by the primary order parameter Q, Φ of the K_3 phonon mode. The parameters are central in all three chapters presenting the results of this work. The alternative presentation of the structure in panel **b**, emphasizes the rigid Y-O_7 polyhedra where each Y is bonding to six apical oxygens (O1 and O2) and one planar oxygen (O3 or O4). For less ionic compositions of the hexagonal manganites, such as InMnO_3, the coupling to the polarization is weaker. Hence, both an anti-polar structure with the higher $P\bar{3}c1$ symmetry and the polar structure have been reported as the ground state[113,122]. The anti-polar symmetry is related to the polar symmetry by ro-

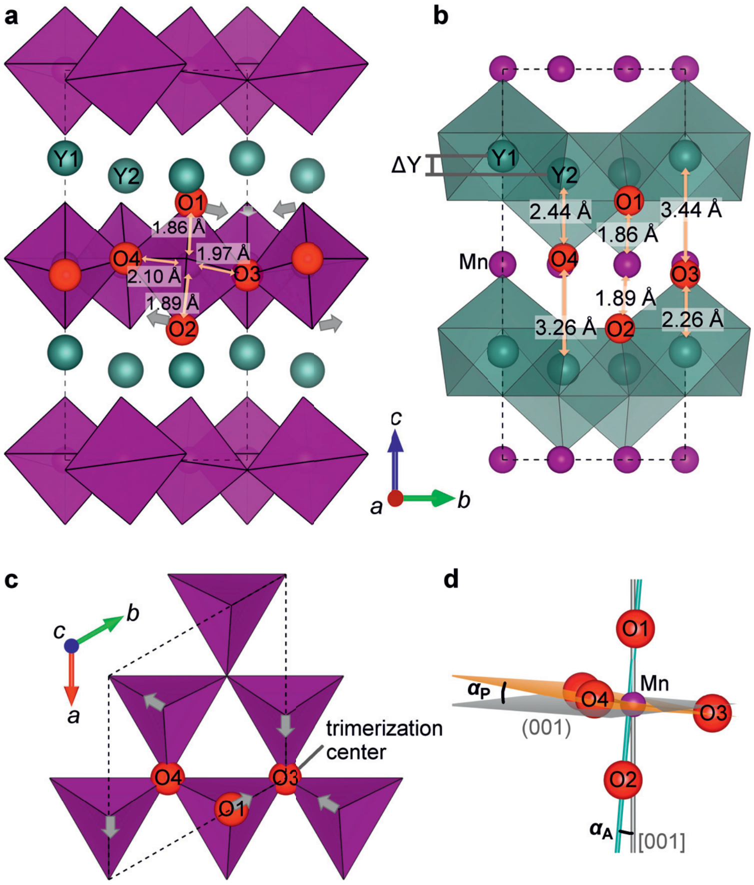

Figure 2.11: The polar hexagonal manganite structure. (a) Unit cell of the prototypical hexagonal manganite $YMnO_3$ with space group $P6_3cm$, visualized with the traditional MnO_5 trigonal bipyramids (purple with red oxygen atoms) emphasizing the atom sites, up-down-down pattern of the Y atoms (blue-green) and the tilting pattern of the bipyramids. **(b)** Similar unit cell of $YMnO_3$ visualized with YO_7 polyhedra. The Y corrugation, ΔY describes the summed off-centering of Y1 and Y2 from high-symmetry symmetry positions (all Y in the same plane) along the c axis, calculated as $\Delta Y = c(z_{Y1} - z_{Y2})$. **(c)** The bipyramidal tilting pattern seen along the c axis showing that O3 are trimerization centers. **(d)** Definition of planar, α_P, and apical α_A tilting angles of the trigonal bipyramids. Bond lengths are taken from X-ray diffraction measurements by Van Aken *et al.*[118].

tating the trimerization angles in Fig. 2.11**c** by 30° such that the out-of-plane dipoles cancel. This competition between the polar and non-polar symmetry of the hexagonal manganites is highly temperature dependent and is the reason for the unusual symmetry breaking across the ferroelectric transition, as will be discussed in Chapter 4.

The trigonal bipyramidal crystal field around the d^4 electrons of Mn^{3+} leads to four unpaired spins[123,124], as shown in Fig. 2.12**a**. The resulting magnetic moments on neighbouring Mn preferably orders antiferromagnetically. As the lattice is hexagonal, 180° antiferromagnetic order is not possible, and the spins take on a frustrated ordering with 120° spin angles[125–130], as illustrated in Fig. 2.12**b**.

The weak improper ferroelectricity and frustrated antiferromagnetism does not make the most interesting combination of multiferroicity for technological purposes. However, the coupling between the two properties and how they are manifested in the domain structures of these material is of fundamental interest. The hexagonal manganites belong to the class I of multiferroics, and have high ferroelectric Curie temperatures T_C around 1250 K[131] and magnetic Néel temperatures T_N below 100 K[132]. There are several allowed trigonally frustrated antiferromagnetic orderings for the hexagonal manganite series[130], and the coupling to the ferroelectric structure (Fig. 2.11**b**) and role of the rare-earth cations on the magnetic order is not yet fully understood[132–139]. The hexagonal manganites are insulators with a band gap of ~1.5 eV due to the Coulombic repulsion between the Mn d^4 electrons[123,140,141].

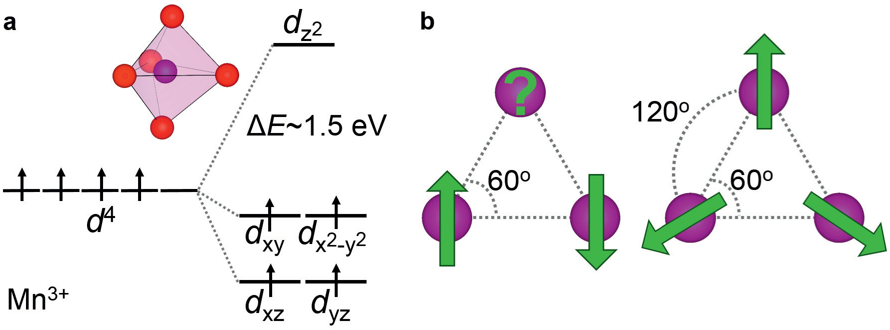

Figure 2.12: Electron structure. (a) Trigonal bipyramidal crystal field splitting of the d^4 electrons of Mn^{3+}. **(b)** Antiferromagnetism imposed on a hexagonal lattice (left) leading to a frustrated antiferromagnetic order with 120° between the magnetic moments (right).

2.3.2 Improper ferroelectricity of the hexagonal manganites

The improper mechanism was first proposed by Fennie and Rabe[24]. They investigated systematically the energy of the allowed structural distortion, as presented in Fig. 2.13. Their first-principles calculations on $YMnO_3$ showed that the zone-boundary K_3 mode, inducing the structural trimerization, was mainly responsible for the energy lowering structural distortions upon the ferroelectric transition. However, as seen from the figure, a zone boundary mode can, due to symmetry, not cause polarization, meaning that there had to be another polar zone-centered mode coupling to the K_3 mode. They found that the polar Γ_2^- mode couples strongly to the K_3 mode, shifting the Y layers along c with respect to the Mn layers. This improper mechanism has also been reported for the hexagonal manganite $LuMnO_3$[142], and accepted for all the polar hexagonal manganites and ferrites. The Laudau free energy and the local symmetry breaking upon the ferroelectric phase transition in the hexagonal manganites are discussed further in Chapter 4.

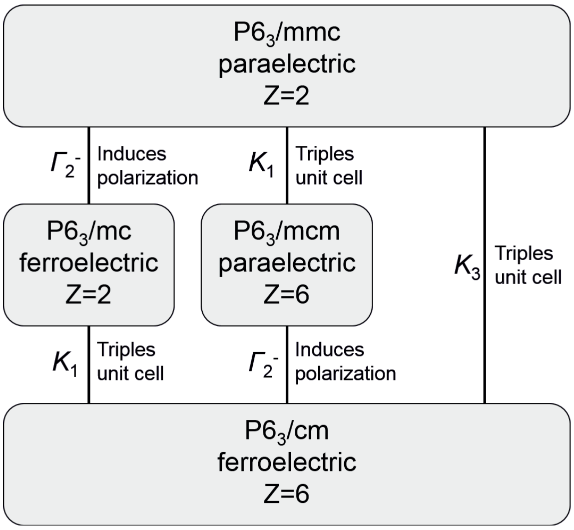

Figure 2.13: Group-subgroup relations. Allowed phase transition phonon modes and their group-subgroup sequence between the high-temperature non-polar $P6_3/mmc$ and polar $P6_3cm$ space groups. Each transition is labelled by a phonon mode in the high-temperature phase which will cause structural distortions corresponding to the possible low-symmetry phases. *Inspired by Fennie and Rabe*[24].

The first pictures of the intricate clover-leaf-like ferroelectric domain structures in the hexagonal manganite $YMnO_3$ were reported already in 1967[143]. Due to different etching rates of the antiparallel domains, the domain structures could be imaged by an optical microscope, shown in Fig. 2.14**a**. The trimerization of the ferroelectric space group gives three different tilting directions of the trigonal bipyramids. Combining these with two possible directions of the polarization, results in six symmetry equivalent domain structures, illustrated in Fig. 2.15. Failed attempts of poling the material into monodomain states by applying electric field upon cooling, show that the domain structures are not electrostatically driven and that the meeting points of the domains are topologically protected[116,144]. These topologically protected domain wall intersections are often referred to as vortices, in the middle of Fig. 2.15, and they cannot be moved or removed below the ferroelectric transition temperature[25,145–152]. Similar domain structures have been imaged in the whole series of hexagonal manganites, and the size of the domains depend strongly on the type of rare-earth cation[81], as seen in Fig. 2.14**b**. The vortex density also depends on the quench rate of the sample through T_C, possibly according to a Kibble-Zurek scaling law[153,154], which was developed within cosmology. The ferroelectric domain structures in the hexagonal manganites have been suggested to form via the same symmetry breaking as cosmological strings in early-universe physics. Hence, the materials

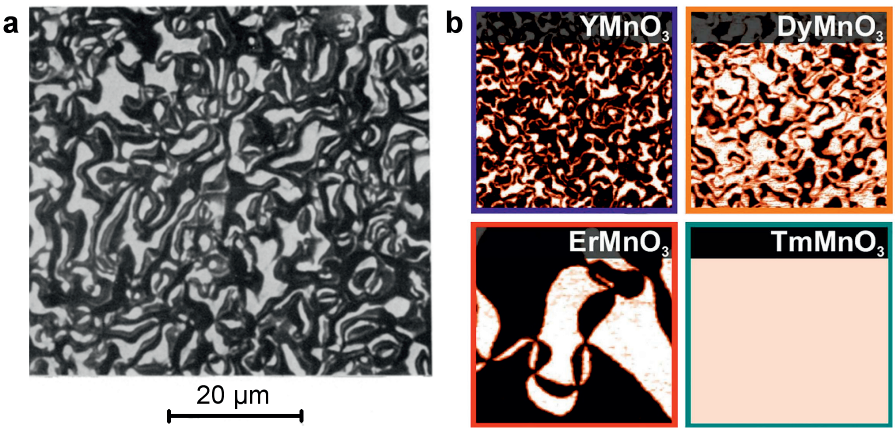

Figure 2.14: Hexagonal manganite domain structure. (a) Optical microscopy picture of $YMnO_3$ cooled at 1 K/min after etching. *Reprinted from ref. 143*. **(b)** Piezo-force microscopy images of material regions of equal size of $RMnO_3$, R = Y, Dy, Er, Tm, cooled at 1 K/min. The domains in $TbMnO_3$ are larger than the pictured area. *Reprinted from ref. 81*.

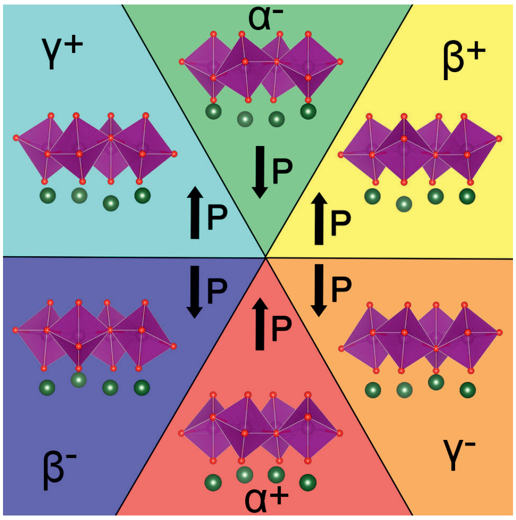

Figure 2.15: Topologically protected vortex where all six domains meet. The polarization alternates by 180° from one domain to the next, and the trimerization angle changes by 60°.

provide a new model system to study the formation of cosmic strings in a relatively low-temperature material system[81,155–157]. The creation of the universe and its behaviour just after the Big Bang is still a fundamental mystery in science. The possibility of studying the symmetry breaking in the early universe through a single material system is a great supplement to the current methods of cosmologists. Experiments to study the physics involved have so far been limited by the temperatures that can be reached by man-made devices.

The technological interest in the domain patterns is due to their structural stability and the material's ability to accommodate point defects. As the failed poling attemps also show, the improper ferroelectricity results in especially stable domain walls. Studies have showed that both neutral and charged domain walls can have higher electrical conductivity than the bulk[26,116,158–160]. It is likely that increased conductivity at charged domain walls arises due to charged ions, electrons or electron holes that screen the electrostatic field[26,158,160]. The increased conductivity at the neutral walls have been proposed to arise from point defects which accumulate at the walls due to strain fields[161] or from low-energy structural dynamics[162]. Which defects that are accumulating at the domain walls and how to tune the concentration of them are still open questions.

2.3.3 Chemical stability, non-stoichiometry, and point defects

The phase diagram for compounds in the Y-Mn-O system[163] is presented in Fig. 2.16, and is qualitatively representative also for the other rare-earth hexagonal manganites. The phase line for the hexagonal manganite $YMnO_3$ in the middle of the phase diagram assumes a compositionally rigid compound which becomes metastable with respect to Y_2O_3 and YMn_2O_5 below 1062 K[164]. The metastable phase will not automatically decompose into the two end members, since it requires a reconstructive phase transition prevented by a high activation barrier. The hexagonal manganite structure is stabilized at ambient conditions for small rare-earth cations (R = Y, In, Sc, Ho,..., Lu) giving a Goldschmidt tolerance factor of $t < 0.857$. For larger rare-earth cations (R = La-Dy) and tolerance factors, the close-packed orthorhombic perovskite $Pnma$ structure is more stable at ambient conditions[165]. The orthorhombic phase can be stabilized for the small rare-earth cation manganites (R = Y, Er, Ho) at ambient pressure by low-temperature chemical synthesis[166,167], by high pressures and temperatures[168,169], or as thin films with compressive epitaxial strain[170].

Cation point defects

The narrow phase line implies low Mn and Y non-stoichiometry in the structure. However, reports show significant chemical flexibility on both cation lattices and the oxygen lattice of the hexagonal manganite structure. Bulk samples of $YbMnO_3$ and $YMnO_3$ prepared with conventional solid-state synthesis exhibit a rather low flexibility of Mn excess of only $R/\mathrm{Mn}=0.96$. The Mn excess increases grain growth and reduces leakage currents compared to stoichiometric samples[171]. Larger Mn excess of $R/\mathrm{Mn} = 0.72$ have been stabilized for R = Y, Er and Dy in epitaxially strained thin films[172], attractive for non-volatile random access memories[173,174], and by low temperature chemical synthesis routes[175]. Whether the Mn excess is in the form of Y vacancies or Mn filling Y sites, and whether the defects are electronically or ionically charge compensated, is largely dependent on the synthesis conditions. R excess, with a maximum of $R/\mathrm{Mn} = 1.53$, has been reported for epitaxially strained thin films of $YMnO_3$ prepared by radio frequency magnetron sputtering in a partial pressure of O_2 of 12.5%[173].

Also extrinsic defects through isovalent and aliovalent substitutional doping

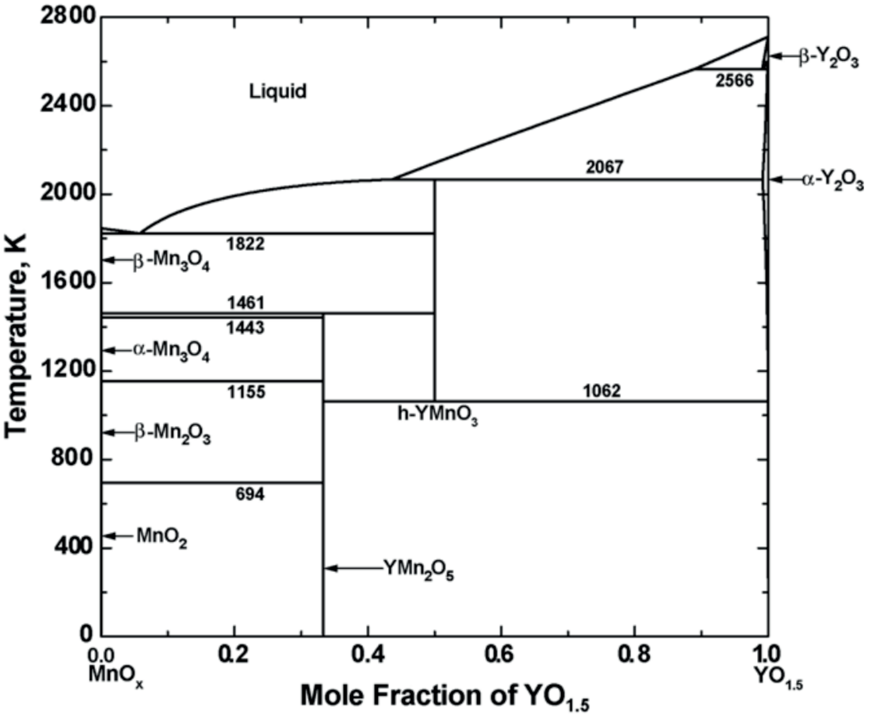

Figure 2.16: Phase diagram of the Y-Mn-O system. *Reprinted from ref. 163.*

of both R and Mn have been studied for their effects on ferroelectric distortion, electrical properties and magnetic order. Isovalent substitution of the Y with other rare-earth cations like Ho, Er, Tm, Yb and Lu has shown an empirical correlation between rare-earth cation size the maximum oxygen concentration, δ, with larger R giving lower leakage currents as it suppresses excess oxygen and formation of Mn^{4+}(ref. 171, 176, 177). The electrical carrier density in samples prepared in air has also been reduced by aliovalent doping of R with Zr^{4+} for the RMnO$_3$, where R = Y, Lu, Sc, by effectively reducing Mn[174,178,179]. The smaller Zr^{4+} cations and the simultaneous reduction of Mn in addition expands the *ab* plane and suppresses the amplitude of trimerization (K_3 mode) and the magnetic moments[180].

Low concentrations of aliovalent substitution of Mn with Ti^{4+} has been shown to enhance magnetocapacitance[181] and suppress the ferroelectric Curie temperature due to expansion of the *ab* plane and contraction of the *c* axis promoting the high-symmetric phase $P6_3/mmc$[182]. In addition to the lattice expansion, the Ti^{4+} doping also reduces Mn^{3+} to Mn^{2+}, which enhances the accommodation of excess oxygen as interstitials. Larger concentrations of Ti causes a phase transition from the hexagonal $P6_3cm$ to layered rhombohedral $R\bar{3}c$[183–185]. Contrary to Ti doping, aliovalent doping of the Mn with divalent Co, Ni and Cu increases the formal positive charge of Mn and thereby enhances the electrical conductivity[186]. Griffin *et al.*[113] recently showed that substitution of Mn with Ga in $InMnO_3$ can be used as a control parameter for the spontaneous polarization of the materials as the more electronegative Ga favours the anti-ferroelectric $P\bar{3}c1$ symmetry. Enhanced spin-lattice coupling has been observed when substituting Mn with isovalent Fe[187,188].

Oxygen point defects

It is well established that control of the oxygen content through synthesis is important to obtain reproducible and desirable structural and electronic properties. Oxygen hyper- or hypostoichiometry in perovskites such as $LaMnO_3$ is well documented and is often tailored to achieve the desired properties[189]. Oxygen vacancies are common in all oxides, and are often formed during the high-temperature synthesis when the entropy favours O_2 (g) (recall Eq. 2.1). Oxygen deficiency in the form of vacancies is known to cause chemical expansion, especially pronounced in transition metal oxides due to localized charge compensating electrons on the nearby transition metal cations[14,94,96,99–101]. For the hexagonal manganites, some studies have shown that oxygen deficient samples have enhanced electrical conductivity at domain walls[26,116], reduced macroscopic spontaneous polarization[190,191], reduced magnetoelectric response[192], and different stability, mobility and shape of ferroic domain walls[115,191,193] compared to stoichiometric samples. The few atomic scale studies that exist on oxygen vacancies in bulk and at domain walls are inconclusive about the positions, structural, and electronic effects of the vacancies. This is discussed further in Chapter 5.

For perovskites and other close-packed oxides, the term *oxygen excess* is used when referring to cation deficiency by vacancies. The perovskite $LaMnO_3$, orthorhombic $YMnO_3$ and FeO with wurtzite structure are examples of materials, which if synthesized in oxidizing atmosphere, will become effectively oxygen rich as the O_2 in the atmosphere reacts with cations that migrate out of the lattice to create new phases. It is established that the multivalency of Mn is the reason for electric leakage currents as it can electronically compensate impurities, dopants, and vacancies. When measurements show existence of oxidized Mn^{4+} in the hexagonal manganites, it is usually explained by cation deficiency[159,178,194]. However, oxides with less densely packed structures, such as fluorites, Ruddlesden-Popper, and hexagonal manganites can in principle accommodate oxygen excess in the form of interstitial oxygen, charge compensated by electron holes. For the hexagonal manganites, large oxygen excess up to $\delta = 0.35$ for $R\mathrm{MnO}_{3+\delta}$ has been reported[119,176,195]. Such high levels of excess oxygen can cause development of secondary oxidized phases, which are easily detected experimentally[177]. Studies on how interstitial oxygens are accommodated in the lattice and how they affect the electronic structure are sparse[182,196], but motivate the investigation of whether this point defect is the origin of the observed p-type conductivity in the hexagonal manganites and the observed anomalies in dielectric measurements[197–201]. Further, how these interstitial oxygens interact with the domain walls has to the authors knowledge not been studied. In particular, the increased conductivity at the neutral walls has not been resolved. This is discussed further in Chapter 6.

Chapter 3

Methods

3.1 Materials modelling: Density functional theory

Density functional theory (DFT) is one of the most applied and successful quantum mechanical approaches to understand matter. It is used in a variety of scientific fields and is routinely used to calculate e.g. the binding energy in molecules and the band structures in solids. DFT is built on a rigid framework consisting of two key concepts: The *Hohenberg-Kohn theorem* and the *Kohn-Sham equations*. In spite of this rigid framework, the flexibility one has in implementing it gives a versatile toolbox for studying many different materials. This chapter gives a short summary of the theory, with focus on non-stoichiometry in extended systems and related functional properties. For more thorough descriptions of DFT and calculations of defects, see e.g. refs. 103, 202, 203.

All information about a system is contained in the system's wavefunction, Ψ, which contains all the information about the positions of the system's electrons. The degree of freedom for the nuclei in the material is included as a potential acting on the electrons. The wavefunction is calculated from the Schrödinger equation, which for a material with N electrons reads

$$\left[-\frac{\hbar^2}{2m}\sum_{i=1}^{N}{\nabla_i}^2+\sum_{i=1}^{N}V(\mathbf{r}_i)+\sum_{i=1}^{N}\sum_{j<i}U(\mathbf{r}_i,\mathbf{r}_j)\right]\Psi=E\Psi \tag{3.1}$$

The left-most term describes the kinetic energy of the electrons, the middle term the interaction energy between each electron and potential from the nuclei, and the third term describes the interaction between the electrons. Since the equation depends on the number of electrons in the system, each with three positional degrees of freedom, the dimensionality of the system is $3N$, which is not feasible for calculations including more than a few atoms.

The full wavefunction in Eq. 3.1 contains all the information about the system, not only the necessary information to describe its electronic ground state. One important observable of the full wavefunction is the electron density, $n(\mathbf{r})$, which describes the probability of finding a non-particular electron at position r. Within density functional theory, the Schrödinger equation is reformulated to depend on the electron density instead of on all the individual electrons, reducing the number of spatial variables from $3N$ to only 3. The total energy of the system is thus described by the following functional:

$$T_0[n] + \int d\mathbf{r}\; n(\mathbf{r})V(\mathbf{r}) + \frac{e^2}{2}\int d\mathbf{r}\int d\mathbf{r}'\frac{n(\mathbf{r})n(\mathbf{r}')}{|\mathbf{r}-\mathbf{r}'|} + E_{xc}[n] = E[n] \tag{3.2}$$

where the first term $T_0[n]$ is a functional of the kinetic energy and the second describes the electrons' interactions with the nuclei. These two terms combined constitute the energy of a non-interacting electron gas in an external potential. The third term describes the Coulombic electron-electron interactions. However, there are other quantum-mechanical interactions described in the full wavefunction which have to be accounted for as well. A fourth term, the exchange-correlation functional, E_{xc}, is therefore included. An exact solution to this functional is not known, as will be revisited further down.

With the total wavefunction replaced by the electron density, the Schrödinger equation can be solved by the help of two theorems proved by Hohenberg and Kohn[204]. The first reads: *The ground-state energy is a unique functional of the electron density.* The word functional means *function of a function*, and the theorem is so important that it has given density functional theory its name. Stated in another way, the theorem says that the potential of the nuclei posed on the electrons, $V(\mathbf{r})$, uniquely defines the ground state electron density and wavefunctions, and vice versa. Although the true total functional of the electron density is not known, the second theorem defines an important property of it: *The electron density that* ***minimizes*** *the energy of the overall functional is the true electron density corresponding to the full solution of the ground state of the Schrödinger equation.* This theorem is used in practice when solving the equation, but the equation is still practically unsolvable due to the many electrons. Kohn and Sham bypassed this difficulty by expressing the equation as a set of equations in which each only involves a single electron[205]. Mathematically, this can be expressed from Eq. 3.2 if the exchange-correlation functional E_{xc} is written in the same form as the two previous terms such that the summation over $\mathbf{r}$ can be separated out from the effective Kohn-Sham potential $V_{KS}(\mathbf{r})$:

$$\left(-\frac{\hbar^2}{2m}\nabla^2 + V_{KS}(\mathbf{r})\right)\psi_n(\mathbf{r}) = \epsilon_n\psi_n(\mathbf{r}) \tag{3.3}$$

$$V_{KS}(\mathbf{r}) = V(\mathbf{r}) + e^2\int d\mathbf{r}'\frac{n(\mathbf{r}')}{|\mathbf{r}-\mathbf{r}'|} + v_{xc}(\mathbf{r}) \tag{3.4}$$

In Eq. 3.3, the wavefunction Ψ of the many-body problem has been replaced by the single-electron wavefunction ψ_n of the n'th electron and the total energy E by the single-electron energy ϵ_n. From the new single-electron wavefunctions, the electron density $n(\mathbf{r})$ can be calculated. The iterations for reaching the energetic ground-state are therefore as follows:

1. Define an initial electron density $n(\mathbf{r})$.
2. Solve the Kohn-Sham equations using the $n(\mathbf{r})$ to find the single-electron wavefunctions $\psi_n(\mathbf{r})$.
3. Calculate a new electron density from the set of ψ_n with $n_{KS}(\mathbf{r}) = 2\sum_n \psi_n^*(\mathbf{r})\psi_n(\mathbf{r})$
4. Compare the new value of $n(\mathbf{r})$ to the initial, and repeat the cycle if the difference is too large.

3.1.1 The exchange-correlation functional

The existence of the exact exchange-correlation functional E_{xc} is guaranteed by the Hohenberg-Kohn theorems, but is cannot be analytically solvable. The simplest approximation is to assume that $n(\mathbf{r})$ is constant at all points in space, such that the exchange-correlation potential $v_{xc}(\mathbf{r})$ can be calculated directly from $n(\mathbf{r})$. This approach is called the *local density approximation* (LDA) and provides an exact solution only for a uniform electron gas. Nevertheless, LDA can give surprisingly good results for complex materials, although it typically underestimates the bond-lengths.

Many other exchange-correlation functionals have been developed, many of which are suited for only one material class. The different functionals employ one of two approaches to improve the accuracy. The first include theoretical derivations forcing the functional to obey constraints set by known features of the exact functional. The other approach employs semi-empirical schemes where one or several parameters are fitted to reproduce experimentally measured parameters, usually energy differences. The most general and known functional a level up from the LDA functional, obtained from the first approach, is the *general gradient approximation* (GGA) functional[206]. In GGA, not only the local density $n(\mathbf{r})$ is used to calculate $v_{xc}(\mathbf{r})$, but also the local gradient in the density, which gives improved values for calculated bond lengths and cohesive energy, compared to LDA. There are many ways to include the local gradient when calculating the $v_{xc}(\mathbf{r})$, giving a variety of different GGA functionals. The two most known for calculating properties of solids are the Perdew-Wang functional (PW91)[207] and the Perdew-Burke-Enzerhof functional (PBE)[208]. The latter has been developed further for solids, called PBEsol, and includes empirical corrections which improve the lattice lattice parameters and bonding energies[209].

DFT calculations can also be performed with spatially localized functions to describe the exchange part of the exchange-correlation functional. These *hybrid functionals* mix exact results for the exchange with approximations of the correlations[210–214].

3.1.2 Plane-waves in reciprocal space

The solutions ψ_n to the Schrödinger equation in periodic systems are plane-waves, which means that the front of the wave lies in a plane, as illustrated in Fig. 3.1. For a periodic system, these solutions must satisfy the boundary conditions given by the periodicity of the system, such that they always have the form

$$\psi_{\mathbf{k}}(\mathbf{r}) = \mathrm{e}^{(\mathrm{i}\mathbf{k}\cdot\mathbf{r})}\ u_{\mathbf{k}}(\mathbf{r}) \tag{3.5}$$

where $u_{\mathbf{k}}(\mathbf{r})$ is periodic in space with the same periodicity as the supercell.[1] Such waves are called Bloch waves[215] and make up the basis for all the energy eigenstates of the system. The position of the plane-wave in real space is given by the vector $\mathbf{r}$, and its wavelength is given by the reciprocal space vector $\mathbf{k}$. DFT problems are in general easier to solve in terms of $\mathbf{k}$ than $\mathbf{r}$, which is why the concept of the reciprocal space is so important. In real space, the smallest unit containing all the necessary information about the material is called a *Wigner-*

---

[1] A supercell consists of several unit cells put together to increase the size of the system in the calculation.

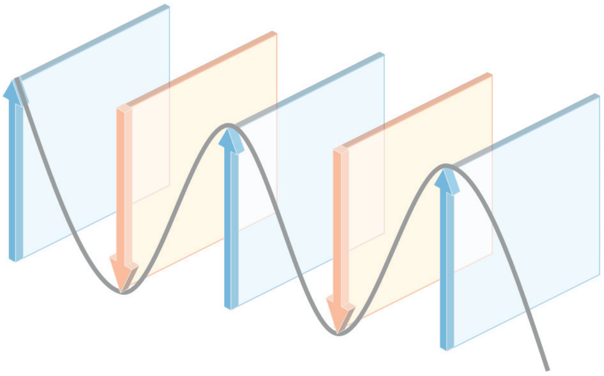

Figure 3.1: Plane wave. Schematic presentation of a planewave where the wave-fronts lie in planes.

Seitz cell, and it can be a simple unit cell or a supercell. The corresponding unit in reciprocal space is called the *Brillouin zone*. DFT calculations are solved by integrating functions over the Brillouin zone, which is mapped by a selection of **k**-points. A method to efficiently evaluate the integrals was developed by Monkhorst and Pack[216], which requires a specific **k**-point mapping. For even numbers of **k**-points along an axis it is often beneficial to specify a *gamma-centered* **k**-mesh. If the real space supercell has equal length in all directions, then a $M \times M \times M$ **k**-grid should be used. More **k**-points give higher accuracy, but larger supercells require fewer **k**-points since the Brillouin zone is smaller.

The factor $u_{\mathbf{k}}(\mathbf{r})$ in Eq. 3.5 has the form

$$u_{\mathbf{k}}(\mathbf{r}) = \sum_{\mathbf{G}} c_{\mathbf{G}} \mathrm{e}^{\mathrm{i}\mathbf{G}\cdot\mathbf{r}} \tag{3.6}$$

such that the full form of the Bloch wave becomes

$$\psi_{\mathbf{k}}(\mathbf{r}) = \sum_{\mathbf{G}} c_{\mathbf{k}+\mathbf{G}} \mathrm{e}^{\mathrm{i}(\mathbf{k}+\mathbf{G})\mathbf{r}} \tag{3.7}$$

This expression suggests that evaluation of each **k**-point involves summation over an infinite number of **G**'s. Fortunately, each solution correspond to values of kinetic energy, by

$$E_k = \frac{\hbar^2}{2m}|\mathbf{k}+\mathbf{G}|^2, \tag{3.8}$$

and one can assume that low kinetic energies are more favoured in the system than high kinetic energies. The sum can therefore be truncated to involve solutions up to a certain value of **k+G**, corresponding to a cutoff energy E_{cut}.

Pseudopotentials

Bonding and other physical properties in materials is mainly determined by the valence electrons of the atoms. The electrons closest to the core have the highest kinetic energies, of which most will be omitted in the calculation from specifying the kinetic energy cutoff as explained in the previous paragraph. Some of these core electrons are also taken care of by replacing them and the atom cores by so-called *pseudopotentials* in a *frozen-core approximation*. The pseudopotential replaces the electron density of a chosen set of core electrons with a smoothed density that reproduces the important physical properties. Although the concept sounds simple, a lot of effort is required to make pseudopotentials that work equally well in all chemical environments. The chosen set of electrons to be included in the pseudopotential, determines the minimum energy cutoff E_{cut}. Hard pseudopotentials leave out some electrons close to the nuclei with high kinetic energy and therefore require high E_{cut}, while soft pseudopotentials require a low E_{cut}. *Ultrasoft pseudopotentials* (USPP)[217] require especially low E_{cut}, but the potentials need to be constructed from a number of empirical parameters. An alternative to the USPPs is the *projector-augmented-wave* (PAW) method[218] which transforms the high-energy plane-waves near the cores into smooth wave-functions which are calculated more efficiently.

3.1.3 Optimization

How accurate and efficient a DFT calculation is depends first of all on the choice of exchange-correlation functional, pseudopotentials and the basis set for the expansion of the Kohn-Sham wavefunctions. Next, the choice of numerical algorithms for minimization is crucial to find a local minimum for the electron density and the geometry of the system. The minimization of the electron density is often referred to as *electronic relaxation* or *static relaxation*. To obtain a fully relaxed system, ionic positions also need to be updated, which is called *ionic relaxation* or *geometric optimization*. The ionic positions are updated after each self-consistent electronic relaxation by moving them according to the *Hellmann-Feynman*[219] forces. The geometric optimization can also update the supercell volume and shape. The opportunity to keep atom positions, certain lattice parameters, or angles fixed gives the necessary variation to deal with multiple problems. Two commonly used ionic relaxation algorithms are the *conjugate gradient*[220], the *quasi-Newton*[221] and *damped molecular-dynamics*[222] methods.

Energy barriers

It is sometimes of interest to calculate the energy barrier for moving an ion or a polaron between stable positions in the lattice. There can be many possible trajectories for the moving specie between the sites, such that the *minimum energy path* is not always trivial to find. The energy barrier for a specific path can be calculated by creating a series of intermediate "images" for which the static energy of each is found by only electronic relaxation. However, in many cases the lattice will in reality distort to accommodate the moving atom or polaron, causing a lower energy barrier given by such static calculations. This poses a special kind of ionic relaxation problem since the calculation would involve relaxing the structure with the moving atom outside of a local energy minimum. This problem can be solved by connecting each "image" by harmonic springs, or "elastic bands", such that each image cannot relax significantly towards the other images without increasing the energy determined by the spring constant. Mathematically this is expressed by the objective function M over the set of images:

$$M(\mathbf{r}_1, \mathbf{r}_2, ..., \mathbf{r}_P) = \sum_{i=1}^{P-1} E(\mathbf{r}_i) + \sum_{i=1}^{P} \frac{K}{2}(\mathbf{r}_i - \mathbf{r}_{i-1})^2 \tag{3.9}$$

where $E(\mathbf{r}_i)$ is the total energy of the ith image, and K is the spring constant. This *elastic band method* works well for small energy barriers and "simple" transition paths, but can give false results if the penalty for stretching one or more of the springs is too low or the transition path involves "sharp" corners. *The nudged elastic band method* (NEB)[223] is developed to deal with these problems by including real forces perpendicular to the band of springs. Another useful addition to the method is the concept of the *climbing image*[224,225] which adapts the NEB such that it places one image precisely at the transition state and thereby gives a more accurate energy barrier. An illustration of a NEB calculation is given in Fig. 3.2.

3.1.4 Electronic structure and magnetic properties

For any DFT calculation, deduced physical properties related to e.g. optics, magnetism and semi-conductivity are dependent on detailed and correct electronic structures. For materials where the electrons are strongly correlated, such as the d electrons in transition metals, DFT has an inherent weakness since the correlation part of the exchange-correlation functional is not known and has to be

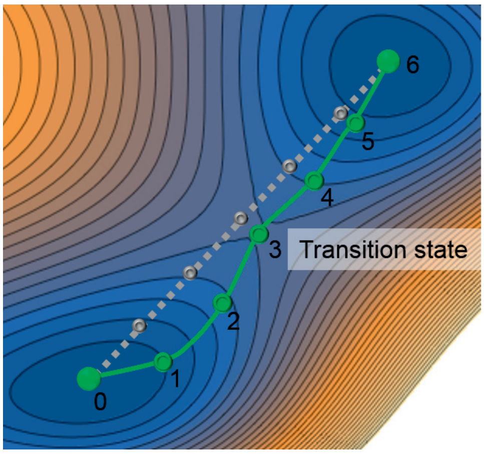

Figure 3.2: Transition state by nudged elastic band. Energy surface with two minima and a transition state at the saddle point. The five intermediate images are initially separated by the same distance along a linear line (grey), but the minimum energy path of the relaxed images is curved (green). The start (0) and end (6) images are not relaxed during the NEB calculation.

approximated. The approximation of the functional does not include electron-electron correlation. This means that DFT has problems describing strongly correlated systems and underestimates the band gap of semiconductors and insulators. Another weakness of DFT is that it cannot calculate exited states, as it is a ground-state technique. This also contributes to the underestimation of the band gap. Much effort has been devoted to develop solutions for this *band gap problem*[226,227].

Often, the use of *hybrid functionals* can provide more accurate band gaps. However, they are computationally heavy and often require thorough calibration. Another simpler method, called DFT+U[228,229], corrects the band gap by including numerical parameters U and J to approximate the on-site Coulomb repulsion between strongly correlated electrons and make them sufficiently localized. The idea of the DFT+U is based on the *Hubbard model*[230], where the electrons are viewed as localized on specific atoms. They therefore experience an "on-site" repulsion from other electrons in the same orbital. The parameters have to be carefully chosen for the specific material system, although there is some transferability between materials containing the same transition metal cation. In the Liechtenstein scheme[231], the U and J are independently specified. In Dudarev's method[232], the $U - J$ is combined to U_{eff}. Beside the ambiguity of the choice of U, the on-site correction by DFT+U is in addition unable to fully capture localization *between* atoms.

When calculating defect formation energies the problem is not the width of the band gap it self, but the positions of the band edges and of the defect energy levels. An oxygen vacancy reducing nearby transition metal cations will introduce new defect levels higher in energy than the valence band maximum. These new levels are thus the new Fermi level and contribute significantly to the defect formation energy.

Although DFT has its limitations for correlated electrons[233], it has been an immensely helpful tool the last decade to unravel the mysteries and phenomena in multiferroics and other functional materials[234,235].

Magnetic order

Magnetic materials have unpaired electron spins which can be disordered or ordered depending on the temperature. It is relatively common to not explicitly include the unpaired spins in DFT calculation, because non-spin-polarized calculations include only half the number of Kohn-Sham equations. This can be justified when the magnetic spins weakly affect the studied properties. However, if the magnetic spins might be important, they need to be implemented in a way which most accurately describes nature. This is easy if the spins are similarly ordered in the material both at the relevant finite temperatures and at 0 K. On the other hand, if the spins tend to be randomly oriented at the relevant temperatures, the ordered spin state at 0 K in the DFT calculation has to be chosen carefully. In frustrated spin lattices, such as the hexagonal manganites, where the spins order in a non-collinear fashion, one needs to consider whether the non-collinear spin order sufficiently improves the description of nature for the computational effort to be worthwhile. Some choices of magnetic order will give a smaller band gap than others, which can be problematic. The magnetic order needs to be chosen in combination with the U for on-site repulsion to reproduce the most accurate physical properties. In frustrated non-collinear antiferromagnetic systems, one attempts to simplify the magnetic order collinearly to reduce computational effort while simultaneously adjusting the U to give the most correct band gap and lattice parameters[141].

3.1.5 Spontaneous polarization

Spontaneous polarization in a ferroelectric material is historically defined as surface charge divided by unit area. Polarization is, however, a bulk property and can therefore also be defined as electric dipole moment per unit volume. The absolute electric dipole moment in a specific volume of the material will depend on the size and position of the unit volume, such that it cannot be unambiguously defined. In the *modern theory of polarization*[236–239] the spontaneous polarization of a periodic system is calculated for several choices of unit cells and distortion amplitudes, such that several *polarization branches* separated by *polarization quanta* can be plotted, as shown in Fig. 3.3. The simplest way of calculating the polarization lattice is to consider all the atoms as point charges with formal charges and sum up their displacements from their centrosymmetric positions. This simple *point-charge model* works well for highly ionic systems where the electron density is confined as spheres around the nuclei. If the bonding in the material has some covalent character, directional variation of the charge density will give an additional contribution to the polarization, and the point charge model becomes inaccurate. In these cases, the polarization can be calculated as a geometric *Berry phase*[240] of the wavefunction, calculating the polarization as the sum of displacements of atoms times their *Born effective charges*. The Born effective charge is analogous to the point charges in the simple model, but also includes the electronic contribution to the polarization by using the charge density $n[\mathbf{r}]$. The *Berry phase method of polarization* is implemented in many DFT codes.

3.1.6 Chemical stability and defects

In a planewave DFT calculation, the temperature is at 0 K, and the material is repeated infinitely such that one does not have to consider any interaction with other chemical environments. This is beneficial if only the bulk properties of the material is of interest. In the real world, materials interact with their surroundings at finite temperatures. Solid oxides strongly interact with the surrounding atmosphere, and can be oxidized or reduced depending on the partial pressure of oxygen. The new oxidized or reduced states can involve phases with different composition, or ionic point defects in the form of interstitials or vacancies. DFT can to a great extent be used to describe thermodynamic phase stability and equilibrium.

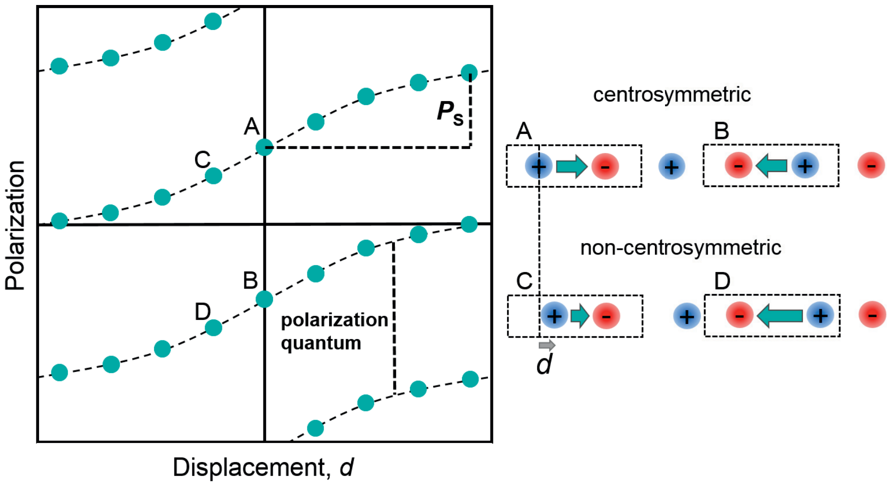

Figure 3.3: Calculation of spontaneous polarization. Polarization as a function of displacement d of the cations in the 1D chain on the right hand side. The polarization branches are centred around zero and separated by polarization quanta. The obtained polarization values from different choices of unit volume are indicated by the letter A-D. *Inspired by ref. 239.*

Chemical stability and phase equilibrium diagram

The stability of an oxide with respect to its related compounds is dependent on the chemical potential of oxygen in the surroundings. For instance, at reducing conditions, $YMnO_3$ can decompose to MnO(s), Y_2O_3(s) and O_2(g), but the particular chemical potential of oxygen when this occurs, is not so easy to calculate directly, as gases are not well-described by a solid-state DFT code. Instead, the ground state energies of all the solid compounds in the related chemical reactions are calculated, and μ_O can be extracted as the only unknown. All the phase equilibria which determine the stability region of h-$YMnO_3$ are presented in the phase equilibrium triangle in Fig. 3.4. Each area of the triangle corresponds to values of the chemical potentials for all three elements, μ_Y, μ_{Mn} and μ_O. Calculations of μ_O from all the areas provide the range in which μ_O can vary. Examples of comprehensible research papers which deal with phase equilibrium confinement, or chemical potential phase space, are given in refs. 241, 242.

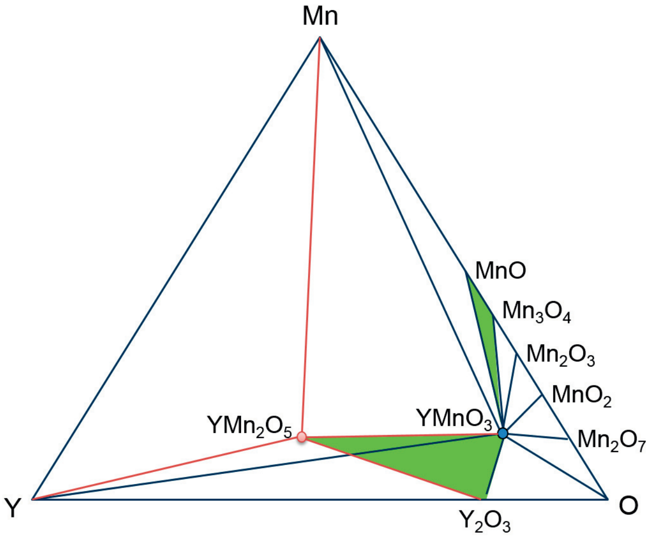

Figure 3.4: Phase equilibrium diagram in the Y-Mn-O system. Each triangle corresponds to phases in chemical equilibrium at specific ranges of the chemical potential of oxygen μ_{O}. The green areas correspond to phase equilibria chosen as the reducing and oxidizing limits for $\mathrm{YMnO_3}$ for the computational work in this thesis.

Non-stoichiometry and point defects

Oxidization or reduction of a material does not have to lead to formation of new phases if point defects can be accommodated in the lattice. The defect formation energy, E^f of a single defect is defined in *dilute limit*. This means that when calculating E^f under periodic boundary conditions, the supercell has to be sufficiently large in order to avoid defect-defect interactions and global change in the supercell volume. The sufficient size of the supercell is determined by the structural distortions around the defect. The defect formation enthalpy for oxygen defects is not equal to the enthalpy of oxidation or reduction, as the latter is the enthalpy required to oxidize or reduce a sample to equilibrium and thus includes defect-defect interactions[243].

Treating the charge difference associated with an aliovalent defects in the lattice is not straight-forward. The defect charge state q in Eq. 2.10 is the total change in charge for the whole system when a defect is implemented. Thus, an oxygen vacancy leaving the lattice as a neutral O atom, will give a charge of $q = 0$, independent on charge transfer between, and formal charges of, the oxygen vacancy and other ions in the cell. On the other hand, if the oxygen leaves as $\mathrm{O^{2-}}$, the system gets a charge of 2+. Charge compensation of defects involving charge transfer between species changes the formal charges of the charge compensating ions. Careful choice of the U parameter for on-site repulsion is important in these situations.

Due to the periodic boundary conditions, charged systems with $q \neq 0$ will have a divergent total charge and spurious interactions between each supercell. These errors may give inaccurate defect formation energies and slow convergence with respect to supercell size[103], and are often corrected by including a correction term E_{corr}, consisting of two parts, to the defect formation energy[244], presented in Eq. 2.10. Numerous correction schemes have been proposed[245–250]. The first term is an alignment of the potential far away from the defect to the neutral bulk potential. Total energies of supercells calculated by DFT are given with respect to the average total electrostatic potential within the supercell[251]. Particularly for charged supercell calculations, the average electrostatic potentials for the pure (neutral) host and the charged defect system must be aligned so that total energies can be consistently compared. Thus, a potential alignment contribution, or a background potential, is added to the correction term E_{corr} in Eq. 2.9 for defect formation energy.

$$E_{\text{corr,PA}} = q(V^r_{\text{D,q}} - V^r_{\text{H}}) \tag{3.10}$$

where the reference potentials V^r of the host (H) and the charged defect (D,q) supercells are determined by averaging the electrostatic potentials in spheres around atomic sites located far from the defect. The second term is a Madelung-correction accounting for the the electrostatic and elastic interactions of repeated charges, scaling with L^{-1} and L^{-3} respectively, which are the origin of the slow convergence. The correction extrapolates the defect formation energy to dilute limit, and a common scheme for cubic systems was provided by Makov and Payne[252], Eq. 3.11. However, this scheme has a tendency to overestimate the charged defect formation energy, and a finite size extrapolation is often a better approach[242,253].

$$E_T\left(\frac{1}{L}\right) = E_T\left(\frac{1}{L} \to 0\right) - \frac{A}{L} - \frac{B}{L^3} \tag{3.11}$$

3.1.7 Project specific details

General

All the DFT calculations were performed with the VASP code[254,255], version 5.3 with the spin-polarized GGA+U implementation of Dudarev[232], and the exchange-correlation described by the PBEsol functional[209]. The projector augmented wave method[218] was used treating Y(4s,4p,4d,5s), Mn(3s,3p,3d,4s) and O(2s,2p) as valence electrons and a plane-wave cutoff energy of 550 eV. Brillouin zone integration was done on a Γ-centred 4×4×2 **k**-mesh for the 30 atom unit cell and with the number of **k**-points reduced proportionally for supercells.

Electronic structure

In most calculations the frustrated *non-collinear* magnetic structure was approximated by a frustrated *collinear* anti-ferromagnetic order (F-AFM)[141] to reduce computational effort. This magnetic order combined with a Hubbard U of 5 eV reproduced the experimental band gap[123] and lattice parameters[118], see Fig. 3.5, which was important in order to obtain accurate defect formation energies for oxygen vacancies. For the calculations of interstitial oxygen in domain wall cells, an A-type antiferromagnetic order combined with $U = 8$ eV was chosen. This magnetic order gave equal spins on all Mn in the same Mn-O layer, such that competing effects between spin direction and domain wall interaction could be avoided. This magnetic order gave artificially weak repulsion between the electrons, rendering the band gap very small even when the Hubbard U was increased to 8 eV. However, interstitial oxygen only creates electron holes at the top of the valence band, leaving the Fermi energy close to unchanged. The size of the band gap, or energy of the lowest unoccupied orbital, is thus less important for the defect formation energy. This simplified magnetic structure would not work well for calculating defect formation energies of oxygen vacancies, as the charge compensating electrons are found in defect states in the band gap. Thus, A-type magnetic order would give artificially low defect formation energies for the oxygen vacancies.

Charge neutral cells were used in most of the simulations due to the relatively high concentration of defects in the chosen supercells, and because, unlike conventional semiconductors, high defect concentrations are observed experimentally in these materials. Simulations with cells of charge -1 and -2, where electrons were artificially added to avoid charge compensating oxidation of Mn^{3+}

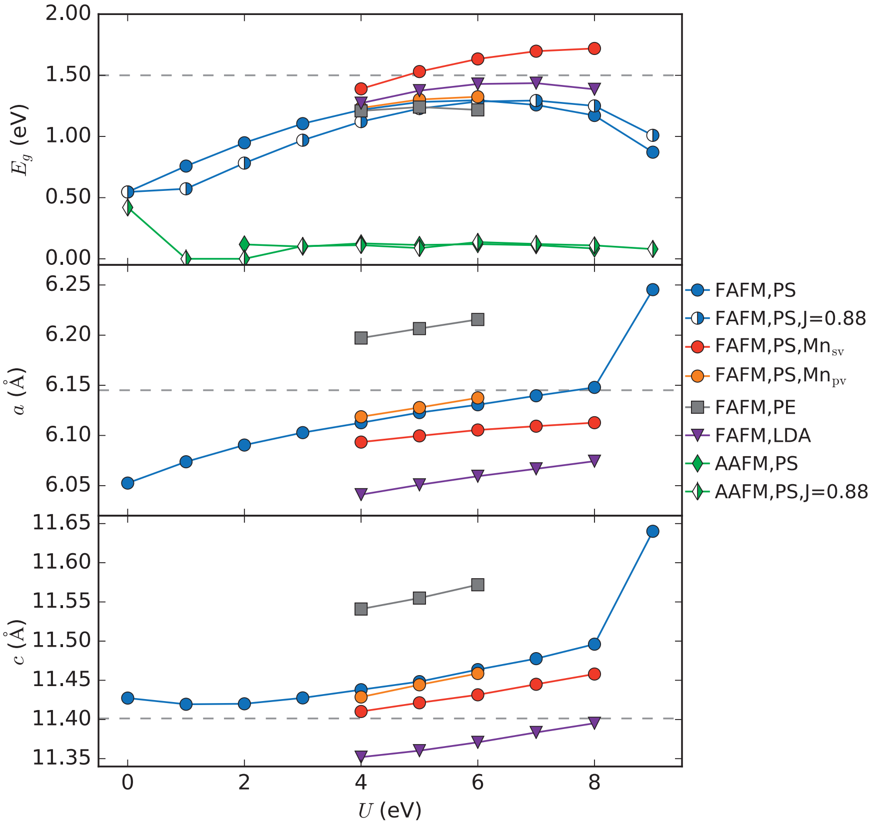

Figure 3.5: Testing of parameters for DFT. Testing of exchange-correlation functionals, magnetic order, on-site Colombic repulsion, and Mn pseudopotential as a function of Hubbard U. FAFM: Frustrated collinear antiferromagnetic order. AAFM: A-type collinear antiferromagnetic order. PE: GGA functional PBE. PS: GGA functional optimized for solids, PBEsol. LDA: Local density approximation functional. The pseudopotential $\mathrm{Mn_{pv}}$ includes only *p* valence electrons, while $\mathrm{Mn_{sv}}$ includes both *s* and *p* valence electrons. For tests with on-site Coulomb potential according to the Liechtenstein scheme, J was set to 0.88 eV. If J is not mentioned, the Dudarev scheme was applied. Experimental values given as dashed horizontal lines.

to Mn^{4+}, gave the same results as neutral cells with respect to the position of interstitial oxygen defects.

Charged (+2) 2×2×1 supercells with oxygen vacancies were also calculated. To calculate the defect formation energies, the potential of the atoms furthest from the defect was aligned to bulk values to obtain a corrected Fermi level according to Eq. 3.10. Electrostatic interaction between periodic images was not corrected.

Supercells and geometric optimization

Different concentrations of defects in bulk were modelled using single unit cells with 30 atoms, 2×2×1 supercells with 120 atoms, or 3×3×2 supercells with 540 atoms. A 2×2×1 supercell was found to be sufficiently large for structural and electronic investigations as it provided small defect-defect interactions compared to the computational cost, as seen in Fig. 3.6.

Neutral 180 ° domain walls were constructed according to models in Kumagai *et al.*[25], and transmission electron microscopy data from Jiang and Zhang[256], and had different geometries depending on the modelled defect. For oxygen vacancies, 1×8×1 supercells with 240 atoms were used. These supercells gave a defect-defect distance of $a = 6.1$ Å, comparable to the structural screening length of the oxygen vacancies. The short defect-defect distance in these supercells probably gave a slight increase in the defect formation energy for the oxygen vacancies, but the relative defect formation energies as a function of position in the cell was the main interest. For interstitial oxygen defects, 5×2×1 supercells were used to avoid anisotropic defect-defect interaction.

Geometry optimization for neutral bulk cells was iterated until the forces on the ions were at least below 0.005 eV/Å for 30, 0.01 eV/Å for 120 and 0.02 eV/Å for 540 atom cells. Neutral cells with domain walls were more difficult to converge due to strain, and were converged until forces were at least below 0.02 eV/Å for 240 atom and 300 atom cells. Charged bulk cells were more difficult to converge electronically, and a force criterion of 0.02 eV/Å was used for 120 atom cells.

Functional properties

The ferroelectric polarization was calculated with both a simple ionic point charge model using formal charges and with the Berry phase method to include electronic contributions. The ionic nature of $YMnO_3$ gave only a small

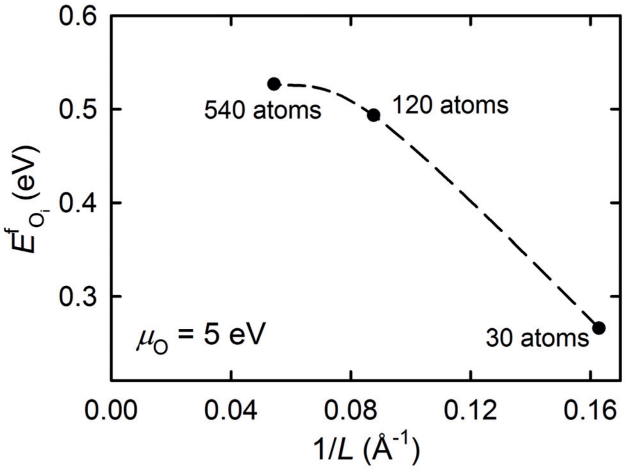

Figure 3.6: Supercell size convergence. Defect formation energy of interstitial oxygen as a function of defect-defect distance L illustrating the effect of supercell size. The 2×2×1 supercell with 120 atoms was found to be sufficiently large for most purposes.

electronic contribution to the polarization, such that the simple point charge model was sufficient to calculate the spontaneous polarization. No significant change in the local ferroelectric polarization was found when increasing the cell size from 121 to 541 atoms including one interstitial oxygen atom.

Migration barriers for interstitial oxygen were calculated with the NEB method using five intermediate images. F-AFM order and a $U = 5$ eV was chosen in order to reproduce the band gap and the localized nature of the electron holes. Test calculations with $U = 0$ eV gave slightly lower migration barriers due to less localized electron holes. Tests with A-type antiferromagnetic ordering and $U = 5$ eV reduced the band gap and the migration barrier due to insufficient localization of the electron holes and very low electron Coulomb repulsion.

3.2 Structure analysis: Total scattering and diffraction

3.2.1 Scattering and diffraction

When materials are irradiated, their electrons and nuclei scatter the incoming radiation in a way which is characteristic for the atomic species. Crystalline materials will scatter radiation to give diffraction patterns with sharp and distinct Bragg peaks which are direct "finger prints" of the crystal structure in reciprocal space. These Bragg peaks are evidence of long-range periodicity in the material which amplifies the constructive interference between scattered waves. For a long time after the development of the X-ray diffraction technique, determination of the atomic arrangements in solids meant determining the average, long-range crystal structure from the Bragg reflections[257]. Materials with no long-range periodicity, such as glasses, were termed "amorphous", i.e. structureless, and the crystallographic analysis would be practically abandoned. Such fully disordered materials with only short-range order are usually studied by local structure techniques such as *X-ray absorption fine structure* (EXAFS) and *nuclear magnetic resonance* (NMR).

Crystalline solids with internal atomic and nanometer scale disorder (see Fig. 3.7) fall between the two categories[258]. The conventional measurement techniques to study either the average or the local structure fail to give any information about how the disorder is mediated though the structure and its spatial extent. To understand how diffraction techniques, originally developed for crystallographic description of long range order, can be extended to obtain this local structure information, one needs to realize that diffraction measurements do not directly measure the actual lattice constants and atomic positions, but the structural coherence of the sample. The structural coherence length, as defined in Section 2.2.1, quantifies the length scale over which the unit cells behave similarly, or coherently. Averaging over regions much larger than the coherence length will give the macroscopic properties, while averaging over regions much smaller than the coherence length may give spatially and temporarily heterogeneous properties.

In conventional reciprocal diffraction, one only analyses the reciprocal signal from structural periodicity with macroscopically long coherence length (see Fig. 3.8). The signal from less periodic disorder is considered noise and is ei-

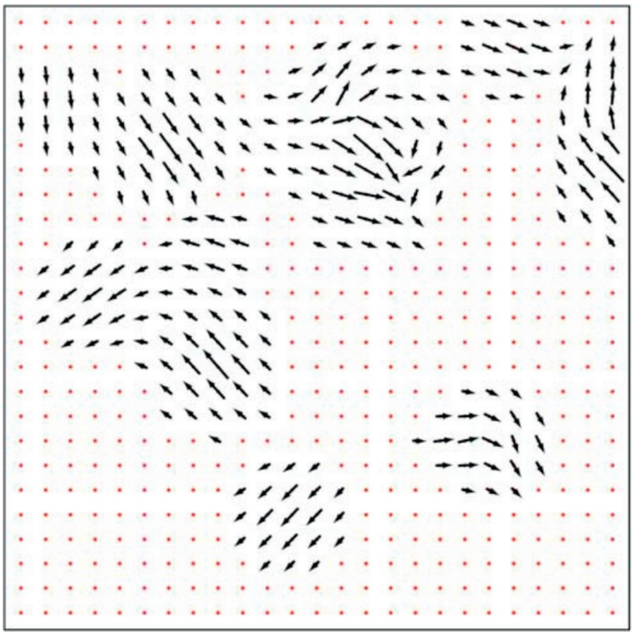

Figure 3.7: When short range order deviates from long-range order. Many functional materials contain regions of short-range order which deviate from the average structure and are key to their properties, yet undetectable within the average structure. The sketch could refer to, for example, ferromagnetic domains within a paramagnetic matrix, or ferroelectric polar nanoregions within a paraelectric matrix. Conventional crystallographic techniques probe long-range structure and will identify only the average extent of disorder; PDF measurements give the atomic pair correlations, from which it is possible to determine how this disorder is correlated throughout the structure. *Reprinted from ref. 259.*

ther approximated by a background polynomial, or as thermal vibration of the atomic positions. To obtain more fruitful information from this diffuse signal, it is much better analysed in real space. In *total scattering* measurements, all the structure relevant scattering from a sample is collected, including both the Bragg reflections and the diffuse signal, over a wide range in reciprocal space. The signal is then analysed in real space as a *pair distribution function* (PDF) showing the distribution of interatomic distances. This makes the technique sensitive to both short- and long-range structural coherence.

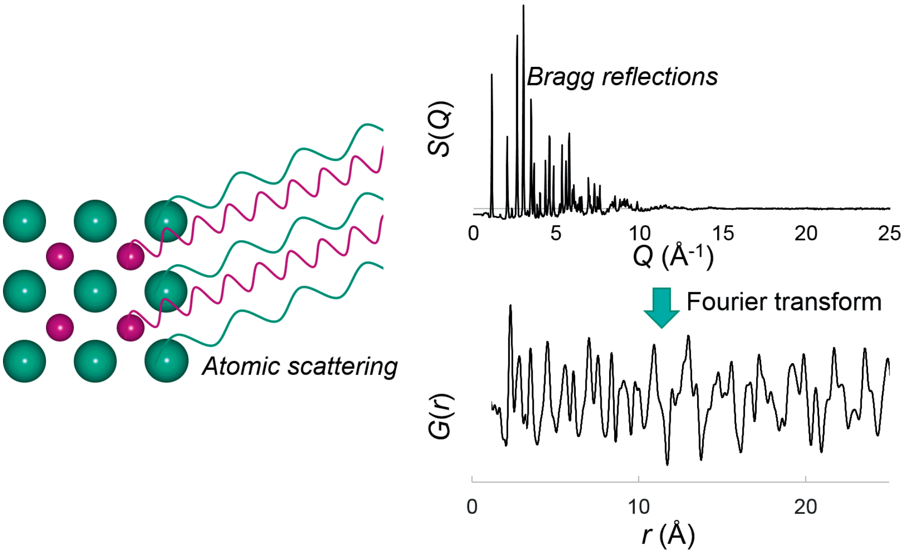

Figure 3.8: Atomic scattering in real and reciprocal space. Atomic scattering from materials with some degree of periodicity will give a reciprocal space diffraction pattern, $S(Q)$, with Bragg reflections as evidence of the periodicity. Diffuse scattering from disorder can be better analysed by Fourier transforming the $S(Q)$ to a pair distribution function $G(r)$ which shows the probability of finding pairs of atoms separated by a distance r.

3.2.2 Wavelength and energy

Diffraction from specific objects is strongest if the wavelength of the radiation is on the length scale of, or preferably smaller than, the size of the objects. Therefore, for a diffraction experiment to give accurate information about small deviations from the average structure, the radiation must have short wavelength. The shorter the wavelength, the higher energy the wave has. High-energy X-rays are usually produced in large facilities called *synchrotrons*. Here, electrons are accelerated to almost the speed of light in a large circle, and then deflected through magnetic fields which slow them down such that they emit high-energy electromagnetic radiation. Synchrotron X-rays can have wavelengths corresponding to a reciprocal space vector $|\mathbf{Q}|$ larger than 100 Å^{-1}. High energy neutrons are created by spallation of mercury, tantalum, lead or another heavy metal when struck by high-energy protons and can reach $|\mathbf{Q}|$ up to $\sim$ 30-50 Å^{-1}. In some scientific fields it is common to present reciprocal space data in terms of the scattering angle, 2θ, which is related to the reciprocal space vector and the wavelength of the radiation by Eq. 3.12.

$$|\mathbf{Q}| = \frac{4\pi\sin(\theta)}{\lambda} \tag{3.12}$$

3.2.3 Radiation types

The use of X-rays and neutrons in diffraction measurements will give different, and in many cases, complementary information. X-rays interact mainly with the electrons of the atoms, such that the scattered intensity increases with the atomic number Z of the atom. As the electron clouds are diffuse, described by atomic form factors, the intensity of the scattered X-rays will decrease significantly with the scattering angle. Neutrons penetrate deeper into the materials than X-rays and interact directly with the atomic cores. There is no relationship between atom number Z and the scattered intensity of the neutrons, but it differs between isotopes. X-ray scattering intensity from electron clouds always have a positive value. On the other hand, some elements such as manganese can have a negative scattering length for neutrons. The diffractograms obtained with X-rays and neutrons can therefore be highly complementary. As an example, vanadium is a strong scatterer of X-rays, but its nuclei hardly scatters neutrons, and is for this reason often used as a container material for neutron scattering measurements. Another feature of the neutrons is that even though they have zero charge, they carry a spin, which means that they are sensitive to the magnetic spin of electrons. They are therefore widely used to study magnetic properties and phase transitions. Furthermore, since the nuclei are practically discrete, and not described by a form factor, the scattered neutron intensity is close to independent of angle. This makes it possible to measure diffractograms with good resolution up to very high reciprocal space vectors.

3.2.4 Formalism

The observable in diffraction measurements is the intensity, $I(Q)$. The *total scattering structure function* $S(Q)$ is the corrected intensity normalized with respect to the compositional average of the scattering amplitude, $\langle b \rangle^2$ for neutrons,

$$S(Q) = \frac{I(Q)}{\langle b \rangle^2} \tag{3.13}$$

and compositional average of the form factor for X-rays:

$$S(Q) = \frac{I(Q)}{\langle f(Q) \rangle^2} \tag{3.14}$$

In some cases it is more practical to use the reduced structure function $F(Q)$ which is related to $S(Q)$ by $F(Q) = Q[S(Q) - 1]$.

The atomic PDF, $g(r)$ is defined as

$$g(r) = 4\pi r[\rho(r) - \rho_0], \tag{3.15}$$

where $\rho(r)$ is the atomic pair density and ρ_0 is the average atomic density and r is the radial distance. The PDF gives the probability of finding pairs of atoms separated by the distance r. The reduced pair distribution $G(r)$ is defined as $G(r) = 4\pi r\rho_0(g(r) - 1)$. It is obtained directly by Fourier transforming the reciprocal space total scattering function $S(Q)$

$$G(r) = \frac{2}{\pi} \int_0^\infty Q[S(Q) - 1] \sin(Qr) \mathrm{d}Q. \tag{3.16}$$

3.2.5 The PDF mindset: Analysing diffraction data in real space

The fundamental goal in crystallography is to reduce the long-range structural information about a material into one unit cell with a specific space group symmetry. This is handily done by studying diffraction data in reciprocal space, where the long-range structure makes itself visible as distinct Bragg peaks. One aims to describe these Bragg peaks by the highest possible symmetry space group, since allowing more structural degrees of freedom would only give excessive information. When dealing with components of disorder, these are often taken into account by adding non-thermal displacement parameters to the atoms causing the disorder, or by mixed occupancy of sites.

When analysing pair distribution functions in real space to investigate disorder, the average structure space group does not necessarily describe the local structure. Hence, the space group symmetry will depend on the coherence length of the structure. The first key when studying disorder is to investigate *how* the measured signal differs from long range space group symmetry. After learning how the long range models fail, one can proceed with separating the information into smaller meaningful pieces. One of the strengths of PDF analysis is that one can learn much from mere visual inspection. For example, the evolution of peak position with temperature can tell whether a specific bond is becoming shorter or longer. Integrating the area under peaks gives direct information about coordination number of atoms. The probability distribution of bond lengths with temperature can be found by investigating broadening and shape of peaks. It should be noted that all such visual analyses are only feasible for rather simple systems, and as complexity increases, one needs to rely more on Rietveld-like analysis in real-space of the PDF data.

For more information about the PDF technique and its versatility in studying structural coherence in complex functional materials, please see refs. 257, 259, 260.

3.2.6 Project specific details

High temperature neutron PDF measurements

Structural characterization was performed over two visits with spallation neutrons at the Nanoscale-Ordered Materials Diffractometer (NOMAD) at the Spallation Neutron Source (SNS) at Oak Ridge National Laboratory (ORNL). About 1.5 mg of sample was placed in a vanadium container with vacuum and measured in the ILL-type vacuum furnace. The NOMAD detectors were calibrated using scattering from diamond powder, and standard Si powder was measured to obtain the instrument parameter file for the reciprocal space Rietveld refinements. During the first visit, the sample was measured at room temperature and between 473 and 1273 K in steps of 20 K. During the second visit, measurements at higher temperatures were performed to obtain more information about the high symmetric structure, and to study chemical expansion as a function of oxygen loss. To obtain the total scattering function $S(Q)$, the scattering intensity was normalized to the scattering from a solid vanadium rod and the background was subtracted using an identical, empty vanadium can measured for the same time as the powder samples. The pair distribution function (PDF) was calculated by the Fourier transform of $S(Q)$ with $Q_{\mathrm{min}} = 0.1$ Å^{-1} and $Q_{\mathrm{max}} = 22$ Å^{-1}.

Post-processing

The average crystal structure over the entire temperature range was determined by reciprocal space Rietveld refinements of the data to the space groups $P6_3/mmc$,

$P6_3cm$[118] and $P\bar{3}c1$ using the TOPAS Academic software, v. 5[261]. Background, absorption (Lobanov), instrument back-to-back exponentials, and sample displacement correction were refined for the 473 K dataset and held fixed to these values for the datasets measured at higher temperatures. Scale and structural parameters were refined for all datasets. Isotropic atomic displacements parameters were used, summarized in Table 3.1. Anisotropic parameters and distinction between Wyckoff sites improved the fits insignificantly while making them more unstable. The input file used for the reciprocal space refinements in TOPAS is given in Appendix B.

The local structure was studied by refining the data to the same three space groups at different ranges of r using the program PDFGUI[262] with a single 30 atom unit cell as the model space group. Refinements at r = 1.6-22 Å gave lattice parameters comparable to those obtained from reciprocal space refinements. Scale, Q_{broad} and Q_{damp} were refined at room-temperature for all three space groups, and kept fixed for all other temperatures. The lattice parameters were then fixed to the values obtained at this range as the r_{max} was lowered to 12 Å in order to probe only local structure within the range of one unit cell. Nearest neighbour correlations ($\delta 1$) and all structural parameters were refined for all datasets.

Table 3.1: Isotropic atomic displacement parameters used in the both reciprocal space and real space refinements of the scattering data.

Position	x	y	z
Y1	$U1$	$U1$	$U1$
Y2	$U2$	$U2$	$U2$
Mn	$U3$	$U3$	$U3$
O1	$U4$	$U4$	$U4$
O2	$U4$	$U4$	$U4$
O3	$U4$	$U4$	$U4$
O4	$U4$	$U4$	$U4$

3.3 In-house synthesis and characterization of bulk samples

3.3.1 Synthesis of bulk ceramics and nanocrystalline powder

$YMnO_3$ powder was prepared by solid state reaction between Y_2O_3 (Alfa Aesar >99.9%) and MnO_2 (Sigma-Aldrich, >99%) or Mn_2O_3 (Sigma-Aldrich, >99%). The powders were dried overnight at 500 °C before weighing and mixed in ethanol in a mortar. Uniaxially pressed pellets were fired twice for 24 hours at 1300 °C in air with intermediate grinding and heating and cooling rates of 200 °C h^{-1}. Phase purity was confirmed by X-ray diffraction between each heating step. For electrical conductivity and Seebeck measurements in various atmospheres, porous bars were prepared to increase the total surface area accessible to oxygen surface exchange. Powders for sintering the porous polycrystalline bars were prepared by mixing phase pure $YMnO_3$ powder with 20 wt% carbon black (Merck) followed by ball milling for 4 hours in ethanol with yttrium stabilized zirconia milling balls. Green bodies were isostatically cold pressed at 200 MPa in a Painan Autoclave Engineers CIP and 1 wt% binder of cellulose acetate (Aldrich) dissolved in acetone was added to improve the green body strength. The porous polycrystalline bars were sintered for 2 hours in air at 1500 °C after a binder burn-off step at 435 °C and polished to dimensions of 15 × 5 × 5 mm. The density of the bar was measured by the Archimedes method[263] to be 43 %. A representative fracture surface of a polycrystalline porous bar is shown in Fig. 3.9. Scanning electron microscopy of the fracture surface was done with a Hitachi S-3400N.

Nanocrystalline powder of $YMnO_3$ prepared by Bergum *et al.*[175] was used for thermogravimetic measurements to increase the total surface area and decrease the diffusion length. The powder was prepared by an aqueous sol-gel synthesis where precursors of $Mn(CO_3) \times H_2O$ (Merck, >99.5%) and $Y(O_2C_2H_3)_3 \times H_2O$ (Heraeus, >99%), complexed by citric acid, with ethylene glycol as a polymerization agent during stirring at 150 °C. Annealing at 950 °C for 1 h, gave nanosrystalline powder with crystallite size of $d = 49 \pm 3$ nm determined by Pawley refinement of X-ray diffraction using TOPAS Academic software[261].

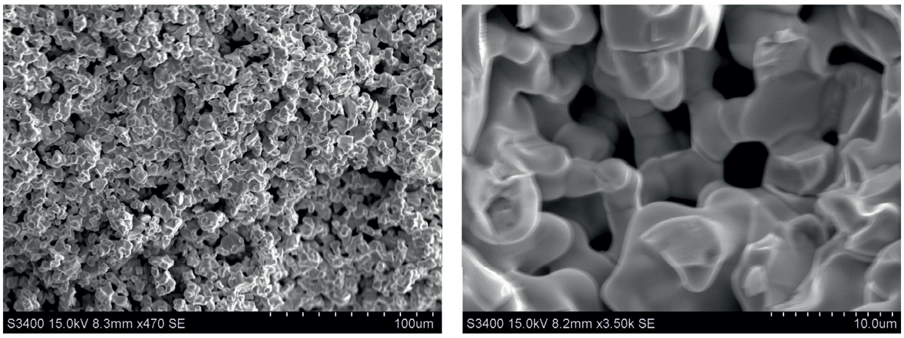

Figure 3.9: Microstructure of porous sample. SEM images of the fracture surface of a porous polycrystalline $YMnO_3$ bar.

3.3.2 Electrical conductivity

The electrical conductivity of bulk polycrystalline samples with dimensions 15.5 ×4.7×4.5 mm and 63% of theoretical density by Archimedes[263] was measured. A home-built instrument described elsewhere[264] with four-point geometry in O_2 and N_2 (Yara Praxair, 5.0) atmospheres was used. Platinum paste was applied to the interface between the platinum electrode wires and the sample and heated *in situ* to 1000 °C to ensure good electrical contact. The conductivity σ was calculated from the equation $\sigma = Id/AV$, where I is the current, d is the distance between the electrodes, A is the sample cross section area, and V is the measured voltage drop between the electrodes. *In situ* heating and cooling was done with 1 °C min^{-1}. The sealed system was not evacuated between the changes of atmosphere. Thus, the exact p_{O_2} in N_2 atmosphere is not known exactly, but estimated to be in the range of 10^{-4} - 10^{-5}. The samples had a porosity of 63% of theoretical density.

3.3.3 Electrical impedance spectroscopy

Impedance spectroscopy measurements (Alpha-A analyzer combined with Novotherm furnace, Novocontrol Technologies) were conducted on disc shaped samples (height 3mm, diameter = 9mm) with sputtered gold electrodes. Samples were subjected to two temperature cycles from 30-350 °C with a heating rate of 2 °C min^{-1}. Frequency sweeps covering a range from 1 Hz and 1 MHz were conducted continuously during the temperature cycles. Prior to measurement, the samples were annealed in flowing O_2 resp. N_2 for 24 hours at 350 °C.

3.3.4 Thermogravimetrical analysis

Thermogravimetric measurements were done on $\sim$ 148 mg $YMnO_3$ nanoparticles with a Netzsch STA 449C Jupiter in flowing N_2 and O_2 (Yara Praxair, 5.0). The sealed system was not evacuated between the changes of atmosphere. Thus, the exact p_{O_2} in N_2 atmosphere is not known exactly, but estimated to be in the range of 10^{-4} - 10^{-5}.

3.3.5 Seebeck coefficient from thermopower measurements

Seebeck-coefficients (S) were measured at 400, 350, 300, 250 and 200 °C in O_2 (Yara Praxair, 5.0) using a ProboStatTM setup (NorECs AS) on a vertically aligned polycrystalline porous (63% of theoretical density) bar (diameter 3 mm, length 12 mm) in tubular furnace[265]. Two S-type thermocouples were used to measure the temperature gradient (20-25 °C), and the voltage across the sample was measured with Pt-electrodes.

Part II

Contribution

Chapter 4

The ferroelectric transition

4.1 Introduction

The content of this chapter has been prepared for publication in manuscript no. 2, given in Appendix A.

4.1.1 Observed anomalies related to the ferroelectric transition in the hexagonal manganites

Although the geometric mechanism and improper nature of the ferroelectricity in the hexagonal manganites is well established, the multiple studies on the structural phase transition, has so far not explained the symmetry breaking and evolution of the polarization with temperature on a microscopic level. A number of previous measurements of the thermal evolution of macroscopic properties on several hexagonal manganite materials (Figs. 4.1 and 4.2) have shown anomalous behaviour at and below the phase transition. In particular, studies based on powder neutron[131,180]/X-ray[101,180,266–269] diffraction have been unable to fit the structural data within standard models. This has led to a range of reported T_C values and also proposals of two distinct structural phase transitions[131,180,266–268], although it is now accepted that there is a single structural transition with the measurable polarization emerging at lower temperatures[24,32,270–272]. This chapter present the results from high-energy neutron total scattering data combined with first principles calculations and explains the local structure across the structural phase transition.

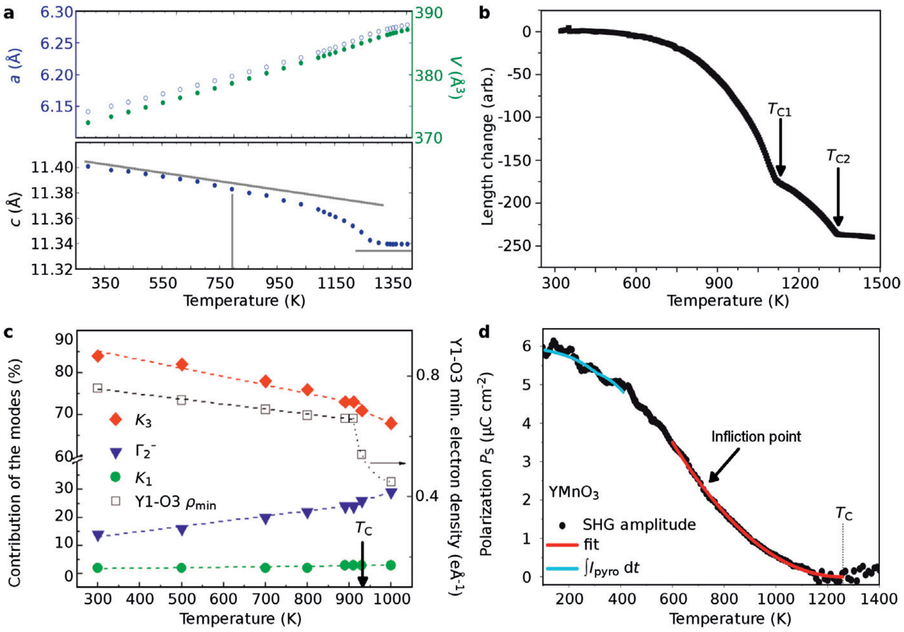

Figure 4.1: Various macroscopic measurements on YMnO$_3$ showing anomalies in the thermal evolution that have been assigned to a structural phase transition. **(a)** Lattice parameters from neutron powder diffraction on YMnO$_3$ with T_C at ∼1270 K. Grey lines have been added to emphasize the deviations from a linear trend below T_C and the flattening above T_C of the c lattice parameter. *Adapted from ref. 131*. **(b)** Thermal expansion from dilatometry on YMnO$_3$ bulk sample. Temperatures T_{C1} and T_{C2} show deviations which were explained by structural phase transitions by the authors. *Adapted from ref. 267*. **(c)** Relative strength of high-symmetric phonon modes and minimum electron density between Y1 and O3 atoms from syncrotron X-ray powder diffration on YMnO$_3$. An abrupt decrease in the Y1-O3 bond length ∼900 K indicates a possible structural phase transition, which was taken as T_C by the authors. *Adapted from ref. 266*. **(d)** Spontaneous polarization from second harmonic generation on YMnO$_3$ single crystal. The evolution of the polarization has an infliction point in the curvature which differs from normal evolution of polarization in proper ferroelectrics, explained as a change in structural coherence by the authors. Note that polarization is not the primary order parameter for the phase transition in an improper ferroelectric. *Adapted from ref. 32*.

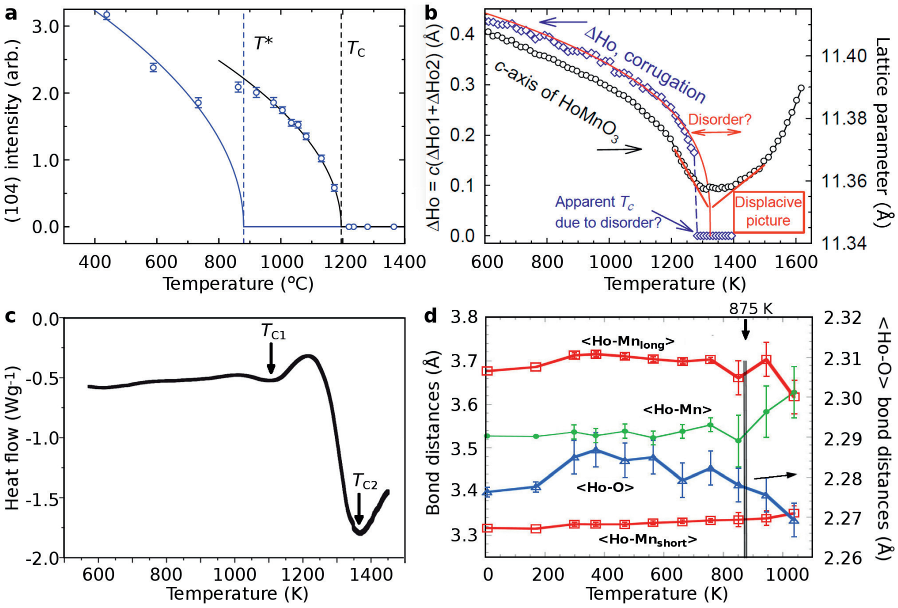

Figure 4.2: Various macroscopic measurements on hexagonal manganites showing anomalies in the thermal evolution that have been assigned to a structural phase transition. **(a)** Intensity of the (104) reflection from quasi-elastic neutron diffraction on $ErMnO_3$. The reflection is associated with the condensating K_3 mode. The anomalies around T^* are evident which were explained by an isosymmetric phase transition by the authors. *Adapted from ref. 273*. **(b)** *c* lattice parameter and degree of off-centring of Ho along c, (ΔHo = $(z_{\mathrm{Y1}} - z_{\mathrm{Y2}}) \times c$) from refinements of X-ray diffraction data on $HoMnO_3$ to the established polar ground state $P6_3cm$. The ΔHo experiences an abrupt jump at T_{C} while the lattice parameter changes continuously. This behaviour indicates that the long range $P6_3cm$ model is unable to refine the data. *Adapted from ref. 101*. **(c)** Measured heat flow with temperature from $YMnO_3$ showing clear anomlies at both T_{C1} and T_{C2}, which are both explained as structural phase transitions by the authors. *Adapted from ref. 267*. **(d)** Short range bond lengths in $HoMnO_3$ versus temperature derived from X-ray adsorption fine structure measurements. The anomalies at 875 K were assigned to a structural phase transition. *Adapted from ref. 268*.

4.1.2 The Landau free energy of h-RMnO$_3$

The high-temperature paraelectric aristotype structure of h-RMnO$_3$ displays $P6_3/mmc$ symmetry. In this structure, the corner-sharing MnO$_5$ trigonal bipyramid are untilted, and the Y^{3+} cations are in their centrosymmetric positions, coordinated by eight oxygens (Fig. 4.3**a**). At the symmetry-lowering phase transition at ∼1250 K, the unit cell triples as a non-centrosymmetric, but zero-polarization zone-boundary K_3 mode condenses[23]. The trimerization upon the transition is described by a two-dimensional order parameter (Q, Φ) corresponding to the amplitude, Q, and the phase, (Φ), of the K_3 mode[270]. Depending on the order parameter angle, corresponding to the tilting direction of the bipyramids, and out-of-plane displacement pattern of the Y cations, the symmetry of the system will be lowered to one of three hettotype symmetries. If the tilt direction corresponds to $\Phi = n\frac{\pi}{3}$, where $n = 0, 1, .., 5$, the system belongs to the polar $P6_3cm$ (P, Fig. 4.3**c**) space group. If $\Phi = \frac{\pi}{6}(2n + 1)$, the system belongs to the antipolar (AP, Fig. 4.3**e**) space group, while all other angles of Φ lead to the intermediate $P3c1$ symmetry (IM, Fig. 4.3**d**). The ground state of the system is the polar $P6_3cm$ (P), in which a polarization of around ∼6 μC/cm^2 at room temperature is induced through coupling of the K_3 trimerization mode to the polar Γ_2^- mode which causes a shift of the Y atoms towards the Mn-O layers. Lowering the symmetry to polar $P6_3cm$ thus results in three possible trimerization angles combined with two polarization directions, giving the total of six domains, recognized in the unusual six-fold domain patterns of the h-RMnO$_3$[143]. Note that polarization P is not the order parameter of the phase transition, since the ferroelectric polarization is only a secondary effect of the trimerization.

Artyukhin *et al.*[270] were the first to derive the Landau free energy of the low-temperature polar structure of the hexagonal manganites, which resembles a Mexican hat with six local minima in the brim, Fig. 4.3**b**. A summary of the derivation is given in Appendix C. This established model of the Mexican hat Landau free energy (Fig. 4.3**b**) describes the average symmetry evolution of the system reduced to the degrees of freedom given by the order parameter. It also reflects the delicate balance between the polar and non-polar structures in the hexagonal manganites due to the weak driving force for polarization[113,122]. However, the model does not address the underlying microscopics. In particular, whether the transition mechanism is closer to the *displacive* (long-range coherence length across T_C) or *order-disorder* (progressively smaller coherence length

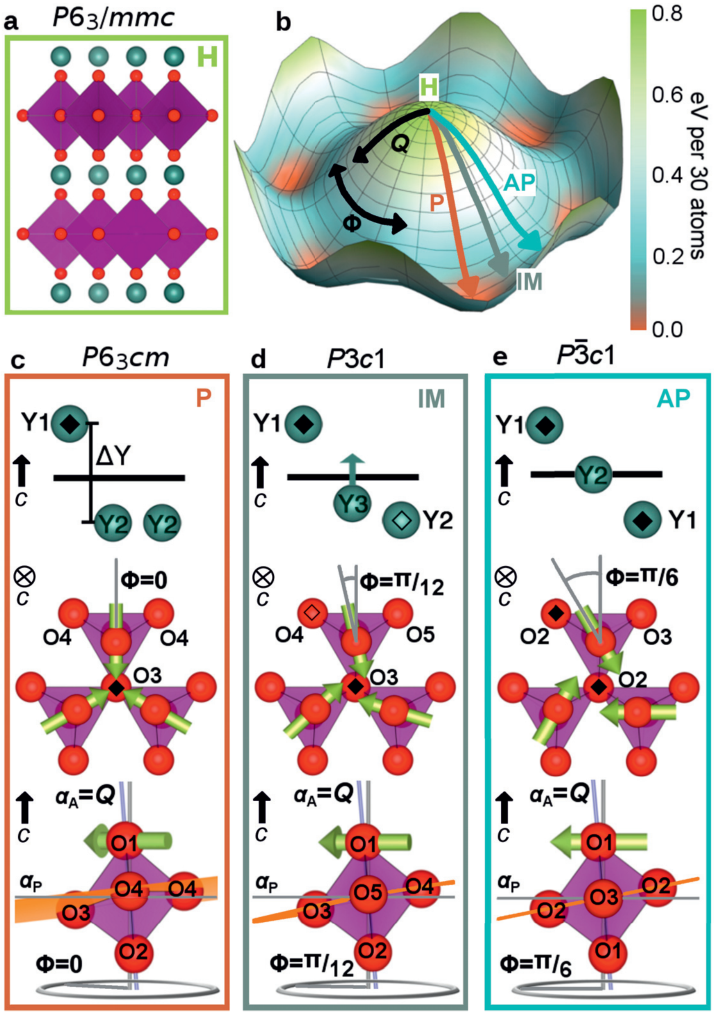

Figure 4.3: Structures of *R*MnO$_3$ phases, **(a)**, The high symmetric $P6_3/mmc$ (H) aristotype crystal structure. **(b)**, The Landau free energy of the hexagonal manganites, resembling a Mexican hat, with the high-symmetry (H) crystal structure at the top of the hat. In the brim of the hat the polar $P6_3cm$ (P), antipolar $P\bar{3}c1$ (AP) and intermediate $P3c1$ (IM) hettotypes occur at the minima, maxima and intermediate regions, respectively. **(c)**-**(e)** show the Y corrugations (top), bipyramidal tilting angles (middle) and the definition of apical and planar tilting angles (bottom) in the three low symmetry crystal structures; Wyckoff sites for the three hettotypes are labeled; Symbols ♢ and ♦ denote atoms aligned in the *c* direction. For the polar $P6_3cm$, ΔY denotes the distance in *c* direction between Y1 and Y2. The angle between O1 and O2 and the *c* axis defines the apical tilt, α_A, and is a direct measure of the order parameter amplitude Q. The plane through the three in-plane oxygens (one O3 and two O4) relative to the ab plane define the planar tilt angle α_P and is related to both the order parameter amplitude Q and angle Φ.

when approaching T_C) limit, as discussed in Section 2.2.1, is not established.

Pair Distribution Function (PDF) analysis has previously been applied successfully to understand the atomic mechanisms behind ferroelectricity in the prototypical ferroelectric perovskites[88,89,274]. Building on these methods, a description of the local atomic structure across the ferroelectric phase transition of h-$YMnO_3$ is given in the next sections. The final section explains the relationship between the local symmetry breaking and the macroscopic polarization. The results are mainly based on spallation neutron scattering measurements on bulk samples of h-$YMnO_3$ from room temperature to above the ferroelectric transition temperature, and the data are analysed with respect to both average and local structure.

In order to investigate the symmetry breaking across T_C, the trimerization order parameter amplitude Q and angle Φ of the K_3 mode are central parameters as they directly mirror the atomic displacements and the symmetries found in the brim of the hat. Three measures of the order parameter can be extracted: the apical and planar tilt angles of the bipyramids, α_A and α_P, and the Y corrugation, ΔY, describing the off-centring of the Y along the c axis. Even though these parameters were presented in Fig. 2.11**d**, a more detailed description is needed here. The order parameter amplitude Q has the same value for all the hettotypes in the brim, and can be extracted directly as α_A, calculated from the positions of the Wyckoff sites O1 and O2 in the polar $P6_3cm$, shown at the bottom of Fig. 4.3**c**. When Φ changes, the symmetry of these Wyckoff sites is preserved for all the IM phases, see bottom of panel **d**. For the special symmetry of the antipolar structure, see bottom of panel **e**, the two Wyckoff sites are merged, but can still be modelled as two, such that the α_A is well defined for all the phases in the brim of the hat. α_P is also a measure of Q, calculated from position of the Wyckoff sites O3 and O4 in the polar $P6_3cm$ (panel **c**). The symmetry lowering upon changing the Φ from the polar hettotype structure to the intermediate structures (panel **d**) is described by an additional Wyckoff site O5, such that α_P can not be calculated from the O3 and O4 Wyckoff sites of the polar structure. The same is the case for ΔY, which in the $P6_3cm$ structure is calculated from the Wyckoff sites Y1 and Y2. The additional Wyckoff site Y3 in the intermediate structures (panel **d**) makes this parameter undefined if the symmetry is broken to the intermediate structure. Although the antipolar structure (panel **e**), has the same number of planar oxygen Wyckoff sites, they obey a mirror symmetry which cannot be reproduced by the Wyckoff sites in the polar structure. Since the ground state of $YMnO_3$ is known to be the polar

$P6_3cm$ hettotype, the obvious choice is to model the local structure data with this structure. However, refinements with the antipolar $P\bar{3}c1$ hettotype will provide additional details about the order parameter angle Φ.

4.2 Average structure inconsistencies

The reciprocal space $S(Q)$ temperature series given in Fig. 4.4 show that the structural phase transition from $P6_3cm$ to $P6_3/mmc$ occurs at 1223 K, as the (102) and (202) super-reflections of the $P6_3cm$ phase disappear above this temperature, in line with previous reports[32,131,267,269]. Lattice parameters, a and c, the structural observables ΔY, α_P and α_A and atomic displacement factors (ADP), U, from Rietveld refinements using the established average low-temperature hettotype $P6_3cm$ over the whole temperature range, are presented in Fig. 4.5**a-c**. Fit residuals r_w for aristotype $P6_3/mmc$ (H) and hettotypes $P6_3cm$ (P) and $P\bar{3}c1$ (AP) are shown in panel **d**.

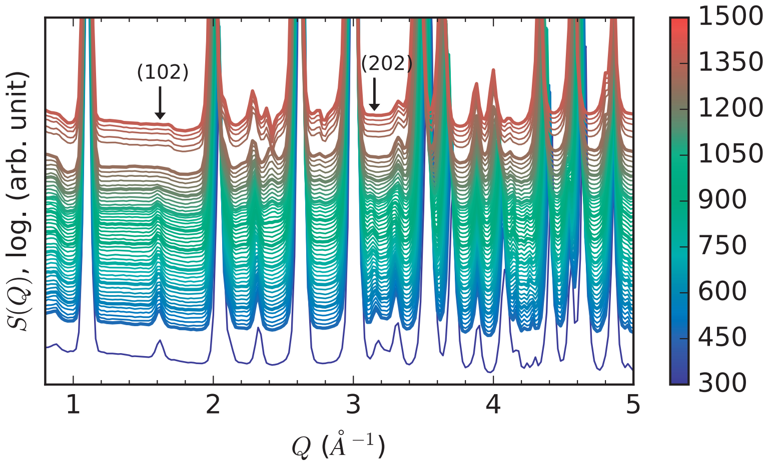

Figure 4.4: Reciprocal space *S*(*Q*). Measured $S(Q)$ of YMnO$_3$ vs. reciprocal space distance Q from two measurement series with high energy neutrons. During the first measurements the sample was measured at 298 K and from 473-1273 K in steps of 20 K. Measurement between 1293 and 1373K is included from the second measurement series, and shifted upwards to distinguish them from the first measurement series. The (102) and (202) super-reflections of the the polar ground state structure $P6_3cm$, indicated by arrows, vanish over 1223 K which we take as the ferroelectric Curie temperature T_C.

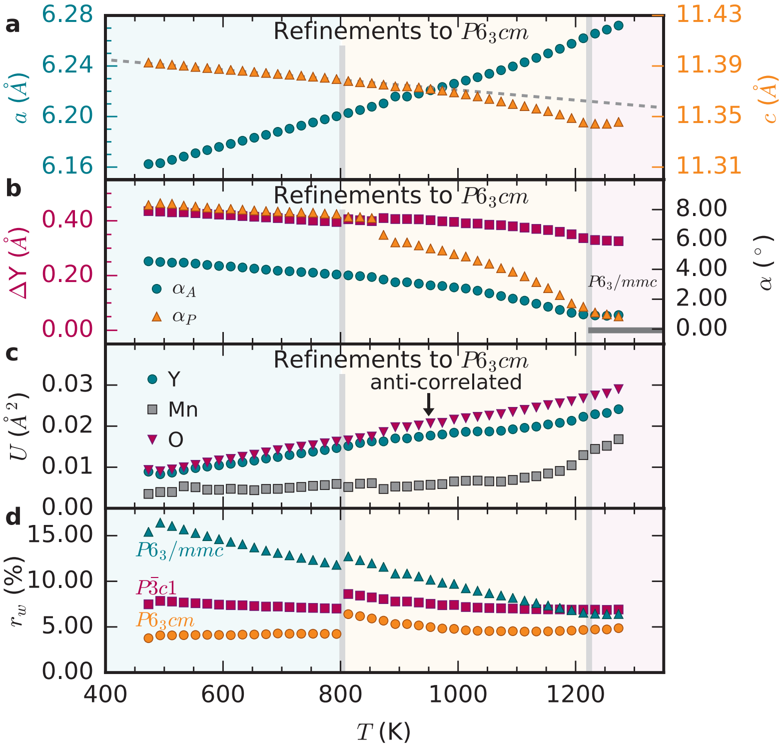

Figure 4.5: Average structure refinements. **(a)** Lattice parameters a and c, **(b)** Y corrugation (ΔY), apical tilt angle (α_A), and planar tilt angle α_P, and **(c)** isotropic atomic displacement parameters, U, from fitting reciprocal space $I(Q)$ to the polar ground state $P6_3cm$. **(d)** Fitting errors r_w of the high-symmetric aristotype $P6_3/mmc$, polar hettotype $P6_3cm$ (P) and antipolar hettotype $P\bar{3}c1$ (AP) to the reciprocal space $I(Q)$ data. The grey vertical line at 1223 K shows the Curie temperature T_C above which aristotype symmetry can be inferred from the Bragg reflections. Centrosymmetric values for ΔY, α_A and α_P in the $P6_3/mmc$ space group are depicted as a grey horizontal line in **(c)**. The grey vertical line at 800 K shows the lower temperature range for incoherent refinements.

In the low-temperature range between room temperature and ~800 K, the lattice parameter a increases linearly, while c decreases linearly. A linear contraction of c and expansion in the ab-plane is expected for displacive untilting of the Mn-O$_5$ polyhedra and Y ions approaching their high-symmetry positions, corresponding to reduced trimerization amplitude Q. This is in line with the linear decrease of all manifestations of the order parameter in Fig. 4.5**b**. Atomic displacement factors U increase linearly, as expected for uncorrelated atomic vibrations. The fit residuals decrease or stay flat for all space groups, as expected since fitting improves when the spectrum broadens.

In the intermediate temperature range between ~800K and T_C, the refinements become less stable, and the slope of the c parameter becomes non-linear. Refinements to a $P6_3cm$ model show that while α_A and α_P go to zero, the value of ΔY decreases only subtly and retains a finite value across T_C (Fig. 4.5**b**). All three parameters are direct measures of the order parameter, as described in relation to Fig. 4.3, and are as such expected to be correlated. This anomalous behaviour is also reflected in the refined atomic displacement parameters U of Y and O becoming anti-correlated, Fig. 4.5**c**. The Mn U increases rapidly with heating from 100 K below T_C~1250K. Such anomalously behaving ADPs are signatures of structural disorder impeding refinements to a space group model which implicitly presumes long range order. Including additional degrees of freedom for the U only marginally improved the fit. The anomalous behaviour is also reflected in the r_w, with an obvious jump at 800 K.

Above T_C, c exhibits close-to-zero thermal expansion over a ~100 K interval before it starts increasing. This plateau is inconsistent with a purely displacive phase transition, and indicates structural disorder. Refinements to the $P6_3cm$ model show that while α_A and α_P go to zero, ΔY retains a finite value across T_C (Fig. 4.5**b**). Also Gibbs *et al.*[131] reported this inconsistency in order parameters across T_C. Their data above T_C were, however, refined to a $P6_3/mmc$ model where ΔY is fixed to zero, effectively enforcing a discontinuity at T_C. The behaviour resembles that of the octahedral rotations in the perovskite $SrSnO_3$, discussed in Section 2.2.1, where a non-vanishing order parameter across a phase transition was assigned to structural disorder[93]. Refinements above T_C to the ground state polar $P6_3cm$ hettotype gave ~2% lower r_w than for the high-symmetric $P6_3/mmc$ structure (H) and the antipolar space group $P\bar{3}c1$ (Fig. 4.5**d**). The difference in r_w at T_C indicates that even though the material becomes paraelectric, the data is better fitted by the ferroelectric space group. However, as $P6_3cm$ has 11 structural degrees of freedom, while $P6_3/mmc$ has only 3, this could be due to over-parametrization at and above T_C.

Vanishing polyhedral tilting (α_A and α_P) and a persistent ΔY indicate a scenario where the Y atoms are still off-centred while the Mn-O_5 polyhedra are completely untilted. This scenario of sublattice disorder is refuted by the density functional theory calculations, shown in Fig. 4.6. The calculations of separate ionic contributions to the K_3 mode show that it is energetically unfavourable for

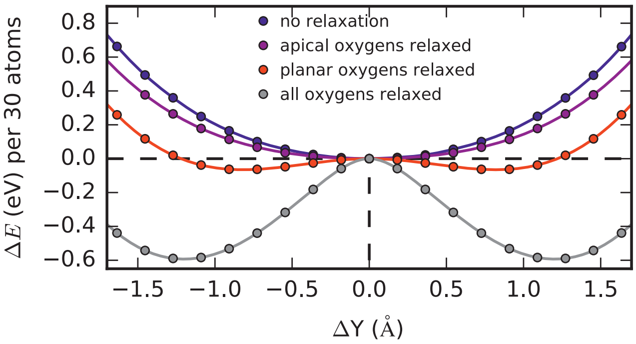

Figure 4.6: Investigation of sublattice coupling. Starting from the high-symmetric aristotype $P6_3/mmc$ of $YMnO_3$, relative energy per unit cell as a function of total displacement of Y in $P6_3cm$ corrugation pattern is calculated when none, some or all the oxygen atoms are allowed to relax to accommodate the Y displacement.

the Y to displace from their centro-symmetric positions if the planar oxygens (O_P) are fixed at their high-symmetry positions. This strong coupling between MnO_5 tilt and ΔY indicates that sublattice disorder is unlikely and suggests that possible disorder involves both sublattices. This strong coupling between the sublattices lies in the fundamental importance of the Y-O_P interaction in this structure, which was also reported by Kim *et al.*[266], whose results were presented in Fig. 4.1**c**.

The temperature for onset of the anomalies coincides well with the reported Ginzburg temperature for $YMnO_3$[81]. Order-disorder transitions are known to have a fluctuation-dominated temperature regime extending far below T_C, enclosed by the Ginzburg temperature, due to a progressively smaller coherence length, as discussed in Section 2.2.1. In this temperature range, renormalized critical exponents for the phase transition are valid.

The presented data show that the average structure has polar $P6_3cm$ symmetry below T_C, but anomalous ADPs and non-selfconsistent lattice parameters and order parameter components signify disorder not captured by a single space group model. Refinements to reciprocal space data, while indicative of the presence of disorder, do not provide sufficient information about the character of the local structure above T_C. The constant lattice parameter c from T_C to ∼100 K above, non-vanishing Y corrugation (ΔY) across T_C and r_w for different space groups all show the need of a local structure sensitive method to probe the ferroelectric phase transition of h-RMnO$_3$.

4.3 Local structure and symmetry breaking

Visual inspection: Evolution of PDF with temperature

The measured neutron PDF, or $G(r)$, temperature series is given in Fig. 4.7. Neutrons provide a strong signal from all three atomic species, with a negative neutron scattering length for Mn, making the neutron PDF especially suitable for distinguishing between local Y-O and Mn-O bonds. The measured PDFs show that large changes occur in the local structure, at several hundred degrees lower than the structural phase transition temperature at 1223 K. In the neutron PDF series, some peaks are merging or disappearing below ∼800-900 K (e.g. ∼3.5 Å and ∼10.5 Å), suggesting that significant displacive structural changes are occurring at much lower temperatures than the ferroelectric transition at ∼1223 K. Comparison of the PDF measured just below and just above T_{C} show only small quantitative changes, as seen in Fig. 4.8. Structures that undergo phase transitions with mainly order-disorder character are expected to change smoothly on a local scale across the transition temperature, such that the PDF just below and just above the transition look qualitatively similar.

Excerpts of the neutron PDFs below $r = 3$ Å give information about the short Mn-O and Y-O bonds. The Mn-O bonds in the MnO_5-polyhedra develop displacively when heating from room temperature, see Fig. 4.9**a**. At 298 K, Mn has bonds to its apical oxygens (O_{A}) of ∼1.9 Å and to its planar oxygens (O_{P}) of ∼2.05 Å, panel **b**. Upon heating, the Mn-O_{P} peaks become broader due to thermal fluctuations, but are not elongating significantly. As these bonds lie in the significantly expanding *ab* plane, presented in Fig. 4.5**a**, the MnO_5-polyhedra must be partially untilting in a displacive manner.

At room temperature Y bonds to its six closest apical oxygens (O1 and O2) with a bond length of ∼2.3 Å (Fig. 4.9**d**). In addition, the two Y atoms bond to one planar oxygen each in the Mn-O layer. The Y1-O3 bond is 2.30 Å, while the Y2-O4 bond is 2.42 Å. In the *average* high-symmetry $P6_3/mmc$ structure, the Y atoms bond to the planar oxygens with a bond of 2.83 Å, while the bonds to the apical oxygens stay relatively unchanged from those in the low temperature structure. Upon heating, the amplitude of the peak in the PDF corresponding to the 2.3 Å Y-O bond decreases substantially more than the other peaks (Fig. 4.9**c**), indicating that Y-O bonds are disordering.

As explained in Section 3.2.5, visual inspection of the PDF might give important information about the shortest bond lengths in the local structure. However,

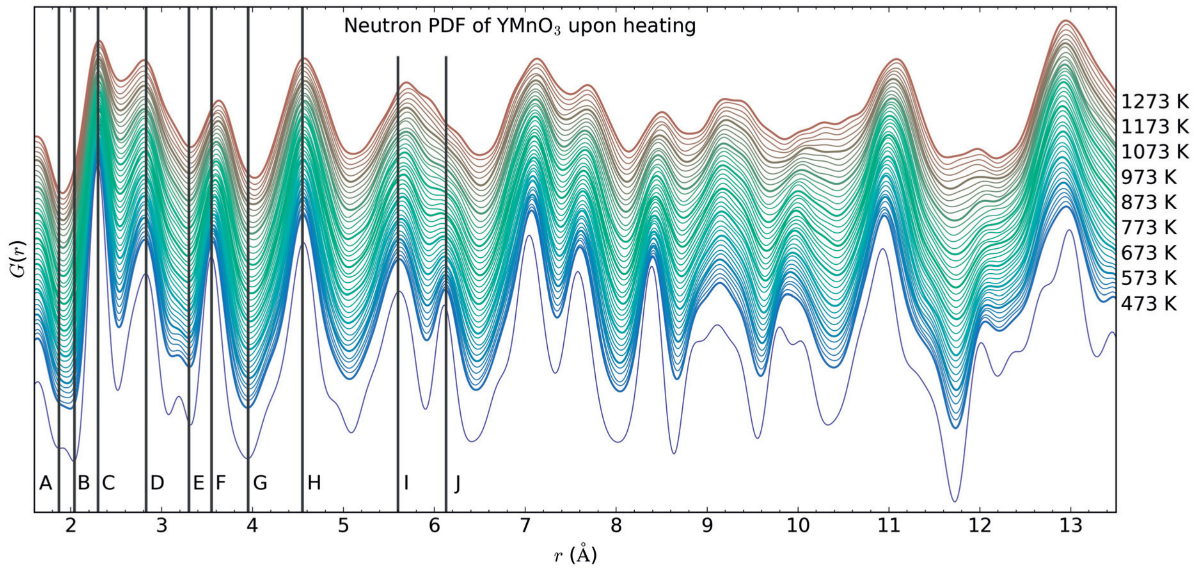

Figure 4.7: Local structure by real space pair distribution function *G*(*r*). Series of PDFs measured with spallation neutrons upon heating from 298 K to 1273 K in steps of 20 K. The letters A-J indicate some important interatomic distances. A) ∼1.9 Å: shortest Mn-O bond in the trigonal bipyramids. B) ∼2.0 Å: next shortest Mn-O bond in the trigonal bipyramids. C) ∼2.3 Å: shortest Y-O bonds. D) ∼2.9 Å: mainly O-O bonds. In the case of evolution to the high symmetry space group $P6_3/mmc$, contribution from out-of-plane Y-O will increase with heating. E) ∼3.3 Å: shortest out-of-plane Y-Mn bond. F) ∼3.6 Å: shortest in-plane Y-Y and Mn-Mn bonds. G) ∼4.0 Å: next shortest Mn-O and Y-O bonds. H) ∼4.6 Å: Y-O and O-O bonds. I) ∼5.6 Å: Half of the c lattice parameter, out-of-plane Y-Y, Mn-Mn and O-O bonds. J) 6.13 Å: a lattice parameter from in-plane Mn-Mn, Y1-Y1 and Y2-Y2 bonds. F) ∼9.4 Å: Y-Y, Y-Mn and Mn-Mn bonds. In-plane refers to the ab plane, while out-of-place refers to the c axis. Note that bonds with Mn give negative intensities.

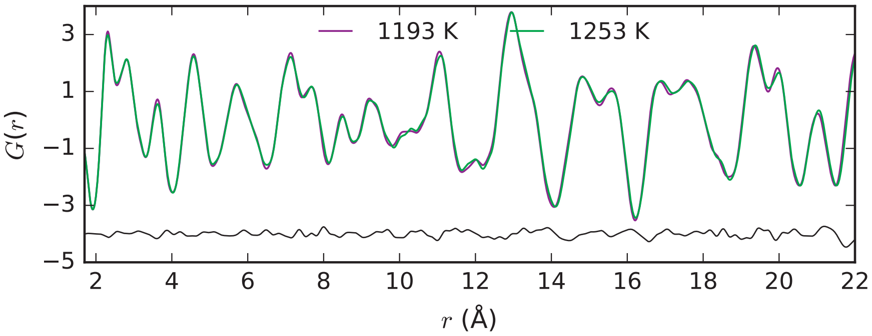

Figure 4.8: Subtle changes across the transition. Measured neutron $G(r)$ from $YMnO_3$ just below and just above the ferroelectric Curie temperature with a difference curve plotted below.

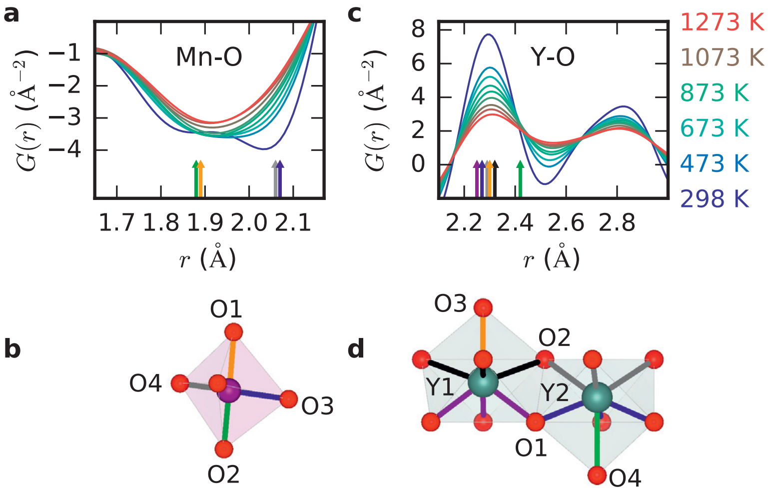

Figure 4.9: Visual inspection of PDF peaks. (a) Excerpt of the neutron PDF, $G(r)$, temperature series of the negative Mn-O peaks between 1.7-2.1 Å and **(b)** MnO_5 bipyramid in a DFT relaxed $P6_3cm$ structure with lattice parameters at 298 K. **(c)** Excerpt of the $G(r)$ temperature series of the positive peaks between 2.1-2.9 Å. The peak at ∼2.3 Å has only contribution from Y-O, while the peak at ∼2.8 Å has contributions from only O-O at up to ∼800 K and both O-O and Y-O at higher temperatures ($>\sim$800 K). Arrows below the PDFs show bond lengths emphasized in colour in the polyhedra in panel **d**. **(d)** YO_7 polyhedron in a DFT relaxed $P6_3cm$ structure with lattice parameters at 298 K.

the high temperatures involved in the study of this phase transition creates significant thermal broadening of the data, making it difficult to distinguish by eye the effects of temperature and symmetry breaking.

Real space refinements of the PDF data

The local structure $G(r)$ temperature data for r = 1.6-12 Å, corresponding to two unit cells in-plane, and one unit cell out-of-plane, were fitted to the established aristotype structure $P6_3/mmc$ (Fig. 4.10) and to the low temperature hettotypes $P6_3cm$ and $P\bar{3}c1$ (Fig. 4.11). Following the evolution with temperature in Fig. 4.10**a-f**, the $P6_3/mmc$ model fits progressively better to the data, although it is still insufficient at 1273 K. This shows that the local structure, even well above T_{C}, is not the high-symmetric $P6_3/mmc$. The long-range model struggles with position and amplitude of many peaks, emphasized by the difference curve between model and data, shown below. Following the evolution with temperature in Fig. 4.11**a-f**, the polar ground state $P6_3cm$ fits the data well at room-temperature while the antipolar $P\bar{3}c1$ fits significantly worse. Upon heating, the two hettotypes give progressively similar fitting errors.

Lattice parameters, a and c, the structural observables ΔY, α_{P} and α_{A} and atomic displacement factors (ADP), U, were extracted also from the local structure $G(r)$ data, shown in Fig. 4.12**a-c**.

In the low-temperature region, lattice parameters obtained from PDF, Fig. 4.12**a**, follow the same thermal evolution as for the reciprocal space data in Fig. 4.5**a**. The different measures for the order parameter ΔY, α_{P} and α_{A} all decrease linearly, as shown in Fig. 4.12**b**, similarly to the same parameters from average structure refinements in Fig. 4.5**b**. Also the atomic displacement factors (U) are well-behaved (Fig. 4.12**c**) in this region. This concludes that below ~800 K, the amplitude Q of the local trimerization is reduced.

Between 800 K and T_{C}, the lattice parameters follow the same trend as in the average structure (panel **a**). α_{A} (panel **b**) behaves monotonically, as in the average structure, although retaining a finite value at T_{C}, in contrast to in the average structure data. Also α_{P} decreases steadily with increasing temperature, although it becomes numerically unstable when approaching T_{C}. ΔY also becomes numerically unstable, indicating that the description of the local structure by the $P6_3cm$ model is inadequate in this temperature region. This is also reflected in the anomalous behaviour of the local atomic displacement factors U, particularly Y2 and Mn exhibit anomalous upturns at elevated temperatures,

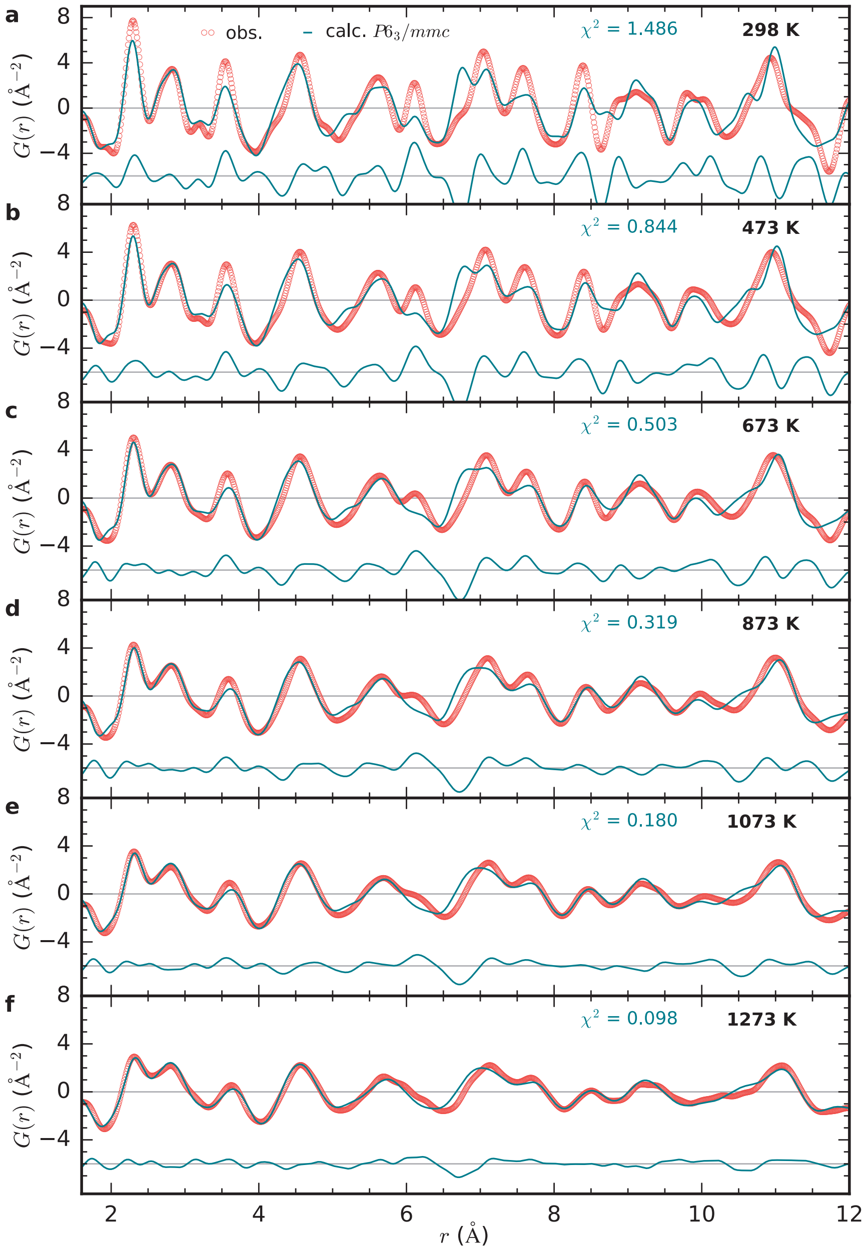

Figure 4.10: PDF fitted to the aristotype. Fits of PDF data to the established average high-temperature space group $P6_3/mmc$ for a selection of temperatures in the range r = 1.6-12 Å. The difference curves between model and data is plotted below and the fitting error χ^2 is given.

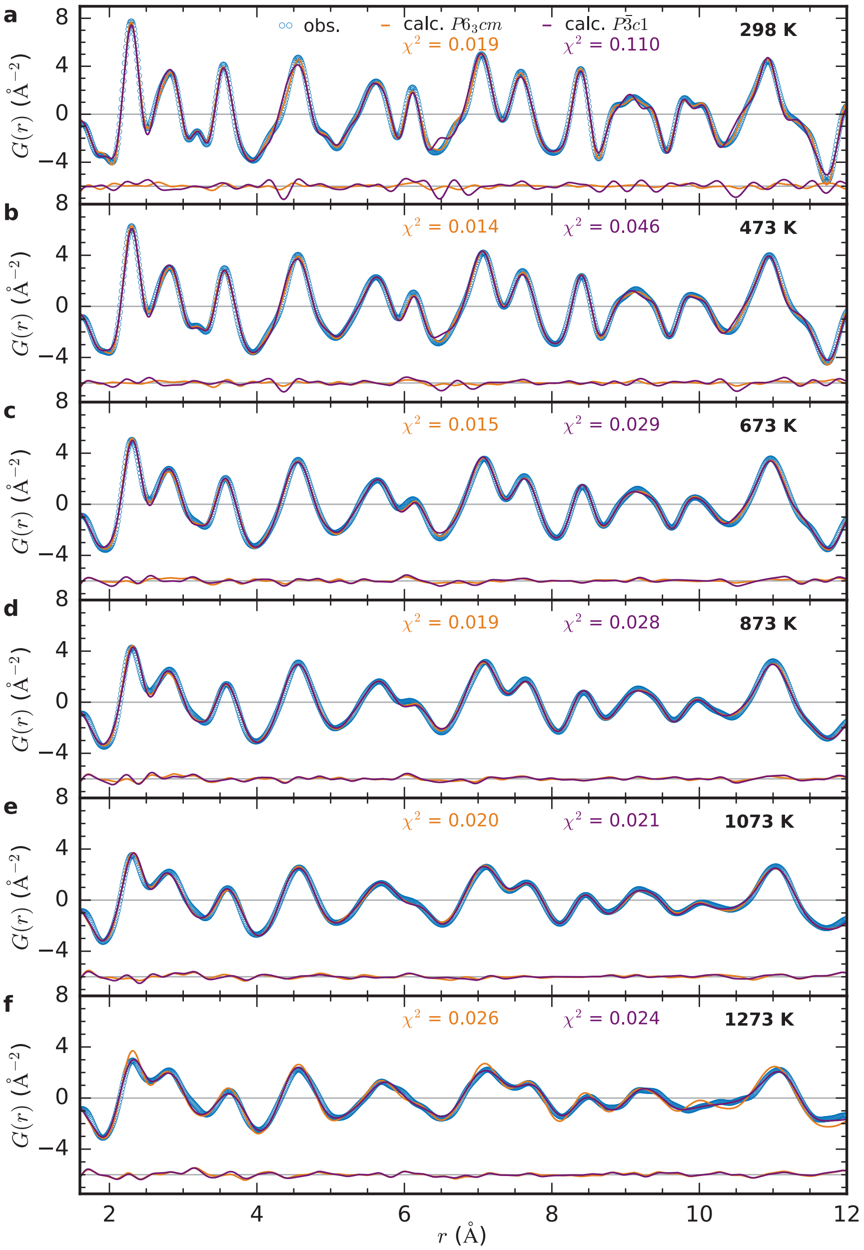

Figure 4.11: PDF fitted to the hettotypes. Fits of PDF data to the established polar hettotype $P6_3cm$ and the antipolar $P\bar{3}c1$ for a selection of temperatures in the range r = 1.6-12 Å. The difference curves between model and data is plotted below and the fitting error χ^2 is given.

panel **c**. When crossing the critical temperature, the c lattice parameter stays at a close-to-constant value in a $\sim$100 K range, as in the average structure data. All measures of the order parameter in Fig. 4.12**b** show a clear softening of Q on approaching T_C. However, neither of them approach zero, once more indicating a locally partially conserved trimerization order parameter and strong order-disorder across T_C.

So far, the analysis has established that the phase transition has a strong order-disorder character. Firstly, the order parameter of the trimerization never vanishes on the local scale. Secondly, the refinements of the order parameter with the polar $P6_3cm$ (P) become worse, and unstable, when approaching the critical temperature. This is observed not only for the average structure, but also for the local structure. Disorder between the six *discrete* minima with polar hettotype symmetry $P6_3cm$ in the Mexican hat cannot describe the observed disorder, as this type of disorder would fit well to $P6_3cm$ on the local scale. Instead, a model where fluctuations of the trimerization order parameter angle Φ *locally lower the symmetry* from the polar hettotype (P) to the intermediate (IM), but still polar, hettotype, is proposed. Comparison of fit residuals of refinements of the PDF data to the aristotype $P6_3/mmc$ (H) and the two special symmetry hettotypes $P6_3cm$ (P) and $P\bar{3}c1$ (AP), is presented in Fig. 4.12**d**. Refining the data to the general intermediate (IM) hettotype is not possible since it allows all angles of Φ.

First of all, the fit residual for the polar ground state hettotype $P6_3cm$ (Fig. 4.12**d**) increases above $\sim$700 K. For well refined systems, fit residuals are expected to decrease with heating, as thermal fluctuations broaden the data (see for example bulk FCC Ni in the left inset). This unusual increase suggests that the polar hettotype (P) alone is not capable of explaining the PDF data on short length scales. This is further corroborated by the difference in fit residuals between the polar and antipolar hettotypes. The fit residuals of the hettotypes become more similar upon heating, finally merging at T_C, suggesting that there is no preference for either space group at and above T_C, and that all structures in the brim of the Mexican hat are equally likely to be observed locally above T_C. However, the trimerization amplitude of the K_3 mode never vanishes on a local scale, as the paraelectric aristotype (H) has a much larger fit residual than the hettotypes (right inset in panel **d**). Thus, above T_C the structure is a disordered mixture between all possible angles of the order parameter angle Φ, accounting for the anomalies in Fig. 4.12**b**. When fluctuations of the order parameter Φ become observable in the neutron data, the Y2 and O4 site sym-

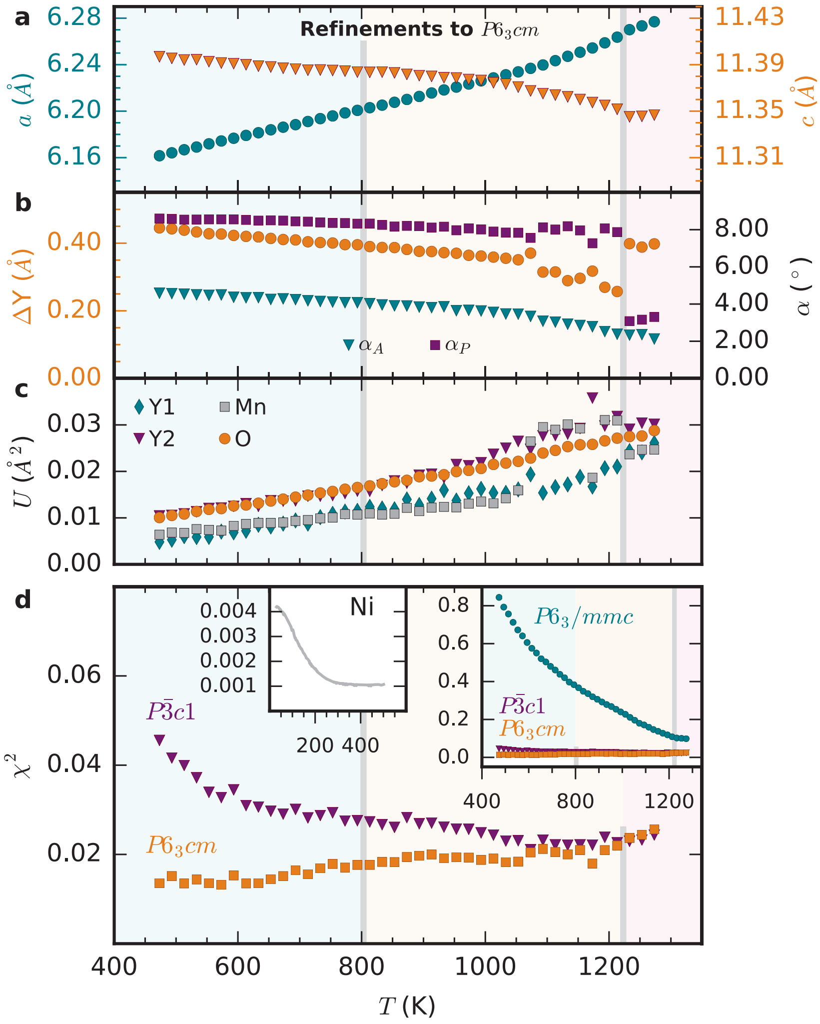

Figure 4.12: Local structure refinements. (a) Lattice parameters a and c, **(b)** Y corrugation, ΔY, apical tilt angle, α_A, planar tilt angle α_P, and **(c)** isotropic atomic displacement parameters, U, from fitting reciprocal space $S(Q)$ to the polar ground state $P6_3cm$. The grey vertical line at 1223 K shows the Curie temperature T_C, while the line at 800 K shows the temperature from where further increase in temperature gives non-coherent refinements. **(d)** Fitting errors χ^2 for fitting real space $G(r)$ to the polar $P6_3cm$ found at the minima and the anti-polar $P\bar{3}c1$ found at local maxima in the brim of the Mexican hat potential. Right inset shows excerpt of the plot emphasizing the difference in fitting error to the two hettotypes compared to the aristotype $P6_3/mmc$. Fitting error for Ni shown in the left inset as a reference to an ideal system.

metries are broken (Fig. 4.3) and α_P and $\Delta\mathrm{Y}$ become ill-defined (Fig. 4.5**b** and 4.12**b**). α_A, on the other hand, is well-defined for all symmetries in the brim of the hat, and thereby well-behaved in both reciprocal and real space refinements.

An illustration of the local symmetry breaking is presented in Fig. 4.13. Thermodynamically, the free energy can increase through thermal vibrations (phonons) or order parameter inhomogeneity. At low temperature (Fig. 4.13**a**), the main entropy contribution is vibrational: The six distinct minima are well separated by energy barriers of around 100 meV, such that the system adopts one of the six ground states over a large spatial range. On heating, the trimerization amplitude Q is reduced (Fig. 4.5**b** and 4.12**b**), first reducing the energy barriers in the brim of the Mexican hat. In this regime, the system continues to adopt one of the six ground states, with increasingly large fluctuations in trimerization order parameter angle Φ. Between $\sim$800 K and T_C, the minima become so faint, that all trimerization angles are accessible, although the system maintains its long-range coherence. Above T_C, the trimerization amplitude remains locally non-zero, but long-range coherence is lost as Φ is continuously disordered.

4.4 Discussion

Explaining previous anomalies

The discovery of the onset of structural fluctuations explains the previously reported anomalies in thermal expansion[267], conventional neutron diffraction[131], ferroelectric polarization[32] and quasi-elastic X-ray scattering[273] around $\sim$800-900 K. These anomalies are caused by a progressively increasing signal from regions with the low symmetry $P3c1$ structure. The explanation of this unusual order-disorder transition reconciles previously reported anomalies at and above T_C. It further excludes the picture of a second phase transition, as the symmetry breaking caused by the fluctuations, is only on the local scale.

Implications for polarization and domain structures

The polarization P emerges from a coupling to the order parameter Q, Φ through the coupling term $g_3 P Q^3 \cos 3\Phi$, as shown in Appendix C. In the average structure both P and Q goes to zero. In the local structure, Q_loc is partially conserved. If the local structure was described by only the polar hettotype, the coupling

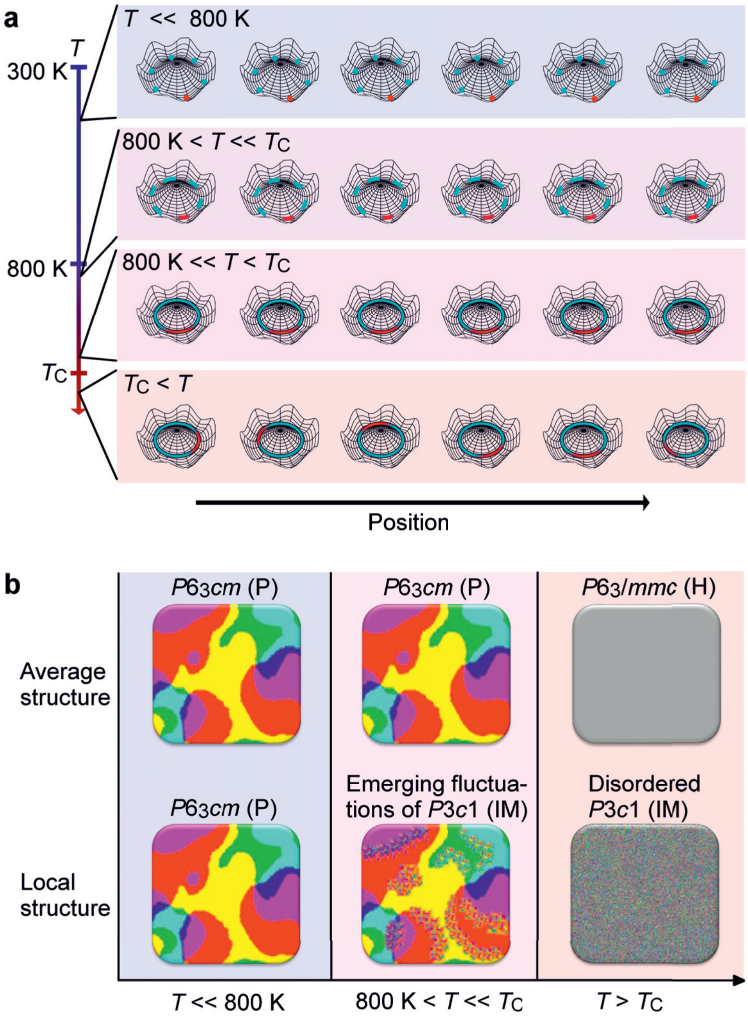

Figure 4.13: Local structure disorder through fluctuations. **(a)** Temperature evolution of the local trimerization order parameter Q, Φ for neighbouring unit cells within one domain. The values are projected onto the ground state Mexican hat potential. The accessible states to the order parameter are marked with blue, wheras the distribution of the order parameter is marked with red. $T <<$ 800 K: Q, Φ is firmly confined to one of the six ground states. 800 K $< T < T_{\text{C}}$: fluctuations smear out the local distribution of Φ but long range coherence is still present. $T > T_{\text{C}}$: coherence of the order parameter is lost and the system disorders between all possible states in the mexican hat. **(b)** Illustration showing the difference between average and local structure based on the reasoning in **(a)**. The average structure will from diffraction appear to have $P6_3cm$ at all temperatures below T_{C}. In the local structure, the order parameter angle Φ disorders between all possible values, lowering the symmetry to intermediate $P3c1$. The phase transition is reached when fluctuations span the entire sample.

term for the local structure would be $P_{\mathrm{loc}}{Q^3}_{\mathrm{loc}} \cos\frac{n\pi}{3} = P_{\mathrm{loc}}{Q^3}_{\mathrm{loc}}$. However, as the fluctuations lower the symmetry from the polar hettotype to a continuum of phases with $\Phi \in [0, 2\pi]$, the local coupling term becomes on average $^1\!/_2 P_{\mathrm{loc}}{Q^3}_{\mathrm{loc}}$. This means that the structure remains locally polar, but the expectation value of the local polarization decreases towards the limit of $^1\!/_2$ compared to discrete disorder of the polar hettotype.

Due to the increasing degeneration of the local structure by low energy fluctuations, the domain walls will broaden upon heating. At the domain walls, Q is locally reduced[270], lowering the cost of order parameter fluctuations. The fluctuations are thus expected emerge first at the domain walls, as shown in Fig. 4.13**b**. This implies that the domain walls become more mobile on heating, while the vortices are less affected, in compliance with previous studies[155,275].

Chemical expansion as a systematic error

When heating an oxide in reducing conditions to high temperature, loss of oxygen from the lattice in inevitable. A second measurement series of PDF by neutron was performed to study the effect of chemical expansion at high temperatures. The chemical expansion from heating the material up to 1373 K is small, as seen in Fig. 4.14, with the a and c parameters increasing on average by 0.08% between the two heating cycles. This expansion corresponds to an oxygen stoichiometry of $3 + \delta = 2.98 - 2.99$ from interpolation of previous data[190], and is considered to affect the conclusions of this work insignificantly.

4.5 Conclusion

This chapter has presented a description of the ferroelectric phase transition in hexagonal $YMnO_3$ at different length scales, which is expected to apply for all hexagonal manganites. At room temperature, the system is ordered according to the six minima with $P6_3cm$ symmetry in the Mexican hat potential. Upon heating, the the observed expectation value of the trimerization order parameter amplitude gradually decreases at all length scales. Above ∼800 K, the polar hettotype $P6_3cm$ structure fails to fully describe the local structure, and the anti-polar hettotype $P\bar{3}c1$ describes the structure equally well at T_{C}. *Local symmetry lowering upon heating* to a continuum of phases due to trimerization angle fluctuations is proposed as the microscopic description of the phase transition.

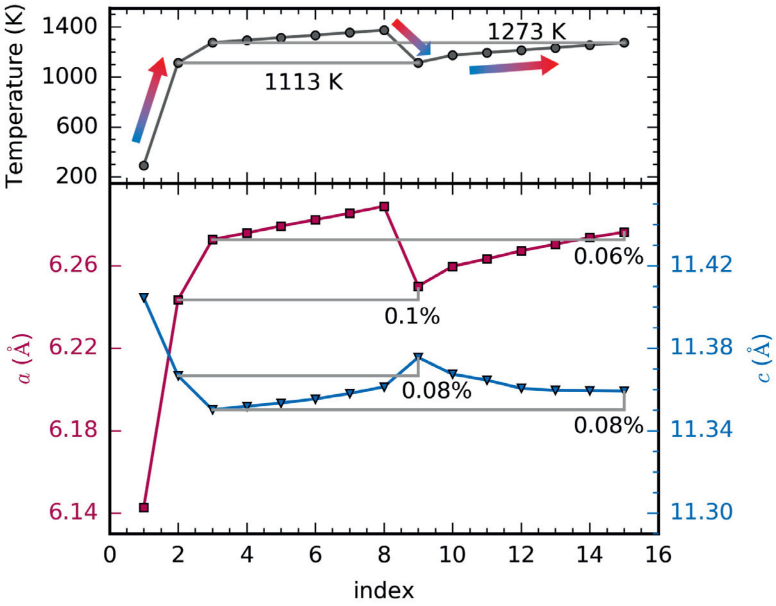

Figure 4.14: Chemical expansion due to oxygen loss. Top panel shows temperature upon heating from room-temperature (298 K) to 1373 K, followed by cooling to 1113 K, and then heating a second time to 1273 K. Horizontal lines indicate when the sample was at similar temperature. Bottom panel shows a and c lattice parameters throughout the temperature treatment, with horizontal lines indicating when the sample was at similar temperature. % chemical expansion is shown next to the lines for the second heating cycle.

Chapter 5

Oxygen vacancies and their interplay with neutral domain walls

5.1 Introduction

The content in this chapter has been prepared for publication in manuscript no. 3, which can be found in Appendix A.

Exotic properties at ferroelectric domain walls, e.g., domain wall conductivity, are often attributed to oxygen vacancies[114,115,161,191,276,277]. Both charged and neutral walls have shown increased conductivity in the hexagonal manganites[26,116,158–160]. Accumulation of oxygen vacancies to charged domain walls can be rationalized from the attraction induced by the electric field at the walls. Such electric driving force for charge accumulation does not exist at the neutral domain walls. However, recent atomic simulations suggest that oxygen vacancies accumulate at neutral domain walls in hexagonal manganites[256], implying an elastic driving force for point defect segregation to the walls.

Chapter 4 explained how fluctuations of the trimerization order parameter angle Φ lower the symmetry of the local structure across the structural phase transition in the hexagonal manganites. The results give two keys about the accommodation of the oxygen vacancies. Firstly, the mechanism for trimerization is dependent on the strong bonds between Y and planar O_P. Breaking of these bonds is thus expected to have large impact on the trimerization. Secondly, the much lower cost for changing the Φ compared to the Q, gives important clues to how the structure can accommodate point defects. When a point defect is introduced, the structure is expected to change in the least energetically costly way. Further, the order parameter, especially the angle Φ, is different at the ferroelectric domain walls, which probably affects the way the structure accommodates the point defect. This chapter presents first principles calculations on the structural and electronic effects of oxygen vacancies in bulk and at neutral domain walls in h-$YMnO_3$.

5.2 Oxygen vacancy ordering in bulk

Electronic structure and defect formation enthalpy

The ferroelectric structure of $YMnO_3$ with space group $P6_3cm$ was presented in Fig. 2.11. The calculated electronic density of states for each of the four vacant oxygen sites are presented in Fig. 5.1**a-d**. All electronic structures show that an oxygen vacancy reduces the structure, as the Fermi level is lifted above the valence band maximum. For the apical oxygen vacancies v_{O1} and v_{O2}, the Fermi level is lifted into the conduction band, with a value of ~5.0 eV for charge neutral cells (Fig. 5.1**e**). The charge compensating electrons are localized in Mn d_{z^2} states, formally reducing two Mn^{3+} to Mn^{2+}, as seen from the magnetic moments (Mn^{3+}: 3.75 μB, Mn^{2+}: 4.25 μB). For the planar oxygen vacancies v_{O3} and v_{O4}, the Fermi level is lifted only up to a d_{z^2} defect state in the band gap, with a value of ~4.5 eV for charge neutral cells. The charge compensating electrons are even more localized than the ones charge compensating the apical oxygen vacancies (Mn^{3+}: 3.73 μB, Mn^{2+}: 4.35 μB). The lower Fermi level for the planar oxygen naturally leads to a lower defect formation enthalpy (panel **e**). The calculations of oxygen vacancies in charged cells of +2 give equal Fermi energy for all four vacancies, underlining the role of the electron localization on the defect formation energies. The electronic density of states cannot explain the difference in formation enthalpy between the two planar sites, favouring the O4 site by 0.37 eV. Thus, the difference is likely due to elastic and/or electrostatic differences in the structural accommodation of the vacancies, which is discussed next.

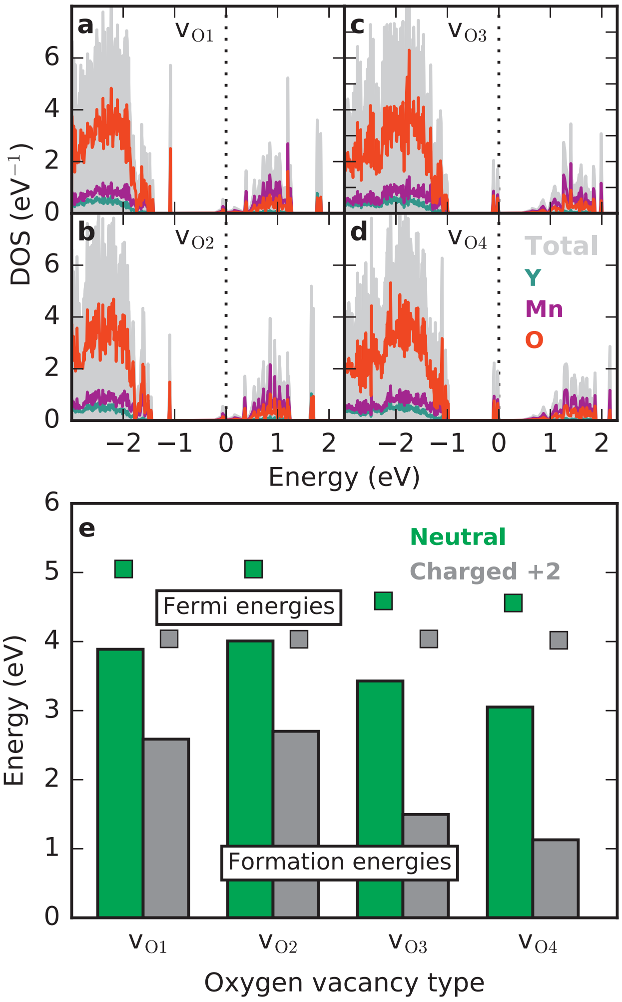

Figure 5.1: Bulk defect formation and electronic structure. **(a)**-**(d)** Electronic densities of states for all the oxygen vacancy types in neutral cells and **(e)** formation energies and Fermi energies for all oxygen vacancy types (2×2×1 supercell) for both neutral and +2 charged cells.

Structural accommodation in bulk

The difference between O3 and O4 is in their bonding to nearby Y atoms and structural flexibility of the YO_7 polyhedra. In the $P6_3cm$ structure, the MnO_5 bipyramids tilt in groups of three away from, or towards, an O3, which was illustrated in Fig. 2.11**c**. The strong coupling between the bipyramidal tilt and the alternating displacements of the Y along c, results in a shorter bond between O3 and Y1 than between O4 and Y2, shown by the bond lengths in Fig. 2.11**b**. It is therefore expected that breaking of Y1-O3 bonds require more energy than breaking Y2-O4 bonds, and that O3 is more important for structural stability than O4. When comparing the structures with either one O3 or O4 vacancy to the initial perfect structures, in Fig. 5.2**a-d** one can see that the tilt patterns around the vacancies are qualitatively different, and that Y1 and Y2 polyhedra have different flexibility to structurally accommodate the vacancies. The v_{O4} causes the closest trigonal bipyramids to mainly rotate, as seen in Fig. 5.2**c**. This corresponds to relatively low-energy changes of the trimerization order parameter angle Φ, as discussed in Chapter 4. On the other hand, the v_{O3} is accommodated by a local increase of the apical tilting angle, α_A of the closest trigonal bipyramids, corresponding to high energy changes of the trimerization amplitude Q.

To quantify the structural perturbations around the planar oxygen vacancies, the *structural screening length* was defined as the distance away from the defect where the perturbations of atoms are smaller than 0.1 Å. Introducing oxygen vacancies causes only short range structural perturbations, as shown in panels **e**-**f**. The structural screening length of a v_{O3} is ∼4 Å, while it is ∼6 Å for v_{O4}. Significant perturbations are found in the Mn-O layer where the vacancies are located, but the perturbations are effectively screened from the third shell from the defect. Perturbation out-of-plane is also seen for the closest Y1 and Y2, directly above or below the vacancies. A v_{O3} repels the closest Y1, while a v_{O4} repels the closest Y2. Perturbations of Y1 along c corresponds to high-energy changes of Q, such that it has little flexibility to move. Perturbations of Y2 are less costly as it mostly changes the Φ, and it therefore moves along c to reinstate a bond with an O4 in the adjacent Mn-O layer. This difference in structural flexibility results in a strong driving force for vacancy ordering on O4 site in bulk $YMnO_3$.

It is worth mentioning, that 0 K first principles calculations give a higher trimerization amplitude than is observed at higher temperatures and thereby

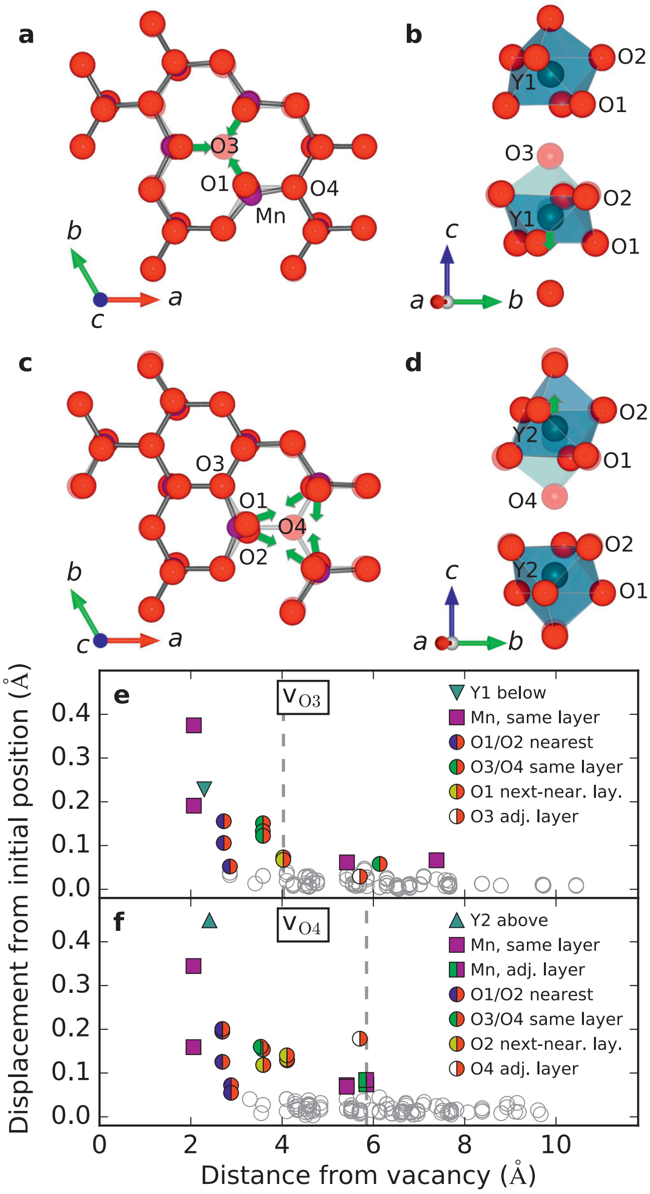

Figure 5.2: Structural effects in bulk. **(a)**-**(d)** Structural relaxations around an O3 or O4 vacancy in 320 atom cells with the initial structure faded in the background. Green arrows indicate significant changes in bipyramidal tilting or Y position after relaxation. **(e)**-**(f)** Displacement from initial position of all atoms in 320 atom 3×3×2 cells as a function of distance from O3 or O4 vacancy. Structural screening lengths are indicated by dashed vertical lines.

a larger difference between the O3 and O4 sites. A decrease in the trimerization amplitude is expected to reduce the difference in defect formation energy between the v_{O3} and v_{O4}, which has been observed by Cheng *et al.*[278].

Effect on bulk polarization

The out-of-plane structural perturbations of Y naturally changes the local trimerization and hence also the local polarization. The calculated polarization for each of the four vacancies shows no correlation with the c lattice parameter (Fig. 5.3**a**), as expected for an improper ferroelectric. Since the oxygen vacancies perturb the lattice only locally, the defect-defect interaction is very small and the polarization changes linearly with respect to vacancy concentration, as seen in Fig. 5.3**b**.

5.3 Oxygen vacancies at neutral domain walls

At neutral domain walls, the domains are, according to symmetry, terminated by either Y1 or Y2. The calculations (Fig. 5.4**a**) show that the walls resemble structural "stacking faults", in line with previous studies by Kumagai *et al.*[25]. None of the Y atoms relax to the high-symmetry positions according to the antipolar $P\bar{3}c1$ structure, discussed in Chapter 4, but the gradual distortions across the wall break the symmetry to the intermediate symmetry $P3c1$. As the O3 and O4 are situated directly below or above an Y1 or Y2, respectively, their distances to the Y1 or Y2 terminated domain walls vary accordingly. The trimerization order parameter amplitude Q is reduced slightly at the domain walls, as seen from α_A and ΔY as a function of cell position, Fig. 5.4**b**. The gradual 60° change of Φ over a $\sim$6 Å range across the walls, are taken as the domain wall width, marked by the grey arrows in the Fig. 5.4**c**. The structural changes of the order parameter across the walls, motivate the study of the interaction between oxygen vacancies and the neutral domain walls.

To study the interaction between the planar oxygen vacancies and the neutral domain walls, the domain walls with a width of one unit cell, were initialized with antipolar $P\bar{3}c1$ symmetry where the middle Y was at high-symmetry positions, shown by the grey Y in Fig. 5.5**a**-**b**. An O3 or O4 vacancy was initialized close to the wall, and the cell was relaxed. As the antipolar symmetry with high-symmetry position of one of the Y are not energetically favourable, structural

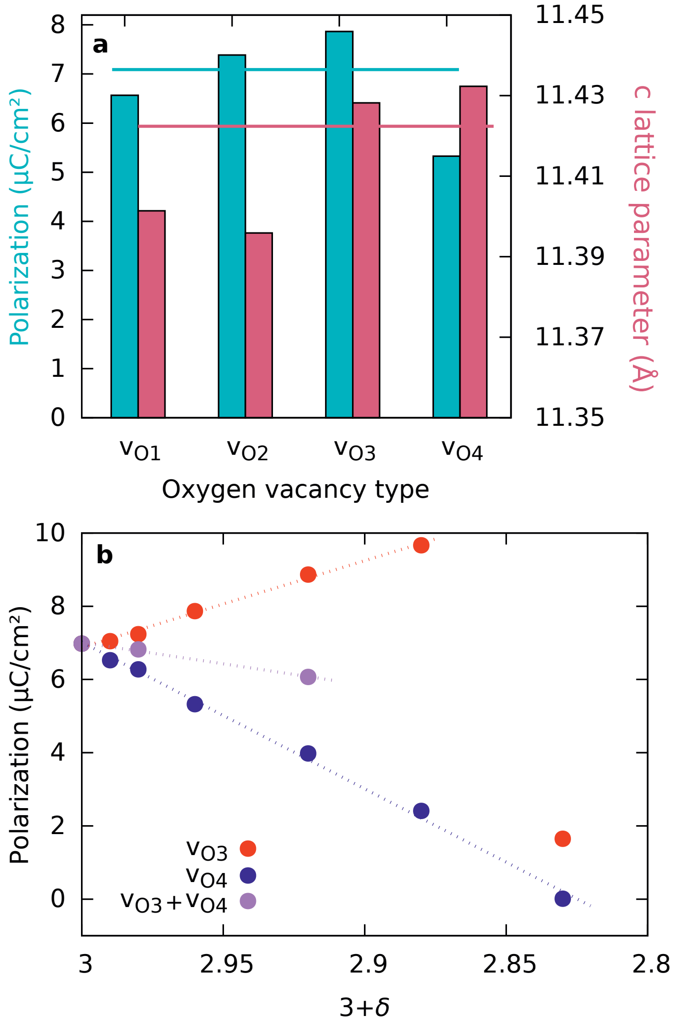

Figure 5.3: Polarization in bulk. **(a)** Polarization and c lattice parameter of a 2×2×1 supercell with one oxygen vacancy. **(b)** Polarization as a function of oxygen stoichiometry (3+δ) for vacancies on only O3 site, only O4 site, or at both sites.

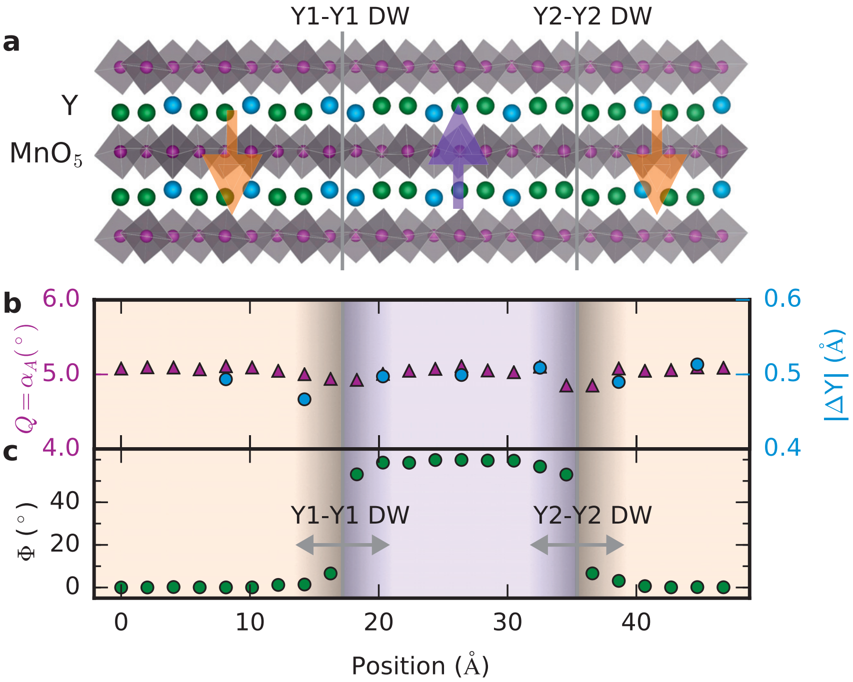

Figure 5.4: Model cell with 180° neutral (120) domain walls. **(a)** DFT relaxed 8×1×1 super cell with neutral domain walls separating domains with polarization up (purple) and down (orange). The walls are terminated by either Y1 or Y2, leaving two different possibilities for defect accommodation. Y1 is coloured blue and Y2 is coloured green for easier visualization. **(b)** Trimerization order parameter amplitude Q from apical tilting angle, α_{A}, and Y corrugation, ΔY, versus position in the cell. **(c)** Order parameter angle, Φ, versus position in the cell. The grey shaded regions and the two-headed arrows indicate the range of perturbations with $P3c1$ symmetry close to the domain wall and can be seen as the domain wall width.

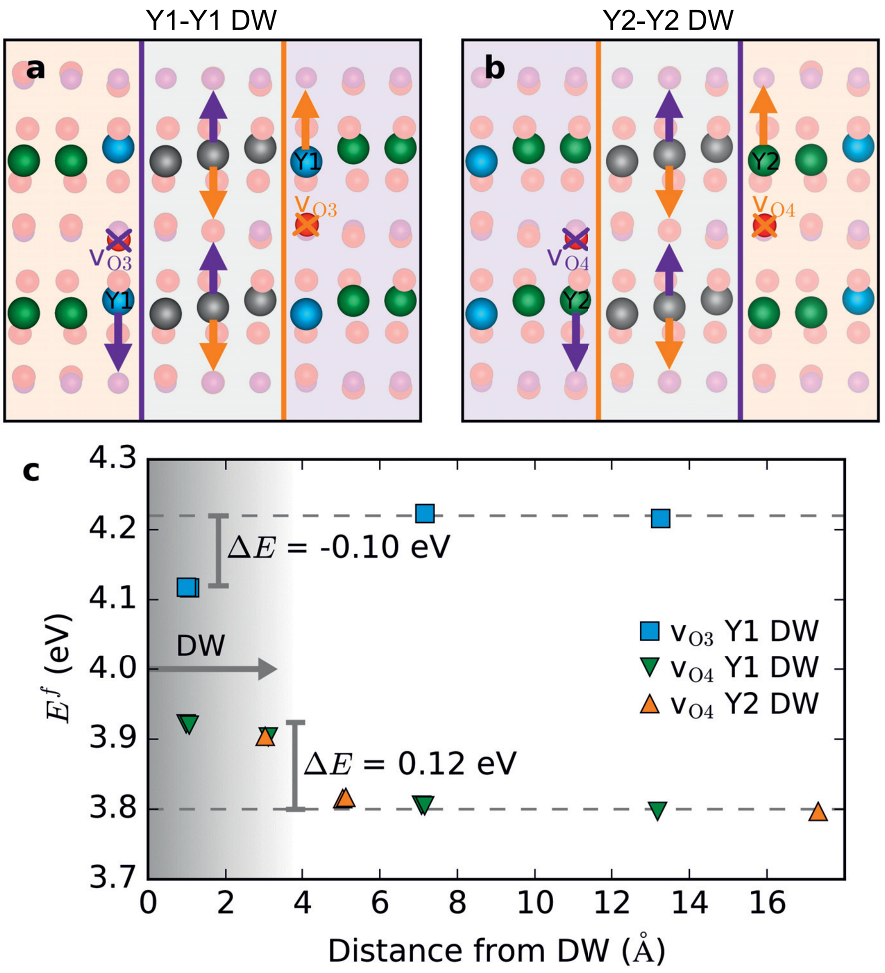

Figure 5.5: Vacancy interaction with domain walls. Initial 8×1×1 supercell, constructed with domain walls of one unit cell (grey background) with antipolar $P\bar{3}c1$ symmetry. The Y1 (blue), Y2 (green) and oxygen vacancies (red) in the domains are highlighted by reducing the visibility of the rest of the structure. For each panel **a** and **b** arrows of equal colours represent atomic movements when removing an O3 or O4 (marked with crosses), and the coloured vertical lines indicate the final position of the domain walls. **(a)** Vacancies on O3 site are attracted to the Y1 terminated domain wall. **(b)** Vacancies on O4 site are repelled by the Y2 terminated domain wall. **c**, Defect formation energy for v_{O3} and v_{O4} as a function of distance to the middle of the domain walls. Chemical potential of oxygen was set to -4.5 eV.

relaxation would lead to the centrosymmetric Y moving either up or down. The two possibilities would result in a ”stacking fault” domain wall either close to the vacancy or one unit cell away from the vacancy. Separate calculations of either O3 or O4 site at either of the domain walls, revealed whether the domain wall - vacancy interaction was attractive or repulsive. To quantify the driving force for segregation of the oxygen vacancies to the domain walls, the segregation energy $\Delta E = E^f_{\mathrm{DW}} - E^f_{\mathrm{bulk}}$, was calculated. v_{O3} are attracted to the domain walls (panel **a**) with a segregation energy of ΔE = -0.10 eV (**c**). v_{O4}, on the other hand, are repelled by the domain wall (**b**) with a segregation energy of ΔE = 0.12 eV (panel **c**). This indicates that the oxygen vacancies order at O4 sites in bulk. The results can be rationalized by considering the Y-O bonds. Y1-O3 bonds in bulk are longer at the neutral domain walls than in the bulk (domain wall: 2.33 Å, bulk: 2.30 Å), indicating that breaking the bond at the domain wall will cost less than breaking the bond in bulk. Oppositely, the Y2-O4 bonds are shorter at the domain wall than in bulk (domain wall: 2.36 Å, bulk: 2.41 Å), meaning that breaking the bond in bulk will cost less than breaking the bond at the domain wall.

These results are not in agreement with previously reported calculations on vacancies at neutral domain walls. Atomistic simulations by Jiang and Zhang[256], using the Born model of ionic solids, showed negative domain wall segregation energies for both v_{O3} and v_{O4}. Such calculations do, however, not include anisotropic distribution of electron density, as the ions are described by pure classical potentials.

The results show that the elastic field that arises at neutral domain walls repels oxygen vacancies. However, the electric field at charged walls may counteract the elastic forces, driving the oxygen vacancies to the domain walls through electrostatic attraction. Moreover, the strong driving force for ordering at O4 sites, may force domain walls into stripe like microstructures if the oxygen vacancy concentration is sufficiently high, as implied by previous studies[191,279].

5.4 Summary

Oxygen vacancies form in the Mn-O layers, where they are charge compensated by formally reducing two of the closest Mn^{3+} to Mn^{2+}. The electropositive character of Y and the structural flexibility are important for the ordering within the planar sites. Oxygen vacancies order at planar O4 sites in the bulk, minimizing the cost of breaking Y-O bonds. The higher cost of vacancies on O3 sites is explained by shorter bond length to Y and high energy perturbations of the trimerization amplitude Q. Vacancies on O4 sites in bulk distort the trimerization angle and reduce the local polarization, as the Y-$\mathrm{O_P}$ reduces the coupling between Y and Mn sublattices.

The vacancies do not segregate to neutral 180° domain walls. The reason is increased cost of breaking the Y2-O4 bonds at the wall due to the strain field.

Chapter 6

Interstitial oxygen as a source of p-type conductivity in bulk and at neutral domain walls

6.1 Introduction

This chapter is based on the publication in ref. 196, and extensions to this work. The published manuscript and its supplementary information is given in Appendix A (no. 1).

Compared with the ternary ABO_3 perovskite oxides, the defect chemistry of h-RMnO$_3$ has received little attention. For perovskite manganites such as $LaMnO_3$, *excess oxygen* is accommodated through cation deficiency, since the crystal structure is too close-packed for interstitial oxygen anions[189]. Oxidation thus requires cation diffusion, which demands higher temperatures than anion diffusion. Remsen *et al.* reported large oxygen excess for h-$R\mathrm{MnO}_{3+\delta}$ (R = Y, Dy) with δ up to 0.35 for R = Dy[176,195]. Moreover, diffusion of oxygen in bulk $YMnO_3$ has been observed below 200 °C[176], making cation vacancy compensation highly unlikely as it would require cation diffusion. The layered h-RMnO$_3$ structure is however ∼11% less dense than the corresponding orthorhombic perovskite structure, suggesting the possibility of interstitial oxygen. This is further supported by the observation that crystallization, which requires cation diffusion, of amorphous $YMnO_3$ only occurs above 800 °C[175].

High levels of excess oxygen can cause development of secondary oxidized phases, which are easily detected experimentally[177]. However, structural effects, energetics and kinetics of point defects in low concentrations have not been addressed. In this chapter, the electronic and structural accommodation of excess oxygen, in the form of highly mobile interstitial anions in the hexagonal manganite structure, is investigated, both in bulk and at neutral domain walls.

6.2 Oxygen stoichiometry and electrical conductivity

Thermal and atmospheric history have strong effects on the conductivity and oxygen stoichiometry of the prototypical hexagonal manganite $YMnO_3$, as shown in Fig. 6.1. The Seebeck coefficient was found to be positive for all temperatures in O_2 atmosphere, with a maximum at 300 °C. In N_2 atmosphere, the Seebeck coefficient is negative. The results imply that p-type electronic conduction dominates in O_2 atmosphere, while n-type conduction, with electrons as majority charge carriers, dominate in the inert N_2 atmosphere. Further measurements on $YMnO_3$ in varying atmosphere revealed that DC electrical conductivity increases faster in O_2 than in N_2 atmosphere. In inert N_2 conditions, the conductivity increases exponentially on heating, as expected for a semiconducting oxide, as more electrons are excited above the band gap. In O_2, the increase is steeper from 100 °C, and the conductivity goes through a maximum value at 270 °C, then decreases and stays relatively constant up to 420 °C, from which the conductivity again increases exponentially.

The increased conductivity in oxidizing atmosphere between ~100-500°C, clearly implies an additional contribution to the conductivity. The observations in Fig. 6.1**a** are consistent with the chemical defect reaction:

$$\frac{1}{2}\mathrm{O}_2(g) + 2\mathrm{Mn}^{\mathrm{x}}_{\mathrm{Mn}} \xrightleftharpoons{\mathrm{YMnO}_3} 2\mathrm{Mn}^{\bullet}_{\mathrm{Mn}} + \mathrm{O}_{\mathrm{i}}'' \tag{6.1}$$

where O_i is interstitial O^{2-}, and $\mathrm{Mn}^{\mathrm{x}}_{\mathrm{Mn}}$ and $\mathrm{Mn}^{\bullet}_{\mathrm{Mn}}$ depict Mn^{3+} and Mn^{4+} on Mn lattice sites, respectively. Tetravalent Mn in oxidized $YMnO_3$ is Mn with localized electron holes: $Mn^{4+} = Mn^{3+} + h^+$. Holes as the majority charge carrier is consistent with the positive sign of the Seebeck coefficient in oxidizing atmosphere. The mobility of negatively charged interstitial O^{2-} is expected to be orders of magnitude smaller than for holes, and this is addressed further below.

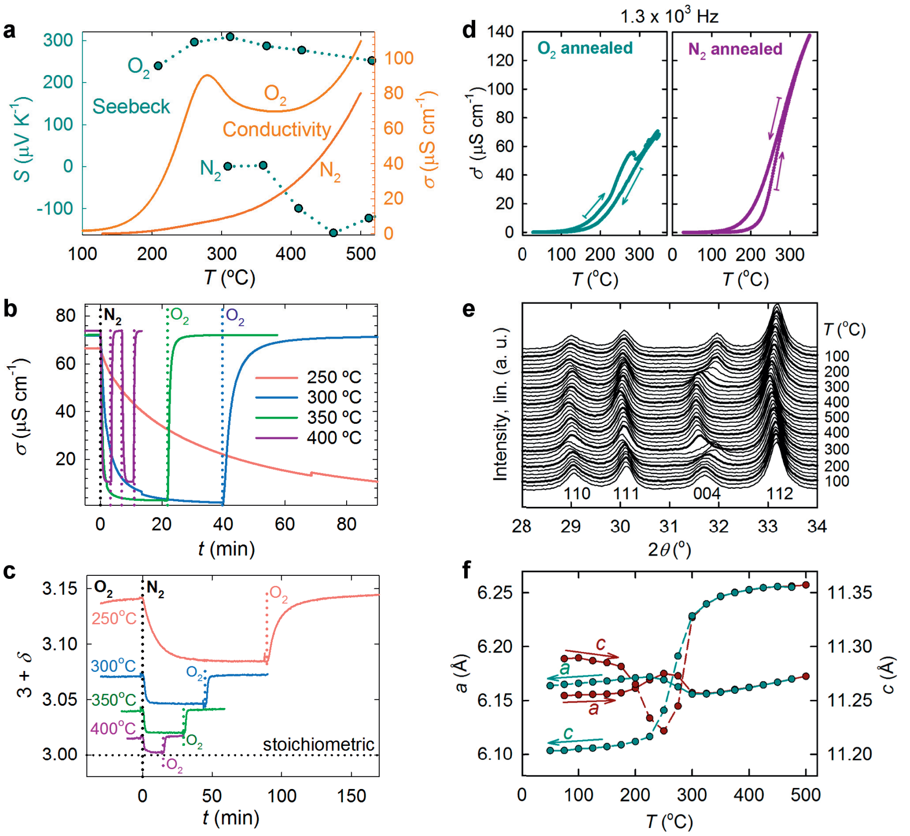

Figure 6.1: Oxygen stoichiometry and related structural and electrical properties. **(a)** Seebeck coefficient, S, calculated from the thermoelectric power, and DC electrical conductivity, σ, in O_2 and N_2 atmosphere of a porous polycrystal of $YMnO_3$, as a function of temperature, T. **(b)** DC electrical conductivity as a function of time, t, of a porous polycrystal upon switching atmosphere (indicated by dotted lines) between flowing O_2 and N_2. The atmosphere is switched twice between O_2 and N_2 at 400 °C. **(c)** Oxygen stoichiometry, $3 + \delta$, as a function of time, t, upon switching atmosphere measured by thermogravimetry for $YMnO_3$ nanoparticles (d_{XRD} = 49 ± 3 nm). **(d)** AC electrical conductivity measurements as a function of temperature, T, of a porous polycrystal annealed in flowing O_2 and N_2, respectively, before measurement. **(e)** High temperature X-ray diffraction (HTXRD) of nanocrystalline $YMnO_3$ upon one heating and cooling cycle in O_2 between 50 and 500 °C plotted on linear scale, and **(f)** lattice parameters, a and c extracted from the measurements of two heating and cooling cycles, showing that interstitial oxygen is incorporated into the lattice, causing anisotropic chemical expansion. No evidence of secondary phases could be seen for any of the temperatures in the 2θ range between 26 and 72°.

The peculiar thermal evolution of the electrical conductivity can be explained from the maximum oxygen stoichiometry observed at about 250°C[176], which coincides with a maximum in electrical conductivity. The deviation in conductivity from the exponential behaviour of a semiconductor stems from the different temperature dependence of the concentration and mobility of holes. While the mobility of holes increases with temperature, this is counterbalanced by the loss of oxygen and charge compensating holes, above 250 °C, as discussed further below. The atypical thermal evolution of the electrical properties of $YMnO_3$ in this temperature range has previously been attributed to the filling of oxygen vacancies[197–201], or to grain boundaries[280]. However, oxygen vacancies would be charge compensated by electrons giving a negative Seebeck effect as long as the cation lattices are stoichiometric. Filling of vacant oxygen sites would thus only give a positive Seebeck effect if the crystal is cation deficient.

Upon isothermal switching of atmosphere from O_2 to N_2, the measured DC conductivity decreased by many orders of magnitude for all the temperatures, Fig. 6.1**b**, in accordance with Eq. 6.1. The initial conductivity is regained after changing the atmosphere back to O_2, demonstrating the reversibility of the reaction. The regained conductivity is similar for all isotherms, owing to the opposing effects of decreasing charge carrier mobility and increasing concentration as the temperature is reduced. The relaxation time before equilibrium is reached is highly temperature dependent, as expected for diffusion of oxygen into the lattice.

The reversibility of the reaction in Eq. 6.1 is also evidenced by the oxygen stoichiometry, $3 + \delta$, when switching between O_2 and N_2 atmospheres, Fig. 6.6**c**. As the length scale of the system is imperative to diffusion controlled processes[14], nanoparticles with an average crystallite size of $d_{\mathrm{XRD}} = 49 \pm 3$ nm[175] were chosen for studying thermogravimetric relaxation on switching atmosphere at a shorter time-scale than in bulk material. With increasing temperature the oxygen stoichiometry equilibrates faster. The rapid change in oxygen stoichiometry in $YMnO_3$ nanoparticles illustrates the increasing importance of thermal and atmospheric history with decreasing system size[14]. The isothermal response of the electrical conductivity (Fig. 6.1**b**) and the oxygen stoichiometry (Fig. 6.1**c**) on change in p_{O_2} is explained by the reaction in Eq. 6.1: oxygen hyperstoichiometry governs the electrical conductivity of h-RMnO$_{3+\delta}$.

AC conductivity measurements of samples annealed in O_2 or N_2 also showed the characteristic maximum at 280 °C on heating, Fig. 6.1**d**, resembling the maximum observed in the DC conductivity measurements in Fig. 6.1**a**. The conductivity measured on cooling is lower compared with the initial heating cycle reflecting the loss of O_i that occurred at higher temperatures. The N_2 annealed sample exhibited a smooth increase of the conductivity with temperature. Subsequent cooling led to higher conductivity in accordance with the reversibility of the O_i incorporation process. The AC conductivity measurements underline that the increase in conductivity upon oxidation can not only be explained by adsorption of oxygen on the surface of the materials, but that accommodation in bulk is the dominating effect to the increased conductivity.

High-temperature X-ray diffraction measurements of nanocrystalline $YMnO_3$ also showed that interstitial oxygen is incorporated into the lattice, causing anisotropic chemical expansion, Fig. 6.6**e**-**f**. The low temperature at which $YMnO_3$ exchanges oxygen with the atmosphere makes cation vacancies and diffusion improbable, and the positive Seebeck coefficient from mobile electron holes points to interstitial oxygen anions, O_i, as the dominating point defect.

6.3 Energy landscape and position of interstitial oxygen

The position of the interstitial oxygen was determined by mapping the potential energy surfaces (PES) as a function of the defect position. The static energy landscape was mapped by positioning the O_i at selected points in several lattice planes, given in Fig. 6.2**a**-**g**. The PES showed that accommodation of O_i is most favourable between three Mn ions in the Mn-O layers at $z = 0$ and $1/2$. This position, due to symmetry, results in 6 equivalent possible sites for O_i in the $P6_3cm$ unit cell, ($1/3$, $1/3$, 0), ($2/3$, 0, 0), (0, $2/3$, 0), ($2/3$, $2/3$, $1/2$), ($1/3$, 0, $1/2$) and (0, $1/3$, $1/2$), as illustrated by green circles in the (0 0 2) (**a**) and (2 0 0) (**f**) planes in the figure. The accommodation of O_i in the Mn-O layers is similar to the accommodation oxygen vacancies, discussed in Chapter 5, and underlines the importance of multivalent Mn for the chemical flexibility of the structure. An excerpt around the most stable position in the (0 0 2) plane was mapped more thoroughly, panel **h**, and revealed an asymmetric triangular energy landscape. This shows how forces between the O_i and the three Mn^{3+} eventually leads to a triple well which O_i can relax into and oxidize two of the Mn^{3+} to Mn^{4+}. The nature of the energy triple well will be discussed in detail in Section 6.5.

Experimental observations of a maximum oxygen stoichiometry δ of $\sim$0.35[176,195]

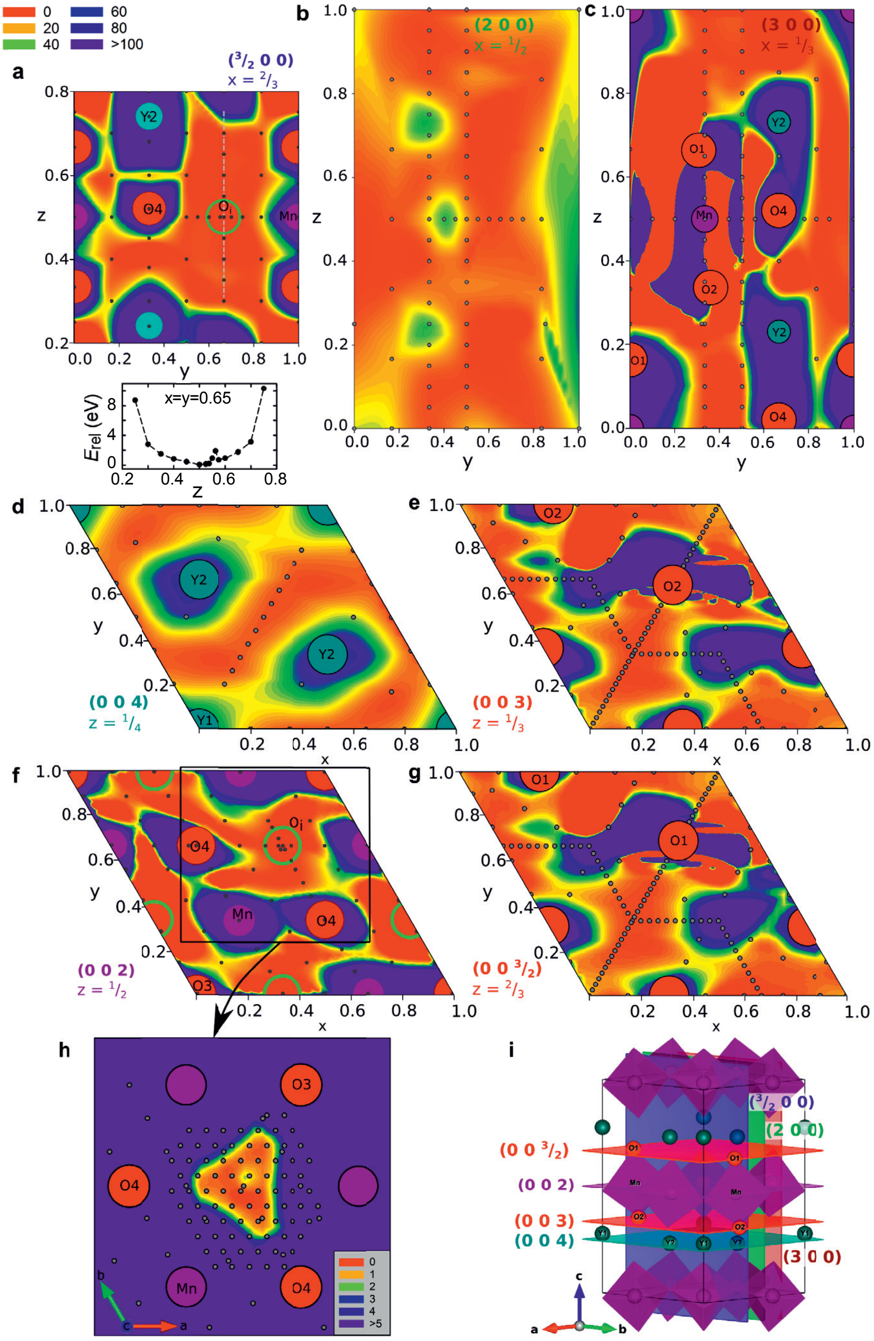

Figure 6.2: Potential energy surface (PES) mapping of O_i in several planes, **(a)**-**h**, in a 2×2×1 supercell (excerpt of only the unit cell) of $YMnO_3$. **(i)**, Unit cell showing the crystallographic planes that were mapped.

can be rationalized from the DFT simulations. If two out of the six possible stable interstitial sites in the unit cell are occupied, a hypothetical fully oxidized structure of $YMnO_3$ would have a chemical formula of $YMnO_{3.33}$ or $Y_3Mn_3O_{10}$. This will result in one O_i and two out of three oxidized Mn in each Mn-O layer of the 30 atom unit cell. Accommodation of more than two O_i per unit cell would require charge compensation across layers or further oxidation of Mn^{4+} to Mn^{5+} within the same layer.

The six equivalent positions for O_i do not correspond to high-symmetry positions in the $P6_3cm$ space group and the presence of a single O_i, without structural relaxation, reduces the symmetry to monoclinic Cm. A fully oxidized structure $YMnO_{3.33}$ with one O_i in each Mn-O layer lowers the symmetry to Cc or $Cmc2_1$[281] depending on which sites the two O_i occupy.

6.4 Structural effects

Accommodation of interstitial oxygen results in only subtle short range structural distortions, as evident from the excerpt of the (002) plane of $YMnO_3$ in Fig. 6.3**a**. The relaxed atomic positions are shown in the foreground, while the atoms in a perfect crystal are included in faded colours in the background for comparison. The Y sublattice is virtually unaffected by the introduction of O_i in the Mn-O layer, as shown in Fig. 6.3**b**. This is very different from the large perturbations of Y atoms for structural accommodation of oxygen vacancies (Chapter 5), indicating a very low defect formation energy of O_i. The local displacements of ions occur mainly within the same layer of trigonal MnO_5 bipyramids as O_i is situated, and the distortions decrease rapidly with increasing distance from O_i. The apical tilting angle, α_A (defined in Fig. 2.11**d** in Section 2.3), of the three bipyramids surrounding O_i, is reduced from 8.7° in the perfect crystal to 6.4° for Mn^{4+} bipyramids, and 4.7° for Mn^{3+} bipyramids, respectively.

The local structural distortions caused by the introduction of O_i are quantified by the displacements of ions relative to the perfect $P6_3cm$ structure as a function of the distance from the O_i, as illustrated in Fig. 6.3**c**. Displacements of Mn and planar oxygen closest to O_i are substantial, apical oxygen in the nearest bipyramids are also displaced, while Y atoms, even close to O_i, are less affected. As in Chapter 5, the structural screening length of the O_i point defect is defined here as the distance away from O_i where the displacement of ions is less than 0.1 Å relative to the perfect structure. A structural screening length can thus be

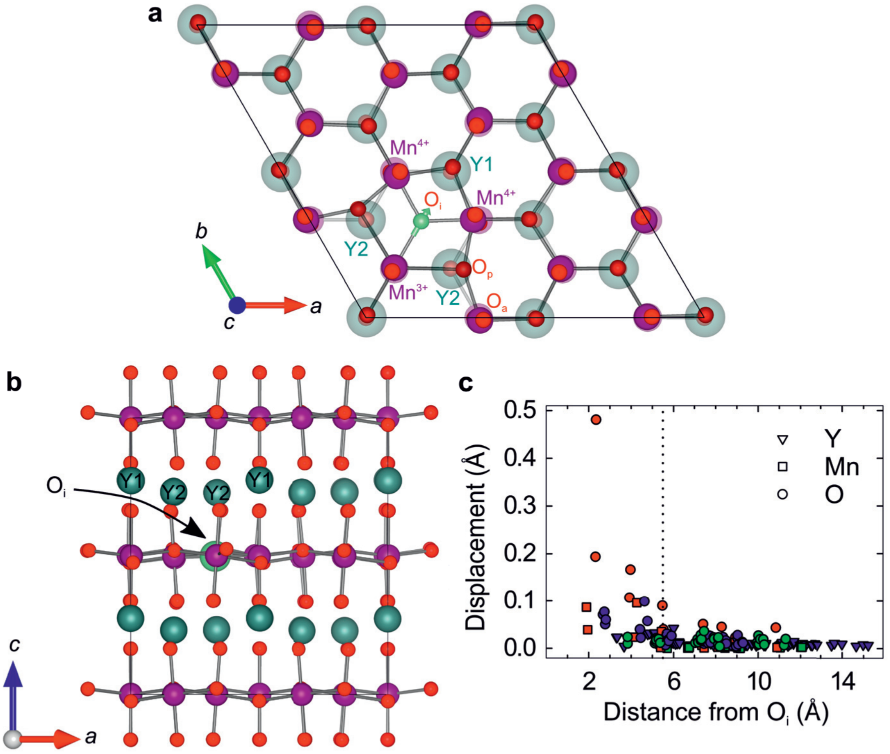

Figure 6.3: Structural effects in bulk. **(a)** Relaxed geometry of the (002) plane of a 2×2×1 supercell of $YMnO_3$ with O_i (green sphere). The perfect structure is faded in the background for comparison, and Y atoms above the (002) Mn-O plane are projected onto the plane. **(b)** Relaxed geometry around O_i viewed along the b-direction. **(c)** Displacements of ions with respect to the perfect structure as a function of distance from O_i. The red symbols represent atoms in the same Mn-O layer as O_i is positioned, the blue symbols represent the apical oxygens and the yttrium atoms closest to the Mn-O layer with O_i, and the green symbols show atoms in the adjacent Mn-O layers. The structural screening length is indicated by a vertical dotted line.

estimated to 5.5 Å, corresponding to the second coordination shell of O_i, and is drawn as a dotted line in Fig. 6.3**d**. This value is very similar to the one found for oxygen vacancies, discussed in Chapter 5, and underlines the flexibility of the hexagonal manganite structure when accommodating point defects. Local charge compensation of O_i by two Mn^{4+}, and bipyramidal tilting, mitigates the effect of O_i on the lattice. The short structural screening length implies that direct experimental detection of O_i is challenging for low concentrations.

6.5 Positional triple well and polaron hopping

The in-plane distances between O_i and Mn after structural relaxation depicted in Fig. 6.3**a** show that there are two shorter and one longer Mn-O_i bond. O_i is displaced towards two d^3 Mn^{4+} ions (with a calculated magnetic moment of 3.06 μB), and away from one d^4 Mn^{3+} ion (3.74 μB). The localization of holes on the two oxidized Mn ions gives three possible configurations of O_i and surrounding Mn ions, Fig. 6.4**a**. The origin of the triple wells is asymmetric electrostatic attraction: O_i with formal charge 2- has shorter bonds to the two Mn^{4+} than to the single Mn^{3+}. The O_i favours to relax in the [110] direction (Fig. 6.4**b**), towards the O3 trimerization centre. The O3 sites are surrounded by trigonal bipyramids which are all tilting towards or away from the site, and strongly bonded to Y1 directly above and below. The [110] triple well position of the O_i results in an Y1-O_i bond length which is shorter than the corresponding Y2-O_i bond length in the two other positions. Just as oxygen vacancies order at sites to avoid the breaking of Y1-O3 bonds, discussed in Chapter 5, the formation of an additional Y1-O_i bond is likely to stabilize the structure.

An additional driving force for the triple well at 0 K is introduced by the non-collinear magnetic order, which is coupled to the trimerization, as shown in Fig. 6.5**a**. The magnetic order follows the trimerization pattern and emphasizes the energy asymmetry. In most calculations, the non-collinear magnetic structure was approximated by a synthetic collinear frustrated anti-ferromagnetic (F-AFM) ordering, and this simplification gives an additional contribution to the asymmetry, as shown in Fig. 6.4**b**. The F-AFM order is believed to create stronger electron repulsions than the true non-collinear spin and emphasizes the energy asymmetry in the triple well. Setting an A-type antiferromagnetic (A-AFM) order also results in an energy asymmetric triple well, although less pronounced, as seen when comparing the magnetic orders in panel **b**. If the

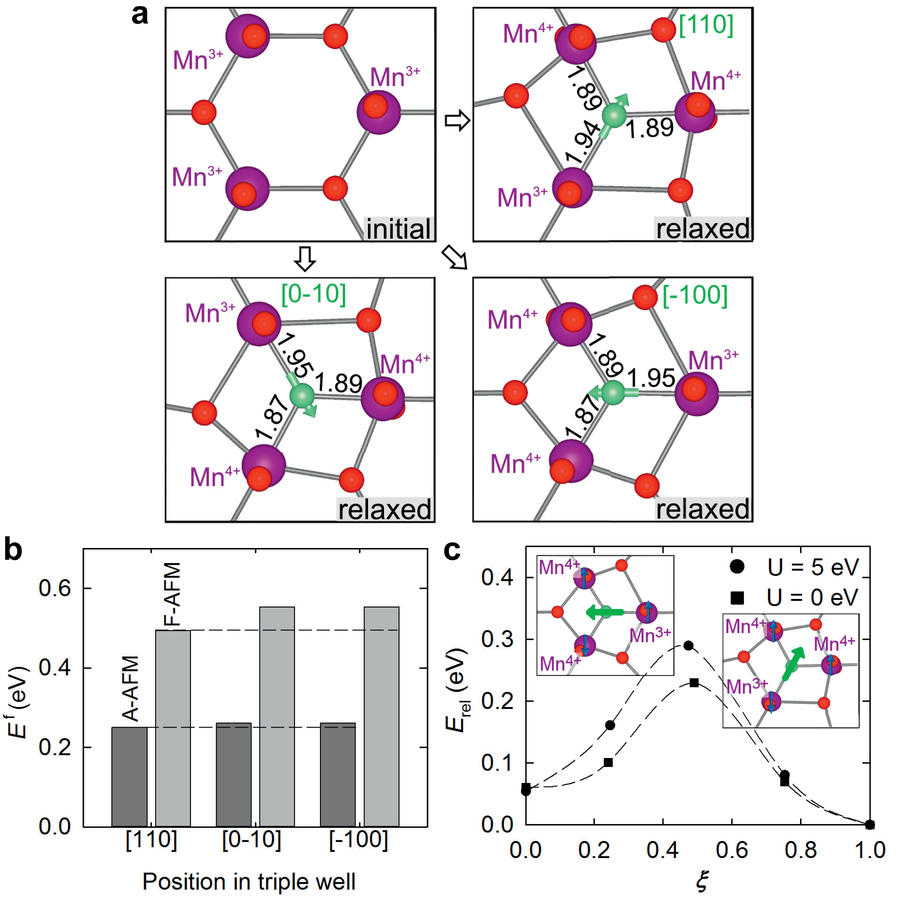

Figure 6.4: Energetic triple well. **(a)** Unrelaxed structure in upper left panel compared to relaxed structures around O_i in the three triple-well positions around the $(^2/_3, ^2/_3, ^1/_2$ position). The green arrows on O_i indicate the displacement towards the two Mn^{4+}. Bond lengths between O_i and Mn are given in Å. **(b)** Defect formation energies of O_i in the three triple well positions calculated with the F-AFM and A-AFM orders, comparing contributions from magnetism and structural trimerization. **(c)** Energy barrier as a function of the relative reaction coordinate for moving one of the charge compensating electron holes between two Mn cations. This corresponds to moving O_i from one site in the triple well to another. The blue arrows show the collinear frustrated antiferromagnetic (F-AFM) order used in the calculations. The apparent energy difference between the start and end configuration is caused by the energy asymmetry of the triple well.

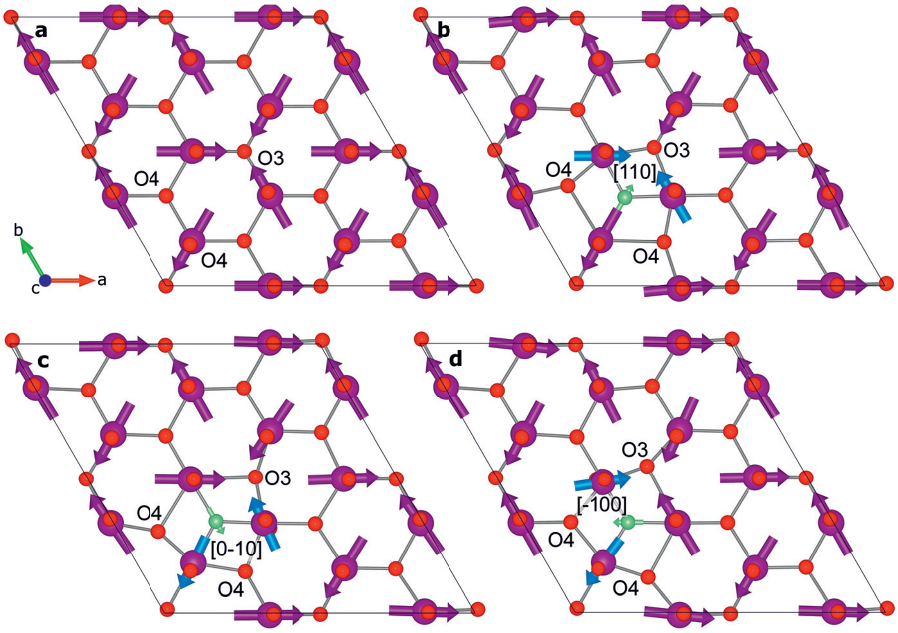

Figure 6.5: Effect of O_i on true non-collinear magnetic order. Static calculations with Hubbard U = 5 eV and the true non-collinear order of structurally 2×2×1 relaxed cells with O_i. **(a)** Stoichiometric cell, and **(b)**-**(d)**, defective cells with O_i relaxed in one of the three triple well positions. Vector arrows denote magnetic moments with relative lengths, where light blue is used for Mn^{4+} and purple is used for Mn^{3+}. The relaxation direction of the O_i (green) is given by the green arrow. Notice how relaxation of O_i towards O3 in the [110] direction gives more symmetric ion positions and magnetic order.

F-AFM order is not set in a way which preserves the structural symmetry of the triple well, additional local minima can trap O_i and the structure distorts unphysically. The F-AFM order should be set such that the most favoured triple well position is in the direction of two Mn with equal spin. The A-AFM order is believed to give even smaller electronic repulsion than the true non-collinear magnetic order. Static calculations of the triple well energies with non-collinear magnetic order showed that O_i caused only subtle changes of the magnetic order, Fig. 6.5**b**-**d**. It should be noted that the material is paramagnetic above ∼70 K, making the choices of magnetic order relevant only for computational technicalities.

Localization of holes on Mn, and the resulting p-type polaronic conduction, stems from electrostatic attraction between positive holes and negative interstitial anions. In contrast, hole doping by substituting Y^{3+} with Ca^{2+} gives holes in Bloch states, while electron doping by Zr^{4+} for Y^{3+} substitution gives a polaronic state[160,282]. Nudged elastic band calculations between the different sites in the triple well showed that the energy barrier for displacing the O_i between different Mn pairs is 0.29 eV, see Fig. 6.4**c**. The barrier is found to be mainly determined by electron transfer between Mn^{3+}/Mn^{4+}, including spin flipping because of the synthetic collinear frustrated antiferromagnetic (F-AFM) order, and can thus be seen as the barrier for polaron hopping. The high energy barrier suggests that the electron holes will be localized in the whole temperature stability range of O_i in the $P6_3cm$ structure. When the on-site Coulomb potential is reduced by not setting a Hubbard U ($U = 0$ eV), the energy barrier is reduced by 0.06 eV. The calculated energy barrier is lower than the reported activation energy of 0.38-0.50 eV for polaron hopping in $YMnO_3$[283–285].

6.6 Energetics of interstitial oxygen

The formation energy for O_i in $YMnO_3$ as a function of the chemical potential of oxygen is shown in Fig. 6.6 (See Section 3.1.6 for details on the thermodynamic stability region for bulk $YMnO_3$). For $p_{O_2} = 0.21$, corresponding to air, the chemical potential of oxygen yields a negative formation energy at temperatures up to ∼900 °C, which is well above the temperature were O_i becomes entropy destabilized, as seen from the experimental measurements in Fig. 6.1. The negative formation enthalpy is rationalized from the formation of stable Y1-O_i bonds, as discussed in the previous section.

It should be noted that the enthalpy of formation for O_i is expected to decrease progressively with increasing oxygen excess δ due to O_i-O_i repulsion and a gradual loss of the driving force for oxidation. The negative formation enthalpy of the interstitial oxygen can be explained by the metastability of the $YMnO_3$ composition with respect to the related compounds Y_2O_3 and YMn_2O_5, seen in the Y-Mn-O phase diagram in Fig. 2.16 (Chapter 2.3). Both these phases gain more stability from higher oxygen coordination of the Y than the hexagonal manganite phase[286].

It must also be pointed out that the formation enthalpy for O_i is calculated in the dilute limit, while a finite concentration of O_i is necessary to detect mass changes by thermogravimetry. The consumption of the gaseous species O_2 (g) in the reaction in Eq. 6.1 means that the entropy of this reaction is negative, hence the entropy contribution to the Gibbs free energy of the reaction

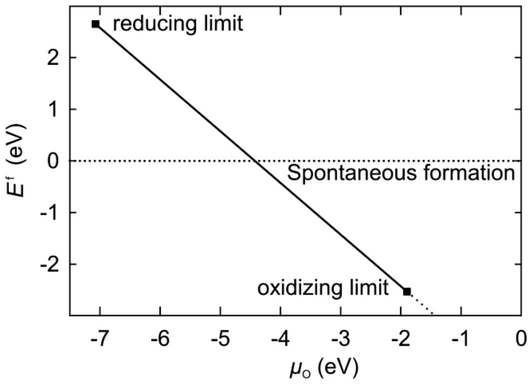

Figure 6.6: Defect formation energy of O_i in a charge neutral 2×2×1 supercell of $YMnO_3$ as a function of chemical potential of oxygen.

is positive. Given the negative enthalpy of the reaction from DFT, the Gibbs' free energy becomes less negative with increasing temperature, gradually shifting the reaction towards the left hand side where O_i leaves the lattice to form O_2 molecules. The equilibrium concentration of O_i hence decreases with increasing temperature, in line with the results in Fig. 6.1.

The negative formation enthalpy does not conform to conventional defect thermodynamics with positive defect formation enthalpies and entropies. The oxygen vacancies discussed in Chapter 5 behave according to conventional defect thermodynamics, such that high temperature or low partial pressure of oxygen is required to stabilize the defects. In analogy to brownmillerite AB_2O_5 and perovskite ABO_3, O_i in $YMnO_3$ could be considered filled oxygen vacancies in the hypothetical compound $Y_3Mn_3O_{10}$. With $Y_3Mn_3O_{10}$ as the reference state, vacant O_i sites would be oxygen vacancies, and thus conform to conventional point defect thermodynamics with positive enthalpies and entropies of formation.

6.7 Migration of interstitial oxygen

The NEB calculations show that O_i is not likely to migrate through a simple interstitial path, where O_i migrates alone out of the Mn-O plane, giving a high calculated energy barrier of almost 6 eV (Fig. 6.7**b**). The transition path is instead in the plane of the Mn-O layer, in which O_i migrates through a cooperative interstitial*cy* mechanism, see (Fig. 6.7**a**). Because of the two different Wyckoff

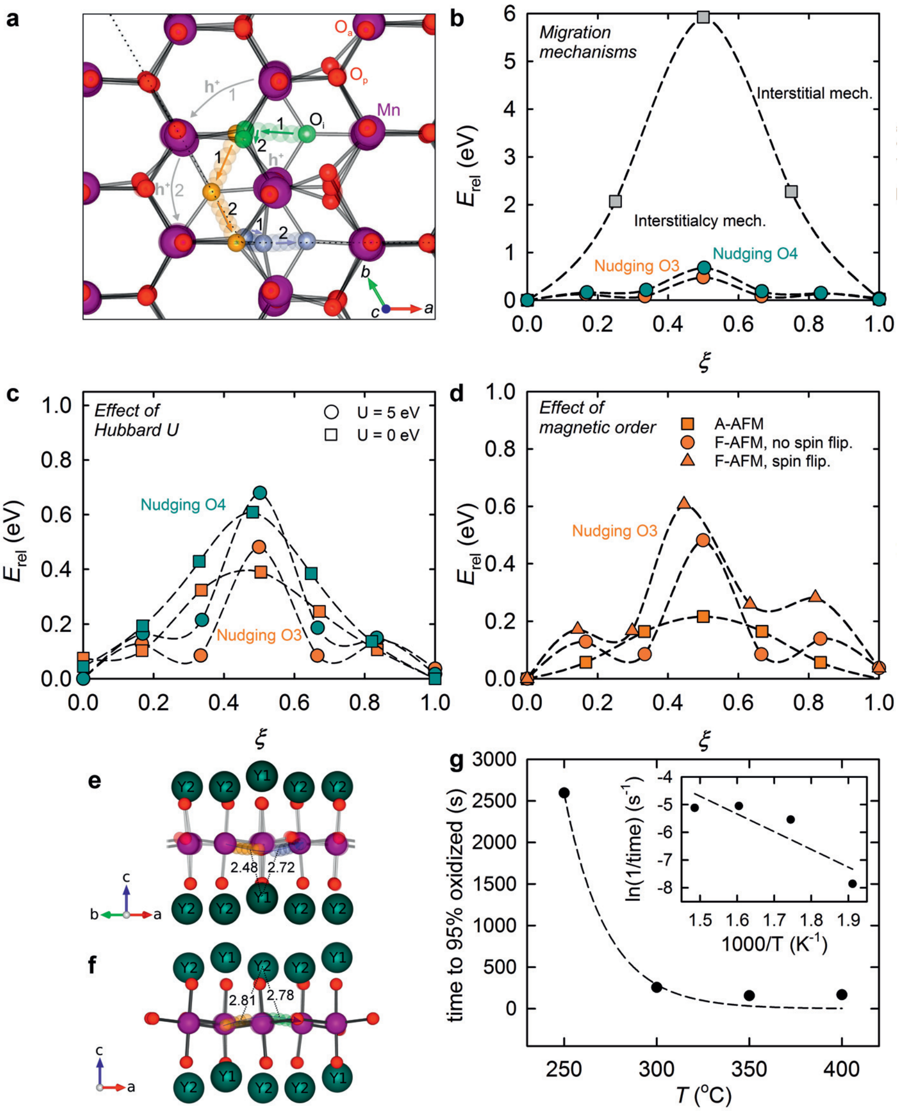

Figure 6.7: Migration. **(a)** Subsequent migration paths of O$_i$ (green, then yellow, then blue) through an interstitial*cy* mechanism nudging first an O4 (path 1) and then an O3 (path 2). The hopping of holes (h$^+$) between Mn are shown by grey arrows. **(b)** Interstitial*cy* energy barriers for the migration of O$_i$, through path 1 and 2, compared to an interstitial mechanism as a function of relative reaction coordinate, ξ. Interstitialcy energy barriers comparing **(c)** the effect of on-site Coulomb repulsion by Hubbard U = 0 and 5 eV and **(d)** the magnetic orders F-AFM with or without spin flipping and A-AFM. **(e)** Bond lengths in Å between Y2 and the moving oxygens in the middle of path 2. **(f)** Bond lengths in Å between Y1 and the moving oxygens in the middle of path 1. **(g)** Time to 95% oxidation of nanoparticles as a function of temperature from thermogravimetric isotherms. The inset shows the Arrhenius-type plot used to extract energy barrier for diffusion.

sites of the planar O3 and O4, O_i can push either the O4, path 1, or the O3, path 2, subsequently taking up the regular planar oxygen lattice position itself. The maximum energy along the minimum energy path is found when the distance between O_i and planar lattice oxygen goes through a minimum. Migration through path 2, in which O_i nudges an O3 site, gives an energy barrier of 0.48 eV, while the similar migration through path 1, nudging an O4 site, resulted in a higher energy barrier of 0.62 eV. The difference is explained by Y1 being closer to the moving O3 (which is a trimerization centre) and O_i in path 2 compared with the corresponding distance between Y2 and the moving O4 and O_i in path 1, as illustrated in Fig. 6.7**e**-**f**. Migration through path 2 will therefore be aided by Y1 bonding to the two moving oxygen atoms, which is supported by the electronic density of states in Fig. 6.8**d**.

The structural effects during migration of O_i are well screened, mainly due to the high structural flexibility of the trigonal bipyramids. Since they are not rigid polyhedra, the introduction of an O_i is structurally screened by changing the bond angles of the polyhedra, rather than rotating the polyhedra. As the O_i passes by the Mn atoms in the migration path, the apical tilting of the nearest trigonal bipyramids is reduced. The calculated energy barrier for migration is not even twice as high as the barrier for polaron hopping, implying that mobility of O_i is strongly determined by the mobility of the charge carriers. When on-site repulsion by Hubbard U was removed, the barrier decreased by $\sim$30%, as seen in panel **c**. Calculations with $U = 0$ eV suffered from slower convergence due to charge sloshing and less localized electron holes.

The calculated barriers with F-AFM magnetic order are likely to be slightly higher than in reality due larger repulsion between the electrons than in the paramagnetic state. The F-AFM order was set in such a way that spin flipping on Mn ions did not occur during migration of O_i, in order to isolate the effect of only migration. Calculations where spin flipping occurred during migration gave 0.14 eV higher energy barrier, as shown in panel **d**. The A-AFM order is, on the other hand, likely to give lower energy barriers than in reality.

An energy barrier was also estimated from the experimental TGA data by plotting time to 95% oxidation as a function of annealing temperature in O_2 atmosphere, as shown in Fig. 6.7**g**. Least square fitting to an Arrhenius-type relationship $k = A\mathrm{e}^{-E_\mathrm{a}/RT}$ gave an energy barrier of 0.55 ± 0.21 eV, in agreement with the DFT calculated values. For comparison, oxygen transport through vacancy diffusion in ABO_3 perovskites has an energy barrier in the range of 0.5-2.8 eV[287].

6.8 Functional properties

Electrical conductivity from density of states

The impact of O_i on the electronic properties were studied by electronic density of states calculations. The introduction of O_i between three Mn (Fig. 6.3**a**) gives three edge-sharing octahedra. As these octahedra are strongly distorted, the crystal field experienced by the d-electrons of Mn coordination O_i does not change significantly compared with the trigonal bipyramidal crystal field in the perfect crystal. The most obvious change in the electronic structure of $YMnO_{3.04}$ (2×2×1 supercell), in Fig. 6.8, caused by O_i is the appearance of a non-bonding defect state in the band gap mainly consisting of Mn^{4+} $d_{x^2-y^2}$ states and O_i $2p_x$ and $2p_y$ states. A fraction of the occupied Mn d states closest to the Fermi energy is lifted above E_F on inclusion of O_i, as electron density is donated from Mn 3d to O 2p. The corresponding binding states are easily seen at the bottom of the valence band. Even though charge transfer is not complete, this can formally be regarded as the oxidation of Mn^{3+} to Mn^{4+}, creating holes in the valence band and p-type electronic conductivity. The p-DOS of interstitial oxygen is very similar to that of planar oxygen, which is also coordinated by only Mn, while it differs significantly from the p-DOS of apical oxygen, which is coordinated by both Mn and Y. The highly localized character of the defect state in the band gap is characteristic for the electronic structure of an acceptor doped material, and direct experimental detection of O_i in low concentrations, by for example spectroscopic techniques, would be challenging. With increasing O_i concentration, the defect state becomes less localized, as expected, see Fig. 6.9 for DOS and band structure of a 30 atom unit cell, $YMnO_{3.16}$.

Spontaneous polarization and segregation of O_i to ferroelectric domain walls

To address the impact of O_i on the ferroelectric properties, the spontaneous polarization P was calculated. The Berry phase method gave 7.8 μC cm^{-2} for the perfect structure, and 7.2 μC cm^{-2} after inclusion of one O_i in a 2×2×1 supercell ($YMnO_{3.04}$). A simple point charge model gave 7.8 and 7.0 μC cm^{-2} for stoichiometric $YMnO_3$ and oxidized $YMnO_{3.04}$, respectively.

The subtle changes in polarization is in line with the close-to-zero perturbations out-of-plane from the defect (Fig. 6.3**c**), and in contrast to the large

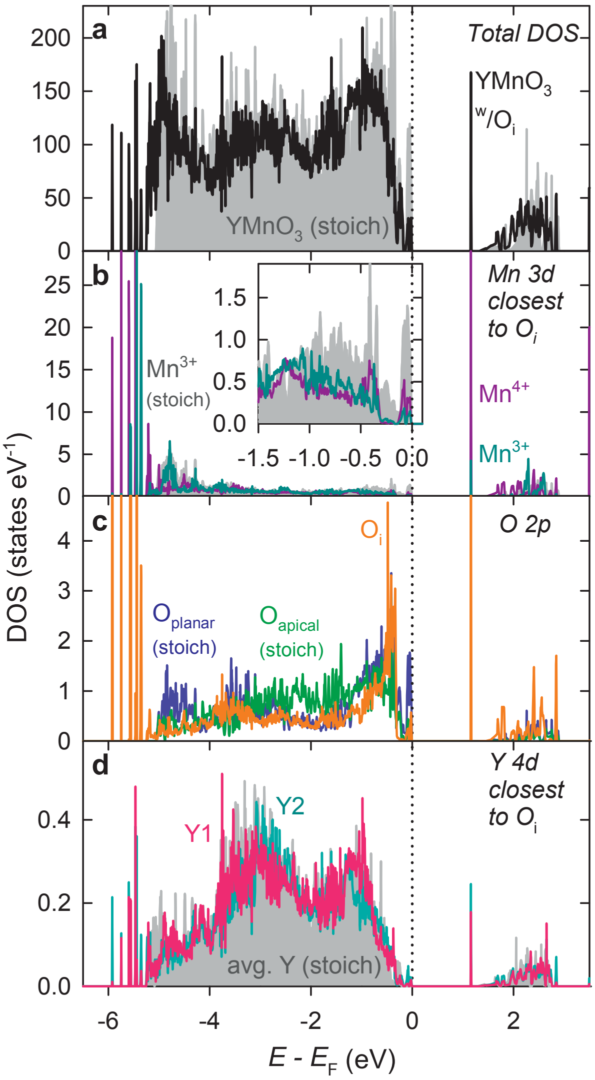

Figure 6.8: Electronic structure of supercell. (a) Total electronic density of states (DOS) for a perfect 120 atom YMnO$_3$ supercell and a 121 atom supercell with one O$_i$ (YMnO$_{3.04}$). **(b)** Atomic DOS showing the d states for Mn^{3+} and Mn^{4+} coordinating O$_i$ compared with Mn^{3+} d states in a stoichiometric cell. **(c)** Atomic DOS showing the p states of O$_i$ compared with p states for apical and planar oxygens in a stoichiometric cell. **(d)** Atomic DOS showing the d states of the closest Y1 and Y2 to O$_i$ compared with the average Y d states in a stoichiometric cell.

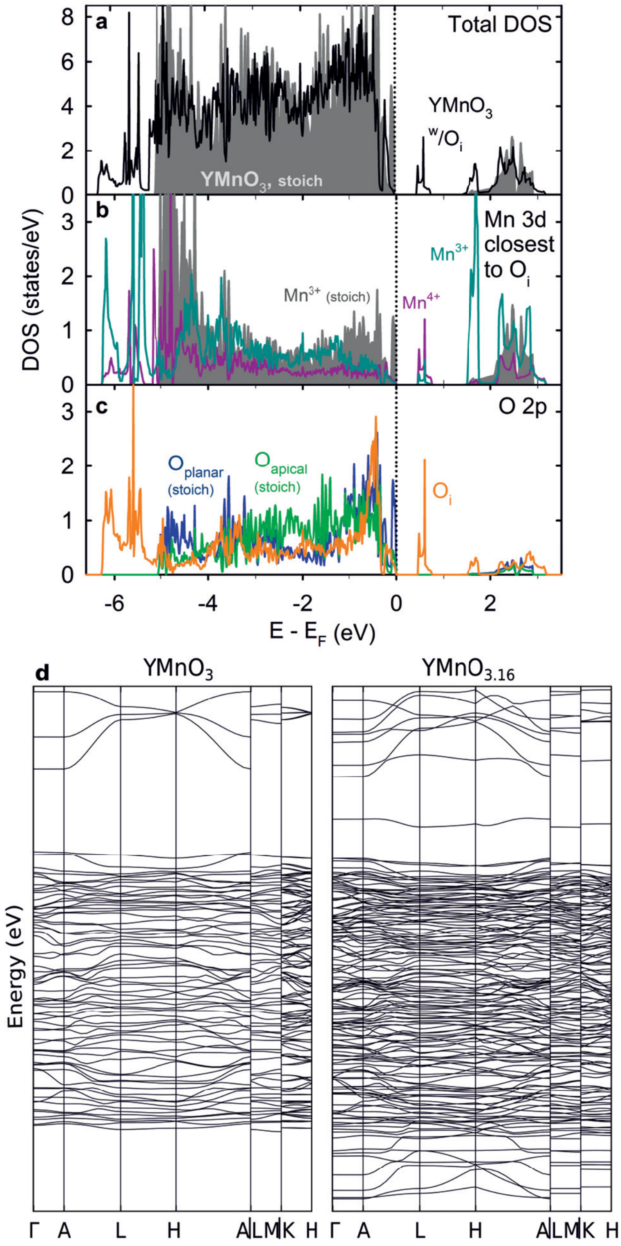

Figure 6.9: Electronic structure of unitcell. (a) Total electronic density of states (DOS) per formula unit for perfect 30 atom unit cell of YMnO$_3$ and a 31 atom unit cell with one O$_i$ (YMnO$_{3.16}$). **(b)** Atomic DOS showing the d states for Mn^{3+} and Mn^{4+} coordinating O$_i$ compared with Mn^{3+} d states in a stoichiometric cell. **(c)** Atomic DOS showing the p states of O$_i$ compared to p states for apical and planar oxygens in a stoichiometric cell. **(d)** Electronic band structure of a stoichiometric 30 atom unit cell compared a similar cell with one O$_i$.

perturbations of Y close to oxygen vacancies (Chapter 5). Although the effect of O_i on the spontaneous polarization is subtle, the charge compensating holes will raise the electrical conductivity and be detrimental to the macroscopic ferroelectric performance. This increased electronic conductivity can possibly be exploited technologically if the mobile charge carriers accumulate at the ferroelectric domain walls. Both neutral and charged improper ferroelectric domain walls in RMnO$_3$ have shown increased conductivity compared to the bulk[26,158–161,288]. However, the mechanism for conduction at neutral walls is not understood. As interstitial oxygen causes p-type conductivity, the accumulation of O_i, and its charge compensating holes, to these walls could therefore be one reason for the conductivity. Hence, calculations were performed to investigate the interaction between the interstitial oxygen and the neutral domain walls.

The neutral domain wall supercell used for calculations with O_i is presented in Fig. 6.10**a**. Although the cell had different dimensions than the one presented in Chapter 5, the relaxed domain wall structure was similar. Shaded grey areas and arrows indicate the domain wall width of ∼5-6 Å resulting from the structural strain across the walls. While the domains display $P6_3cm$ symmetry, the neutral domain walls have $P3c1$ symmetry, smoothly changing from one domain to the other by rotating the trimerization angle (Φ) by 60°, as shown in Fig. 6.10**b**. The formation enthalpy of interstitial oxygen is lower close to the two domain walls, see panel **c**. The additional stabilization is explained by stronger Y coordination around the interstitial oxygen, when approaching the domain walls, as seen from panel **d**. This gives the interstitial oxygen its lowest defect formation enthalpy close to the Y1-terminated wall. The outlier energy close to the Y2 terminated wall is explained by higher distortion of the Mn-O bipyramids when the interstitial cannot be coordinated by an Y1. The domain wall segregation enthalpy of about -0.036 eV is comparable to the thermal energy at 150 °C, from which O_i is mobile in bulk RMnO$_3$. The trimerization amplitude and crystal structure does not change appreciably between ambient temperature and 150 °C. The driving force for defect segregation to the walls can be reduced at elevated temperatures if the domain walls broaden. Such broadening can be neglected at 150°, according to Landau theory, such that the calculated segregation enthalpy from DFT is still expected to be valid. The accumulation of O_i and its charge compensating holes, will thus raise the local charge carrier density at the neutral walls. Neutral domain walls oriented in (110) planes have slightly higher energy than the (120) domain walls considered here[25]. The strain field at these walls is hence expected to be higher, possibly

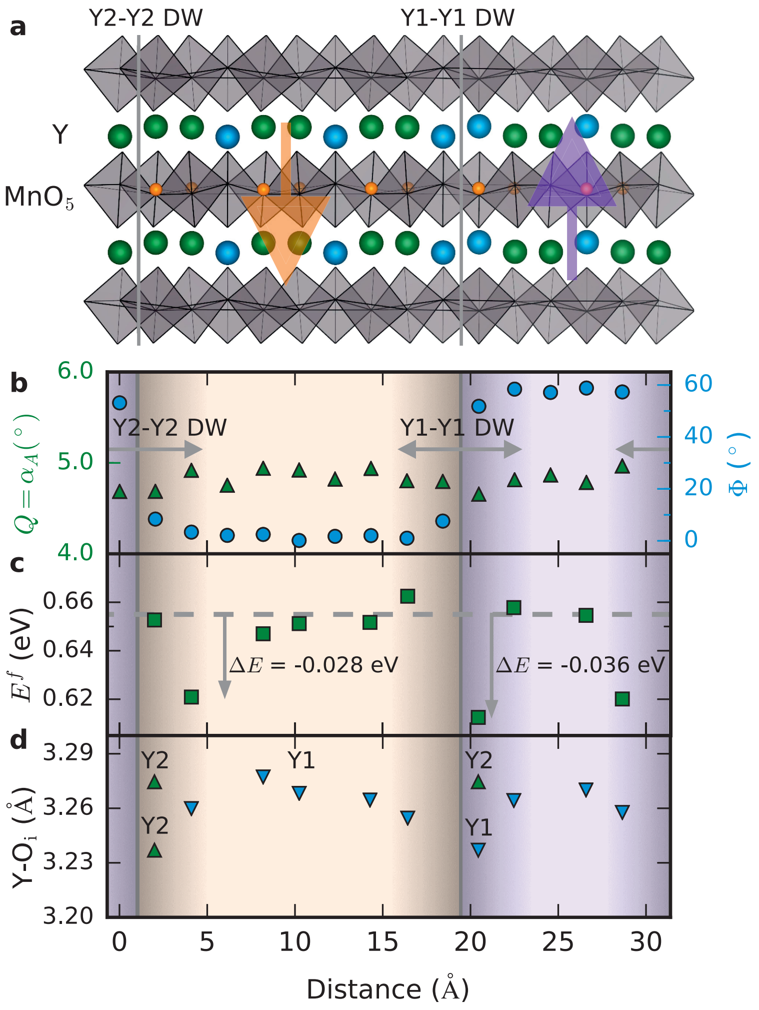

Figure 6.10: O$_i$ at neutral domain walls. (a) DFT relaxed 5×2×1 supercell with neutral (120) domain walls. The walls are either Y1 (blue) or Y2 (green) terminated, leaving different possibilities for defect accommodation. Orange spheres represent the positions of O$_i$ in the different relaxations. **(b)** Trimerization order parameter amplitude Q by apical tilting angle, α_A, and order parameter angle, Φ, versus position in the domain wall cell. **(c)** Defect formation energy of O$_i$ emphasizing the segregation energy ($\Delta E = E^f_{\mathrm{DW}} - E^f_{\mathrm{bulk}}$) to the domain walls compared to the average defect formation of the positions in the middle of the domains (marked with dashed line). Chemical potential of oxygen is set to -4.5 eV. **(d)** Y1-O$_i$ bonds for relaxations of O$_i$ at different positions in the cell.

creating even larger driving force for O_i segregation than the (120) domain walls, and should be followed up on.

6.9 Summary

Interstitial oxygen are accommodated in the Mn-O layers of the structure, causing only subtle and local distortions of the surrounding lattice, making experimental detection difficult for small concentrations. The interstitial oxygen oxidizes the two closest Mn^{3+} to Mn^{4+} and is thus the predominating origin of p-type conductivity in the hexagonal manganites.

Unlike the oxygen vacancies discussed in Chapter 5, the oxygens are enthalpy stabilized in the structure below 400-500 °C, but are driven out by entropy upon heating as O_2 is favoured. This implies that $YMnO_3$ is not only metastable with respect to Y_2O_3 and YMn_2O_5, in accordance with the phase diagram[163], it is also metastable with respect to oxidation towards the limiting case of $Y_3Mn_3O_{10}$. Thermo-atmospheric history is thus important when synthesising hexagonal manganites, as cooling in oxygen containing atmospheres will oxidize the samples. It is important to note that a bulk $YMnO_3$ sample will not oxidize completely at ambient conditions for kinetic reasons; the diffusion length in bulk is too large compared with the relatively low ionic mobility at room temperature. However, at the nanoscale, in thin films and at surfaces, oxidation will occur spontaneously also at ambient conditions.

Moreover, interstitial oxygen is likely to segregate at neutral ferroelectric domain walls due to stronger bonding with Y. This mechanism is different from the electrostatic driving force for defect segregation at charged head-to-head and tail-to-tail domain walls. The results emphasize the necessity and potential which lies in controlling the thermal and atmospheric history of hexagonal manganite materials in order to tailor the point defect population, charge carrier concentration, and functional properties.

Chapter 7

Connecting the parts: Improper ferroelectricity and oxygen stoichiometry

The unconventional order-disorder ferroelectric transition is expected to occur in all hexagonal manganites, originating in the special Mexican hat energy landscape which creates strong driving force for trimerization, but relatively weak driving force for ferroelectricity. Moving from the top of the hat and down to the brim lowers the energy of the system with as much as ∼500 meV[270], an energy corresponding to a temperature of ∼5000 K. This energy difference reflects the tremendous driving force for the trimerization and the small likelihood of a displacive phase transition from the symmetry in the brim of the hat to a high-symmetry structure at the top of the hat. The amount of bipyramidal tilt and R cation off-centring, described by the trimerization order parameter amplitude Q, see Fig. 7.1**a**-**b**, are fairly independent on the type of R cation[155,289], and will always exist due to strong short range forces. Previous reports[266] and calculations presented in Chapter 4 show that strong out-of-plane R-O_P bonds are the structural "glue", coupling the trimerization distortions of the cation sublattices. Further, these R-O_P bonds are the main reason for the much higher cost associated with changing the trimerization amplitude Q compared to the angle Φ, deciding the structural flexibility.

The improper ferroelectricity means that the trimerization with order parameter Q, Φ does not alone lower the energy for the polar ground state. Coupling between only the amplitude Q and the angle Φ will, in fact, create very

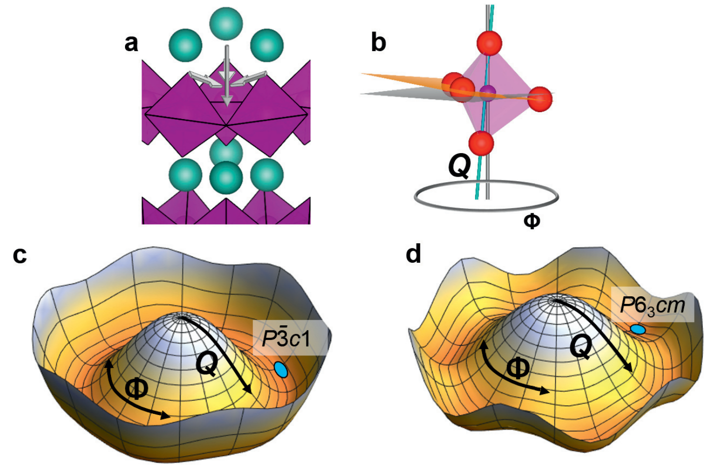

Only K_3 mode ($\boldsymbol{Q}$, $\boldsymbol{\Phi}$)

$$G(Q,\Phi,P) = aQ^2 + bQ^4 + fQ^6\left(C + \cos 6\Phi\right)$$

K_3 mode ($\boldsymbol{Q}$, $\boldsymbol{\Phi}$) coupled with Γ_2^- ($\boldsymbol{P}$)

$$G(Q,\Phi,P) = aQ^2 + bQ^4 + fQ^6\left(C + \cos 6\Phi\right) + a'P^2 + gP^2Q^2 - g'PQ^3\cos 3\Phi$$

Figure 7.1: (a) Excerpt of the polar $P6_3cm$ structure with arrows showing the tilting of the trigonal bipyramids and its relation to the trimerization order parameter amplitude Q and angle Φ **(b)**. **(c)** The Landau free energy including only the Q, Φ and their coupling terms breaking the symmetry towards anti-polar $P\bar{3}c1$. **(d)** All terms including Q, Φ, P and a negative coupling term between P and Q, reversing the coupling between Q and Φ to give the polar hettotype $P6_3cm$.

shallow minima in the brim at angles corresponding to the anti-polar structure, see Fig. 7.1**c**. Deeper minima and improper ferroelectric distortion only emerges when the Q, Φ of the trimerization K_3 mode couples to the polarization P of the Γ_2^- mode, see Fig. 7.1**d**. The coupling induces a shift of the R cation layers along c with respect to the MnO layers[24].

As with the trimerization, the driving force for ferroelectricity and energy lowering of the polar phase relative to the antipolar phase is largely dependent on the interactions between the R cations and oxygens. The *geometric* ferroelectric distortion effectively optimizes two out of three R-O_P bonds[23]. The interaction between R and O_P probably has contributions from both ionic and covalent bonding, and pure steric effects due to crystallographic packing of electronegative ions of different size. The effect of R cation on the trimerization angle Φ has been studied previously. Y stabilizes the polar structure, possibly due to its electropositivity and highly ionic bonds to the surrounding O[23]. For less ionic R cations, such as In in $InMnO_3$, the R-O bond has more covalent character, possibly reducing the driving force towards the polar structure[290]. Hence, the compound can be stabilized in both the polar $P6_3cm$ and the antipolar $P\bar{3}c1$ structures due to very similar energies of formation[113,122,291]. For this reason, $InMnO_3$ is expected to host fluctuations of the trimerization order parameter at even lower temperatures than $YMnO_3$. For the same reason, $InMnO_3$ has broader domain walls than $YMnO_3$ at low temperatures[292], and they are expected to broaden more upon heating.

The new insight on the structural flexibility and the importance of the R-O bonds can help to explain previous reports showing that oxygen deficiency both suppresses the trimerization[101] and reduces the macroscopic polarization[190]. The microscopic mechanism for this, presented in Chapter 5, shows that low concentrations of oxygen vacancies order at sites where they mainly cause changes of the trimerization angle, reducing the polarization without significantly reducing the trimerization amplitude. At the walls, the relevant Y-O_P bonds are longer, and the structural flexibility is lower, hence increasing the formation enthalpy of the oxygen vacancies. At higher concentrations, the vacancies must order also at sites where they reduce the trimerization amplitude.

The results further shed light on how the delicate relationship between the polar and antipolar phases can be reversibly tuned. Cooled samples of $InMnO_3$ in air have been previously shown to become polar, while quenched samples become antipolar[122]. The authors of the particular study suggested that the antipolar structure was kinetically stabilized, while the polar structure was the true ground state. The results on interstitial oxygen in Chapter 6, rather imply that oxygen excess might be the reason. Other studies have reported that interstitial oxygen increases the stability of the polar phase in $InMnO_3$[113], in line with these results. This implies that interstitial oxygen stabilizes the $P6_3cm$ structure and increases the local energy barriers in the hat. Despite of the walls having a symmetry closer to the anti-polar structure, the interstitial oxygen segregated to the neutral walls, presented in Chapter 6. It was shown that the increased stability at the walls was due to shorter Y-O_i bonds, possibly because of the local strain field. The strain field associated with the 60° change in trimerization angle when crossing a domain wall, originates in the structural difference between the polar and antipolar phases, followed by an energy difference visualized as climbing over one of the local maxima in the hat. The larger the local barrier is, the larger the strain field is expected to be. The size of the barrier is determined by the coupling between the trimerization order parameter (Q, Φ) and the polarization P. This coupling is still not fully understood, but as this work shows, understanding the R-O bonds is imperative.

Understanding the driving force for trimerization and polarization in the hexagonal manganites lays the foundation for future investigations on the structural and electronic properties in these materials. The structural flexibility, as described by the energy landscape of the order parameter, is of great importance for understanding the accommodation and migration of point defects.

Chapter 8

Conclusions and outlook

The local structure and structural coherence across the ferroelectric phase transition of h-$YMnO_3$ was investigated using high-energy neutron total scattering. The oxygen defect chemistry was investigated by experimental techniques and density functional theory, in order to reveal the microscopic mechanisms.

The structural flexibility, which is established at the unusual order-disorder phase transition, is strongly coupled to the oxygen defect chemistry of h-RMnO$_3$. Although the multivalent nature of manganese is the reason why oxygen point defects form in the Mn-O layers, the electropositivity of Y, and flexibility of the structure, described by trimerization order parameter, determines the defect positions within these layers. Further, the strain field at neutral domain walls reduces the flexibility of the trimerization angle and changes the lengths of the Y-O_P bonds. This results in higher formation energy of oxygen vacancies at these walls. In contrast to the oxygen vacancies, interstitial oxygen enthalpy stabilizes the structure, leading to p-type conductivity. Segregation of interstitial oxygen to the neutral domain walls, further suggest that this point defect may be a source of conductivity at neutral domain walls.

Outlook

The unusual order-disorder transition in h-$YMnO_3$, presented in Chapter 4, is expected to apply for other hexagonal manganites. Compounds where the anomalous behaviour is expected to emerge at lower temperatures, can possibly make the study of the transition accessible with other experimental techniques. As previously suggested in Chapter 7, the covalent bonding in h-InMnO$_3$, reducing the energy barriers in the Mexican hat potential[293], may induce order-parameter fluctuations at much lower temperatures than in h-YMnO$_3$. This should be studied further to investigate the coupling between electronegativity of the rare-earth cation and the improper ferroelectricity. Further, isovalent doping of the Mn may also serve as a route to understand these mechanisms, as have already been implied for substitution with Ga[113]. More insight may also be gained by studying the analogous phase transition in hexagonal perovskite 2H-BaMnO$_3$. The ferroelectric phase transition in this material occurs at a much lower temperature of 130 K[294,295] and will thus give a much lower trimerization amplitude.

The study of the domain and vortex formation in hexagonal manganites has provided the first system experimentally compatible with the Kibble-Zurek scaling-law to investigate the formation of cosmological strings beyond mean-field[156]. The formation of the vortices when cooling through T_{C} involves the condensation of the trimerization order parameter Q, Φ. The vortex density has been shown previously to depend strongly on the cooling rate, and the type of R cation[81,155,156]. However, there are still open questions regarding the vortex density. In particular, the relationship between vortex density and type of rare-earth cation, has not been understood. The results in this thesis imply that oxygen vacancies can be important for the vortex formation, especially since some oxygen deficiency is likely at high temperatures. The formation energy of oxygen vacancies is expected to depend on the type of R cation. High concentration of vacancies may impede the the onset of fluctuations, as they reduce the driving force for trimerization, as shown in Chapter 5.

The defect chemistry and especially simple tuning of oxygen non-stoichiometry in the hexagonal manganites makes these materials candidates for chemical design of ferroelectric domain walls. Although the types of defects, their charge compensation mechanisms, and potential for tuning domain wall conductivity is becoming more known, several parts of the puzzle are still missing before a functional device can be made. Firstly, future research in this field must aim to learn how the electrical properties can be tuned without destroying the mechanical integrity of the material and how the dominant charge carrier can be switched between electrons and electron holes. Secondly, it is also favourable if the conductivity can be turned off and on by applying an external field. This is the property of a memristor, or memory resistor, an electric circuit element where a hysteretic voltage-current dependence gives the possibility to write the logic states "0" and "1"(refs. 110, 112). Thirdly, the mobility of domain walls interacting with point defects should be investigated more, as the possibility of moving the domain walls in the component is important.

The high concentration of excess oxygen in hexagonal manganites, makes them interesting for oxygen storage technology. Oxygen excess through interstitial oxygen ions give excellent ionic mobility, even in bulk, comparable to the best optimized state-of-the-art perovskite compounds used for oxygen storage and gas-separation techniques[296–300]. In addition to excellent mobility, the oxygen can diffuse in and out at many hundred degrees lower than in the perovskites, suggesting tremendous possibilities for reducing the operational energy costs. This holds potential for a paradigm shift in oxygen storage and separation technologies. However, large chemical expansion follows the highly varying oxygen content, causing microscopic cracking and mechanical degradation. Tuning of the defect chemistry to reduce the anisotropic chemical expansion is one path to mend this problem, although only a few studies cover it[301–305].

Bibliography

[1] Valasek, J. Piezo-Electric and Allied Phenomena in Rochelle Salt. *Phys. Rev.* **17**, 475–481 (1921).

[2] Martin, R. M. Piezoelectricity. *Phys. Rev. B* **5**, 1607–1613 (1972).

[3] Schmid, H. On a magnetoelectric classification of materials. *Int. J. Magn.* **4**, 337–361 (1973).

[4] Fiebig, M. Revival of the magnetoelectric effect. *J. Phys. D: Appl. Phys.* **38**, R123–R152 (2005).

[5] Scott, J. F. Applications of magnetoelectrics. *J. Mater. Chem.* **22**, 4567–4574 (2012).

[6] Spaldin, N. A. & Fiebig, M. The Renaissance of Magnetoelectric Multiferroics. *Science* **309**, 391–392 (2005).

[7] Vopson, M. M. Fundamentals of Multiferroic Materials and Their Possible Applications. *Crit. Rev. Solid State* **40**, 223–250 (2015).

[8] Scott, J. F. Data storage: Multiferroic memories. *Nat. Mater.* **6**, 256–257 (2007).

[9] Aschauer, U. & Spaldin, N. A. Interplay between strain, defect charge state, and functionality in complex oxides. *Appl. Phys. Lett.* **109**, 031901 (2016).

[10] Kalinin, S. V., Borisevich, A. & Fong, D. Beyond Condensed Matter Physics on the Nanoscale: The Role of Ionic and Electrochemical Phenomena in the Physical Functionalities of Oxide Materials. *ACS Nano* **6**, 10423–10437 (2012).

[11] Kalinin, S. V. Multiferroics: Making a point of control. *Nat. Phys.* **13**, 115–116 (2017).

[12] Stambouli, A. B. & Traversa, E. Solid oxide fuel cells (SOFCs): a review of an environmentally clean and efficient source of energy. *Renew. Sustainable Energy Rev.* **6**, 433–455 (2002).

[13] Tarascon, J.-M. & Armand, M. Issues and challenges facing rechargeable lithium batteries. *Nature* **414**, 359–367 (2001).

[14] Grande, T., Tolchard, J. R. & Selbach, S. M. Anisotropic Thermal and Chemical Expansion in Sr-Substituted $LaMnO_{3+\delta}$: Implications for Chemical Strain Relaxation. *Chem. Mater.* **24**, 338–345 (2012).

[15] Catalan, G., Seidel, J., Ramesh, R. & Scott, J. F. Domain wall nanoelectronics. *Rev. Mod. Phys.* **84**, 119–156 (2012).

[16] Seidel, J., Martin, L. W., He, Q., Zhan, Q., Chu, Y.-H., Rother, A., Hawkridge, M. E., Maksymovych, P., Yu, P., Gajek, M., Balke, N., Kalinin, S. V., Gemming, S., Wang, F., Catalan, G., Scott, J. F., Spaldin, N. A., Orenstein, J. & Ramesh, R. Conduction at domain walls in oxide multiferroics. *Nat. Mater.* **8**, 229–234 (2009).

[17] Meier, D. Functional domain walls in multiferroics. *J. Phys.: Condens. Matter* **27**, 463003 (2015).

[18] Kalinin, S. V. & Spaldin, N. A. Functional Ion Defects in Transition Metal Oxides. *Science* **341**, 858–859 (2013).

[19] Bertaut, F. & Forrat, F. Sur les déformations dans les pérovskites a base de terres rares et d'élements de transition trivalents. *J. Phys. Rad.* **17**, 129–131 (1956).

[20] Bertaut, F., Fang, P. & Forrat, F. Physique des solides - Les manganites de terres rares et d'yttrium - Une nouvelle classe de ferroelectriques. *Comp. Rend. Hebd. Sci.* **256**, 1958 (1963).

[21] Yakel, H. L., Koehler, W. C., Bertaut, E. F. & Forrat, E. F. On the crystal structure of the manganese (III) trioxides of the heavy lanthanides and yttrium. *Acta Crystallogr.* **16**, 957–962 (1963).

[22] Fiebig, M., Lottermoser, T., Lonkai, T., Goltsev, A. & Pisarev, R. Magnetoelectric effects in multiferroic manganites. *J. Magn. Magn. Mater.* **290-291**, 883–890 (2005).

[23] Van Aken, B. B., Palstra, T. T., Filippetti, A. & Spaldin, N. A. The origin of ferroelectricity in magnetoelectric $YMnO_3$. *Nat. Mater.* **3**, 164–170 (2004).

[24] Fennie, C. J. & Rabe, K. M. Ferroelectric transition in $YMnO_3$ from first principles. *Phys. Rev. B* **72**, 100103(R) (2005).

[25] Kumagai, Y. & Spaldin, N. A. Structural domain walls in polar hexagonal manganites. *Nat. Commun.* **4**, 1540 (2013).

[26] Meier, D., Seidel, J., Cano, A., Delaney, K., Kumagai, Y., Mostovoy, M., Spaldin, N. A., Ramesh, R. & Fiebig, M. Anisotropic conductance at improper ferroelectric domain walls. *Nat. Mater.* **11**, 284–288 (2012).

[27] Barone, P. & Picozzi, S. Mechanisms and origin of multiferroicity. *C. R. Phys.* **16**, 143–152 (2015).

[28] Fiebig, M., Lottermoser, T., Meier, D. & Trassin, M. The evolution of multiferroics. *Nat. Rev. Mater.* **1** (2016).

[29] Cohen, R. Origin of Ferroelectricity in Perovskite Oxides. *Nature* **358**, 136–138 (1992).

[30] Wang, J., Neaton, J. B., Zheng, H., Nagarajan, V., Ogale, S. B., Liu, B., Viehland, D., Vaithyanathan, V., Schlom, D. G., Waghmare, U. V., Spaldin, N. A., Rabe, K. M., Wuttig, M. & Ramesh, R. Epitaxial $BiFeO_3$ Multiferroic Thin Film Heterostructures. *Science* **299**, 1719–1722 (2003).

[31] Bhide, V. G., Deshmukh, K. G. & Hegde, M. S. Ferroelectric properties of $PbTiO_3$. *Physica* **28**, 871–876 (1962).

[32] Lilienblum, M., Lottermoser, T., Manz, S., Selbach, S. M., Cano, A. & Fiebig, M. Ferroelectricity in the multiferroic hexagonal manganites. *Nat. Phys.* **11**, 1070–1073 (2015).

[33] Brink, J. v. d. & Khomskii, D. I. Multiferroicity due to charge ordering. *J. Phys.: Condens. Matter* **20**, 434217 (2008).

[34] Ikeda, N., Ohsumi, H., Ohwada, K., Ishii, K., Inami, T., Kakurai, K., Murakami, Y., Yoshii, K., Mori, S., Horibe, Y. & Kitô, H. Ferroelectricity from iron valence ordering in the charge-frustrated system $LuFe_2O_4$. *Nature* **436**, 1136–1138 (2005).

[35] de Groot, J., Mueller, T., Rosenberg, R. A., Keavney, D. J., Islam, Z., Kim, J.-W. & Angst, M. Charge order in $LuFe_2O_4$: an unlikely route to ferroelectricity. *Phys. Rev. Lett.* **108**, 187601 (2012).

[36] Tokura, Y., Seki, S. & Nagaosa, N. Multiferroics of spin origin. *Rep. Prog. Phys.* **77**, 076501 (2014).

[37] Levanyuk, A. P. & Sannikov, D. G. Improper ferroelectrics. *Sov. Phys. Usp.* **17**, 199 (1974).

[38] Scott, J. F. Applications of Modern Ferroelectrics. *Science* **315**, 954–959 (2007).

[39] Setter, N., Damjanovic, D., Eng, L., Fox, G., Gevorgian, S., Hong, S., Kingon, A., Kohlstedt, H., Park, N. Y., Stephenson, G. B., Stolitchnov, I., Taganstev, A. K., Taylor, D. V., Yamada, T. & Streiffer, S. Ferroelectric thin films: Review of materials, properties, and applications. *J. Appl. Phys.* **100**, 051606 (2006).

[40] Kittel, C. Theory of the Structure of Ferromagnetic Domains in Films and Small Particles. *Phys. Rev.* **70**, 965–971 (1946).

[41] Junquera, J. & Ghosez, P. Critical thickness for ferroelectricity in perovskite ultrathin films. *Nature* **422**, 506–509 (2003).

[42] Ishibashi, Y. & Dvorak, V. Domain walls in Improper Ferroelectrics. *J. Phys. Soc. Jpn.* **41**, 1650–1658 (1976).

[43] Newnham, R. E. Domains in materials. *Am. Mineral.* **59**, 906–918 (1974).

[44] Newnham, R. E., Miller, C. S., Cross, L. E. & Cline, T. W. Tailored domain patterns in piezoelectric crystals. *Phys. Stat. Sol. (A)* **32**, 69–78 (1975).

[45] Salje, E. K. H. Ferroelastic Materials. *Ann. Rev. Mater. Res.* **42**, 265–283 (2012).

[46] Schmid, H. Multi-ferroic magnetoelectrics. *Ferroelectrics* **162**, 317–338 (1994).

[47] Spaldin, N. A., Cheong, S.-W. & Ramesh, R. Multiferroics: Past, present, and future. *Physics Today* **63**, 38–43 (2010).

[48] Smolenskii, G. A. & Bokov, V. A. Coexistence of Magnetic and Electric Ordering in Crystals. *J. Appl. Phys.* **35**, 915–918 (1964).

[49] Hill, N. A. Why Are There so Few Magnetic Ferroelectrics? *J. Phys. Chem. B* **104**, 6694–6709 (2000).

[50] Hill, N. A. & Filippetti, A. Why are there any magnetic ferroelectrics? *J. Magn. Magn. Mater.* **242**, 976–979 (2002).

[51] Benedek, N. A. & Fennie, C. J. Why Are There So Few Perovskite Ferroelectrics? *J. Phys. Chem. C* **117**, 13339–13349 (2013).

[52] Khomskii, D. Multiferroics: Different ways to combine magnetism and ferroelectricity. *J. Magn. Magn. Mater.* **306**, 1–8 (2006).

[53] Cheong, S.-W. & Mostovoy, M. Multiferroics: a magnetic twist for ferroelectricity. *Nat. Mater.* **6**, 13–20 (2007).

[54] Tokura, Y. Multiferroics – toward strong coupling between magnetization and polarization in a solid. *J. Magn. Magn. Mater.* **310**, 1145–1150 (2007).

[55] Wang, K. F., Liu, J.-M. & Ren, Z. F. Multiferroicity, The coupling between magnetic and polarization. *Adv. Phys.* **58**, 321–448 (2009).

[56] Dong, S., Liu, J.-M., Cheong, S.-W. & Ren, Z. Multiferroic materials and magnetoelectric physics: symmetry, entanglement, excitation, and topology. *Adv. Phys.* **64**, 519–626 (2015).

[57] Eerenstein, W., Mathur, N. D. & Scott, J. F. Multiferroic and magnetoelectric materials. *Nature* **442**, 759–765 (2006).

[58] Fiebig, M., Lottermoser, T., Fröhlich, D., Goltsev, A. V. & Pisarev, R. V. Observation of coupled magnetic and electric domains. *Nature* **419**, 818–820 (2002).

[59] Gajek, M., Bibes, M., Fusil, S., Bouzehouane, K., Fontcuberta, J., Barthélémy, A. & Fert, A. Tunnel junctions with multiferroic barriers. *Nat. Mater.* **6**, 296–302 (2007).

[60] Rikken, G. L. J. A. & Raupach, E. Observation of magneto-chiral dichroism. *Nature* **390**, 493–494 (1997).

[61] Sawada, K. & Nagaosa, N. Optical Magnetoelectric Effect in Multiferroic Materials: Evidence for a Lorentz Force Acting on a Ray of Light. *Phys. Rev. Lett.* **95**, 237402 (2005).

[62] Newnham, R. E., Kramer, J. J., Schulze, W. A. & Cross, L. E. Magnetoferroelectricity in Cr_2BeO_4. *J. Appl. Phys.* **49**, 6088–6091 (1978).

[63] Schmid, H. On the possibility of ferromagnetic, antiferromagnetic, ferroelectric, and ferroelastic domain reorientations in magnetic and electric fields. *Ferroelectrics* **221**, 9–17 (1999).

[64] Kimura, T., Goto, T., Shintani, H., Ishizaka, K., Arima, T. & Tokura, Y. Magnetic control of ferroelectric polarization. *Nature* **426**, 55–58 (2003).

[65] Valencia, S., Crassous, A., Bocher, L., Garcia, V., Moya, X., Cherifi, R. O., Deranlot, C., Bouzehouane, K., Fusil, S., Zobelli, A., Gloter, A., Mathur, N. D., Gaupp, A., Abrudan, R., Radu, F., Barthélémy, A. & Bibes, M. Interface-induced room-temperature multiferroicity in $BaTiO_3$. *Nat. Mater.* **10**, 753–758 (2011).

[66] Scott, J. F. Room-temperature multiferroic magnetoelectrics. *NPG Asia Mater.* **5**, e72 (2013).

[67] Bibes, M. & Barthélémy, A. Multiferroics: Towards a magnetoelectric memory. *Nat. Mater.* **7**, 425–426 (2008).

[68] Chu, Y.-H., Martin, L. W., Holcomb, M. B., Gajek, M., Han, S.-J., He, Q., Balke, N., Yang, C.-H., Lee, D., Hu, W., Zhan, Q., Yang, P.-L., Fraile-Rodriguez, A., Scholl, A., Wang, S. X. & Ramesh, R. Electric-field control of local ferromagnetism using a magnetoelectric multiferroic. *Nat. Mater.* **7**, 478–482 (2008).

[69] Binek, C. & Doudin, B. Magnetoelectronics with magnetoelectrics. *J. Phys.: Condens. Matter* **17**, L39 (2005).

[70] Heron, J. T., Bosse, J. L., He, Q., Gao, Y., Trassin, M., Ye, L., Clarkson, J. D., Wang, C., Liu, J., Salahuddin, S., Ralph, D. C., Schlom, D. G.,

Íñiguez, J., Huey, B. D. & Ramesh, R. Deterministic switching of ferromagnetism at room temperature using an electric field. *Nature* **516**, 370–373 (2014).

[71] Ehrenfest, P. Phasenumwandlungen im ueblichen und erweiterten Sinn, classifiziert nach dem entsprechenden Singularitaeten des thermodynamischen Potentiales. *Verhandlingen der Koninklijke Akademie van Wetenschappen (Amsterdam)* **36**, 153–157 (1933).

[72] Jaeger, G. The Ehrenfest Classification of Phase Transitions: Introduction and Evolution. *Arch. Hist. Exact. Sc.* **53**, 51–81 (1998).

[73] Orobengoa, D., Capillas, C., Aroyo, M. I. & Perez-Mato, J. M. AMPLIMODES: symmetry-mode analysis on the Bilbao Crystallographic Server. *J. Appl. Crystallogr.* **42**, 820–833 (2009).

[74] Landau, L. On the theory of phase transitions. *Ukr. J. Phys.* **53**, 25–35 (2008).

[75] Devonshire, A. F. Theory of ferroelectrics. *Adv. Phys.* **3**, 85–130 (1954).

[76] Chaikin, P. M. & Lubensky, T. C. *Principles of condensed matter physics* (Cambridge University Press, The Edinburgh Building, Cambridge CB2 2RU, UK, 2000).

[77] Kadanoff, L. P. Scaling and universality in statistical physics. *Phys. A: Stat. Mech. Appl.* **163**, 1–14 (1990).

[78] Zheludev, A. Part II: Phase transitions, criticality and scaling. In *Advanced solid state physics – lecture notes* (ETH Zürich, 2016).

[79] Hohenberg, P. C. & Krekhov, A. P. An introduction to the Ginzburg-Landau theory of phase transitions and nonequilibrium patterns. *Phys. Rep.* **572**, 1–42 (2015).

[80] Hohenberg, P. C. & Halperin, B. I. Theory of dynamic critical phenomena. *Rev. Mod. Phys.* **49**, 435–479 (1977).

[81] Meier, Q. N., Lilienblum, M., Griffin, S. M., Conder, K., Pomjakushina, E., Yan, Z., Bourret, E., Meier, D., Lichtenberg, F., Salje, E. K. H., Spaldin, N. A., Fiebig, M. & Cano, A. Global formation of topological defects in the multiferroic hexagonal manganites. *submitted* (2017). ArXiv: 1703.08321.

[82] Wilson, K. G. & Fisher, M. E. Critical Exponents in 3.99 Dimensions. *Phys. Rev. Lett.* **28**, 240–243 (1972).

[83] Fisher, M. E. The renormalization group in the theory of critical behavior. *Rev. Mod. Phys.* **46**, 597–616 (1974).

[84] Dove, M. T. Theory of displacive phase transitions in minerals. *Am. Mineral.* **82**, 213–244 (1997).

[85] Nelmes, R. J. & Kuhs, W. F. The crystal structure of tetragonal $PbTiO_3$ at room temperature and at 700 K. *Solid State Commun.* **54**, 721–723 (1985).

[86] Sollich, P., Heine, V. & Dove, M. T. The Ginzburg interval in soft-mode phase transitions: consequences of the rigid unit mode picture. *J. Phys.: Condens. Matter* **6**, 3171 (1994).

[87] Kwei, G. H., Lawson, A. C., Billinge, S. J. L. & Cheong, S. W. Structures of the ferroelectric phases of barium titanate. *J. Phys. Chem.* **97**, 2368–2377 (1993).

[88] Comes, R., Lambert, M. & Guinier, A. The chain structure of $BaTiO_3$ and $KNbO_3$. *Solid State Commun.* **6**, 715–719 (1968).

[89] Kwei, G. H., Billinge, S. J. L., Cheong, S.-W. & Saxton, J. G. Pair-distribution functions of ferroelectric perovskites: Direct observation of structural ground states. *Ferroelectrics* **164**, 57–73 (1995).

[90] Zalar, B., Laguta, V. V. & Blinc, R. NMR Evidence for the Coexistence of Order-Disorder and Displacive Components in Barium Titanate. *Phys. Rev. Lett.* **90**, 037601 (2003).

[91] Cohen, R. E. & Krakauer, H. Lattice dynamics and origin of ferroelectricity in $BaTiO_3$: Linearized-augmented-plane-wave total-energy calculations. *Phys. Rev. B* **42**, 6416–6423 (1990).

[92] Phillpot, S. R. & Gopalan, V. Coupled displacive and order-disorder dynamics in $LiNbO_3$ by molecular-dynamics simulation. *Appl. Phys. Lett.* **84**, 1916–1918 (2004).

[93] Mountstevens, E. H., Redfern, S. A. T. & Attfield, J. P. Order-disorder octahedral tilting transitions in $SrSnO_3$ perovskite. *Phys. Rev. B* **71**, 220102 (2005).

[94] Tuller, H. L. & Bishop, S. R. Point Defects in Oxides: Tailoring Materials Through Defect Engineering. *Ann. Rev. Mater. Res.* **41**, 369–398 (2011).

[95] Kröger, F. A. & Vink, H. J. Relations between the Concentrations of Imperfections in Crystalline Solids. *Solid State Phys.* **3**, 307–435 (1956).

[96] Adler, S. B. Chemical Expansivity of Electrochemical Ceramics. *J. Am. Ceram. Soc.* **84**, 2117–2119 (2001).

[97] Ullmann, H. & Trofimenko, N. Estimation of effective ionic radii in highly defective perovskite-type oxides from experimental data. *J. Alloys Compd.* **316**, 153–158 (2001).

[98] Aschauer, U., Pfenninger, R., Selbach, S. M., Grande, T. & Spaldin, N. A. Strain-controlled oxygen vacancy formation and ordering in $CaMnO_3$. *Phys. Rev. B* **88**, 054111 (2013).

[99] Bishop, S., Marrocchelli, D., Chatzichristodoulou, C., Perry, N., Mogensen, M., Tuller, H. & Wachsman, E. Chemical Expansion: Implications for Electrochemical Energy Storage and Conversion Devices. *Ann. Rev. Mater. Res.* **44**, 205–239 (2014).

[100] Marrocchelli, D., Bishop, S. R., Tuller, H. L., Watson, G. W. & Yildiz, B. Charge localization increases chemical expansion in cerium-based oxides. *Phys. Chem. Chem. Phys.* **14**, 12070–12074 (2012).

[101] Selbach, S. M., Nordli Løvik, A., Bergum, K., Tolchard, J. R., Einarsrud, M.-A. & Grande, T. Crystal structure, chemical expansion and phase stability of $HoMnO_3$ at high temperature. *J. Solid State Chem.* **196**, 528–535 (2012).

[102] Jedvik, E., Lindman, A., Benediktsson, M. T. & Wahnström, G. Size and shape of oxygen vacancies and protons in acceptor-doped barium zirconate. *Solid State Ionics* **275**, 2–8 (2015).

[103] Freysoldt, C., Grabowski, B., Hickel, T., Neugebauer, J., Kresse, G., Janotti, A. & Van de Walle, C. G. First-principles calculations for point defects in solids. *Rev. Mod. Phys.* **86**, 253–305 (2014).

[104] Van de Walle, C. G., Laks, D. B., Neumark, G. F. & Pantelides, S. T. First-principles calculations of solubilities and doping limits: Li, Na, and N in ZnSe. *Phys. Rev. B* **47**, 9425–9434 (1993).

[105] Zhang, S. B. & Northrup, J. E. Chemical potential dependence of defect formation energies in GaAs: Application to Ga self-diffusion. *Phys. Rev. Lett.* **67**, 2339–2342 (1991).

[106] Aggarwal, S. & Ramesh, R. Point Defect Chemistry of Metal Oxide Heterostructures. *Ann. Rev. Mater. Sci.* **28**, 463–499 (1998).

[107] Scott, J. F. & Dawber, M. Oxygen-vacancy ordering as a fatigue mechanism in perovskite ferroelectrics. *Appl. Phys. Lett.* **76**, 3801–3803 (2000).

[108] Dawber, M. & Scott, J. F. A model for fatigue in ferroelectric perovskite thin films. *Appl. Phys. Lett.* **76**, 1060 (2000).

[109] Schrade, D., Mueller, R., Xu, B. X. & Gross, D. Domain wall pinning by point defects in ferroelectric materials. *Proc. SPIE* **6526**, 65260B–65260B–8 (2007).

[110] Strukov, D. B., Snider, G. S., Stewart, D. R. & Williams, R. S. The missing memristor found. *Nature* **453**, 80–83 (2008).

[111] Waser, R., Dittmann, R., Staikov, G. & Szot, K. Redox-Based Resistive Switching Memories - Nanoionic Mechanisms, Prospects, and Challenges. *Adv. Mater.* **21**, 2632–2663 (2009).

[112] Williams, S. R. How we found the missing memristor. *Spectrum, IEEE* **45**, 28–35 (2008).

[113] Griffin, S. M., Reidulff, M., Selbach, S. M. & Spaldin, N. A. Defect Chemistry as a Crystal Structure Design Parameter: Intrinsic Point Defects and Ga Substitution in $InMnO_3$. *Chem. Mater.* **29**, 2425–2434 (2017).

[114] Du, Y., Wang, X. L., Chen, D. P., Dou, S. X., Cheng, Z. X., Higgins, M., Wallace, G. & Wang, J. Y. Domain wall conductivity in oxygen deficient multiferroic $YMnO_3$ single crystals. *Appl. Phys. Lett.* **99**, 252107 (2011).

[115] Du, Y., Wang, X., Chen, D., Yu, Y., Hao, W., Cheng, Z. & Dou, S. X. Manipulation of domain wall mobility by oxygen vacancy ordering in multiferroic $YMnO_3$. *Phys. Chem. Chem. Phys.* **15**, 20010 (2013).

[116] Choi, T., Horibe, Y., Yi, H. T., Choi, Y. J., Wu, W. & Cheong, S.-W. Insulating interlocked ferroelectric and structural antiphase domain walls in multiferroic $YMnO_3$. *Nat. Mater.* **9**, 253–258 (2010).

[117] Ramesh, R. & Spaldin, N. A. Multiferroics: progress and prospects in thin films. *Nat. Mater.* **6**, 21–29 (2007).

[118] van Aken, B. B., Meetsma, A. & Palstra, T. T. Hexagonal $YMnO_3$. *Acta Crystallogr. C: Cryst. Str. Commun.* **57**, 230–232 (2001).

[119] Abughayada, C., Dabrowski, B., Avdeev, M., Kolesnik, S., Remsen, S. & Chmaissem, O. Structural, magnetic, and oxygen storage properties of hexagonal $Dy_{1-x}Y_xMnO_{3+\delta}$. *J. Solid State Chem.* **217**, 127–135 (2014).

[120] Bosak, A. A., Dubourdieu, C., Sénateur, J.-P., Gorbenko, O. Y. & Kaul, A. R. Epitaxial stabilization of hexagonal $R\mathrm{MnO}_3(R = \mathrm{Eu\text{-}Dy})$ manganites. *J. Mater. Chem.* **12**, 800–801 (2002).

[121] Lee, J.-H., Murugavel, P., Ryu, H., Lee, D., Jo, J., Kim, J., Kim, H., Kim, K., Jo, Y., Jung, M.-H., Oh, Y., Kim, Y.-W., Yoon, J.-G., Chung, J.-S. & Noh, T. Epitaxial Stabilization of a New Multiferroic Hexagonal Phase of $TbMnO_3$ Thin Films. *Adv. Mater.* **18**, 3125–3129 (2006).

[122] Huang, F.-T., Wang, X., Oh, Y. S., Kurushima, K., Mori, S., Horibe, Y. & Cheong, S.-W. Delicate balance between ferroelectricity and antiferroelectricity in hexagonal $InMnO_3$. *Phys. Rev. B* **87**, 184109 (2013).

[123] Degenhardt, C., Fiebig, M., Fröhlich, D., Lottermoser, T. & Pisarev, R. Nonlinear optical spectroscopy of electronic transitions in hexagonal manganites. *Appl. Phys. B* **73**, 139–144 (2001).

[124] Cho, D.-Y., Oh, S.-J., Kim, D. G., Tanaka, A. & Park, J.-H. Investigation of local symmetry effects on the electronic structure of manganites: Hexagonal $YMnO_3$ versus orthorhombic $LaMnO_3$. *Phys. Rev. B* **79**, 035116 (2009).

[125] Fiebig, M., Lottermoser, T. & Pisarev, R. V. Spin-rotation phenomena and magnetic phase diagrams of hexagonal $RMnO_3$. *J. Appl. Phys.* **93**, 8194–8196 (2003).

[126] Solovyev, I. V., Valentyuk, M. V. & Mazurenko, V. V. Magnetic structure of hexagonal $YMnO_3$ and $LuMnO_3$ from a microscopic point of view. *Phys. Rev. B* **86**, 054407 (2012).

[127] Lottermoser, T., Fiebig, M., Fröhlich, D., Leute, S. & Kohn, K. Magnetic structure of hexagonal manganites $RMnO_3$ (R=Sc, Y, Ho, Er, Tm, Yb, Lu). *J. Magn. Magn. Mater.* **226-230**, 1131–1133 (2001).

[128] Fiebig, M., Degenhardt, C. & Pisarev, R. V. Magnetic phase diagram of $HoMnO_3$. *J. Appl. Phys.* **91**, 8867 (2002).

[129] Fiebig, M., Fröhlich, D., Kohn, K., Leute, S., Lottermoser, T., Pavlov, V. V. & Pisarev, R. V. Determination of the Magnetic Symmetry of Hexagonal Manganites by Second Harmonic Generation. *Phys. Rev. Lett.* **84**, 5620–5623 (2000).

[130] Howard, C. J., Campbell, B. J., Stokes, H. T., Carpenter, M. A. & Thomson, R. I. Crystal and magnetic structures of hexagonal $YMnO_3$. *Acta Crystallogr. B: Str. Sci, Cryst. Eng. Mater.* **69**, 534–540 (2013).

[131] Gibbs, A. S., Knight, K. S. & Lightfoot, P. High-temperature phase transitions of hexagonal $YMnO_3$. *Phys. Rev. B* **83**, 094111 (2011).

[132] Lorenz, B. Hexagonal Manganites – ($RMnO_3$): Class (I) Multiferroics with Strong Coupling of Magnetism and Ferroelectricity. *ISRN Condens. Matter Phys.* **2013**, 1–43 (2013).

[133] Huang, Z. J., Cao, Y., Sun, Y. Y., Xue, Y. Y. & Chu, C. W. Coupling between the ferroelectric and antiferromagnetic orders in $YMnO_3$. *Phys. Rev. B* **56**, 2623–2626 (1997).

[134] Lottermoser, T., Fiebig, M. & Fröhlich, D. Symmetry and coupling of magnetic and electric order parameters in $YMnO_3$. *J. Appl. Phys.* **91**, 8251 (2002).

[135] Fiebig, M., Lottermoser, T., Kneip, M. K. & Bayer, M. Correlations between magnetic and electrical orderings in multiferroic manganites (invited). *J. Appl. Phys.* **99**, 08E302 (2006).

[136] Fabrèges, X., Petit, S., Mirebeau, I., Pailhès, S., Pinsard, L., Forget, A., Fernandez-Diaz, M. T. & Porcher, F. Spin-Lattice Coupling, Frustration, and Magnetic Order in Multiferroic $R\mathrm{MnO}_3$. *Phys. Rev. Lett.* **103**, 067204 (2009).

[137] Varignon, J., Petit, S., Gellé, A. & Lepetit, M. B. An *ab initio* study of magneto-electric coupling of $YMnO_3$. *J. Phys.: Condens. Matter* **25**, 496004 (2013).

[138] Singh, K., Lepetit, M.-B., Simon, C., Bellido, N., Pailhès, S., Varignon, J. & De Muer, A. Analysis of the multiferroicity in the hexagonal manganite $YMnO_3$. *J. Phys.: Condens. Matter* **25**, 416002 (2013).

[139] Ye, M. & Vanderbilt, D. Magnetic charges and magnetoelectricity in hexagonal rare-earth manganites and ferrites. *Phys. Rev. B* **92**, 035107 (2015).

[140] Qian, M., Dong, J. & Zheng, Q. Electronic structure of the ferroelectromagnet $\mathrm{YMnO_3}$. *Phys. Lett. A* **270**, 96–101 (2000).

[141] Medvedeva, J. E., Anisimov, V. I., Korotin, M. A., Mryasov, O. N. & Freeman, A. J. The effect of Coulomb correlation and magnetic ordering on the electronic structure of two hexagonal phases of ferroelectromagnetic $\mathrm{YMnO_3}$. *J. Phys.: Condens. Matter* **12**, 4947 (2000).

[142] Song, S., Lee, J.-H. & Jang, H. M. Mode coupling between nonpolar and polar phonons as the origin of improper ferroelectricity in hexagonal $\mathrm{LuMnO_3}$. *J. Mater. Chem. C* **2**, 4126 (2014).

[143] Šafránková, M., Fousek, J. & KiŽaev, S. A. Domains in ferroelectric $\mathrm{YMnO_3}$. *Czech J. Phys.* **17**, 559–560 (1967).

[144] Jungk, T., Hoffmann, A., Fiebig, M. & Soergel, E. Electrostatic topology of ferroelectric domains in $\mathrm{YMnO_3}$. *Appl. Phys. Lett.* **97**, 012904 (2010).

[145] Lilienblum, M., Soergel, E. & Fiebig, M. Manipulation of ferroelectric vortex domains in hexagonal manganites. *J. Appl. Phys.* **110**, 052007 (2011).

[146] Zhang, Q. H., Wang, L. J., Wei, X. K., Yu, R. C., Gu, L., Hirata, A., Chen, M. W., Jin, C. Q., Yao, Y., Wang, Y. G. & Duan, X. F. Direct observation of interlocked domain walls in hexagonal $R\mathrm{MnO_3}$, (R = Tm, Lu). *Phys. Rev. B* **85**, 020102 (2012).

[147] Matsumoto, T., Ishikawa, R., Tohei, T., Kimura, H., Yao, Q., Zhao, H., Wang, X., Chen, D., Cheng, Z., Shibata, N. & Ikuhara, Y. Multivariate Statistical Characterization of Charged and Uncharged Domain Walls in Multiferroic Hexagonal $\mathrm{YMnO_3}$ Single Crystal Visualized by a Spherical Aberration-Corrected STEM. *Nano Lett.* **13**, 4594–4601 (2013).

[148] Cheng, S., Zhao, Y., Sun, X. & Zhu, J. Polarization Structures of Topological Domains in Multiferroic Hexagonal Manganites. *J. Am. Ceram. Soc.* **97**, 3371–3373 (2014).

[149] Lin, S.-Z., Wang, X., Kamiya, Y., Chern, G.-W., Fan, F., Fan, D., Casas, B., Liu, Y., Kiryukhin, V., Zurek, W. H., Batista, C. D. & Cheong, S.-W.

Topological defects as relics of emergent continuous symmetry and Higgs condensation of disorder in ferroelectrics. *Nat. Phys.* **10**, 970–977 (2014).

[150] Schaab, J., Trassin, M., Scholl, A., Doran, A., Yan, Z., Bourret, E., Ramesh, R. & Meier, D. Ferroelectric domains in the multiferroic phase of $ErMnO_3$ imaged by low-temperature photoemission electron microscopy. *J. Phys.: Conf. Ser.* **592**, 012120 (2015).

[151] Tian, L., Wang, Y., Ge, B., Zhang, X. & Zhang, Z. Direct observation of interlocked domain walls and topological four-state vortex-like domain patterns in multiferroic $YMnO_3$ single crystal. *Appl. Phys. Lett.* **106**, 112903 (2015).

[152] Zheng, Y. & Chen, W. J. Characteristics and controllability of vortices in ferromagnetics, ferroelectrics and multiferroics. *Rep. Prog. Phys.* (2017).

[153] Kibble, T. W. B. Topology of cosmic domains and strings. *J. Phys. A: Math. Gen.* **9**, 1387 (1976).

[154] Zurek, W. H. Cosmological experiments in superfluid helium? *Nature* **317**, 505–508 (1985).

[155] Chae, S. C., Lee, N., Horibe, Y., Tanimura, M., Mori, S., Gao, B., Carr, S. & Cheong, S.-W. Direct Observation of the Proliferation of Ferroelectric Loop Domains and Vortex-Antivortex Pairs. *Phys. Rev. Lett.* **108**, 167603 (2012).

[156] Griffin, S. M., Lilienblum, M., Delaney, K. T., Kumagai, Y., Fiebig, M. & Spaldin, N. A. Scaling Behavior and Beyond Equilibrium in the Hexagonal Manganites. *Phys. Rev. X* **2**, 041022 (2012).

[157] Spaldin, N. A. Multiferroics: from the cosmically large to the subatomically small. *Nat. Rev. Mater.* **2**, 17017 (2017).

[158] Wu, W., Horibe, Y., Lee, N., Cheong, S.-W. & Guest, J. R. Conduction of Topologically Protected Charged Ferroelectric Domain Walls. *Phys. Rev. Lett.* **108**, 077203 (2012).

[159] Campbell, M. P., McConville, J. P. V., McQuaid, R. G. P., Prabhakaran, D., Kumar, A. & Gregg, J. M. Hall effect in charged conducting ferroelectric domain walls. *Nat. Commun.* **7**, 13764 (2016).

[160] Mundy, J. A., Schaab, J., Kumagai, Y., Cano, A., Stengel, M., Krug, I. P., Gottlob, D. M., Doğanay, H., Holtz, M. E., Held, R., Yan, Z., Bourret, E., Schneider, C. M., Schlom, D. G., Muller, D. A., Ramesh, R., Spaldin, N. A. & Meier, D. Functional electronic inversion layers at ferroelectric domain walls. *Nat. Mater.* **16**, 622–627 (2017).

[161] Kim, D. J., Connell, J. G., Seo, S. S. A. & Gruverman, A. Domain wall conductivity in semiconducting hexagonal ferroelectric $\mathrm{TbMnO_3}$ thin films. *Nanotechnology* **27**, 155705 (2016).

[162] Wu, X., Petralanda, U., Zheng, L., Ren, Y., Hu, R., Cheong, S.-W., Artyukhin, S. & Lai, K. Low-energy structural dynamics of ferroelectric domain walls in hexagonal rare-earth manganites. *Sci. Adv.* **3**, e1602371 (2017).

[163] Chen, M., Hallstedt, B. & Gauckler, L. J. Thermodynamic assessment of the Mn–Y–O system. *J. Alloys Compd.* **393**, 114–121 (2005).

[164] Vedmid', L. B., Yankin, A. M., Fedorova, O. M. & Balakirev, V. F. Evolution of phase equilibrium states in the Y-Mn-O system in the thermal dissociation of the compound $\mathrm{YMn_2O_5}$. *Russ. J. Inorg. Chem.* **59**, 519–523 (2014).

[165] Zhou, J.-S., Goodenough, J. B., Gallardo-Amores, J. M., Morán, E., Alario-Franco, M. A. & Caudillo, R. Hexagonal versus perovskite phase of manganite $R\mathrm{MnO_3}$ (R = Y, Ho, Er, Tm, Yb, Lu). *Phys. Rev. B* **74**, 014422 (2006).

[166] Brinks, H. W., Fjellvåg, H. & Kjekshus, A. Synthesis of Metastable Perovskite-type $\mathrm{YMnO_3}$ and $\mathrm{HoMnO_3}$. *J. Solid State Chem.* **129**, 334–340 (1997).

[167] Alonso, J. A., Martínez-Lope, M. J., Casais, M. T. & Fernández-Díaz, M. T. Evolution of the Jahn-Teller Distortion of $\mathrm{MnO_6}$ Octahedra in $\mathrm{RMnO_3}$ Perovskites (R = Pr, Nd, Dy, Tb, Ho, Er, Y): A Neutron Diffraction Study. *Inorg. Chem.* **39**, 917–923 (2000).

[168] Waintal, A. & Chenavas, J. Transformation sous haute pression de la forme hexagonale $\mathrm{MnT'O_3}$ (T'= Ho, Er, Tm, Yb, Lu) en une forme perovskite. *Mater. Res. Bull.* **2**, 819–822 (1967).

[169] Uusi-Esko, K., Malm, J., Imamura, N., Yamauchi, H. & Karppinen, M. Characterization of $RMnO_3$ (R=Sc, Y, Dy-Lu): High-pressure synthesized metastable perovskites and their hexagonal precursor phases. *Mater. Chem. Phys.* **112**, 1029–1034 (2008).

[170] Salvador, P. A., Doan, T.-D., Mercey, B. & Raveau, B. Stabilization of $YMnO_3$ in a Perovskite Structure as a Thin Film. *Chem. Mater.* **10**, 2592–2595 (1998).

[171] Shimura, T., Fujimura, N., Yamamori, S., Yoshimura, T. & Ito, T. Effects of Stoichiometry and A-site Substitution on the Electrical Properties of Ferroelectric $YMnO_3$. *Jpn. J. Appl. Phys.* **37**, 5280 (1998).

[172] Gélard, I., Jehanathan, N., Roussel, H., Gariglio, S., Lebedev, O. I., Van Tendeloo, G. & Dubourdieu, C. Off-Stoichiometry Effects on the Crystalline and Defect Structure of Hexagonal Manganite $REMnO_3$ Films (RE = Y, Er, Dy). *Chem. Mater.* **23**, 1232–1238 (2011).

[173] Fujimura, N., Ishida, T., Yoshimura, T. & Ito, T. Epitaxially grown $YMnO_3$ film: New candidate for nonvolatile memory devices. *Appl. Phys. Lett.* **69**, 1011 (1996).

[174] Fujimura, N., Sakata, H., Ito, D., Yoshimura, T., Yokota, T. & Ito, T. Ferromagnetic and ferroelectric behaviors of A-site substituted $YMnO_3$-based epitaxial thin films. *J. Appl. Phys.* **93**, 6990–6992 (2003).

[175] Bergum, K., Okamoto, H., Fjellvåg, H., Grande, T., Einarsrud, M.-A. & Selbach, S. M. Synthesis, structure and magnetic properties of nanocrystalline $YMnO_3$. *Dalton Trans.* **40**, 7583 (2011).

[176] Remsen, S. & Dabrowski, B. Synthesis and Oxygen Storage Capacities of Hexagonal $Dy_{1-x}Y_xMnO_{3+\delta}$. *Chem. Mater.* **23**, 3818–3827 (2011).

[177] Parkkima, O., Malo, S., Hervieu, M., Rautama, E.-L. & Karppinen, M. New $R\mathrm{MnO}_{3+\delta}$ (R=Y, Ho; $\delta \simeq 0.35$) phases with modulated structure. *J. Solid State Chem.* **221**, 109–115 (2015).

[178] Kitahata, H., Tadanaga, K., Minami, T., Fujimura, N. & Ito, T. Origin of Leakage Current of $YMnO_3$ Thin Films Prepared by the Sol-Gel Method. *MRS Proc.* **596** (1999).

[179] Kitahata, H., Tadanaga, K., Minami, T., Fujimura, N. & Ito, T. Ferroelectricity of $YMnO_3$ thin films prepared via solution. *Appl. Phys. Lett.* **75**, 719–721 (1999).

[180] Katsufuji, T., Masaki, M., Machida, A., Moritomo, M., Kato, K., Nishibori, E., Takata, M., Sakata, M., Ohoyama, K., Kitazawa, K. & Takagi, H. Crystal structure and magnetic properties of hexagonal RMnO$_3$ ($R =$ Y, Lu, and Sc) and the effect of doping. *Phys. Rev. B* **66**, 134434 (2002).

[181] Aikawa, Y., Katsufuji, T., Arima, T. & Kato, K. Effect of Mn trimerization on the magnetic and dielectric properties of hexagonal $YMnO_3$. *Phys. Rev. B* **71**, 184418 (2005).

[182] Levin, I., Krayzman, V., Vanderah, T. A., Tomczyk, M., Wu, H., Tucker, M. G., Playford, H. Y., Woicik, J. C., Dennis, C. L. & Vilarinho, P. M. Oxygen-storage behavior and local structure in Ti-substituted $YMnO_3$. *J. Solid State Chem.* **246**, 29–41 (2017).

[183] Asaka, T., Nemoto, K., Kimoto, K., Arima, T. & Matsui, Y. Crystallographic superstructure of Ti-doped hexagonal $YMnO_3$. *Phys. Rev. B* **71** (2005).

[184] Mori, S., Tokunaga, J., Horibe, Y., Aikawa, Y. & Katsufuji, T. Magnetocapacitance effect and related microstrucuture in Ti-doped $YMnO_3$. *Phys. Rev. B* **72**, 224434 (2005).

[185] Mori, S., Tokunaga, J., Horibe, Y., Asada, T., Koyama, Y. & Katsufuji, T. Doping Effect on Ferroelectric Microstructure in $YMn_{1-x}Ti_xO_3$. *Ferroelectrics* **348**, 170–176 (2007).

[186] Asokan, K., Chen, Y. S., Pao, C. W., Tsai, H. M., Lee, C. W. O., Lin, C. H., Hsueh, H. C., Ling, D. C., Pong, W. F., Chiou, J. W., Tsai, M.-H., Peña, O. & Moure, C. Effect of Co, Ni, and Cu substitution on the electronic structure of hexagonal $YMnO_3$ studied by X-ray absorption spectroscopy. *Appl. Phys. Lett.* **95**, 131901 (2009).

[187] Kim, S. B., Kim, S. J., Park, J.-G., Cheong, S.-W. & Kim, C. S. Mössbauer studies of Fe-doped $HoMnO_3$. *J. Appl. Phys.* **99**, 08Q313 (2006).

[188] Samal, S. L., Green, W., Lofland, S. E., Ramanujachary, K. V., Das, D. & Ganguli, A. K. Study on the solid solution of $YMn_{1-x}Fe_xO_3$: Structural, magnetic and dielectric properties. *J. Solid State Chem.* **181**, 61–66 (2008).

[189] Van Roosmalen, J. A. M., Cordfunke, E. H. P., Helmholdt, R. B. & Zandbergen, H. W. The Defect Chemistry of $LaMnO_{3\pm\delta}$: 2. Structural Aspects of $LaMnO_{3+\delta}$. *J. Solid State Chem.* **110**, 100–105 (1994).

[190] Overton, A. J., Best, J. L., Saratovsky, I. & Hayward, M. A. Influence of Topotactic Reduction on the Structure and Magnetism of the Multiferroic $YMnO_3$. *Chem. Mater.* **21**, 4940–4948 (2009).

[191] Chen, D. P., Du, Y., Wang, X. L., Cheng, Z. X., Dou, S. X., Lin, Z. W., Zhu, J. G. & Xu, B. Oxygen-vacancy effect on structural, magnetic, and ferroelectric properties in multiferroic $YMnO_3$ single crystals. *J. Appl. Phys.* **111**, 07D913 (2012).

[192] Vermette, J., Jandl, S., Orlita, M. & Gospodinov, M. M. Role of the apical oxygen in the low-temperature magnetoelectric effect in RMnO$_3$ (R = Ho and Lu). *Phys. Rev. B* **85**, 134445 (2012).

[193] Wang, X., Huang, F.-T., Hu, R., Fan, F. & Cheong, S.-W. Self-poling with oxygen off-stoichiometry in ferroelectric hexagonal manganites. *APL Mater.* **3**, 041505 (2015).

[194] Subba Rao, G. V., Wanklyn, B. M. & Rao, C. N. R. Electrical transport in rare earth ortho-chromites, -manganites and -ferrites. *J. Phys. Chem. Solids* **32**, 345–358 (1971).

[195] Dabrowski, B., Remsen, S., Mais, J. & Kolesnik, S. Synthesis and characterization of non-stoichiometric hexagonal $Dy_{1-x}Y_xMnO_{3+\delta}$. *Funct. Mater. Lett.* **04**, 147–150 (2011).

[196] Skjærvø, S. H., Wefring, E. T., Nesdal, S. K., Gaukås, N. H., Olsen, G. H., Glaum, J., Tybell, T. & Selbach, S. M. Interstitial oxygen as a source of p-type conductivity in hexagonal manganites. *Nat. Commun.* **7**, 13745 (2016).

[197] Moure, C., Fernandez, J. F., Villegas, M. & Duran, P. Non-Ohmic Behaviour and Switching Phenomena in $YMnO_3$-Based Ceramic Materials. *J. Eur. Ceram. Soc.* **19**, 131–137 (1999).

[198] Tomczyk, M., Vilarinho, P. M., Moreira, A. & Almeida, A. High temperature dielectric properties of $YMnO_3$ ceramics. *J. Appl. Phys.* **110**, 064116 (2011).

[199] Liu, P., Wang, X.-L., Cheng, Z.-X., Du, Y. & Kimura, H. Structural, dielectric, antiferromagnetic, and thermal properties of the frustrated hexagonal $Ho_{1-x}Er_xMnO_3$ manganites. *Phys. Rev. B* **83**, 144404 (2011).

[200] Ren, P., Fan, H. & Wang, X. Bulk conduction and nonlinear behaviour in multiferroic $YMnO_3$. *Appl. Phys. Lett.* **103**, 152905 (2013).

[201] Bogusz, A., Müller, A. D., Blaschke, D., Skorupa, I., Bürger, D., Scholz, A., Schmidt, O. G. & Schmidt, H. Resistive switching in polycrystalline $YMnO_3$ thin films. *AIP Adv.* **4**, 107135 (2014).

[202] Kohn, W. Nobel Lecture: Electronic structure of matter – wave functions and density functionals. *Rev. Mod. Phys.* **71**, 1253–1266 (1999).

[203] Capelle, K. A bird's-eye view of density-functional theory. *Braz. J. Phys.* **36**, 4 (2006).

[204] Hohenberg, P. & Kohn, W. Inhomogeneous Electron Gas. *Phys. Rev.* **136**, B864–B871 (1964).

[205] Kohn, W. & Sham, L. J. Self-Consistent Equations Including Exchange and Correlation Effects. *Phys. Rev.* **140**, A1133–A1138 (1965).

[206] Perdew, J. P., Chevary, J. A., Vosko, S. H., Jackson, K. A., Pederson, M. R., Singh, D. J. & Fiolhais, C. Atoms, molecules, solids, and surfaces: Applications of the generalized gradient approximation for exchange and correlation. *Phys. Rev. B* **46**, 6671–6687 (1992).

[207] Wang, Y. & Perdew, J. P. Correlation hole of the spin-polarized electron gas, with exact small-wave-vector and high-density scaling. *Phys. Rev. B* **44**, 13298–13307 (1991).

[208] Perdew, J. P., Burke, K. & Ernzerhof, M. Generalized Gradient Approximation Made Simple. *Phys. Rev. Lett.* **77**, 3865–3868 (1996).

[209] Perdew, J. P., Ruzsinszky, A., Csonka, G. I., Vydrov, O. A., Scuseria, G. E., Constantin, L. A., Zhou, X. & Burke, K. Restoring the Density-Gradient Expansion for Exchange in Solids and Surfaces. *Phys. Rev. Lett.* **100**, 136406 (2008).

[210] Bilc, D. I., Orlando, R., Shaltaf, R., Rignanese, G.-M., Íñiguez, J. & Ghosez, P. Hybrid exchange-correlation functional for accurate prediction

of the electronic and structural properties of ferroelectric oxides. *Phys. Rev. B* **77**, 165107 (2008).

[211] Heyd, J., Scuseria, G. E. & Ernzerhof, M. Hybrid functionals based on a screened Coulomb potential. *J. Chem. Phys.* **118**, 8207–8215 (2003).

[212] Becke, A. D. A new mixing of Hartree-Fock and local density-functional theories. *J. Chem. Phys.* **98**, 1372–1377 (1993).

[213] Becke, A. D. Density-functional thermochemistry. IV. A new dynamical correlation functional and implications for exact-exchange mixing. *J. Chem. Phys.* **104**, 1040–1046 (1996).

[214] Perdew, J. P., Ernzerhof, M. & Burke, K. Rationale for mixing exact exchange with density functional approximations. *J. Chem. Phys.* **105**, 9982–9985 (1996).

[215] Bloch, F. Über die Quantenmechanik der Elektronen in Kristallgittern. *Z. Physik* **52**, 555–600 (1929).

[216] Monkhorst, H. J. & Pack, J. D. Special points for Brillouin-zone integrations. *Phys. Rev. B* **13**, 5188–5192 (1976).

[217] Vanderbilt, D. Soft self-consistent pseudopotentials in a generalized eigenvalue formalism. *Phys. Rev. B* **41**, 7892–7895 (1990).

[218] Blöchl, P. E. Projector augmented-wave method. *Phys. Rev. B* **50**, 17953 (1994).

[219] Feynman, R. P. Forces in Molecules. *Phys. Rev.* **56**, 340–343 (1939).

[220] Fletcher, R. & Reeves, C. M. Function minimization by conjugate gradients. *Comput. J.* **7**, 149–154 (1964).

[221] Davidon, W. C. Variable Metric Method for Minimization. *SIAM Journal on Optimization; Philadelphia* **1**, 17 (1991).

[222] Car, R. & Parrinello, M. Unified Approach for Molecular Dynamics and Density-Functional Theory. *Phys. Rev. Lett.* **55**, 2471–2474 (1985).

[223] Jònsson, H., Mills, G. & Jacobsen, K. W. Nudged elastic band method for finding minimum energy paths of transitions. In *Classical and Quantum Dynamics in Condensed Phase Simulations*, 385–404 (World Scientific Publishing Co., 1998).

[224] Henkelman, G., Uberuaga, B. P. & Jónsson, H. A climbing image nudged elastic band method for finding saddle points and minimum energy paths. *J. Chem. Phys.* **113**, 9901 (2000).

[225] Henkelman, G. & Jònsson, H. Improved tangent estimate in the nudged elastic band method for finding minimum energy paths and saddle points. *J. Chem. Phys.* **113**, 9978 (2000).

[226] Cohen, A. J., Mori-Sánchez, P. & Yang, W. Fractional charge perspective on the band gap in density-functional theory. *Phys. Rev. B* **77**, 115123 (2008).

[227] Mori-Sánchez, P., Cohen, A. J. & Yang, W. Localization and Delocalization Errors in Density Functional Theory and Implications for Band-Gap Prediction. *Phys. Rev. Lett.* **100**, 146401 (2008).

[228] Himmetoglu, B., Floris, A., de Gironcoli, S. & Cococcioni, M. Hubbard-corrected DFT energy functionals: the LDA+U description of correlated systems. *Int. J. Quantum Chem.* **114**, 14–49 (2014).

[229] Anisimov, V. I., Zaanen, J. & Andersen, O. K. Band theory and Mott insulators: Hubbard U instead of Stoner I. *Phy. Rev. B* **44**, 943 (1991).

[230] Hubbard, J. Electron Correlations in Narrow Energy Bands. *Proc. Royal Soc. London A: Math. Phys. Eng. Sci.* **276**, 238–257 (1963).

[231] Liechtenstein, A. I., Anisimov, V. I. & Zaanen, J. Density-functional theory and strong interactions: Orbital ordering in Mott-Hubbard insulators. *Phys. Rev. B* **52**, R5467–R5470 (1995).

[232] Dudarev, S. L., Botton, G. A., Savrasov, S. Y., Humphreys, C. J. & Sutton, A. P. Electron-energy-loss spectra and the structural stability of nickel oxide: An LSDA+U study. *Phys. Rev. B* **57**, 1505–1509 (1998).

[233] Burke, K. Perspective on density functional theory. *J. Chem. Phys.* **136**, 150901 (2012).

[234] Ederer, C. & Spaldin, N. A. Recent progress in first-principles studies of magnetoelectric multiferroics. *Curr. Opin. Solid State Mater. Sci.* **9**, 128–139 (2005).

[235] Spaldin, N. A. & Pickett, W. E. Computational design of multifunctional materials. *J. Solid State Chem.* **176**, 615–632 (2003).

[236] Resta, R. Theory of the electric polarization in crystals. *Ferroelectrics* **136**, 51–55 (1992).

[237] Resta, R. Electrical polarization and orbital magnetization: the modern theories. *J. Phys.: Condens. Matter* **22**, 123201 (2010).

[238] King-Smith, R. D. & Vanderbilt, D. Theory of polarization of crystalline solids. *Phys. Rev. B* **47**, 1651 (1993).

[239] Spaldin, N. A. A beginner's guide to the modern theory of polarization. *J. Solid State Chem.* **195**, 2–10 (2012).

[240] Berry, M. V. Quantal Phase Factors Accompanying Adiabatic Changes. *Proc. Royal Soc. London A: Math. Phys. Eng. Sci.* **392**, 45–57 (1984).

[241] Shigemi, A. & Wada, T. Evaluations of phases and vacancy formation energies in $KNbO_3$ by first-principles calculation. *Jpn. J. Appl. Phys.* **44**, 8048 (2005).

[242] Ertekin, E., Srinivasan, V., Ravichandran, J., Rossen, P. B., Siemons, W., Majumdar, A., Ramesh, R. & Grossman, J. C. Interplay between intrinsic defects, doping, and free carrier concentration in $SrTiO_3$ thin films. *Phys. Rev. B* **85**, 195460 (2012).

[243] Rørmark, L., Mørch, A. B., Wiik, K., Stølen, S. & Grande, T. Enthalpies of Oxidation of $CaMnO_{3-\delta}$, $Ca_2MnO_{4-\delta}$ and $SrMnO_{3-\delta}$ Deduced Redox Properties. *Chem. Mater.* **13**, 4005–4013 (2001).

[244] Taylor, S. E. & Bruneval, F. Understanding and correcting the spurious interactions in charged supercells. *Phys. Rev. B* **84**, 075155 (2011).

[245] Leslie, M. & Gillan, N. J. The energy and elastic dipole tensor of defects in ionic crystals calculated by the supercell method. *J. Phys. C: Solid State Phys.* **18**, 973 (1985).

[246] Schultz, P. A. Charged Local Defects in Extended Systems. *Phys. Rev. Lett.* **84**, 1942–1945 (2000).

[247] Castleton, C. W. M., H oglund, A. & Mirbt, S. Managing the supercell approximation for charged defects in semiconductors: Finite-size scaling, charge correction factors, the band-gap problem, and the *ab initio* dielectric constant. *Phys. Rev. B* **73**, 035215 (2006).

[248] Lany, S. & Zunger, A. Assessment of correction methods for the band-gap problem and for finite-size effects in supercell defect calculations: Case studies for ZnO and GaAs. *Phys. Rev. B* **78**, 235104 (2008).

[249] Lany, S. & Zunger, A. Accurate prediction of defect properties in density functional supercell calculations. *Modelling Simul. Mater. Sci. Eng.* **17**, 084002 (2009).

[250] Kumagai, Y. & Oba, F. Electrostatics-based finite-size corrections for first-principles point defect calculations. *Phys. Rev. B* **89**, 195205 (2014).

[251] Ihm, J., Zunger, A. & Cohen, M. L. Momentum-space formalism for the total energy of solids. *J. Phys. C: Solid State Phys.* **12**, 4409 (1979).

[252] Makov, G. & Payne, M. C. Periodic boundary conditions in *ab initio* calculations. *Phys. Rev. B* **51**, 4014 (1995).

[253] Tanaka, T., Matsunaga, K., Ikuhara, Y. & Yamamoto, T. First-principles study on structures and energetics of intrinsic vacancies in $SrTiO_3$. *Phys. Rev. B* **68** (2003).

[254] Kresse, G. & Furthmüller, J. Efficient iterative schemes for *ab initio* total-energy calculations using a plane-wave basis set. *Phys. Rev. B* **54**, 11169 (1996).

[255] Kresse, G. & Joubert, D. From ultrasoft pseudopotentials to the projector augmented-wave method. *Phys. Rev. B* **59**, 1758–1775 (1999).

[256] Jiang, N. & Zhang, X. Atomistic simulation study of transverse domain wall in hexagonal $YMnO_3$. *J. Phys. D: Appl. Phys.* **48**, 435503 (2015).

[257] Egami, T. & Billinge, S. J. L. *Underneath the Bragg peaks, Structural analysis of Complex Materials* (Elsevier, The Boulevard, Langford Lane Kidlington, Oxford OX5 1GB, UK, 2003).

[258] Keen, D. A. & Goodwin, A. L. The crystallography of correlated disorder. *Nature* **521**, 303–309 (2015).

[259] Young, C. A. & Goodwin, A. L. Applications of pair distribution function methods to contemporary problems in materials chemistry. *J. Mater. Chem.* **21**, 6464 (2011).

[260] Petkov, V. Nanostructure by high-energy X-ray diffraction. *Mater. Today* **11**, 28–38 (2008).

[261] Coelho, A. A. TOPAS Academic: General Profile and Structure Analysis Software for Powder Diffraction Data; Bruker AXS (2004).

[262] Farrow, C. L., Juhas, P., Liu, J. W., Bryndin, D., Božin, E. S., Bloch, J., Proffen, T. & Billinge, S. J. L. PDFfit2 and PDFgui: computer programs for studying nanostructure in crystals. *J. Phys.: Condens. Matter* **19**, 335219 (2007).

[263] International Organization for Standardization. [ISO 5017:2013] Dense shaped refractory products - Determination of bulk density, apparent porosity and true porosity.

[264] Selbach, S. M., Tybell, T., Einarsrud, M.-A. & Grande, T. High-temperature semiconducting cubic phase of $BiFe_{0.7}Mn_{0.3}O_{3+\delta}$. *Phys. Rev. B* **79** (2009).

[265] Wefring, E. T., Einarsrud, M.-A. & Grande, T. Electrical conductivity and thermopower of (1-x)$BiFeO_3$ - x$Bi_{0.5}K_{0.5}TiO_3$ (x = 0.1, 0.2) ceramics near the ferroelectric to paraelectric phase transition. *Phys. Chem. Chem. Phys.* **17**, 9420–9428 (2015).

[266] Kim, J., Cho, K. C., Koo, Y. M., Hong, K. P. & Shin, N. Y-O hybridization in the ferroelectric transition of $YMnO_3$. *Appl. Phys. Lett.* **95**, 132901 (2009).

[267] Nénert, G., Pollet, M., Marinel, S., Blake, G. R., Meetsma, A. & Palstra, T. T. M. Experimental evidence for an intermediate phase in the multiferroic $YMnO_3$. *J. Phys.: Condens. Matter* **19**, 466212 (2007).

[268] Tyson, T. A., Wu, T., Chen, H. Y., Bai, J., Ahn, K. H., Pandya, K. I., Kim, S. B. & Cheong, S.-W. Measurements and *ab initio* molecular dynamics simulations of the high temperature ferroelectric transition in hexagonal $RMnO_3$. *J. Appl. Phys.* **110**, 084116 (2011).

[269] Jeong, I.-K., Hur, N. & Proffen, T. High-temperature structural evolution of hexagonal multiferroic $YMnO_3$ and $YbMnO_3$. *J. Appl. Crystallogr.* **40**, 730–734 (2007).

[270] Artyukhin, S., Delaney, K. T., Spaldin, N. A. & Mostovoy, M. Landau theory of topological defects in multiferroic hexagonal manganites. *Nat. Mater.* **13**, 42–49 (2013).

[271] Thomson, R. I., Chatterji, T., Howard, C. J., Palstra, T. T. M. & Carpenter, M. A. Elastic anomalies associated with structural and magnetic phase transitions in single crystal hexagonal $\mathrm{YMnO_3}$. *J. Phys.: Condens. Matter* **26**, 045901 (2014).

[272] Cano, A. Hidden order in hexagonal $R\mathrm{MnO_3}$ multiferroics (R = Dy - Lu, In, Y, and Sc). *Phys. Rev. B* **89**, 214107 (2014).

[273] Barbour, A., Alatas, A., Liu, Y., Zhu, C., Leu, B. M., Zhang, X., Sandy, A., Pierce, M. S., Wang, X., Cheong, S.-W. & You, H. Partial glass isosymmetry transition in multiferroic hexagonal $\mathrm{ErMnO_3}$. *Phys. Rev. B* **93**, 054113 (2016).

[274] Phillpot, S. R. & Gopalan, V. Coupled displacive and order-disorder dynamics in $\mathrm{LiNbO_3}$ by molecular-dynamics simulation. *Appl. Phys. Lett.* **84**, 1916 (2004).

[275] Mori, S., Kurushima, K., Kamo, H., Ishii, Y., Huang, F.-T., Horibe, Y., Kastufuji, T. & Cheong, S.-W. Ferroelectric and Structural Antiphase Domain and Domain Wall Structures in $\mathrm{Y(Mn,Ti)O_3}$. *Ferroelectrics* **462**, 50–54 (2014).

[276] Zhang, Y., Li, J. & Fang, D. Oxygen-vacancy-induced memory effect and large recoverable strain in a barium titanate single crystal. *Phys. Rev. B* **82**, 064103 (2010).

[277] Gaponenko, I., Tückmantel, P., Karthik, J., Martin, L. W. & Paruch, P. Towards reversible control of domain wall conduction in $\mathrm{Pb(Zr_{0.2}Ti_{0.8})O_3}$ thin films. *Appl. Phys. Lett.* **106**, 162902 (2015).

[278] Cheng, S., Li, M., Meng, Q., Duan, W., Zhao, Y. G., Sun, X. F., Zhu, Y. & Zhu, J. Electronic and crystal structure changes induced by in-plane oxygen vacancies in multiferroic $\mathrm{YMnO_3}$. *Phys. Rev. B* **93**, 054409 (2016).

[279] Zhang, Q. H., Shen, X., Yao, Y., Wang, Y. G., Jin, C. Q. & Yu, R. C. Oxygen vacancy ordering and its mobility in $\mathrm{YMnO_3}$. *J. Alloys Compd.* **648**, 253–257 (2015).

[280] Wang, W., Xu, B., Gao, P., Zhang, W. & Sun, Y. Electrical and dielectric properties of $HoMnO_3$ ceramics. *Solid State Commun.* **177**, 7–9 (2014).

[281] Stokes, H. T. & Hatch, D. M. FINDSYM: program for identifying the space-group symmetry of a crystal. *J. Appl. Crystallogr.* **38**, 237–238 (2005).

[282] Van Aken, B. B., Bos, J.-W. G., de Groot, R. A. & Palstra, T. T. M. Asymmetry of electron and hole doping in $YMnO_3$. *Phys. Rev. B* **63**, 125127 (2001).

[283] Moure, C., Villegas, M., Fernandez, J. F., Tartaj, J. & Duran, P. Phase transition and electrical conductivity in the system $YMnO_3$-$CaMnO_3$. *J. Mater. Sci.* **34**, 2565–2568 (1999).

[284] Balamurugan, C. & Lee, D. W. Perovskite hexagonal $YMnO_3$ nanopowder as p-type semiconductor gas sensor for H_2S detection. *Sens. Actuators B: Chem.* **221**, 857–866 (2015).

[285] Ma, Y., Wang, X., Wang, Z., Liu, H., Wang, Z., Yang, C., Zou, Q. & Zeng, W. Investigation of magnetic, dielectric and electrical properties of Ce-substituted $YMn_{0.8}Fe_{0.2}O_3$ multiferroic ceramics. *J. Mater. Sci.: Mater. Electron.* **26**, 398–404 (2014).

[286] Abrahams, S. C. & Bernstein, J. L. Crystal Structure of Paramagnetic $DyMn_2O_5$ at 298°K. *J. Chem. Phys.* **46**, 3776–3782 (1967).

[287] Chroneos, A., Vovk, R., Goulatis, I. & Goulatis, L. Oxygen transport in perovskite and related oxides: A brief review. *J. Alloys Compd.* **494**, 190–195 (2010).

[288] Farokhipoor, S., Magén, C., Venkatesan, S., Íñiguez, J., Daumont, C. J. M., Rubi, D., Snoeck, E., Mostovoy, M., de Graaf, C., Müller, A., Döblinger, M., Scheu, C. & Noheda, B. Artificial chemical and magnetic structure at the domain walls of an epitaxial oxide. *Nature* **515**, 379–383 (2014).

[289] Abrahams, S. C. Ferroelectricity and structure in the $YMnO_3$ family. *Acta Crystallogr. B Struct. Sci.* **57**, 485–490 (2001).

[290] Oak, M.-A., Lee, J.-H., Jang, H. M., Goh, J. S., Choi, H. J. & Scott, J. F. $4d$-$5p$ Orbital Mixing and Asymmetric In$4d$-O$2p$ Hybridization in $InMnO_3$:

A New Bonding Mechanism for Hexagonal Ferroelectricity. *Phys. Rev. Lett.* **106** (2011).

[291] Reidulff, M. *Phase stability and Point Defects in InMnO*$_3$. Master's thesis, NTNU, Trondheim (2014).

[292] Huang, F.-T., Wang, X., Griffin, S., Kumagai, Y., Gindele, O., Chu, M.-W., Horibe, Y., Spaldin, N. & Cheong, S.-W. Duality of Topological Defects in Hexagonal Manganites. *Phys. Rev. Lett.* **113**, 267602 (2014).

[293] Kumagai, Y., Belik, A. A., Lilienblum, M., Leo, N., Fiebig, M. & Spaldin, N. A. Observation of persistent centrosymmetricity in the hexagonal manganite family. *Phys. Rev. B* **85**, 174422 (2012).

[294] Varignon, J. & Ghosez, P. Improper ferroelectricity and multiferroism in 2H-BaMnO$_3$. *Phys. Rev. B* **87**, 140403 (2013).

[295] Kamba, S., Nuzhnyy, D., Savinov, M., Tolédano, P., Laguta, V., Brázda, P., Palatinus, L., Kadlec, F., Borodavka, F., Kadlec, C., Bednyakov, P., Bovtun, V., Kempa, M., Kriegner, D., Drahokoupil, J., Kroupa, J., Prokleška, J., Chapagain, K., Dabrowski, B. & Goian, V. Unusual ferroelectric and magnetic phases in multiferroic 2H-BaMnO$_3$ ceramics. *Phys. Rev. B* **95**, 174103 (2017).

[296] Vente, J. F., McIntosh, S., Haije, W. G. & Bouwmeester, H. J. M. Properties and performance of Ba$_x$Sr$_{1-x}$Co$_{0.8}$Fe$_{0.2}$O$_{3-\delta}$ materials for oxygen transport membranes. *J. Solid State Electrochem.* **10**, 581–588 (2006).

[297] Leo, A., Liu, S., Diniz da Costa, J. & Shao, Z. Oxygen permeation through perovskite membranes and the improvement of oxygen flux by surface modification. *Sci. Tech. Adv. Mater.* **7**, 819–825 (2006).

[298] Zhang, K., Sunarso, J., Shao, Z., Zhou, W., Sun, C., Wang, S. & Liu, S. Research progress and materials selection guidelines on mixed conducting perovskite-type ceramic membranes for oxygen production. *RSC Advances* **1**, 1661 (2011).

[299] Hendriksen, P. V., Larsen, P. H., Mogensen, M., Poulsen, F. W. & Wiik, K. Prospects and problems of dense oxygen permeable membranes. *Catalysis Today* **56**, 283–295 (2000).

[300] Sahini, M. G., Tolchard, J. R., Wiik, K. & Grande, T. High temperature X-ray diffraction and thermo-gravimetrical analysis of the cubic perovskite $Ba_{0.5}Sr_{0.5}Co_{0.8}Fe_{0.2}O_{3-\delta}$ under different atmospheres. *Dalton Trans.* **44**, 10875–10881 (2015).

[301] Nesdal, S. K. *Development of hexagonal manganites for use in oxygen permeable membranes.* Master's thesis, NTNU (2013).

[302] Frydenlund, M. M. *Development of a new class of oxygen ion mixed conductors.* Master's thesis, NTNU, Trondheim (2014).

[303] Østlie, E. R. *Optimization of chemical composition of novel manganite oxides for oxygen permeable membranes.* Master's thesis, NTNU, Trondheim (2015).

[304] Gaukås, N. H. *The Effect of Donor Doping with* Ti^{4+} *on the Oxygen Absorption Properties of h-*$YMnO_3$. Master's thesis, NTNU, Trondheim (2016).

[305] Adnan, M. M. *A new material for oxygen-permeable membranes.* Master's thesis, NTNU, Trondheim (2017).

Appendix A

Published scientific papers and prepared manuscripts

1. **S. H. Skjærvø**, E. T. Wefring, S. K. Nesdal, N. H. Gaukås,G. H. Olsen, J. Glaum, T. Tybell, S. M. Selbach, Interstitial oxygen as a source of p-type conductivity in hexagonal manganites. *Nat. Commun.* **7**, 13745 (2016).
2. **S. H. Skjærvø**, Q. N. Meier, E. S. Bozin, S. J. L. Billinge, M. Feygenson, N. A. Spaldin, S. M. and Selbach, Unconventional order-disorder phase transition in improper ferroelectric hexagonal manganites, *Submitted* (2017).
3. **S. H. Skjærvø**, D. R. Småbråten, N. A. Spaldin, T. Tybell, and S. M. Selbach, Oxygen vacancy ordering and the interplay with neutral domain walls in h-$YMnO_3$. *In preparation.*

nature COMMUNICATIONS

ARTICLE

Received 18 Oct 2015 | Accepted 26 Oct 2016 | Published 7 Dec 2016

DOI: 10.1038/ncomms13745

OPEN

Interstitial oxygen as a source of *p*-type conductivity in hexagonal manganites

Sandra H. Skjærvø[1], Espen T. Wefring[1], Silje K. Nesdal[1], Nikolai H. Gaukås[1], Gerhard H. Olsen[1], Julia Glaum[1], Thomas Tybell[2] & Sverre M. Selbach[1]

Hexagonal manganites, h-$RMnO_3$ (R = Sc, Y, Ho–Lu), have been intensively studied for their multiferroic properties, magnetoelectric coupling, topological defects and electrically conducting domain walls. Although point defects strongly affect the conductivity of transition metal oxides, the defect chemistry of h-$RMnO_3$ has received little attention. We use a combination of experiments and first principles electronic structure calculations to elucidate the effect of interstitial oxygen anions, O_i, on the electrical and structural properties of h-$YMnO_3$. Enthalpy stabilized interstitial oxygen anions are shown to be the main source of *p*-type electronic conductivity, without reducing the spontaneous ferroelectric polarization. A low energy barrier interstitialcy mechanism is inferred from Density Functional Theory calculations to be the microscopic migration path of O_i. Since the O_i content governs the concentration of charge carrier holes, controlling the thermal and atmospheric history provides a simple and fully reversible way of tuning the electrical properties of h-$RMnO_3$.

---

[1] Department of Materials Science and Engineering, NTNU Norwegian University of Science and Technology, NO-7491 Trondheim, Norway. [2] Department of Electronics and Telecommunications, NTNU Norwegian University of Science and Technology, NO-7491 Trondheim, Norway. Correspondence and requests for materials should be addressed to S.M.S. (email: selbach@ntnu.no).

Point defects are imperative to the functional properties of oxides used in electrochemical devices like solid oxide fuel cells, batteries and memristors[1–3]. In contrast, point defects in general have a detrimental effect on physical properties of oxides for electronics, such as for example fatigue and domain wall pinning in ferroelectrics[4]. As components are made smaller, the available length for point defects in materials to diffuse is made shorter. This reduces the time required for the point defect to diffuse through the samples compared with bulk materials, where they effectively freeze in[5]. Understanding point defects in functional oxides thus becomes ever more important with decreasing component dimensions[6,7].

Rare earth ternary manganites with $RMnO_3$ stoichiometry are stable in the hexagonal manganite structure with space group $P6_3cm$ (185) for $R =$ Sc, Y and Ho–Lu. The structure consists of layers of five-coordinated Mn^{3+} corner-sharing trigonal bipyramids separated by layers of Y^{3+} in the *ab*-plane. The MnO_5 bipyramids are tilted in a pattern of trimers, while the Y^{3+} are displaced in opposite directions along the polar *c*-axis[8]. A subtle shift of the trigonal bipyramid layer with respect to the Y^{3+} layer, caused by an improper ferroelectric transition at 1,250 K, is the origin of the ferroelectric polarization[9]. The Mn^{3+} sublattice has a frustrated non-collinear antiferromagnetic order on a trigonal lattice, with a Néel temperature of 75 K (ref. 10).

Compared with the ternary ABO_3 perovskite oxides, the defect chemistry of h-$RMnO_3$ has received little attention. Oxygen vacancies in $YMnO_3$ have been studied[11–13], and large oxygen *excess* has been reported for h-$RMnO_{3+\delta}$ ($R =$ Y, Dy) with δ up to 0.35 for $R =$ Dy[14]. High levels of excess oxygen can cause development of secondary oxidized phases, which are easily detected experimentally[15]. However, structural effects, energetics and kinetics of point defects in low concentrations have not been addressed. Excess oxygen is well known in perovskite manganites such as $LaMnO_{3+\delta}$. Since the perovskite structure is too close-packed for interstitial oxygen anions, excess oxygen is accommodated by cation vacancies; $La_{1-\delta/3}Mn_{1-\delta/3}O_3$ (ref. 16). Oxidation of perovskite $LaMnO_3$ thus requires cation diffusion, which demands higher temperatures than anion diffusion.

Diffusion of oxygen in bulk $YMnO_3$ has been observed below 200 °C (ref. 14), making cation vacancy compensation highly unlikely. The layered h-$RMnO_3$ structure is however ~11% less dense than the corresponding orthorhombic perovskite structure, suggesting the possibility of interstitial oxygen. This is further supported by the observation that crystallization, which requires cation diffusion, of amorphous $YMnO_3$ only occurs above 800 °C (ref. 17).

Here we investigate how excess oxygen in the form of highly mobile interstitial anions is accommodated in the hexagonal manganite structure, and demonstrate that this enthalpy stabilized point defect gives rise to the observed *p*-type conductivity in $YMnO_3$. This shows the importance of controlling the material's thermo-atmospheric history and opens a new avenue for tuning the physical properties of hexagonal manganites.

Results

Oxygen stoichiometry and electrical conductivity. First we consider the effect of thermal and atmospheric history on the conductivity and oxygen stoichiometry of the prototypical hexagonal manganite $YMnO_3$. Thermoelectric power for a porous polycrystalline $YMnO_3$ bar was measured in O_2 and N_2 atmosphere, Fig. 1a. The Seebeck coefficient is positive for all temperatures in O_2 atmosphere, implying that *p*-type electronic conduction dominates, and a maximum is observed at 300 °C. In N_2 atmosphere, the Seebeck coefficient is negative, implying conduction by electrons as majority charge carriers. The DC electrical conductivity of $YMnO_3$ in O_2 increases exponentially on heating from 100 °C, as expected for a semiconducting oxide. However, the conductivity goes through a maximum value at 270 °C, then decreases and stays relatively constant up to 420 °C, from which the conductivity again increases exponentially. In N_2 atmosphere, the DC conductivity follows an exponential trend on heating, as expected for a semiconductor.

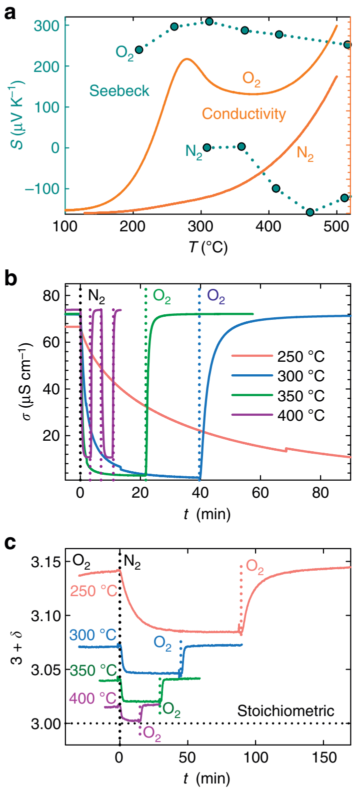

Figure 1 | *p*-type conductivity and excess oxygen. (**a**) Seebeck coefficient, *S*, and DC electrical conductivity, *σ*, in O_2 and N_2 atmosphere of a porous polycrystal of $YMnO_3$, as a function of temperature, *T*. (**b**) DC electrical conductivity as a function of time, *t*, of a porous polycrystal upon switching atmosphere (indicated by dotted lines) between flowing O_2 and N_2. The atmosphere is switched twice between O_2 and N_2 at 400 °C. (**c**) Oxygen stoichiometry, $3+\delta$, as a function of time, *t*, upon switching atmosphere measured by thermogravimetry for $YMnO_3$ nanoparticles ($d_{XRD} = 49 \pm 4$ nm).

The observations in Fig. 1a is consistent with the chemical defect reaction:

$$1/2\,O_2(g) + 2Mn_{Mn}^{x} \xrightarrow{YMnO_3} 2Mn_{Mn}^{\bullet} + O_i^{''} \qquad (1)$$

where $O_i^{''}$ is interstitial O^{2-}, and Mn_{Mn}^{x} and $Mn_{Mn}^{\bullet}$ depicts Mn^{3+} and Mn^{4+} on Mn lattice sites, respectively. Tetravalent Mn in oxidized $YMnO_3$ is Mn with localized electron holes: $Mn^{4+} = Mn^{3+} + h^{+}$. Holes as the majority charge carrier is consistent with the positive sign of the Seebeck coefficient. The mobility of negatively charged interstitial O^{2-} is expected to be orders of magnitude smaller than for holes, and this is addressed further below.

The peculiar thermal evolution of the electrical conductivity can be explained from the maximum oxygen stoichiometry observed at about 250 °C (ref. 14), which coincides with a maximum in electrical conductivity. The deviation in conductivity from the exponential behaviour of a semiconductor stems from the different temperature dependence of the concentration and mobility of holes. While the mobility of holes increases with temperature, this is counterbalanced by the loss of oxygen and charge compensating holes, above 250 °C, as we will show further below. The atypical thermal evolution of the electrical properties of $YMnO_3$ in this temperature range has previously been attributed to the filling of oxygen vacancies[18–20], but charge compensating electrons would give a negative Seebeck coefficient.

DC conductivity measurements were then performed on isothermal change of atmospheres between O_2 and N_2. When the partial pressure of oxygen, pO_2, is reduced by switching from O_2 to N_2 atmosphere, the oxygen excess decreases according to equation (1) and a relaxation towards a lower conductivity is observed in Fig. 1b. The initial conductivity is regained after changing the atmosphere back to O_2, demonstrating the reversibility of reaction (1). The regained conductivity is similar for all isotherms, owing to the opposing effects of decreasing charge carrier mobility and increasing concentration as the temperature is reduced. The relaxation time before equilibrium is reached is highly temperature dependent, as expected for diffusion of oxygen into the lattice.

AC conductivity measurements were performed on samples annealed in flowing O_2 and N_2, respectively, before measurement (Supplementary Fig. 1). The conductivity of the O_2 annealed sample shows the characteristic maximum at 280 °C on heating, resembling the maximum observed in Fig. 1a. The conductivity measured on cooling is lower compared with the initial heating cycle reflecting the loss of O_i that occurred at higher temperatures. The N_2 annealed sample exhibits a smooth increase of the conductivity with temperature. Subsequent cooling leads to higher conductivity in accordance with the reversibility of the O_i incorporation process.

The reversibility of reaction (1) is also evidenced by the oxygen stoichiometry when switching between O_2 and N_2 atmospheres, Fig. 1c. As the length scale of the system is imperative to diffusion controlled processes[5], nanoparticles with an average crystallite size of $d_{XRD} = 49 \pm 4$ nm (ref. 17) were chosen for studying thermogravimetric relaxation on switching atmosphere at a shorter time-scale than in bulk material. With increasing temperature the oxygen stoichiometry equilibrates faster. The rapid change in oxygen stoichiometry in $YMnO_3$ nanoparticles illustrates the increasing importance of thermal and atmospheric history with decreasing system size. The isothermal response of the electrical conductivity (Fig. 1b) and the oxygen stoichiometry (Fig. 1c) on change in pO_2 is explained by reaction (1): oxygen hyperstoichiometry governs the electrical conductivity of h-$RMnO_{3+\delta}$.

Position of interstitial oxygen and structural effects. The low temperature at which $YMnO_3$ exchanges oxygen with the atmosphere makes cation vacancies and diffusion unrealistic, and the positive Seebeck coefficient from mobile holes points to interstitial oxygen anions, O_i, as the dominating point defect. High-temperature X-ray diffraction measurements of nanocrystalline $YMnO_3$ show that interstitial oxygen is incorporated into the lattice, causing anisotropic chemical expansion (Supplementary Fig. 2). We now turn our attention to the position of interstitial oxygen in $YMnO_3$. Potential energy surfaces (PES) were determined by mapping the energy landscape of the O_i position in several lattice planes by static Density Functional Theory (DFT) calculations (See details in Supplementary Fig. 3 and Supplementary Note 1). For illustration, the PES of O_i in the (002) (**a**) and ($^3/_2$00) (**b**) planes are included in Fig. 2 along wth a unit cell with the corresponding lattice planes (**d**). The relative energy of O_i along the grey line in Fig. 2b is shown in Fig. 2c. The most stable positions of O_i was found to be between three Mn in the Mn–O planes at $z = 0$ and $^1/_2$, resulting in six equivalent possible sites for O_i in the $P6_3cm$ unit cell, ($^1/_3$, $^1/_3$, 0), ($^2/_3$, 0, 0), (0, $^2/_3$, 0), ($^2/_3$, $^2/_3$, $^1/_2$), ($^1/_3$, 0, $^1/_2$) and (0, $^1/_3$, $^1/_2$), as illustrated by green circles in panels **a** and **b**.

Experimental observations of a maximum δ of ~ 0.35 (refs 14,15) can be rationalized from our DFT simulations. If two out of the six possible stable interstitial sites in the unit cell are occupied, a hypothetical fully oxidized structure of $YMnO_3$ would have a chemical formula of $YMnO_{3.33}$ or $Y_3Mn_3O_{10}$. This will result in one O_i and two out of three oxidized Mn in each Mn–O layer of the 30 atom unit cell. Accommodation of more than two O_i per unit cell would require charge compensation across layers or further oxidation of Mn^{4+} to Mn^{5+} within the same layer.

The in-plane distances between O_i and Mn after structural relaxation depicted in Fig. 3a,b show that there are two shorter and one longer Mn–O_i bond. O_i is displaced towards two d^3 Mn^{4+} ions (with a calculated magnetic moment of 3.06 μ_B), and away from one d^4 Mn^{3+} ion (3.74 μ_B). The localization of holes on the two oxidized Mn ions gives three possible configurations of O_i and its three surrounding Mn ions. The most stable positions of O_i are triple wells due to asymmetric electrostatic attraction: O_i with formal charge -2 has shorter bonds to the two Mn^{4+} than to the single Mn^{3+}. Details and discussion about the energetic asymmetry of this triple well and the effect of O_i on the magnetism can be found in Supplementary Figs 4 and 5 and Supplementary Note 2.

Localization of holes on Mn, and the resulting p-type polaronic conduction, stems from electrostatic attraction between positive holes and negative interstitial anions. In contrast, hole doping by substituting Y^{3+} with Ca^{2+} gives holes in Bloch states, while electron doping by Zr^{4+} for Y^{3+} substitution gives a polaronic state[21]. The energy barrier for moving the holes associated with O_i between different Mn^{4+} pairs is 0.29 eV from nudged-elastic band (NEB) calculations (See details in Supplementary Fig. 6 and Supplementary Note 3). Our calculated energy barrier is lower than the reported activation energy of 0.38–0.50 eV for polaron hopping in $YMnO_3$ (refs 22–24).

Interstitial oxygen causes only subtle local structural distortions, as evident from the excerpt of the (002) plane of $YMnO_3$ in Fig. 3a. The relaxed atomic positions are shown in the foreground, while the atoms in a perfect crystal are included in faded colours in the background for comparison. The Y sublattice is virtually unaffected by the introduction of O_i in the Mn–O layer, as shown in Fig. 3c. The local displacements of ions occur mainly within the same layer of trigonal MnO_5 bipyramids as O_i is situated, and the distortions decrease rapidly with increasing distance from O_i. The apical tilting angle, defined in Fig. 3d, of the three bipyramids surrounding O_i is reduced from 8.7° in the perfect crystal to 6.4° for Mn^{4+} bipyramids and 4.7° for Mn^{3+} bipyramids, respectively.

The local structural distortions caused by the introduction of O_i can be quantified by the displacements of ions relative to the perfect $P6_3cm$ structure as a function of the distance from the O_i, as illustrated in Fig. 3e. Displacements of Mn and planar oxygen closest to O_i are substantial, apical oxygen in the nearest bipyramids are also displaced, while Y even close to O_i are less affected. The structural screening length of the O_i point defect is defined here as the distance away from O_i where the displacement

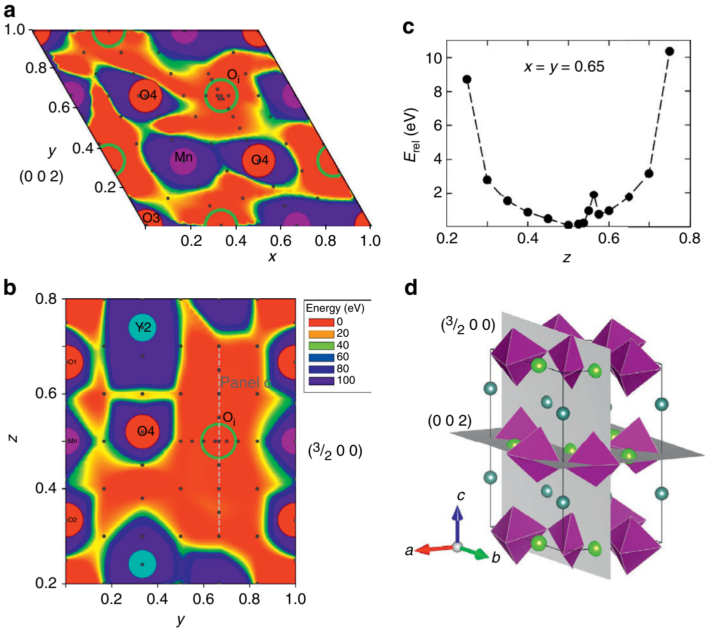

Figure 2 | Position of interstitial oxygen. Potential energy surfaces (PES) showing the energy landscape for the position of interstitial oxygen in a neutral $YMnO_3$ unit cell in (**a**) the (002) plane and (**b**) the ($^3/_2$00) plane. (**c**) Relative energy along the *z* direction for $x = y = 0.65$ indicated by a light grey line in panel **b**. The anomaly at $z = 0.56$ stems from that the PES mapping was done with static calculations. (**d**) Crystal structure of $YMnO_3$ showing purple MnO_5 polyhedra, turquoise Y atoms, and green spheres marking the six equivalent stable positions for O_i in the unit cell along with the two crystal planes in (**a**),(**b**).

is less than 0.1 Å relative to the perfect structure. A structural screening length can thus be estimated to 5.5 Å, corresponding to the second coordination shell of O_i, and is shown by a dotted line in Fig. 3e. Local charge compensation of O_i by two Mn^{4+} and polyhedral tilting mitigates the effect of O_i on the lattice. The short structural screening length implies that direct experimental detection of O_i is challenging.

The calculations also show that the non-collinear triangular magnetic order is only subtly affected by O_i (Supplementary Fig. 5). At the relevant temperatures for O_i transport, the material is paramagnetic and the properties are therefore not expected to be significantly affected by magnetic order. The relaxed structure is not affected by substituting the true non-collinear magnetic ground state structure with a synthetic collinear magnetic order.

Energetics of O_i. An essential thermodynamic quantity for point defects is the energy of formation. Using the formalism of Zhang *et al.*[25] for neutral cells we can define the energy of formation, E^f, for interstitial oxygen as:

$$E^{f}_{O_i} = E_{YMnO_{3+\delta}} - E_{YMnO_3} - \mu_O, \quad (2)$$

where $E_{YMnO_{3+\delta}}$ and E_{YMnO_3} are the total energies of oxidized and stoichiometric $YMnO_3$, respectively, and μ_O is the chemical potential of oxygen. The formation energy for O_i in $YMnO_3$ as a function of the chemical potential of oxygen is shown in Fig. 4a (See Supplementary Fig. 7 and Supplementary Methods for details on the thermodynamic stability region for bulk $YMnO_3$). For $p_{O_2} = 0.21$, corresponding to air, the chemical potential of oxygen yields a negative formation energy at temperatures up to ~900 °C, which is well above the temperature were O_i becomes entropy destabilized, as seen from the experimental measurements in Fig. 1. However, it must be pointed out that the formation enthalpy for O_i is calculated in the dilute limit, while a finite concentration of O_i is necessary to detect mass changes by thermogravimetry. The consumption of the gaseous species O_2 (g) in reaction (1) means that the entropy of this reaction is negative, hence the entropy contribution to the Gibbs free energy of (1) is positive. Given the negative enthalpy of reaction (1) from DFT, the Gibbs' free energy of (1) becomes less negative with increasing temperature, gradually shifting (1) towards the left hand side where O_i leaves the lattice to form O_2 molecules. The equilibrium concentration of O_i hence decreases with increasing temperature, in line with the results in Fig. 1, but in contrast to entropy stabilized oxygen vacancies which have a positive enthalpy of formation under conditions where the oxide is stable. In analogy to brownmillerite AB_2O_5 and perovskite ABO_3, O_i in $YMnO_3$ could be considered filled oxygen vacancies in the hypothetical compound $Y_3Mn_3O_{10}$. With $Y_3Mn_3O_{10}$ as the reference state, vacant O_i sites would be oxygen vacancies, and thus conform to conventional point defect thermodynamics with positive enthalpies and entropies of formation. We note that the enthalpy of formation for O_i is expected to decrease progressively with increasing oxygen excess δ due to O_i–O_i repulsion and a gradual loss of the driving force for oxidation.

Migration of O_i. To investigate the ionic mobility of interstitial oxygen, migration paths for O_i between two stable positions were investigated by NEB calculations. Simple interstitial migration, with a calculated energy barrier of almost 6 eV (Supplementary Fig. 8a), is not likely to occur. In the interstitialcy mechanism, O_i pushes an adjacent planar oxygen into a neighbouring interstitial

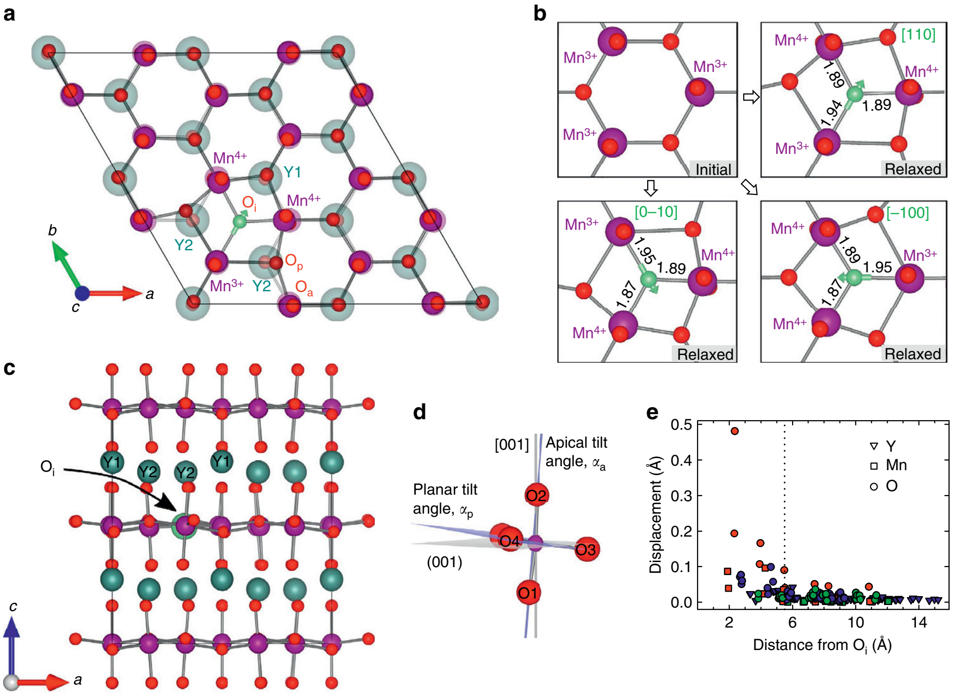

Figure 3 | Structural distortions and screening length. (**a**) Relaxed geometry of the (002) plane of a 2 × 2 × 1 supercell of $YMnO_3$ with the perfect structure faded in the background for comparison. Y atoms above the (002) Mn–O plane are projected onto the plane. (**b**) Unrelaxed structure in upper left panel compared with relaxed structures around O_i in the three triple-well positions around the $^2/_3$, $^2/_3$, $^1/_2$ position. The green arrows on O_i indicate the displacement towards the two Mn^{4+}. Bond lengths between O_i and Mn are given in Å. (**c**) $YMnO_3$ with O_i (green sphere in the (002) Mn–O layer) viewed along the **b**-direction. (**d**) Apical and planar tilting angles of the trigonal bipyramids. O1 and O2; and O3 and O4 being apical and planar oxygens, respectively. (**e**) Displacements of ions with respect to the perfect structure as a function of distance from O_i. The red symbols represent atoms in the same Mn–O layer as O_i is positioned, the blue symbols represent the apical oxygens and the yttrium atoms closest to the Mn–O layer with O_i, and the green symbols show atoms in the adjacent Mn–O layers. The structural screening length is indicated by a vertical dotted line.

site, subsequently taking up a regular planar oxygen lattice position itself. The maximum energy along the minimum energy path is found when the distance between O_i and planar lattice oxygen goes through a minimum. When O_i nudges a regular oxygen at an O3 site, (Fig. 4b) an energy barrier of 0.48 eV was found (Fig. 4c). A similar mechanism where O_i nudges a regular oxygen at an O4 site resulted in a higher energy barrier of 0.62 eV (See Supplementary Fig. 8b,c for effect of magnetic order and Hubbard U). This is explained by Y1 being closer to the moving O3 (which is a trimerization centre) and O_i in path 2 compared with the corresponding distance between Y2 and the moving O4 and O_i in path 1 (Fig. 4b) (See Supplementary Fig. 8e and f for illustration of bond lengths). Migration through path 2 will therefore be aided by Y1 bonding to the two moving oxygen atoms, which is supported by the electronic density of states in Fig. 5d. An energy barrier was also estimated from the experimental TGA data by plotting time to oxidation as a function of annealing time in O_2 atmosphere, as shown in Supplementary Figure 8d. The Arrhenius-type relation gave an energy barrier of 0.55 ± 0.21 eV, in agreement with our DFT calculated values. For comparison, oxygen transport through vacancy diffusion in ABO_3 perovskites has an energy barrier in the range of 0.5–2.8 eV (ref. 26). See Supplementary Note 4 for more details about the migration barriers.

Functional properties. We now address the impact of O_i on the electronic properties. The introduction of O_i between three Mn (Fig. 3a) gives three edge-sharing octahedra. As these octahedra are strongly distorted, the crystal field experienced by the d-electrons of Mn coordination O_i does not change significantly compared with the trigonal bipyramidal crystal field in the perfect crystal. The most obvious change in electronic structure, in Fig. 5, caused by O_i is the appearance of a non-bonding defect state in the band gap mainly consisting of Mn^{4+} $d_{x^2y^2}$ states and O_i $2p_x$ and $2p_y$ states. A fraction of the occupied Mn d states closest to the Fermi energy is lifted above E_F on inclusion of O_i as electron density is donated from Mn $3d$ to O $2p$. The corresponding binding states are easily seen at the bottom of the valence band. Even though charge transfer is not complete, this can formally be regarded as the oxidation of Mn^{3+} to Mn^{4+}, creating holes in the valence band and p-type electronic conductivity. The p-DOS of interstitial oxygen is very similar to that of planar oxygen, which is also coordinated by only Mn, while it differs significantly from the p-DOS of apical oxygen, which is coordinated by both Mn and Y. The highly localized character of the defect state in the band gap is characteristic for the electronic structure of an acceptor doped material, and direct experimental detection of O_i in low concentrations, by for example spectroscopic techniques, would be challenging. With increasing O_i concentration, the

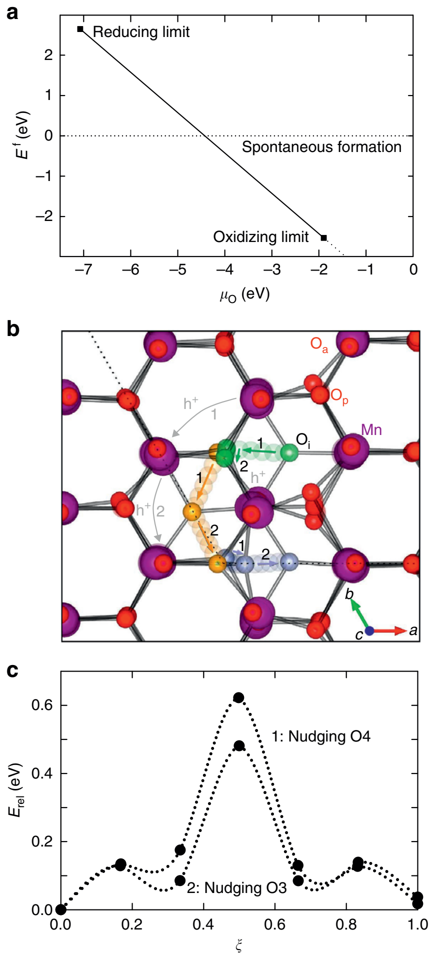

Figure 4 | Energetics and kinetics. (**a**) Defect formation energy of O_i in a 2x2x1 supercell of $YMnO_3$ as a function of chemical potential of oxygen. (**b**) Subsequent migration paths of O_i (green, then yellow and finally blue) through an interstitialcy mechanism nudging first a planar lattice oxygen at an O4 site (path 1) and then a planar lattice oxygen at an O3 site (path 2). The hopping of holes (h^+) between Mn sites are shown by grey arrows. (**c**) The migration energy barriers for path 1 (nudging an O4) and path 2 (nudging an O3) as functions of the relative reaction coordinate, ξ.

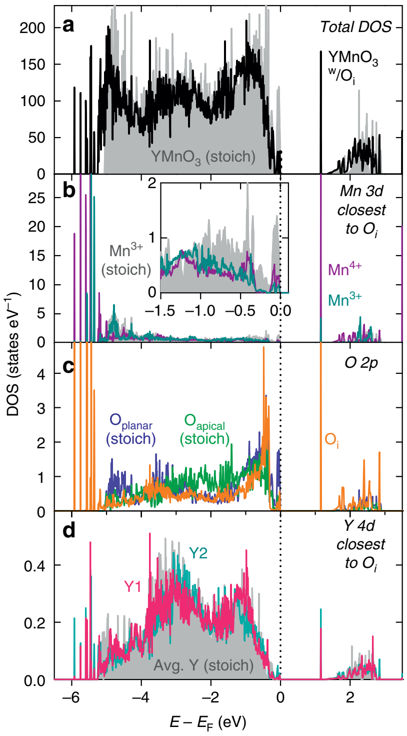

Figure 5 | Electronic structure. (**a**) Total electronic density of states (DOS) for a perfect 120 atom $YMnO_3$ cell and a 121 atom cell of $YMnO_3$ with one O_i ($YMnO_{3.04}$). (**b**) Atomic DOS showing the *d* states for Mn^{3+} and Mn^{4+} coordinating O_i compared with Mn^{3+} *d* states in a stoichiometric cell. (**c**) Atomic DOS showing the *p* states of O_i compared with *p* states for apical and planar oxygens in a stoichiometric cell. (**d**) Atomic DOS showing the *d* states of the closest Y1 and Y2 to O_i compared with the average Y *d* states in a stoichiometric cell.

defect state becomes less localized, as expected (See Supplementary Figure 9 for DOS and band structure of a 30 atom unit cell, $YMnO_{3.16}$).

To address the impact of O_i on the ferroelectric properties we calculated the spontaneous polarization (P_S) by the Berry phase method to $7.8\,\mu C\,cm^{-2}$ for the perfect structure, and $7.2\,\mu C\,cm^{-2}$ after inclusion of one O_i in a 120 atom supercell. A simple point charge model gave 7.8 and $7.0\,\mu C\,cm^{-2}$ for stoichiometric $YMnO_3$ and oxidized $YMnO_{3.04}$, respectively. Although the effect of O_i on the spontaneous polarization is subtle, the charge compensating holes will raise the electrical conductivity and be detrimental to the macroscopic ferroelectric performance. However, in improper ferroelectrics like $YMnO_3$, charged domain walls (DW) display anisotropic conductance due to the accumulation of mobile charge carriers[27]. Interstitial oxygen with formal charge −2 can screen the electrostatic field at head-to-head DWs, while charge compensating holes can screen tail-to-tail DW. Engineering point defect populations at DWs has great potential for tuning the properties of DWs as functional elements for electronics[28–31].

To summarize, we have shown that interstitial oxygen is the dominating point defect in $YMnO_3$ and the source of *p*-type electronic conductivity at ambient conditions. Interstitial oxygen is an enthalpy stabilized point defect, implying that $YMnO_3$ is not only metastable with respect to Y_2O_3 and YMn_2O_5, in accordance with the phase diagram[32], it is also metastable with respect to oxidation towards the limiting case of $Y_3Mn_3O_{10}$. A bulk $YMnO_3$ sample will however not oxidize completely at ambient conditions for kinetic reasons; the diffusion length is too large compared with the relatively low ionic mobility at room temperature. However, at the nanoscale, in thin films and at surfaces, oxidation will occur spontaneously also at ambient conditions. This emphasizes the necessity and potential which lies in controlling the thermal and atmospheric history of hexagonal manganite materials in order to tailor the point defect population, charge carrier concentration and physical properties.

Methods

Experimental. Bulk $\mathrm{YMnO_3}$ powder was prepared by firing pressed pellets of dried and mixed $\mathrm{Y_2O_3}$ and $\mathrm{MnO_2}$ twice for 24 h at 1,300 °C in air. Porous polycrystalline bars with a density of 43% were sintered from phase pure $\mathrm{YMnO_3}$ powder with 20 wt% carbon black as a pore filler for 2 h at 1,500 °C in air and scanning electron micrographs of the fracture surfaces of the porous bars are given in Supplementary Fig. 10. Porous bars were used to increase the total surface area accessible to oxygen surface exchange. Four-point electrical conductivity measurements were performed on a porous polycrystalline bar in flowing $\mathrm{O_2}$ and $\mathrm{N_2}$ (ref. 33). Impedance spectroscopy measurements (Novotherm, Novocontrol Technologies) were conducted within a temperature range from 30 to 350 °C on disc shaped samples using frequencies between 1 Hz and 1 MHz. Before measurement the samples were annealed in flowing oxygen resp. nitrogen for 24 h at 350 °C. Thermogravimetry (TGA) was done with a Netzsch STA 449C Jupiter in flowing $\mathrm{N_2}$ and $\mathrm{O_2}$ on nanoparticles with $d_{\mathrm{XRD}} = 49 \pm 4$ nm (ref. 17). Seebeck coefficients were measured at 200–500 °C in flowing $\mathrm{O_2}$ and $\mathrm{N_2}$ with a ProboStat setup (NorECs AS) on a porous bar in a vertical tubular furnace[34]. More details on the synthesis and characterization can be found in Supplementary Methods.

Computational. Density functional theory calculations were performed with the VASP[35,36] code and the spin polarized GGA + U implementation of Dudarev[37] with the PBEsol functional[38]. A Hubbard U of 5 eV was applied to the Mn 3d orbitals in order to reproduce the experimental band gap[39] and lattice parameters[40]. The projector augmented wave[41] method was used treating Y(4s,4p,4d,5s), Mn(3s,3p,3d,4s) and O(2s,2p) as valence electrons and a plane-wave cutoff energy of 550 eV. Brillouin zone integration was done on a Γ-centered $4 \times 4 \times 2$ mesh for the 30 atom unit cell and with the number of k-points reduced accordingly for supercells. The non-collinear magnetic structure was approximated by a frustrated collinear antiferromagnetic (F-AFM)[42] order in most of the calculations, which does not give significantly different results from calculations with the true non-collinear magnetic order. Geometry optimization was done until the forces on the ions were below 0.005 eV Å^{-1} for 121 atom cells and 0.02 for 541 atom cells. The reducing and oxidizing limit for the chemical potential of oxygen varies from -7.1 to -1.9 eV. The defect formation energy of $\mathrm{O_i}$ was 0.03 eV lower in a 121 atom cell than in a 541 atom cell (See Supplementary Fig. 11). Bader analysis[43] gave charges of $+1.90$ and $+1.73$ for $\mathrm{Mn^{4+}}$ and $\mathrm{Mn^{3+}}$, respectively. For the nudged elastic band[44] (NEB) calculations we used five intermediate images for the $\mathrm{O_i}$ migration path and a Hubbard $U = 5$ eV was applied to reproduce the nature of the localized electron holes (comparison with $U = 0$ eV can be found in the Supplementary Fig. 8b). A frustrated antiferromagnetic (F-AFM) order was also used for the calculation of the energy barriers. Comparison between A-type AFM and F-AFM magnetic order is given in Supplementary Fig. 8c, and was set so that no spin flipping on the Mn ions occurred during the migration of $\mathrm{O_i}$ in order to isolate the effect of pure migration. The ferroelectric polarization was calculated with the Berry phase method[45]. VESTA was used for visualizing structures[46].

Data availability. The data that support the findings of this study are available from the authors on reasonable request.

References

1. Bagotsky, V. S. *Fuel Cells: Problems and Solutions* (Wiley, 2009).
2. Tarascon, J.-M. & Armand, M. Issues and challenges facing rechargeable lithium batteries. *Nature* **414,** 359–367 (2001).
3. Waser, R., Dittmann, R., Staikov, G. & Szot, K. Redox-based resistive switching memories–nanoionic mechanisms, prospects, and challenges. *Adv. Mater.* **21,** 2632–2663 (2009).
4. Aggarwal, S. & Ramesh, R. Point defect chemistry of metal oxide heterostructures. *Annu. Rev. Mater. Sci.* **28,** 463–499 (1998).
5. Grande, T., Tolchard, J. R. & Selbach, S. M. Anisotropic thermal and chemical expansion in Sr-substituted $\mathrm{LaMnO_{3+\delta}}$: implications for chemical strain relaxation. *Chem. Mater.* **24,** 338–345 (2012).
6. Kalinin, S. V. & Spaldin, N. A. Functional ion defects in transition metal oxides. *Science* **341,** 858–859 (2013).
7. Kalinin, S. V., Borisevich & Fong, D. Beyond condensed matter physics on the nanoscale: the role of ionic and electrochemical phenomena in the physical functionalities of oxide materials. *ASC Nano* **6,** 10423–10437 (2012).
8. Gibbs, A. S., Knight, K. S. & Lightfoot, P. High-temperature phase transitions of hexagonal $\mathrm{YMnO_3}$. *Phys. Rev. B* **83,** 094111 (2011).
9. Van Aken, B. B., Palstra, T. T. M., Filippetti, A. & Spaldin, N. A. The origin of ferroelectricity in magnetoelectric $\mathrm{YMnO_3}$. *Nat. Mater.* **3,** 164–170 (2004).
10. Fiebig, M., Lottermoser, T., Frohlich, D., Goltsev, A. V. & Pisarev, R. V. Observation of coupled magnetic and electric domains. *Nature* **419,** 818–820 (2002).
11. Overton, A. J., Best, J. L., Saratovsky, I. & Hayward, M. Influence of topotactic reduction on the structure and magnetism of the multiferroic $\mathrm{YMnO_3}$. *Chem. Mater.* **21,** 4940–4948 (2009).
12. Du, Y. *et al.* Manipulation of domain wall mobility by oxygen vacancy ordering in multiferroic $\mathrm{YMnO_3}$. *Phys. Chem. Chem. Phys.* **15,** 20010–20015 (2013).
13. Cheng, S., Deng, S. Q., Zhao, Y. G., Sun, X. F. & Zhu, J. Correlation between oxygen vacancies and sites of Mn ions in $\mathrm{YMnO_3}$. *Appl. Phys. Lett.* **106,** 062905 (2015).
14. Remsen, S. & Dabrowski, B. Synthesis and oxygen storage capacities of hexagonal $\mathrm{Dy_{1-x}Y_xMnO_{3+\delta}}$. *Chem. Mater.* **23,** 3818–3827 (2011).
15. Parkkima, O., Malo, S., Hervieu, M., Rautama, E.-L. & Karppinen, M. New $R\mathrm{MnO_{3+\delta}}$ ($R = $ Y, Ho; $\delta \approx 0.35$) phases with modulated structure. *J. Solid State Chem.* **221,** 109–115 (2015).
16. Roosmalen, J. A. & Cordfunke, E. H. The defect chemistry of $\mathrm{LaMnO_{3+\delta}}$: 4. defect model for $\mathrm{LaMnO_3}$. *J. Solid State Chem.* **110,** 109–112 (1994).
17. Bergum, K. *et al.* Synthesis, structure and magnetic properties of nanocrystalline $\mathrm{YMnO_3}$. *Dalt. Trans.* **40,** 7583–7589 (2011).
18. Tomczyk, M., Vilarinho, P. M., Moreira, A. & Almeida, A. High temperature dielectric properties of $\mathrm{YMnO_3}$ ceramics. *J. Appl. Phys.* **110,** 064116 (2011).
19. Ren, P., Fan, H. & Wang, X. Bulk conduction and nonlinear behaviour in multiferroic $\mathrm{YMnO_3}$. *Appl. Phys. Lett.* **103,** 152905 (2013).
20. Bogusz, A. *et al.* Resistive switching in polycrystalline $\mathrm{YMnO_3}$ thin films. *AIP Adv.* **4,** 107135 (2014).
21. Van Aken, B. B., Bos, J.-W. G., de Groot, R. A. & Palstra, T. T. M. Asymmetry of electron and hole doping in $\mathrm{YMnO_3}$. *Phys. Rev. B* **63,** 125127 (2001).
22. Moure, C., Villegas, M., Fernandez, J. F., Tartaj, J. & Duran, P. Phase transition and electrical conductivity in the system $\mathrm{YMnO_3}$-$\mathrm{CaMnO_3}$. *J. Mater. Sci.* **34,** 2565–2568 (1999).
23. Balamurugan, C. & Lee, D. W. Perovskite hexagonal $\mathrm{YMnO_3}$ nanopowder as p-type semiconductor gas sensor for $\mathrm{H_2S}$ detection. *Sens. Actuators B: Chem.* **221,** 857–866 (2015).
24. Ma, Y. *et al.* Investigation of magnetic, dielectric and electrical properties of Ce-substituted $\mathrm{YMn_{0.8}Fe_{0.2}O_3}$ multiferroic ceramics. *J. Mater. Sci.: Mater. Electron.* **26,** 398–404 (2015).
25. Zhang, S. B. & Northrup, J. E. Chemical potential dependence of defect formation energies in GaAs: application to Ga self-diffusion. *Phys. Rev. Lett.* **67,** 2339–2342 (1991).
26. Chroneos, A., Vovk, R. V., Goulatis, I. L. & Goulatis, L. I. Oxygen transport in perovskite and related oxides: A brief review. *J. Alloy. Compd.* **494,** 190–195 (2010).
27. Meier, D. *et al.* Anisotropic conductance at improper ferroelectric domain walls. *Nat. Mater.* **11,** 284–288 (2012).
28. Griffin, S. M. *et al.* Scaling behavior and beyond equilibrium in the hexagonal manganites. *Phys. Rev. X* **2,** 041022 (2012).
29. Choi, T. *et al.* Insulating interlocked ferroelectric and structural antiphase domain walls in multiferroic $\mathrm{YMnO_3}$. *Nat. Mater.* **9,** 253–258 (2010).
30. Meier, D. Functional domain walls in multiferroics. *J. Phys.: Condens. Matter* **27,** 463003 (2015).
31. Kumagai, Y. & Spaldin, N. A. Structural domain walls in polar hexagonal manganites. *Nat. Commun.* **4,** 1540 (2013).
32. Chen, M., Hallstedt, B. & Gauckler, L. J. Thermodynamic assessment of the Mn–Y–O system. *J. Alloy. Compd.* **393,** 114–121 (2005).
33. Selbach, S. M., Tybell, T., Einarsrud, M.-A. & Grande, T. High-temperature semiconducting cubic phase of $\mathrm{BiFe_{0.7}Mn_{0.3}O_{3+\delta}}$. *Phys. Rev. B* **79,** 214113 (2009).
34. Wefring, E. T., Einarsrud, M. A. & Grande, T. Electrical conductivity and thermopower of $(1-x)$ $\mathrm{BiFeO_3} - x\mathrm{Bi_{0.5}K_{0.5}TiO_3}$ ($x = 0.1$, 0.2) ceramics near the ferroelectric to paraelectric phase transition. *Phys. Chem. Chem. Phys.* **17,** 9420–9428 (2015).
35. Kresse, G. & Furthmüller, J. Efficient iterative schemes for *ab initio* total-energy calculations using a plane-wave basis set. *Phys. Rev. B* **54,** 11169–11186 (1996).
36. Kresse, G. & Joubert, D. From ultrasoft pseudopotentials to the projector augmented-wave method. *Phys. Rev. B* **59,** 1758–1775 (1999).
37. Dudarev, S. L., Botton, G. A., Savrasov, S. Y., Humphreys, C. J. & Sutton, A. P. Electron-energy-loss spectra and the structural stability of nickel oxide: An LSDA + U study. *Phys. Rev. B* **57,** 1505–1509 (1998).
38. Perdew, J. P. *et al.* Restoring the density-gradient expansion for exchange in solids and surfaces. *Phys. Rev. Lett.* **100,** 136406 (2008).
39. Degenhardt, C., Fiebig, M., Fröhlich, D., Lottermoser, T. & Pisarev, R. V. Nonlinear optical spectroscopy of electronic transitions in hexagonal manganites. *Appl. Phys. B* **73,** 139–144 (2001).
40. Van Aken, B. B., Meetsma, A. & Palstra, T. T. M. Hexagonal $\mathrm{YMnO_3}$. *Acta Crystallogr. C* **57,** 230–232 (2001).
41. Blöchl, P. E. Projector augmented-wave method. *Phys. Rev. B* **50,** 17953–17979 (1994).
42. Medvedeva, J. E., Anisimov, V. I., Korotin, M. A., Mryasov, O. N. & Freeman, A. J. The effect of Coulomb correlation and magnetic ordering on the electronic structure of two hexagonal phases of ferroelectromagnetic $\mathrm{YMnO_3}$. *J. Phys.: Condens. Matter* **12,** 4947–4958 (2000).

43. Henkelman, G., Arnaldsson, A. & Jónsson, H. A fast and robust algorithm for Bader decomposition of charge density. *Comput. Mater. Sci.* **36,** 354–360 (2006).
44. Henkelman, G., Uberuaga, B. P. & Jonsson, H. A climbing image nudged elastic band method for finding saddle points and minimum energy paths. *J. Chem. Phys.* **113,** 9901–9904 (2000).
45. Spaldin, N. A. A beginner's guide to the modern theory of polarization. *J. Solid State Chem.* **195,** 2–10 (2012).
46. Momma, K. & Izumi, F. VESTA: a three-dimensional visualization system for electronic and structural analysis. *J. Appl. Crystallogr.* **41,** 653–658 (2008).

Acknowledgements

The Research Council of Norway (FRINATEK project no.231430/F20) and Norwegian University of Science and Technology (NTNU) are acknowledged for financial support. Computational resources were provided by NOTUR (The Norwegian Metacenter for High Performance Computing) through the project NN9264K and the Euler cluster at ETH, Zürich. Dr Kristin Bergum is acknowledged for preparing the nanoparticles for TGA.

Author contributions

S.H.S. and G.H.O. performed DFT calculations; E.T.W. conducted thermoelectric measurements; S.K.N. and N.H.G. performed DC conductivity and prepared bulk samples; J.G. and S.H.S. performed AC impedance measurements; S.M.S. performed TGA; S.M.S. and N.H.G. performed HTXRD; S.H.S., T.T. and S.M.S. wrote the paper; all authors discussed the results; S.M.S. conceived the project; T.T. and S.M.S. supervised the project.

Additional information

Supplementary Information accompanies this paper at http://www.nature.com/naturecommunications

Competing financial interests: The authors declare no competing financial interests.

Reprints and permission information is available online at http://npg.nature.com/reprintsandpermissions/

How to cite this article: Skjærvø, S. H. *et al.* Interstitial oxygen as a source of *p*-type conductivity in hexagonal manganites. *Nat. Commun.* **7,** 13745 doi: 10.1038/ncomms13745 (2016).

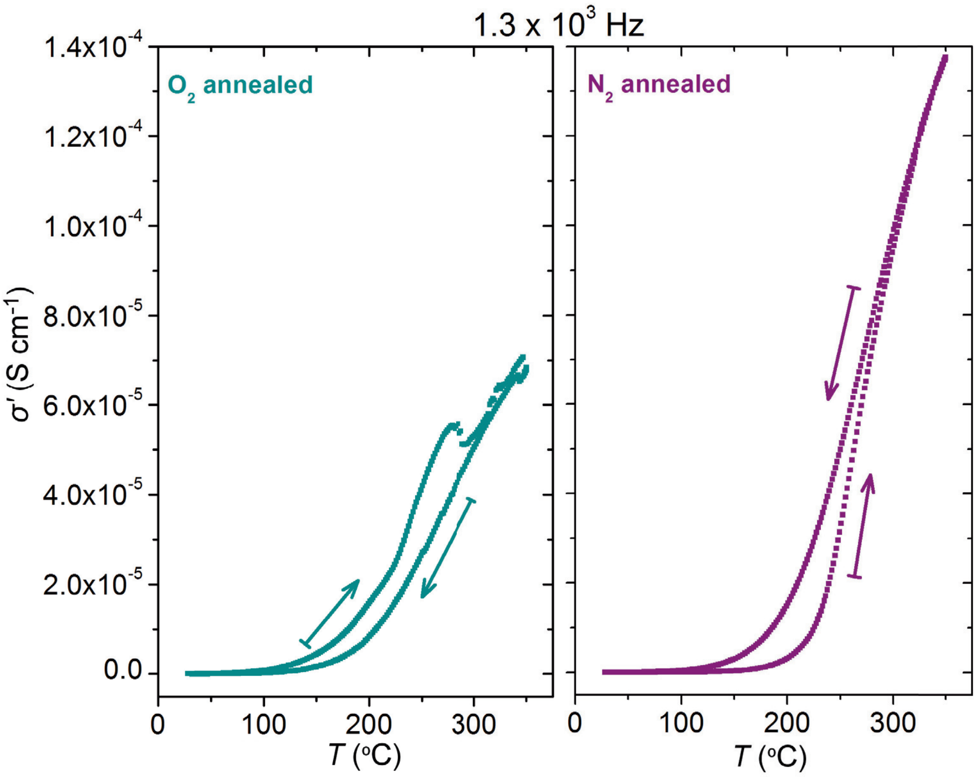

Supplementary Figure 1: AC conductivity, σ', measured on an $YMnO_3$ polycrystal between room temperature and 350 °C in air. The measurement frequencies ranged from 1 Hz to 1 MHz. The results for f = 1.3 kHz are shown for illustration. The left hand panel depicts the result for a sample annealed in flowing O_2, the right hand panel for a sample annealed in flowing N_2. In both cases the heat treatment was conducted for 24 hours at 350 °C prior to measurement.

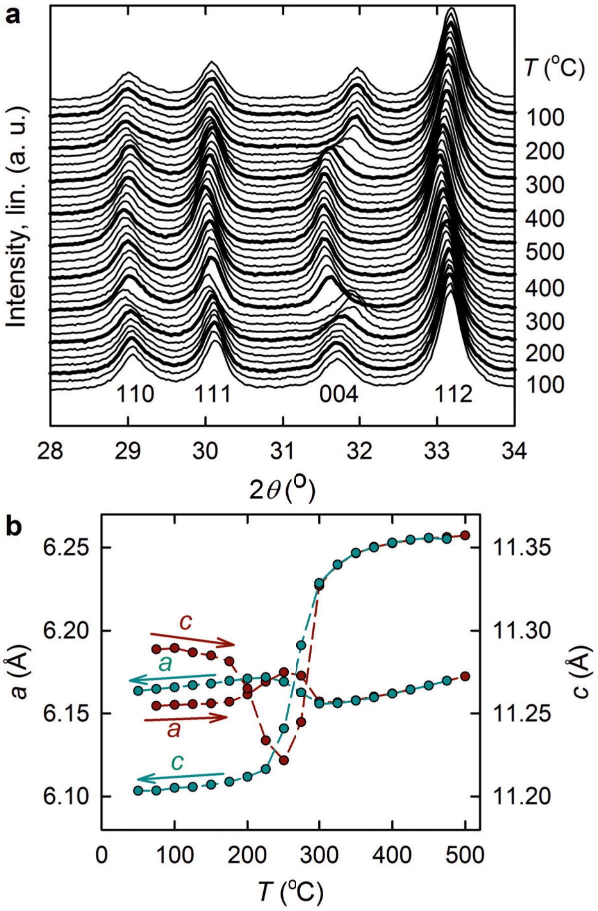

Supplementary Figure 2: a) High temperature X-ray diffraction (HTXRD) of nanocrystalline $YMnO_3$ upon one heating and cooling cycle in O_2 between 50 and 500 ^{o}C plotted on linear scale, and **b)** lattice parameters, *a* and *c* extracted from the measurements of two heating and cooling cycles, showing that interstitial oxygen is incorporated into the lattice, causing anisotropic chemical expansion. No evidence of secondary phases could be seen for any of the temperatures in the 2θ range between 26 and 72^{o}.

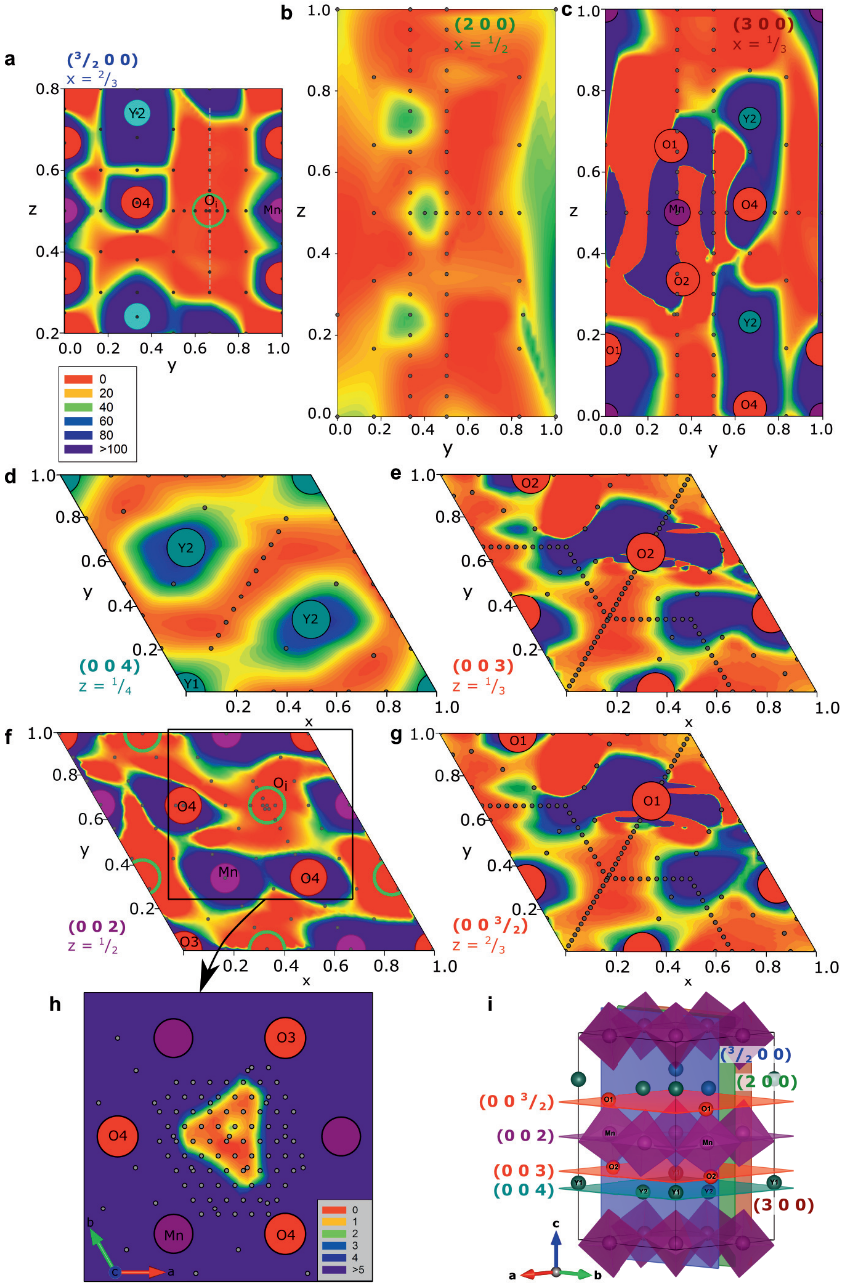

Supplementary Figure 3: a-h) Potential energy surface (PES) mapping of several planes in a 2x2x1 supercell (excerpt of only the unit cell) of $YMnO_3$. **i**) Unit cell showing the crystallographic planes that were mapped.

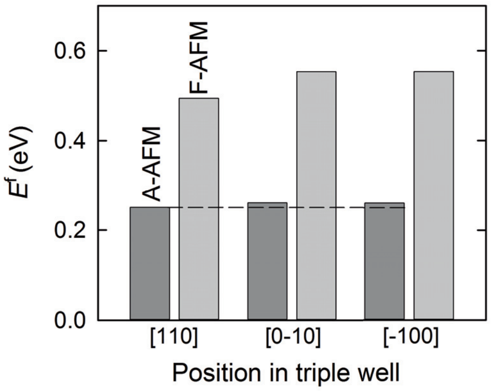

Supplementary Figure 4: Energetic asymmetry of the O_i triple well. Defect formation energies of O_i in the three triple well positions calculated with the F-AFM and A-AFM order, comparing contributions from magnetism and structural trimerization.

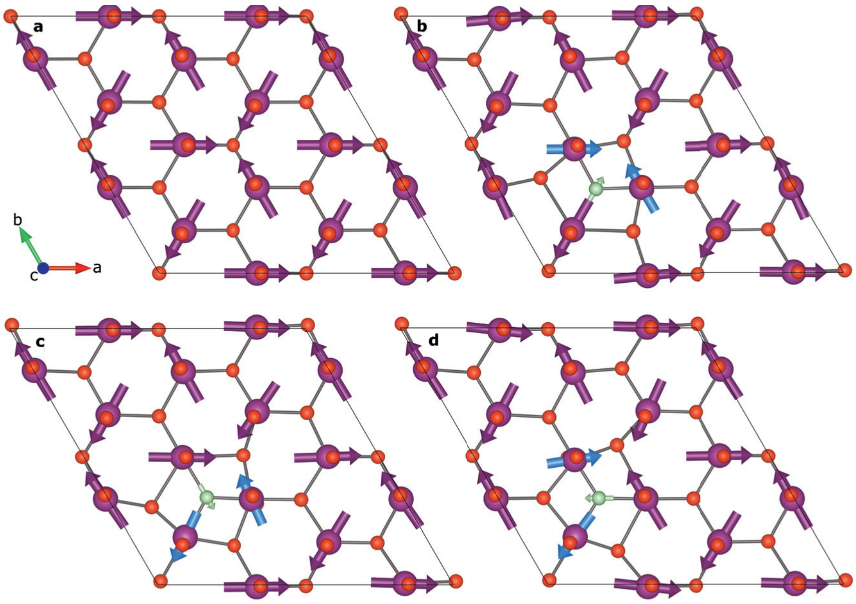

Supplementary Figure 5: Effect of O_i on true non-collinear magnetic order. Static calculations with Hubbard U = 5 eV and the true non-collinear order of structurally relaxed cells with O_i. **a)** stoichiometric cell, and **b-d)** defective cells with O_i relaxed in one of the three triple well positions.

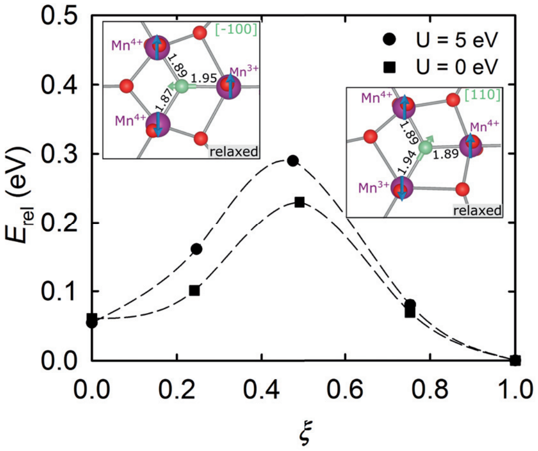

Supplementary Figure 6: Polaron hopping barrier. Energy barrier as a function of the relative reaction coordinate for moving O_i and the charge compensating electron holes from one site in the triple well to another. The blue arrows show the collinear frustrated antiferromagnetic (F-AFM) order used in the calculations. The apparent energy difference in the start and end configuration is caused by the energy asymmetry of the triple well.

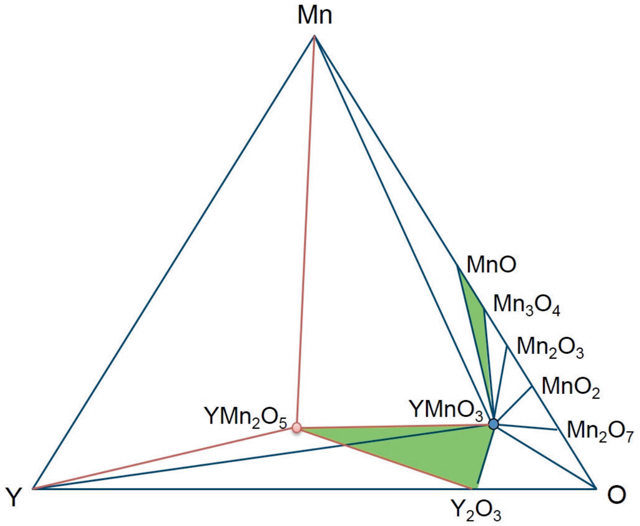

Supplementary Figure 7: Phase equilibrium triangle showing the phase equilibria which determine the phase stability of h-$YMnO_3$. The green areas show the phase equilibria which were used to define the stability region of $YMnO_3$.

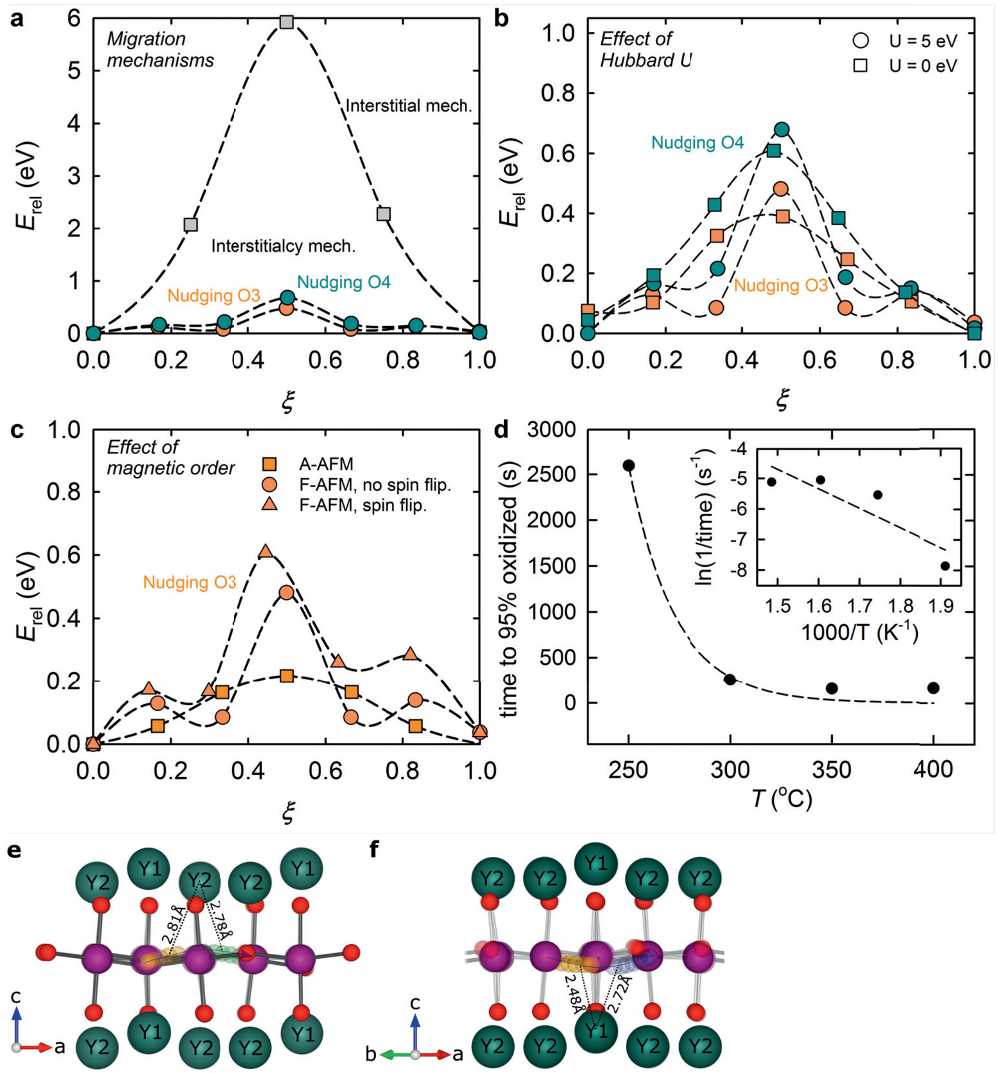

Supplementary Figure 8: Migration barriers for O_i a) Energy barriers for migration by interstitialcy mechanism (nudging O3 or O4) compared to an interstitial mechanism as a function of relative reaction coordinate, *ξ*. **b)** Calculated energy barriers for migration of interstitial oxygen interstitialcy mechanism comparing the effect of on-site Coulomb repulsion by Hubbard $U = 0$ eV and $U = 5$ eV. **c)** Calculated energy barriers for interstitialcy migration through O3 comparing the effect of the magnetic orders frustrated antiferromagnetic (F-AFM) with or without spin flipping and A-type antiferromagnetic (A-AFM). **d)** Time to 95% oxidation of nanoparticles as a function of temperature from thermogravimetric isotherms. The inset shows the data in an Arrhenius-type plot used to extract energy barrier for diffusion. **e)** Bonds between Y2 and the moving oxygens in the middle of path 2. **f)** Bonds between Y1 and the moving oxygens in the middle of path 1.

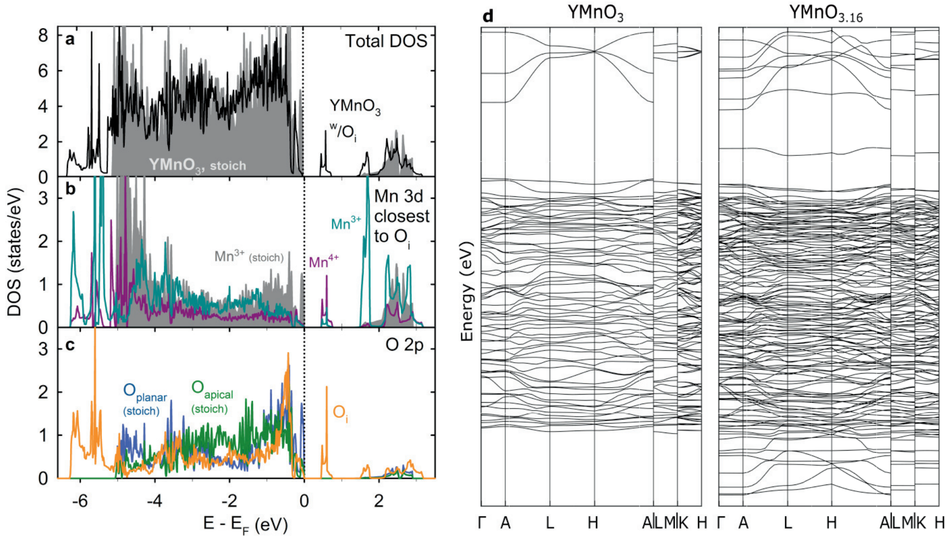

Supplementary Figure 9: Electronic structure. a, Total electronic density of states (DOS) per formula unit for perfect YMnO$_3$ and a 30 atom cell of YMnO$_3$ with one O$_i$ (YMnO$_{3.16}$). **b**, Atomic DOS showing the d states for Mn^{3+} and Mn^{4+} coordinating O$_i$ compared to Mn^{3+} d states in a stoichiometric cell. **c**, Atomic DOS showing the p states of O$_i$ compared to p states for apical and planar oxygens in a stoichiometric cell. **d**, Electronic band structure of a stoichiometric 30 atom unit cell compared to a 30 atom unit cell with one O$_i$.

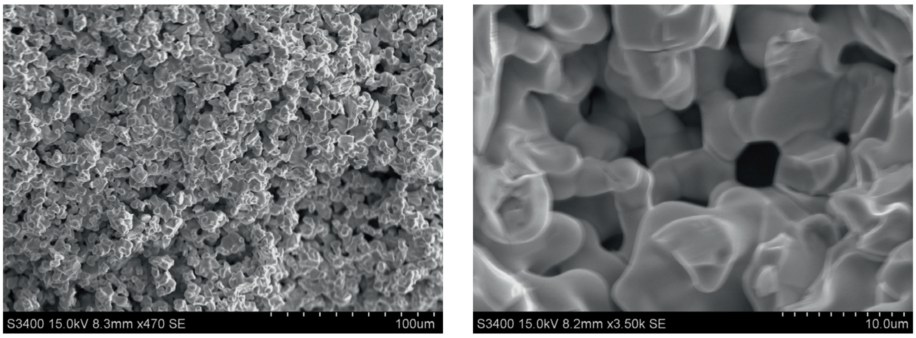

Supplementary Figure 10: SEM images of the fracture surface of a porous polycrystalline YMnO$_3$ bar.

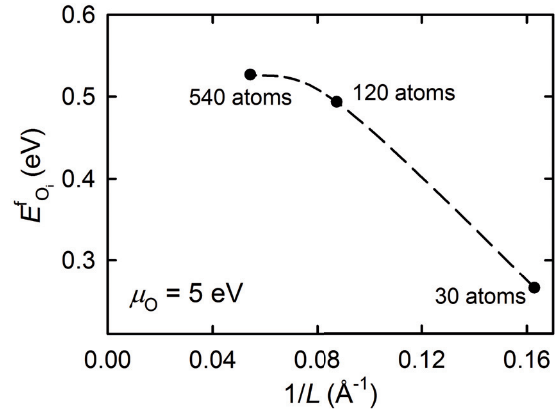

Supplementary Figure 11: Effect of supercell size on defect formation energy. Defect formation energy as a function of defect-defect distance illustrating the effect of supercell size.

Supplementary Note 1: Mapping the energy landscape of interstitial oxygen

Potential energy surfaces (PES) were determined by mapping the energy landscape of the O_i position in several lattice planes by static DFT calculations. Seven different lattice planes were mapped, as shown in Supplementary Figure 3 a-g along with a unit cell with the corresponding lattice planes, panel i. The most stable positions of O_i was found to be between three Mn in the Mn-O planes at $z = 0$ and $^1/_2$, which, due to symmetry, results in 6 equivalent possible sites for O_i in the $P6_3cm$ unit cell, ($^1/_3$, $^1/_3$, 0), ($^2/_3$, 0, 0), (0, $^2/_3$, 0), ($^2/_3$, $^2/_3$, $^1/_2$), ($^1/_3$, 0, $^1/_2$) and (0, $^1/_3$, $^1/_2$), as illustrated by green circles in the (002) plane in the figure. An excerpt around the most stable position in the (2 0 0) plane was mapped more thoroughly, panel h, and revealed an asymmetric triangular energy landscape. This shows how forces between the O_i and the three Mn^{3+} eventually leads to a triple well which O_i can relax into and oxidize two of the Mn^{3+} to Mn^{4+}.

The six equivalent positions for O_i do not correspond to high-symmetry positions in the $P6_3cm$ space group and the presence of a single O_i, without structural relaxation, reduces the symmetry to monoclinic Cm.[1] A fully oxidized structure $YMnO_{3.33}$ with one O_i in each Mn-O layer lowers the symmetry to Cc or $Cmc2_1$[1] depending on which sites the two O_i occupy.

Supplementary Note 2: Energetic asymmetry of the O_i triple well

Depending on which two Mn^{3+} are oxidized to Mn^{4+} by O_i, the O_i can relax into one of three positions. The origin of the energy asymmetry of this triple well is caused by the characteristic trimerization pattern of the structure and magnetic order. As seen in Supplementary Figure 4, the O_i favours to relax in the [110] direction, which is towards a trimerization center, an O3 atom, towards which the surrounding trigonal bipyramids are all tilting towards or away from. This position results in an Y1-O_i bond length which is shorter than the corresponding Y2-O_i bond length in the two other positions. The magnetic order follows the trimerization pattern and emphasizes the energy asymmetry. In most calculations, the non-collinear magnetic structure[2] was approximated by a synthetic collinear frustrated anti-ferromagnetic (F-AFM) ordering, and this simplification gives an additional unwanted contribution to the asymmetry. The F-AFM order is believed to create stronger electron repulsions than the true non-collinear spin and creates an additional asymmetry in the structure. If the F-AFM order is not set in a way which preserves the structural symmetry of the triple well, additional local minima can trap O_i and the structure distorts unphysically. The F-AFM order should be set so the most favoured triple well position is in the direction of two Mn with equal spin. Setting an A-type antiferromagnetic (A-AFM) order also results in the same triple well asymmetry, but not as pronounced. It is believed to give even smaller electronic repulsion than the true non-collinear magnetic order. Attempts of calculating the defect formation energies in the triple well with non-collinear magnetic order failed due to VASP not being able to reproduce the true non-collinear magnetic ground state. In conclusion, the most favoured O_i triple well position causes minimal and more symmetric distortion of the surrounding bipyramids.

Supplementary Note 3: Polaron hopping barrier

Nudged elastic band calculations between the different sites in the triple well show that the energy barrier for displacing the O_i between different Mn pairs is 0.29 eV, as shown in Supplementary Figure 6. The barrier is found to be mainly determined by electron transfer between Mn^{3+}/Mn^{4+}, including spin flipping because of the synthetic collinear frustrated antiferromagnetic (F-AFM) order, and can thus be seen as the barrier for polaron hopping. The high energy barrier suggests that the electron holes will be localized in the whole temperature stability range of O_i in the $P6_3cm$ structure. When the on-site Coulomb potential is reduced by not setting a Hubbard U ($U = 0$ eV), the energy barrier is reduced by 0.06 eV.

Supplementary Note 4: Migration of interstial oxygen

The interstitial oxygen can migrate through the structure by an interstitialcy mechanism nudging a lattice oxygen O3, with an energy barrier of 0.48 eV as shown in Supplementary Figure 8 a and b. The O_i can also migrate through a similar mechanism nudging a lattice oxygen O4 instead, but this gives a higher migration barrier of 0.62 eV. We expect all the calculated barriers to be slightly higher than in reality due to the synthetic collinear magnetic (F-AFM) order which can give larger repulsion between the electrons than in the paramagnetic state. Diffusion through this interstitialcy mechanism is highly favoured over a pure interstitial mechanism where the O_i migrates alone out of the Mn-O plane, shown in Supplementary Figure 8 a. The structural effects of the O_i are well screened, mainly due to the high structural flexibility of the trigonal bipyramids. Since they are not rigid polyhedra, the introduction of an O_i is structurally screened by changing the bond angles of the polyhedra, rather than rotating the polyhedra. As the O_i passes by the Mn atoms in the migration path, the tilting of the nearest trigonal bipyramids is reduced.

The migration path of O_i was analyzed using the nudged elastic band method as implemented in VASP with five intermediate images[3]. A Hubbard $U = 5$ eV was used because it described the nature of the localized electron holes better and thereby also capturing the polaron hopping as one of the main contributions to the energy barrier. Test calculations with $U = 0$ eV gave on average 0.07 eV lower energy barriers, as seen in Supplementary Figure 8 b, but the calculations suffered from slower convergence due to charge sloshing and often less physical results.

Our calculations show that a frustrated antiferromagnetic (F-AFM) order gives energy barriers which are in accordance with experimental energy barriers, both for migration of O_i and polaron hopping. Setting an A-type antiferromagnetic (AFM) order gave on average 0.27 eV lower energy barrier. This magnetic order gives equal spin direction for all the Mn within the same layer and a much smaller bandgap, which is believed to be the cause of the lower barrier. The F-AFM order was set in such a way that spin flipping on Mn ions did not occur during migration of O_i, in order to isolate the effect of only migration. Test calculations where spin flipping occurred during migration gave 0.14 eV higher energy barrier, Supplementary Figure 8 c.

The migration energy barrier was also obtained from the thermogravimetric isothermal data in O_2, by plotting the time to 95% oxidation as a function of temperature shown in Supplementary Figure 8 d. Plotting t^{-1} as a function of the inverse temperature gave a linear Arrhenius-type behaviour following ${}^{1}\!/_{t} = Ae^{-E_\mathrm{a}/kT}$. The slope of the line gave an energy barrier of $E_\mathrm{a} = 0.55 \pm 0.21$ eV, which is comparable to the calculated energy barrier of 0.48 eV.

Supplementary Methods

Thermodynamic stability region for h-$YMnO_3$

The stability of a compound with respect to its related binary or ternary compounds is dependent on the chemical potential of oxygen in the surroundings. For instance, at reducing conditions, $YMnO_3$ can decompose to MnO (s), Y_2O_3 (s) and O_2 (g), but the particular chemical potential of oxygen when this occurs, is not so easy to calculate directly, as the chemical potential of a gaseous species is not well defined at 0 K. Instead we calculate the ground state energies of all the solid compounds in the related chemical reaction, and extract μ_O as the only unknown. All the phase equilibria which determine the stability region of h-$YMnO_3$ are presented in Supplementary Figure 7. Each area of the triangle corresponds to values of the chemical potentials for all three elements, μ_Y, μ_{Mn} and μ_O. Calculations of μ_O from all the areas provide the range in which μ_O can vary. The oxidizing and reducing limits were found to be determined by the chemical reactions given below. Chemical equilibria with elemental Y and Mn are omitted.

Reducing conditions:

$$3\,\mathrm{MnO} + \frac{1}{2}\mathrm{O_2(g)} \rightleftarrows \mathrm{Mn_3O_4} \qquad \mu_O = \mu_{Mn_3O_4} - 3\mu_{MnO} = -7.1\ \mathrm{eV}$$

Oxidizing conditions:

$$4\,\mathrm{YMnO_3} + \frac{1}{2}\mathrm{O_2(g)} \rightleftarrows \mathrm{Y_2O_3} + 2\,\mathrm{YMn_2O_5} \qquad \mu_O = \mu_{Y_2O_3} + 2\mu_{YMn_2O_5} - 4\mu_{YMnO_3} = -1.9\ \mathrm{eV}$$

Materials synthesis

$YMnO_3$ powder was prepared by solid state reaction between Y_2O_3 (Alfa Aesar >99.9%) and MnO_2 (Sigma-Aldrich, >99%). The powders were dried overnight at 500 °C before weighing and mixed in ethanol in a mortar. Uniaxially pressed pellets were fired twice for 24 hours at 1300 °C in air with intermediate grinding and heating and cooling rates of 200 °C h^{-1}. Phase purity was confirmed by XRD between each heating step. Powder for sintering porous polycrystalline bars for electrical conductivity and Seebeck measurements were prepared by mixing phase pure $YMnO_3$ powder with 20 wt% carbon black (Merck) followed by ball milling for 4 hours in ethanol with yttrium stabilized zirconia milling balls. Green bodies were isostatically cold pressed at 200 MPa in a Painan Autoclave Engineers CIP and 1 wt% binder of cellulose acetate (Aldrich) dissolved in acetone was added to improve the green body strength. The porous polycrystalline bars were sintered for 2 hours in air at 1500 °C after a binder burn-off step at 435 °C and polished to dimensions of 15 x 5 x 5 mm. The density of the bar was measured by the Archimedes method[4] to be 43 %. A representative fracture surface of a polycrystalline porous bar is shown in Supplementary Figure 10. Scanning electron microscopy of the fracture surface was done with a Hitachi S-3400N.

Materials characterization

Four-point electrical conductivity measurements in O_2 and N_2 (Yara Praxair, 5.0) atmospheres were performed with a home-built instrument described elsewhere[5]. Platinum paste was applied to the interface between the platinum electrode wires and the sample and heated *in situ* to 1000 °C to ensure good electrical contact. The conductivity σ was calculated from the equation $\sigma = {Id}/{AV}$ where I is the current, d is the distance between the electrodes, A is the sample cross section area and V is the measured voltage drop between the electrodes. *In situ* heating and cooling was done with 1 °C min^{-1}. Thermogravimetric measurements were done on $YMnO_3$ nanoparticles[6] with d_{XRD} = 49±4 nm used for electrical conductivity measurements with a Netzsch STA 449C Jupiter in flowing N_2 and O_2 (Yara Praxair, 5.0). For both the conductivity and thermogravimetric measurements, the sealed system for conductivity measurements could not be evacuated between the changes of atmosphere. Thus, the exact pO_2 in N_2 atmosphere is not known exactly, but estimated to be in the range of 10^{-4}-10^{-5}. Seebeck-coefficients (Q) were measured at 400, 350, 300, 250 and 200 ºC in O_2 (Yara Praxair, 5.0) using a ProboStat™ setup (NorECs AS) on a vertically aligned polycrystalline porous bar (radius 3 mm, length 12 mm) in tubular furnace. Two S-type thermocouples (20-25 ºC) were used to measure the temperature gradient and the voltage across the sample was measured with Pt-electrodes.

Impedance spectroscopy measurements (Alpha-A analyzer combined with Novotherm furnace, Novocontrol Technologies) were conducted on disc shaped samples with sputtered gold electrodes. Samples were subjected to two temperature cycles from 30-350 ºC with a heating rate of 2 ºC min^{-1}. Frequency sweeps covering a range from 1 Hz and 1 MHz were conducted continuously during the temperature cycles. Prior to measurement, the samples were annealed in flowing oxygen resp. nitrogen for 24 hours at 350 ºC.

For the purpose of confirming oxygen incorporation into the lattice in the relevant temperature interval we have instead performed high temperature X-ray diffraction with in-situ change of atmosphere on $YMnO_3$ nanoparticles with an average size of 25 nm. The measurements were performed in-house with a Bruker D8 Advance diffractometer with Cu Kα radiation and 20 second collection time per degree from 26 to 72^o 2θ, mapping the evolution of the 004 and 112 Bragg reflections. The lattice parameters a and c upon heating and cooling in O_2 atmosphere were extracted by fitting the d-spacing of the 004 and 112 Bragg reflections to Lorentzian peak shapes.

Computational details

The effects of interstitial oxygen were modeled using 2x2x1 unit cells of 121 atoms and 3x3x2 unit cells of 541 atoms with the number of k-points reduced accordingly. A 2x2x1 supercell was found to be sufficiently large as it provided a small defect-defect interactions compared to the computational cost, as seen in Supplementary Figure 11 where the defect formation energy for neutral cells is calculated for three cell sizes. No significant change in ferroelectric polarization was found for increasing the cell size from 121 to 541 atoms.

Charge neutral cells were used for the simulations due to the relatively high concentration of O_i in a 120 atom cell, and because, unlike conventional semiconductors, high defect concentrations are observed experimentally. Simulations with cells of charge -1 and -2, where electrons were artificially added to avoid charge compensating oxidation of Mn^{3+} to Mn^{4+}, gave the same results as neutral cells with respect to the position of O_i.

Supplementary References

1. Stokes H. T. & Hatch D. M. FINDSYM: program for identifying the space-group symmetry of a crystal. *J. Appl. Cryst.* **38**, 237-238 (2005). 10.1107/S0021889804031528

2. Howard C. J., Campbell B. J., Stokes H. T., Carpenter M. A. & Thomson R. I. Crystal and magnetic structures of hexagonal $YMnO_3$. *Acta Crystallogr. B* **69**, 534-540 (2013). 10.1107/S205251921302993X

3. Henkelman G., Uberuaga B. P. & Jonsson H. A Climbing image nudged elastic band method for finding saddle points and minimum energy paths. *J. Chem. Phys.* **113**, 9901-9904 (2000). 10.1063/1.1329672

4. ISO 5017:1998 *Dense shaped refractory products - Determination of bulk density, apparent porosity and true porosity*.

5. Selbach S. M., Tybell T., Einarsrud M.-A. & Grande T. High-temperature semiconducting cubic phase of $BiFe_{0.7}Mn_{0.3}O_{3+\delta}$. *Phys. Rev. B* **79**, 214113 (2009). 10.1103/PhysRevB.79.214113

6. Bergum K., Okamoto, H, Fjellvåg H., Grande, T, Einarsrud M.-A. & Selbach, S. M. Synthesis, structure and magnetic properties of nanocrystalline $YMnO_3$. *Dalton Trans.* **40**, 7583-7589 (2011). 10.1039/c1dt10536a

Unconventional order-disorder phase transition in improper ferroelectric hexagonal manganites

Sandra H. Skjærvø,[1] Quintin Meier,[2] Emil S. Bozin,[3] Simon J. L. Billinge,[3, 4]
Mikhail Feygenson,[5, 6] Nicola A. Spaldin,[2] and Sverre M. Selbach[1]
[1]*NTNU Norwegian University of Science and Technology,*
Department of Materials Science and Engineering, NO-7491 Trondheim, Norway
[2]*ETH, Materials Theory, Wolfgang Pauli Str. 27, CH-8093 Zürich, Switzerland*
[3]*Brookhaven National Laboratory, Condensed Matter Physics and Materials Science Department, Upton, NY 11973, USA*
[4]*Columbia University, Department of Applied Physics and Applied Mathematics, New York, NY 10027, USA*
[5]*Forschungszentrum Jülich, JCNS, D-52425 Jülich, Germany*
[6]*Chemical and Engineering Materials Division, Oak Ridge National Laboratory, Oak Ridge, TN 37831, USA*

The improper ferroelectricity in $YMnO_3$ and related hexagonal manganites is known to cause topologically protected ferroelectric domains that give rise to rich and diverse physical phenomena. The local structure and structural coherence across the transition, however, are not well understood. Here we reveal the evolution of the local structure in multiferroic $YMnO_3$ using a combination of neutron total scattering and first-principles calculations. We find that, at room temperature, the local and average structures are consistent with the established ferroelectric $P6_3cm$ structure. On heating, both local and average structural analyses show striking anomalies consistent with increasing fluctuations of the order parameter angle from ∼800 K up to the Curie temperature. The result is an unusual local symmetry lowering on heating which was previously misinterpreted as a second structural phase transition. This local symmetry breaking persists into the high-temperature paraelectric phase, constituting an unconventional type of order-disorder transition.

The hexagonal manganites, h-RMnO$_3$ (R= Dy-Lu, In, Y or Sc) are multiferroics in which the spontaneous ferroelectric polarization emerges from coupling to a rotational distortion that drives a polar shift of the R cations relative to the Mn-O sub-lattice. The improper nature of the ferroelectricity results in unusual ferroelectric domain structures in which topological protection of the domain wall intersections causes fundamentally and technologically interesting physical properties ranging from early universe analogues [1–3] to nanoscale conducting channels [4–11]. In spite of multiple studies, the evolution of the polarization with temperature has not been explained on a microscopic level. In particular, studies based on powder neutron [12, 13] and X-ray [13–18] diffraction have been unable to fit the structural data within standard models. This has led to a range of reported T_C values and also proposals of two distinct structural phase transitions [12–16], although it is now accepted that there is a single structural transition with the measurable polarization emerging at lower temperatures [19–23].

The high-temperature paraelectric aristotype structure of h-RMnO$_3$ displays $P6_3/mmc$ symmetry. This structure has corner-sharing MnO_5 trigonal bipyramids separated by planes of Y^{3+} coordinated by eight oxygens (Fig. 1a). At the symmetry-lowering phase transition at ∼1250 K, the unit cell triples as a non-centrosymmetric, but zero-polarization zone-boundary K_3 mode condenses [24]. The distortions at the transition are described by a two-dimensional order parameter (Q,Φ) corresponding to the amplitude, Q, and the angle, Φ, of the K_3 mode [20]. Depending on the order parameter angle, corresponding to the tilting direction of the bipyramids and out-of-plane displacement pattern of the Y cations, the symmetry of the system will be lowered to one of three hettotype space groups. If the tilt angle corresponds to $\Phi = n\frac{\pi}{3}$, where $n = 0, 1, .., 5$, the system belongs to the polar hettotype with $P6_3cm$ symmetry (P, Fig. 1c). If $\Phi = \frac{\pi}{6}(2n + 1)$, the system belongs to the antipolar hettotype with $P\bar{3}c1$ symmetry (AP, Fig. 1e), while all other angles lead to the intermediate $P3c1$ symmetry (IM, Fig. 1d). The ground state of the system is the polar $P6_3cm$ (P), in which a polarization of around ∼6 μC cm^{-2} at room temperature is induced through coupling of the K_3 mode to a polar Γ_2^- mode which causes a shift of the Y atoms towards the Mn-O layers. The resulting Z_6 symmetry of the configuration space causes the unusual six-fold ferroelectric domain patterns characteristic of the h-RMnO$_3$ [25]. The energy landscape, calculated by following methods described by Artyukhin *et al.* [20], resembles a Mexican hat with six minima in its brim (Fig. 1b).

This established model of the Mexican hat Landau free energy (Fig. 1b) describes the average symmetry evolution of the system reduced to the degrees of freedom given by the order parameter, but does not address the underlying microscopics. In particular, whether the transition mechanism is closer to the *displacive* (order parameter goes to zero both locally and on average at T_C) or *order-disorder* (local order parameter conserved) limit is not established.

Here we present a description of the local atomic structure of h-YMnO$_3$ from ambient temperature to 1373 K, above the ferroelectric T_C of ∼1250 K. We combine pair distribution function (PDF) analysis of neutron total scattering data with conventional Rietveld refine-

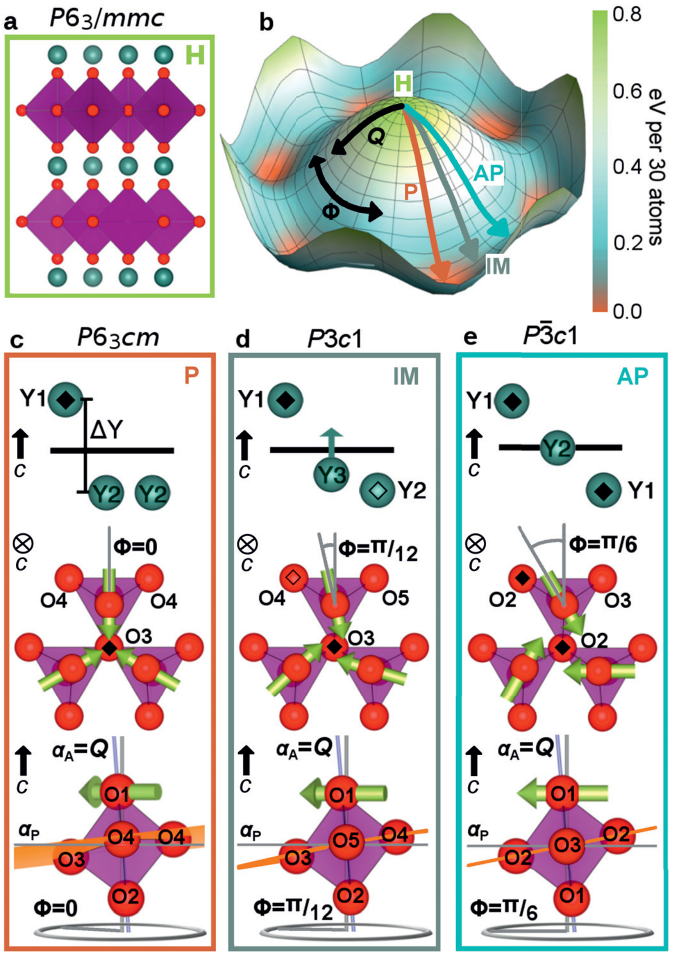

FIG. 1. **Structures of RMnO$_3$ phases**. **a**, The high symmetric $P6_3/mmc$ (H) aristotype structure with purple Mn-O$_5$ bipyramids and blue-green R cations. **b**, The Landau free energy of the hexagonal manganites, resembling a Mexican hat, with the aristotype structure (H) at the top of the peak. In the brim of the hat the polar $P6_3cm$ (P), antipolar $P\bar{3}c1$ (AP) and intermediate $P3c1$ (IM) hettotypes occur at the minima, maxima and intermediate regions, respectively. **c**-**e**, Y corrugations (top), bipyramidal tilting directions (middle), and the definition of apical and planar tilting angles (bottom) in the three hettotypes; Wyckoff sites for the three hettotypes are labeled; Symbols ◇ and ♦ denote atoms aligned in the c direction. For the polar $P6_3cm$, ΔY denotes the distance in c direction between Y1 and Y2. The angle between O1 and O2 and the c axis defines the apical tilt, α_{A}, and is a direct measure of the order parameter amplitude Q. The plane through the three in-plane oxygens (one O3 and two O4) relative to the ab plane define the planar tilt angle, α_{P}, and is related to both the order parameter amplitude Q and angle Φ.

ment to probe structural coherence, and to distinguish short range from average long-range order. Our main findings are that the average and local structure evolve consistently up to ∼800 K, with smoothly decreasing distortions, while between ∼800 K and T_{C}, the average and local structures diverge progressively, leading to a local symmetry lowering upon heating. Above T_{C} the *average* structure is paraelectric $P6_3/mmc$, whereas the local structure cannot be described by a single space group. Our findings are consistent with a model in which fluctuations of the order parameter angle increase on heating until, from ∼800 K, much of the system occupies intermediate-angle low-symmetry states in the brim of the Mexican hat. As T_{C} is approached, the extent of fluctuations increases, leading to an unconventional type of order-disorder transition. These two key discoveries – the unconventional order-disorder transition and symmetry lowering fluctuation region below T_C – reconcile the previous literature inconsistencies.

Extraction of the order parameter

The displacement pattern in h-RMnO$_3$ from the paraelectric structure $P6_3/mmc$ (H) to its low-symmetry structure $P6_3cm$ (P) is complex and involves all the atoms, as is shown in Fig. 1. In this work we relate the order parameter to three sets of atomic displacements. The first is the apical tilt angle of the apical oxygens (O1, O2) relative to the c axis, α_A, the second is the out-of-plane movement/corrugation of the yttrium ions $\Delta Y = (z_{Y1} - z_{Y2})$, and the third is the planar tilt angle, α_P, defined as the angle of the plane through three planar oxygens (O3, O4) relative to the ab plane. Note that the latter two are strictly defined only for $P6_3cm$ symmetry (Fig. 1c) since a change in the order parameter angle Φ (Fig. 1d-e) breaks the symmetry of the Y2 and O4 sites and the corresponding planar tilt angles, such that α_P and ΔY can no longer be calculated from the same Wyckoff sites.

Average structure

We performed spallation neutron diffraction of bulk samples to investigate the structure. Our reciprocal space diffraction data show that the (102) and (202) superreflections of the $P6_3cm$ structure disappear above 1223 K, corresponding to the ferroelectric Curie temperature T_C (Supplementary Fig. 1), in line with previous reports [12, 15, 18, 23]. Rietveld refinements, using the established average low-temperature structure space group model $P6_3cm$ over the whole temperature range comply with previous findings [12]. We inspect the Rietveld refinements using refined lattice parameters a, c, the structural observables ΔY, α_P, α_A, atomic displacement factors U and the fit residual r_w (Fig. 2a-d).

In the low-temperature range between room temperature and ~800 K, the lattice parameter a increases linearly, while c decreases linearly. A linear contraction of c and expansion in the ab-plane is expected for displacive untilting of the Mn-O$_5$ polyhedra and Y ions approaching their high-symmetry positions. This is in line with the linear decrease of all manifestations of the order parameter in Fig. 2b. Atomic displacement factors U increase linearly, as expected for uncorrelated atomic vibrations. The fit residuals decrease or stay flat for all space groups, as expected since fitting improves when the spectrum broadens.

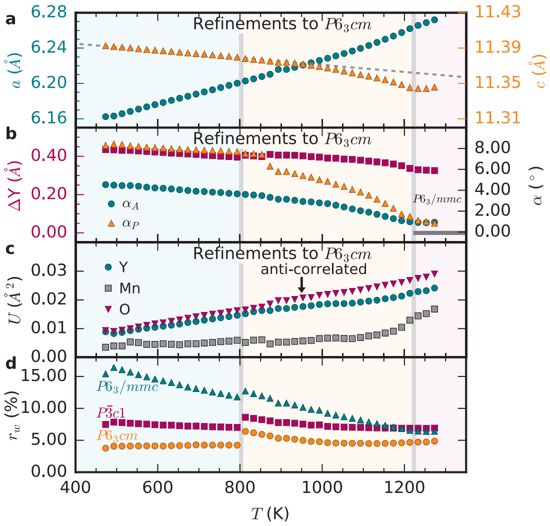

FIG. 2. **Average structure refinements of YMnO$_3$.** **a**, Lattice parameters a and c, **b**, Y corrugation, ΔY, apical tilt angle, α_A, and planar tilt angle, α_P, and **c**, isotropic atomic displacement parameters, U, all obtained from fitting reciprocal space $I(Q)$ to the polar ground state hettotype $P6_3cm$. **d**, Fitting errors r_w of the high-symmetric aristotype $P6_3/mmc$, polar hettotype $P6_3cm$ (P) and antipolar hettotype $P\bar{3}c1$ (AP) to $I(Q)$. The grey vertical line at 1223 K shows the Curie temperature T_C above which aristotype symmetry can be inferred from the Bragg reflections. Expectation value for ΔY, α_A and α_P in the $P6_3/mmc$ aristotype are marked by a horizontal grey line above T_C in panel **c**. The grey vertical line at 800 K separate low- and intermediate region region, and the grey vertical line at 1223 K indicates T_C

In the intermediate temperature range between ~800K and T_C, the refinements become less stable, and we observe an anomalous non-linear evolution of the c parameter. Refinements to a $P6_3cm$ model show that while α_A and α_P go to zero, the value of ΔY decreases only subtly and retains a finite value across T_C (Fig. 2b). All three parameters are direct measures of the order parameter, as described in relation to Fig. 1, and as such they are expected to be correlated. This anomalous behaviour is also reflected in the refined atomic displacement parameters U of Y and O becoming anti-correlated, Fig. 2c. The Mn U increases rapidly with heating from 100 K below T_C~1250K. Such anomalously behaving ADPs are signatures of structural disorder impeding refinements to a space group model which implicitly presumes long range order. Including additional degrees of freedom for the U only marginally improved the fit. The anomalous behaviour is also reflected in the r_w, with an obvious jump at 800 K.

Next we inspect the behaviour throughout and above the phase transition. Above T_C, c exhibits close-to-zero thermal expansion over a ~100 K interval before it starts increasing. This plateau is inconsistent with a purely displacive phase transition, and indicates structural disorder. Similar plateaus are observed for α_A, α_P and ΔY (panel b). Studies of octahedral rotations in perovskites have also shown that a non-vanishing order parameter across a phase transition can be a sign of structural disorder [26]. This was also observed by Gibbs et al. [12] up to T_C. However, their data above T_C were refined with a $P6_3/mmc$ model where ΔY is fixed to zero, effectively enforcing a discontinuity at T_C. Atomic displacement factors U of our own refinements to $P6_3/mmc$ can be found in Supplementary Fig. 2). Refinements above T_C to the ground state polar $P6_3cm$ hettotype gave ∼2% lower r_w than for the high-symmetric $P6_3/mmc$ aristotype (H) and the antipolar hettotype $P\bar{3}c1$ (Fig. 2d). The difference in r_w at T_C indicates that even though the material becomes paraelectric, the data is better fitted by the ferroelectric space group. However, as $P6_3cm$ has 11 structural degrees of freedom, while $P6_3/mmc$ has only 3, this could be due to over-parameterization at and above T_C.

Vanishing polyhedral tilting α_A, α_P and a persistent ΔY could indicate a scenario in which the structure has off-centered Y ions combined with untilted Mn-O_5 polyhedra. To test this possibility of sublattice disorder, we performed density functional theory calculations of the energy landscape for the separate ionic contributions to the K_3 distortion. We found that it is energetically unfavourable for the Y ions to displace from their centrosymmetric positions if the planar oxygens (O_P) are fixed at their high-symmetry positions, that is if MnO_5 tilting is not allowed (Supplementary Fig. 3). This strong coupling between MnO_5 tilt and ΔY indicates that sublattice disorder is unlikely and suggests that possible disorder involves both sublattices. This strong coupling between the sublattices lies in the fundamental importance of the Y-O_P interaction in this structure [14].

The temperature for onset of the anomalies coincides well with the reported Ginzburg temperature for $YMnO_3$ [3]. Order-disorder transitions are known to have a fluctuation-dominated temperature regime extending far below T_C, enclosed by the Ginzburg temperature. In this temperature range, renormalized critical exponents for a 3D XY system are valid.

The presented data show that the average structure has polar $P6_3cm$ symmetry below T_C, but anomalous ADPs and non-selfconsistent lattice parameters and order parameter components signify disorder not captured by a single space group model. Refinements to reciprocal space data, while indicative of the presence of disorder, do not provide sufficient information about the character of the local structure above T_C. The constant lattice parameter c from T_C to ∼100 K above, non-vanishing Y corrugation (ΔY) across T_C and r_w for different space groups all show the need of a local structure sensitive method to probe the ferroelectric phase transition of h-$R$$MnO_3$.

Local structure investigation by PDF

In order to investigate the local structure, we performed pair-distribution function (PDF) analysis on the neutron diffraction data. The obtained temperature-dependent pair distribution functions, $G(r)$ shown in Fig. 3a display significant qualitative changes upon heating (detailed excerpt in Supplementary Fig. 4). To quantify the changes in the local structure we performed structural refinements in a range of $r = 1.5 - 12$ Å, which corresponds to one unit cell along the c axis and two in the ab plane. At low temperatures, the PDF measured at 298 K fits well with the polar ground state $P6_3cm$ (P) model, while r_w with the antipolar (AP) $P\bar{3}c1$ structure is significantly larger, Fig. 3b. Hence the $P6_3cm$ model fits consistently to the average and local structure at room temperature, as expected. When compared to the dataset collected at 1273 K (above T_C), we also find that the $P6_3cm$ provides a good fit, but importantly, $P\bar{3}c1$ space group provides an equally good fit. The decreasing difference of fitting residual χ^2 with increasing temperature between the two hettotypes would be consistent with the structure changing towards aristotype symmetry. However, in contrast to this, the fit to the aristotype $P6_3/mmc$ (H) model, as shown in Fig. 3d, is very poor, as neither the positions nor amplitudes of several $G(r)$ peaks could be reproduced. This poor fit to the aristotype model above T_C in combination with the better fit of the hettotypes indicates that the order parameter is locally *conserved* and thus that the phase transition is strongly order-disorder in character. This is in agreement with the smoothly changing PDFs across T_C (see Supplementary Fig. 5).

To further investigate the local structure further we extract structural parameters from refining the polar $P6_3cm$ model to the PDF data, as shown in Fig. 4. In the low-temperature region, lattice parameters obtained from PDF, Fig. 4a, follow the same thermal evolution as for the reciprocal space data in Fig. 2a. The different measures for the order parameter ΔY, α_P and α_A all decrease linearly (Fig. 4b), similarly to the same parameters from average structure refinements, Fig. 2b. Also the atomic displacement factors (U) are well-behaved (Fig. 4c) in this region. Thus, we conclude that within this temperature region, the amplitude Q of the local tilt mode is reduced.

Between 800 K and T_C, the lattice parameters follow the same trend as in the average structure. For the order parameter we find that α_A decreases steadily with increasing temperature. The refined values for ΔY and α_P become numerically unstable, indicating that the description of local structure by the $P6_3cm$ model is inadequate. This is also reflected in the anomalous behaviour of the local atomic displacement factors U, particularly Y2 and Mn exhibit anomalous upturns at elevated temperatures, see Fig. 4c. When crossing the critical temperature, we find again that the c lattice parameter flattens out. In addition, all our measures of the order parameter in Fig. 4b show a clear softening of Q approaching

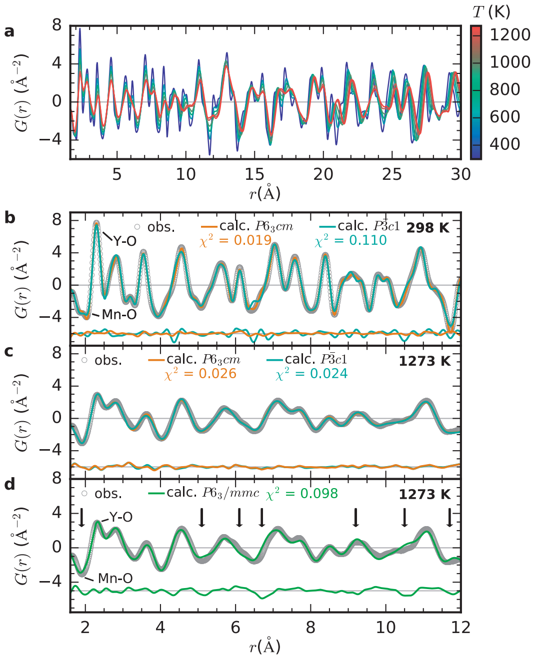

FIG. 3. **Pair-distribution function of YMnO$_3$ of the local structure**. **a**, Temperature series of the measured $G(r)$ between room temperature and 1273 K from $r = 1.6$-30 Å. **b**, The $G(r)$ between $r = 1.6$-12 Å at 298 K fitted to the low-symmetric hettotypes $P6_3cm$ (P) and $P\bar{3}c1$ (AP) with difference curves and overall fit residuals χ^2 below. The polar hettotype fits the low-temperature data well. **c**, Fit of the $G(r)$ between $r = 1.6$-12 Å at 1273 K to the low-symmetric hettotypes $P6_3cm$ (P) and $P\bar{3}c1$ (AP). Both fit the data equally well. **d**, Measured $G(r)$ between $r = 1.6$-12 Å at 1273 K fitted to the high-symmetric aristotype $P6_3/mmc$ space group. Arrows indicate regions of particularly bad fits. The fit residuals below show that this paraelectric model does not fit to the high-temperature data. Fits of the PDF data for additional temperatures are given in Supplementary Figs. 6 and 7.

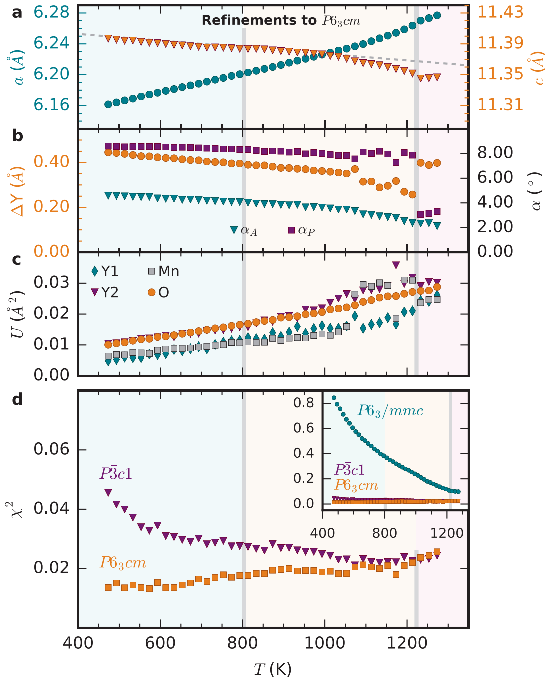

FIG. 4. **Local structure refinements**. **a**, Refined lattice parameters for the $P6_3cm$ space group for $r = 1.6$-22 Å, **b**, Y corrugation, ΔY, planar α_P and apical α_A bipyramidal tilt angles and **c**, atomic displacement parameters U from fitting the polar $P6_3cm$ hettotype model to the data between $r = 1.6$-12 Å with fixed lattice parameters shown in panel **a**. **d**, Fitting errors χ^2 for fitting real space $G(r)$ between 1.6-12 Å for the polar $P6_3cm$ found at the minima and the nonpolar $P\bar{3}c1$ found at local maxima in the brim of the Mexican hat potential using fixed lattice parameters found from refinements between 1.6-22 Å. The grey vertical line at 1223 K shows the Curie temperature T_C, the line at 800 K shows the temperature where refinements become incoherent. Right inset shows the error of the two hettotypes compared to the non-polar aristotype ($P6_3/mmc$).

T_C, neither of them approach zero, once more indicating a locally partially conserved order parameter and strong order-disorder across T_C.

So far, we have established that the phase transition has a strong order-disorder character, since the order parameter never vanishes on the local scale. In addition, we show that refinements of the order parameter with the ferroelectric structure $P6_3cm$ (P) become worse, and unstable, when approaching the critical temperature. This is observed not only for the average structure, but also for the local structure. Disorder between the six *discrete* minima with polar hettotype symmetry $P6_3cm$ in the Mexican hat cannot describe the observed disorder, as this type of disorder would fit well to $P6_3cm$ on the local scale. Instead, we suggest a model where fluctuations of the order parameter angle Φ locally lower the symmetry from the polar space group (P) to the intermediate, but still polar $P3c1$ (IM) space group. We investigate this by comparing fit residuals of refinements of the PDF data to the paraelectric aristotype ($P6_3/mmc$) (H) and the two special symmetry hettotypes $P6_3cm$ (P) and $P\bar{3}c1$ (AP). We cannot refine to the general $P3c1$ (IM) model since it allows all angles of Φ, and thus cannot be used to refine a mixture of Φ.

The fit residual χ^2 of the PDF refinements, presented in Fig. 4d show several important points. First of all the fit residuals for the polar ground state $P6_3cm$ increases above ~700 K. For well refined systems, fit residuals are expected to decrease with heating as thermal fluctuations broaden the data (see for example bulk FCC Ni in Supplementary Fig. 8). This unusual increase suggests that the polar phase (P) alone is not capable of explaining the PDF data on short length scales. This is further corroborated by the difference in fit residuals between the polar $P6_3cm$ (P) and antipolar $P\bar{3}c1$ (AP) hettotypes. As seen in Fig. 4, the fit residuals of these hettotypes become more similar upon heating, finally merging at T_C, suggesting that there is no preference for either of the two hettotypes above T_C, and that all structures in the brim of the Mexican hat are equally likely to be observed locally above T_C. However, the K_3-distortion never vanishes on a local scale, as the paraelectric aristotype (H) has a much larger fit residual than the hettotypes (inset in panel d). Thus, above T_C the structure will become a disordered mixture between all possible angles of the order parameter angle Φ, accounting for the anomalies in Fig. 4b. When fluctuations of the order parameter Φ become observable in the neutron data, the Y2 and O4 site symmetries are broken (Fig. 1). This means that the structural refinements will become unstable for ΔY and α_P above ~800 K (Fig. 4b). The amplitude of the bipyramidal tilting angles (α_A) on the other hand is well-defined for all symmetries in the brim of the hat, and thereby well-behaved in both reciprocal and real space refinements, as shown in Fig. 2b and 4b.

Summary & Discussion

We have presented a description of the ferroelectric phase transition in hexagonal $YMnO_3$ at different length scales. At room temperature, the symmetry of the system is ordered according to the six minima with $P6_3cm$ symmetry in the Mexican hat potential. Upon heating we find that the expectation value of the order parameter amplitude gradually decreases at all length scales. Above ~800 K, we observe that the polar hettotype $P6_3cm$ structure fails to fully describe the local structure, and that the antipolar hettotype $P\bar{3}c1$ describes the structure equally well at T_C. We can explain this by a *local symmetry lowering upon heating*, due to order parameter fluctuations.

We illustrate this behaviour in Fig. 5. Thermodynamically, the free energy can increase through thermal vibrations (phonons) or order parameter inhomogeneity. At low temperature (Fig 5a), the main entropy contribution is vibrational: The six distinct minima are well separated by energy barriers of around 100 meV, such that the system adopts one of the six ground states over a large spatial range. On heating, the amplitude Q of the K_3 distortion is reduced (Fig. 2b and 4b), first reducing the energy barriers in the brim of the Mexican hat (Fig. 5b). In this regime, the system continues to adopt one of the six ground states, with increasingly large fluctuations in order parameter angle. Between ~800 K and T_C, the minima become so faint, that all order parameter angles are accessible, although the system maintains its long-range order (Fig. 5c). Above T_C (Fig. 5d), the order parameter remains locally non-zero, but long-range order is lost.

Our finding of the onset of structural fluctuations explains the previously reported anomalies in thermal expansion [15], conventional neutron diffraction [12], ferroelectric polarization [23] and quasi-elastic X-ray scattering [27] around ~800-900 K. These anomalies are caused by a progressively increasing signal from regions with the low symmetry $P3c1$ structure. Our explanation of this unusual order-disorder transition reconciles previously reported anomalies at and above T_C. Our data exclude the picture of a second phase transition, as the symmetry breaking caused by the fluctuations is only on the local scale.

Methods

Bulk powder of $YMnO_3$ was prepared by firing uniaxially pressed pellets of dried and mixed Y_2O_3 (>99.99%, Aldrich) and Mn_2O_3 (>99%, Aldrich) twice for 24 h at 1573 K in air with intermediate grinding.

Neutron total scattering was performed at the Nanoscale-Ordered Materials Diffractometer (NOMAD) at the Spallation Neutron Source at Oak Ridge National Laboratory. ~1.5 g of powder was sealed in a vacuum container and measured in an ILL-type vacuum furnace. The NOMAD detectors were calibrated using scattering from diamond powder, and standard Si powder was measured to obtain the instrument parameter file for Rietveld refinements. The sample was measured between room temperature and 1273 K in steps of 20 K. Measurements of two subsequent temperature cycles between 1113K and 1373 K on the same sample were performed to investigate chemical expansion as a function of oxygen loss, and was found to be small (Supplementary Fig. 9). The structural factor $S(Q)$ was obtained by normalizing the scattering intensity to the scattering from a solid vanadium rod and the background was subtracted using an identical, empty vanadium can. Pair distribution functions (PDF) were obtained by Fourier transform of $S(Q)$ with $Q_\mathrm{min} = 0.1$ Å^{-1} and $Q_\mathrm{max} = 22$ Å^{-1}.

The average crystal structure over the whole temperature range was determined by Rietveld refinements with the space groups $P6_3/mmc$ and $P6_3cm$ [28], using TOPAS Academic v.5 [29]. PDFs were fitted to the same space groups at different ranges of r using PDFGUI [30]. Isotropic atomic displacement factors (U) were used (see Supplementary for details of the refinements). Details of the PDF method can be found elsewhere [31].

For our density functional calculations we used the LDA+U approximation [32, 33] as implemented in the abinit PAW planewave code [34–37], with a cutoff energy of 30 Hartree and a k-point mesh of 6×6×2. A collinear A-type magnetic ordering with a U of 8 eV on the Mn

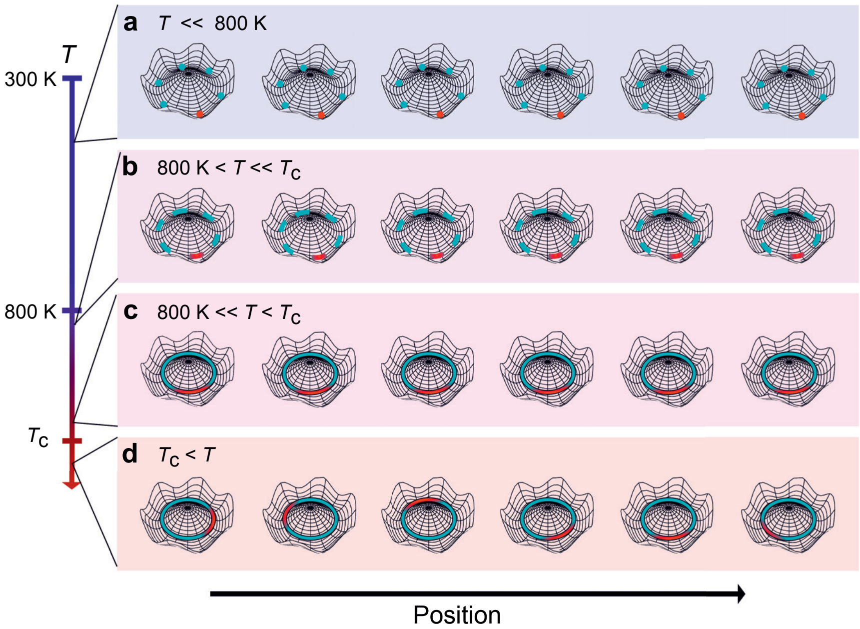

FIG. 5. **Unconventional order-disorder transition.** Local value of the order parameter in the different temperature regions within one domain. The blue lines describe accessible states to the order parameter and the red color shows the distribution of the order parameter. **a**, In the low temperature region, the order parameter is firmly fixed within one of the six ground states. **b**, Between 800 K and T_C fluctuations smear out the local distribution of the order parameter angle (red), but the average angle within each domain remains constant. **c**, Close to T_C the energy landscape becomes flat. **d**, At and above T_C, coherence of the order parameter is lost and the system disorders between all possible states in the Mexican hat.

d orbitals was applied. Even if this magnetic ordering underestimates the bandgap, it does not break the space group symmetry, which is important for this study. 30 atom unit cells with lattice parameters from our PDF refinements were relaxed with respect to atomic positions such that the forces were converged within 1E-6 Ha/Bohr (See Supplementary Methods for more details).

Acknowledgements

This research used resources at the Spallation Neutron Source, a DOE Office of Science User Facility operated by the Oak Ridge National Laboratory. Computational resources were provided the Euler cluster at ETH, Zürich. Financial support from the Research Council of Norway (project no. 231430), NTNU and Advanced Grant (N.A.S.) (no. 291151) from the European Research Council are acknowledged. Work at Brookhaven National Laboratory was supported by US DOE, Office of Science, Office of Basic Energy Sciences (DOE-BES) under contract DE-SC00112704. Matt Tucker and Marshall McDonnell are acknowledged for assisting the neutron measurements. Matt Tucker is acknowledged for constructing TOPAS input files for reciprocal space Rietveld refinements.

Author contributions

S.H.S., S.M.S., M.F., E.S.B. and S.J.L.B. conducted neutron scattering measurements; S.M.S prepared samples; S.J.L.B. and E.S.B. supervised the PDF analysis; Q.M. performed DFT calculations; S.H.S., Q.M., N.A.S. and S.M.S. wrote the paper; all authors discussed the results; S.M.S. conceived the project; N.A.S. and S.M.S. supervised the project.

[1] Griffin, S. M. *et al.* Scaling Behavior and Beyond Equilibrium in the Hexagonal Manganites. *Phys. Rev. X* **2**, 041022 (2012).

[2] Lin, S.-Z. *et al.* Topological defects as relics of emergent continuous symmetry and Higgs condensation of disorder in ferroelectrics. *Nat. Phys.* **10**, 970–977 (2014).

[3] Meier, Q. N. *et al.* Global formation of topological defects in the multiferroic hexagonal manganites. *arXiv:1703.08321 [cond-mat]* (2017).

[4] Fujimura, N., Ishida, T., Yoshimura, T. & Ito, T. Epitaxially grown $YMnO_3$ film: New candidate for nonvolatile memory devices. *Appl. Phys. Lett.* **69**, 1011 (1996).

[5] Kumagai, Y. *et al.* Observation of persistent centrosym-

metricity in the hexagonal manganite family. *Phys. Rev. B* **85**, 174422 (2012).

[6] Lottermoser, T., Fiebig, M. & Frohlich, D. Symmetry and coupling of magnetic and electric order parameters in $\mathrm{YMnO_3}$. *J. Appl. Phys.* **91**, 8251 (2002).

[7] Choi, T. *et al.* Insulating interlocked ferroelectric and structural antiphase domain walls in multiferroic $\mathrm{YMnO_3}$. *Nat. Mater.* **9**, 253–258 (2010).

[8] Jungk, T., Hoffmann, A., Fiebig, M. & Soergel, E. Electrostatic topology of ferroelectric domains in $\mathrm{YMnO_3}$. *Appl. Phys. Lett.* **97**, 012904 (2010).

[9] Meier, D. *et al.* Anisotropic conductance at improper ferroelectric domain walls. *Nat. Mater.* **11**, 284–288 (2012).

[10] Geng, Y., Lee, N., Choi, Y. J., Cheong, S.-W. & Wu, W. Collective Magnetism at Multiferroic Vortex Domain Walls. *Nano Lett.* **12**, 6055–6059 (2012).

[11] Mundy, J. A. *et al.* Functional electronic inversion layers at ferroelectric domain walls. *Nat. Mater.* **16**, 622–627 (2017).

[12] Gibbs, A. S., Knight, K. S. & Lightfoot, P. High-temperature phase transitions of hexagonal $\mathrm{YMnO_3}$. *Phys. Rev. B* **83**, 094111 (2011).

[13] Katsufuji, T. *et al.* Crystal structure and magnetic properties of hexagonal $R\mathrm{MnO_3}$ (R = Y, Lu, and Sc) and the effect of doping. *Phys. Rev. B* **66**, 134434 (2002).

[14] Kim, J., Cho, K. C., Koo, Y. M., Hong, K. P. & Shin, N. Y-O hybridization in the ferroelectric transition of $\mathrm{YMnO_3}$. *Appl. Phys. Lett.* **95**, 132901 (2009).

[15] Nénert, G. *et al.* Experimental evidence for an intermediate phase in the multiferroic $\mathrm{YMnO_3}$. *J. Phys.: Condens. Matter* **19**, 466212 (2007).

[16] Tyson, T. A. *et al.* Measurements and ab initio molecular dynamics simulations of the high temperature ferroelectric transition in hexagonal $\mathrm{RMnO_3}$. *J. Appl. Phys.* **110**, 084116 (2011).

[17] Selbach, S. M. *et al.* Crystal structure, chemical expansion and phase stability of $\mathrm{HoMnO_3}$ at high temperature. *J. Solid State Chem.* **196**, 528–535 (2012).

[18] Jeong, I.-K., Hur, N. & Proffen, T. High-temperature structural evolution of hexagonal multiferroic $\mathrm{YMnO_3}$ and $\mathrm{YbMnO_3}$. *J. Appl. Crystallogr.* **40**, 730–734 (2007).

[19] Fennie, C. J. & Rabe, K. M. Ferroelectric transition in $\mathrm{YMnO_3}$ from first principles. *Phys. Rev. B* **72**, 100103(R) (2005).

[20] Artyukhin, S., Delaney, K. T., Spaldin, N. A. & Mostovoy, M. Landau theory of topological defects in multiferroic hexagonal manganites. *Nat. Mater.* **13**, 42–49 (2013).

[21] Thomson, R. I., Chatterji, T., Howard, C. J., Palstra, T. T. M. & Carpenter, M. A. Elastic anomalies associated with structural and magnetic phase transitions in single crystal hexagonal $\mathrm{YMnO_3}$. *J. Phys.: Condens. Matter* **26**, 045901 (2014).

[22] Cano, A. Hidden order in hexagonal $R\mathrm{MnO_3}$ multiferroics (R = Dy - Lu, In, Y, and Sc). *Phys. Rev. B* **89**, 214107 (2014).

[23] Lilienblum, M. *et al.* Ferroelectricity in the multiferroic hexagonal manganites. *Nat. Phys.* **11**, 1070–1073 (2015).

[24] Van Aken, B. B., Palstra, T. T., Filippetti, A. & Spaldin, N. A. The origin of ferroelectricity in magnetoelectric $\mathrm{YMnO_3}$. *Nat, Mater.* **3**, 164–170 (2004).

[25] Šafránková, M., Fousek, J. & Kižaev, S. A. Domains in ferroelectric $\mathrm{YMnO_3}$. *Czech. J. of Phys. B* **17**, 559–560 (1967).

[26] Mountstevens, E. H., Redfern, S. A. T. & Attfield, J. P. Order-disorder octahedral tilting transitions in $\mathrm{SrSnO_3}$ perovskite. *Phys. Rev. B* **71**, 220102 (2005).

[27] Barbour, A. *et al.* Partial glass isosymmetry transition in multiferroic hexagonal $\mathrm{ErMnO_3}$. *Phys. Rev. B* **93**, 054113 (2016).

[28] van Aken, B. B., Meetsma, A. & Palstra, T. T. Hexagonal $\mathrm{YMnO_3}$. *Acta Crystallogr. C: Cryst. Str. Commun.* **57**, 230–232 (2001).

[29] Coelho, A. A. TOPAS Academic: General Profile and Structure Analysis Software for Powder Diffraction Data; Bruker AXS (2004).

[30] Farrow, C. L. *et al.* PDFfit2 and PDFgui: computer programs for studying nanostructure in crystals. *J. Phys.: Condens. Matter* **19**, 335219 (2007).

[31] Egami, T. & Billinge, S. J. L. *Underneath the Bragg peaks, Structural analysis of Complex Materials* (Elsevier, The Boulevard, Langford Lane Kidlington, Oxford OX5 1GB, UK, 2003).

[32] Perdew, J. P. & Wang, Y. Accurate and simple analytic representation of the electron-gas correlation energy. *Phys. Rev. B* **45**, 13244–13249 (1992).

[33] Liechtenstein, A. I., Anisimov, V. I. & Zaanen, J. Density-functional theory and strong interactions: Orbital ordering in Mott-Hubbard insulators. *Phys. Rev. B* **52**, R5467–R5470 (1995).

[34] Gonze, X. *et al.* First-principles computation of material properties: the ABINIT software project. *Comp. Mater. Sci.* **25**, 478–492 (2002).

[35] Gonze, X. A brief introduction to the ABINIT software package. *Z. Kristallog. – Cryst. Mater.* **220** (2005).

[36] Torrent, M., Jollet, F., Bottin, F., Zérah, G. & Gonze, X. Implementation of the projector augmented-wave method in the ABINIT code: Application to the study of iron under pressure. *Comp. Mater. Sci.* **42**, 337–351 (2008).

[37] Amadon, B., Jollet, F. & Torrent, M. γ and β cerium: LDA+U calculations of ground-state parameters. *Phys. Rev. B* **77**, 155104 (2008).

Paper 3

is not included due to
copyright

Appendix B

Input file for reciprocal space TOPAS refinements

The following input file, provided by Matt Tucker at the Advanced Diffraction Group, Chemical Engineering and Materials Division, Oak Ridge National Lab, was used for Rietveld refinements in TOPAS.

```
'jEdit friendly TOPAS input file for POWGEN calibration
'folds used in file to allow for collapsing sections

'{{{  'TOF macros
'prm !Lf 60.183  ' POWGEN 90 degree flightpath
'prm !Lf 20.5  ' NOMAD 90 degree flightpath
'prm !h_bar 6.626176e-34 ' Plank's constant
'prm !m_n 1.67495e-27 ' neutron mass
'local !lambda = Xo 10^4 h_bar/(m_n Lf); 'TOF to wavelength

macro TOF_d {
 pk_xo = zero + dif_c D_spacing + dif_a D_spacing^2;
 }
macro GSAS_btb
{

   push_peak                 'GSAS TOF peak shape 3
        exp_conv_const = alpha0 + alpha1 / D_spacing;
   bring_2nd_peak_to_top
      exp_conv_const = beta0 + beta1 / D_spacing^4;
   add_pop_1st_2nd_peak

}

'Description: alternative description of sample contribution to tof peak shape
'from TOPAS Wiki contributed by: John Evans
'#ifndef tof_sample_peakshape
'#define macro tof_sample_peakshape(lor,lor_val,dsp,dsp_val,dspsq,dspsq_val)
'{
'      prm dsp dsp_val del = 0.05 Val + 1; min 1
'      prm dspsq dspsq_val del = 0.05 Val + 1; min 0
'      peak_type pv
'         pv_lor lor lor_val
'         pv_fwhm  = dsp D_spacing + dspsq D_spacing^2;
'}
'#endif

macro Abs_Lobanov  'Lobanov absorption macro with calculated lambda for wavelength dependence of mu (as
per GSAS manual)
{
prm !h_bar 6.626176e-34 ' Plank's constant
prm !m_n 1.67495e-27 ' neutron mass
local !lambda = Xo 10^4 h_bar/(m_n Lf); 'TOF to wavelength
local !td_const = 10^4 h_bar/(m_n Lf);
local !sintheta = Sin(Deg_on_2 two_theta);
local !k0 = 1.697653;
local !k1 = (25.99978 - (0.01911 sintheta^0.5)Exp(-0.024514 sintheta^2)) + 0.109561 sintheta - 26.0456;
local !k2 = -0.02489 - (0.39499 sintheta^2) + (1.219077 sintheta^3) - (1.31268 sintheta^4) + (0.871081
sintheta^5)
           - (0.2327 sintheta^6);
local !k3 = 0.003045 + (0.018167 sintheta^2) - (0.03305 sintheta^4);
local !k4 = 1.433902 + (11.07504 sintheta^2) - (8.77629 sintheta^4) + (10.02088 sintheta^6) - (3.36778
sintheta^8);
local !k5 = ((0.013869 - 0.01249 sintheta^2)Exp(3.27094 sintheta^2)) + ((0.337894 + (13.77317
sintheta^2))/((1 + 11.53544 sintheta^2)^1.555039));
local !k6 = (1.933433 / (1 + 23.12967 sintheta^2)^1.686715) - 0.13576 sintheta + 1.163198;
local !k7 = 0.044365 - (0.04259/((1 + 0.41051 sintheta^2)^148.4202));
scale_pks = If( (mu*lambda) < 3, Exp(-k0 (mu*lambda) - k1 (mu*lambda)^2 - k2 (mu*lambda)^3 - k3
(mu*lambda)^4),
                                Exp((k4 - k7/(1 + k5 ((mu*lambda)-3))^k6)+k7)
                                );
}
macro TOF_Powder_extinction(c, v) {   'extinction for TOF powder data; value = mosaic block size in
micron^2
   #m_argu c
        If_Prm_Eqn_Rpt(c, v, min = Val-.1; max = Val+.1; del 0.001)
      local !xx = CeV(c,v) (lambda I_no_scale_pks / Get(cell_volume))^2;
```

```
      local !Eb = 1/Sqrt(1 + xx);
      local !El = If(xx < 1,
                        1 - xx/2 + xx^2/4 - (5 xx^3)/48,
                        Sqrt(2/Pi xx) (1 - 8/xx - 3/(128 xx^3) - 15/(1024 xx^5))
                        );
      scale_pks = 1/(Eb Sin(two_theta Deg_on_2)^2 + El Cos(two_theta Deg_on_2)^2);
}
'#define Version6 macro V6 {gui_tof_t0 = zero;  gui_tof_t1 = dif_c;} 'enable d-spacing and Q display in
version 6
'}}}

'-----------------------------------------------------------------
'NOMAD LaB6 back-to-back calibration
'
'-----------------------------------------------------------------

'{{{ r-factors and control information
r_exp           0.574124267
r_exp_dash      0.757802304
r_wp                    3.75757334
r_wp_dash       4.9597237
r_p                     3.26263096
r_p_dash        6.49111094
gof                     6.54487809
weighted_Durbin_Watson  0.573194239
continue_after_convergence
do_errors

'}}}

'{{{ select banks to use here and enter filenames
#define USE_BANK2  macro filename_bank2 {..\dat_to_xye\temp200-detector-2.xye}  macro start_end_bank2
{start_X 2500 finish_X 20500}
#define USE_BANK3  macro filename_bank3 {..\dat_to_xye\temp200-detector-3.xye}  macro start_end_bank3
{start_X 2500 finish_X 17000}
#define USE_BANK4  macro filename_bank4 {..\dat_to_xye\temp200-detector-4.xye}  macro start_end_bank4
{start_X 3800 finish_X 16050}
'}}}


'-----------------------------------------------------------------

'{{{ information specific to bank 2 refinement here
#ifdef USE_BANK2
TOF_XYE(filename_bank2, = Yobs_dx_at(Xo) .5;) start_end_bank2
r_wp  3.42124828 'bank 2
gof                     7.78471842
bkg @  0.194605678`_0.00143556729 -0.0427362711`_0.00244641643  0.0533542007`_0.00212205108
-0.0467236802`_0.00181731674
0.0225171792`_0.00161589136 -0.00102808483`_0.00144141643  0.000860170419`_0.00112232213
0.00175525825`_0.000889203892
#ifdef VERSION6 gui_tof_t0 = zero;  gui_tof_t1 = dif_c; #endif
   weighting = 1 / SigmaYobs^2;
        TOF_LAM(0.001) 'reduce value if cutoff in tails observable
        scale_pks = D_spacing^4;
   local Q = 2 Pi Constant(dif_c) / (X - Constant(zero));

TOF_d     'TOF to d-spacing
GSAS_btb  'back-to-back exponentials
Abs_Lobanov 'absorption correction
local !Lf 20.64  ' total flightpath
local !zero -0.84943_2.86430 'instrument TOF-to-d ; don't refine
local !dif_c  6017.22193_4.73728 'instrument TOF-to-d ; don't refine
local !alpha0  15.81350_7.30506 'instrument back-to-back exponential ; refine with care only if necessary
local !alpha1 -20.44174_8.59164 'instrument back-to-back exponential ; refine with care only if necessary
local !beta0 -69.93634_2.53153 'instrument back-to-back exponential ; refine with care only if necessary
local !beta1    5.47295_0.58030 'instrument back-to-back exponential ; refine with care only if necessary
```

```
local !dif_a -3.89172_0.13590 'will take out sample displacement - refine if needed
local !mu  0.02772_0.00324
local !two_theta 90

str
   phase_name LaB6
   r_bragg  1.26674338
   scale sc2  0.0530897122`_0.0001812
   peak_type pv
     TOF_PV(@, 1484.27838`_7.69050, @, 0.377847668`_0.0222145831, dif_c)
     TOF_CS_L(@, 10000.00000`_130638.17975, dif_c)
     TOF_CS_G(@, 25.54463`_0.64374, dif_c)
    '   tof_sample_peakshape(!lor_bank2, 2.28292051e-022_0.0919829893,!dsp_bank2, 40.13172_1.47429,!
dspsq_bank2, 15.50643_5.13887)  'alternative sample broadening description


 #endif
'}}}


'{{{ information specific to bank 3 refinement here
#ifdef USE_BANK3
TOF_XYE(filename_bank3, = Yobs_dx_at(Xo) .5;) start_end_bank3
r_wp  3.67615274 'bank 3 only
gof                     5.75791213
bkg @  0.218474056`_0.00133946812 -0.133595581`_0.00201190696  0.060849128`_0.00124333378
-0.0232679559`_0.0010224052 -0.00766375802`_0.000972679373
#ifdef VERSION6 gui_tof_t0 = zero;  gui_tof_t1 = dif_c; #endif
   weighting = 1 / SigmaYobs^2;
        TOF_LAM(0.001) 'reduce value if cutoff in tails observable
        scale_pks = D_spacing^4;
   local Q = 2 Pi Constant(dif_c) / (X - Constant(zero));

TOF_d     'TOF to d-spacing
GSAS_btb  'back-to-back exponentials
Abs_Lobanov 'absorption correction
local !Lf 20.61  ' total flightpath
local !zero   8.59453_0.86037 'instrument TOF-to-d ; don't refine
local !dif_c   9462.04599_2.00215 'instrument TOF-to-d ; don't refine
local !alpha0   432.42446_7.84738 'instrument back-to-back exponential ; refine with care only if
necessary
local !alpha1 -236.18525_5.92818 'instrument back-to-back exponential ; refine with care only if necessary
local !beta0   91.07307_6.44814 'instrument back-to-back exponential ; refine with care only if necessary
local !beta1   1.73310_0.72593 'instrument back-to-back exponential ; refine with care only if necessary

local !dif_a  16.33322_0.25401                                      'will take out sample displacement -
refine if needed
local !mu  0.03773_0.00496
local !two_theta 122
str
   phase_name ZnO
   r_bragg  1.53132182
   scale sc3  0.0929983402`_0.0005505
    peak_type pv
     TOF_PV(@, 349.42591`_11.63467, @, 0.458282221`_0.0636882401, dif_c)
     TOF_CS_L(@, 201.71700`_61.91071, dif_c)
     TOF_CS_G(@, 29.67787`_0.72379, dif_c)
        'tof_sample_peakshape(!lor_bank3, 0.400966602_0.0111844616,!dsp_bank3, 16.29408_1.15888,!
dspsq_bank3, 26.94261_0.84931)  'alternative sample broadening description

#endif
'}}}

'{{{ information specific to bank 4
#ifdef USE_BANK4
TOF_XYE(filename_bank4, = Yobs_dx_at(Xo) .5;) start_end_bank4
```

```
r_wp  4.93039262 'bank 4
gof                   6.01364725
bkg @  0.226246603`_0.00146012227 -0.0889442953`_0.00201987456  0.041043073`_0.00134587934
-0.0244345319`_0.00125292273
#ifdef VERSION6 gui_tof_t0 = zero;  gui_tof_t1 = dif_c; #endif
   weighting = 1 / SigmaYobs^2;
        TOF_LAM(0.001) 'reduce value if cutoff in tails observable
        scale_pks = D_spacing^4;
   local Q = 2 Pi Constant(dif_c) / (X - Constant(zero));

TOF_d     'TOF to d-spacing
GSAS_btb  'back-to-back exponentials
Abs_Lobanov 'absorption correction
local !Lf 20.31  ' total flightpath assuming all detectors present
local !zero  6.29258_0.42203 'instrument TOF-to-d ; don't refine
local !dif_c  10564.62235_1.05435 'instrument TOF-to-d ; don't refine
local !alpha0  378.19399_7.27167 'instrument back-to-back exponential ; refine with care only if necessary
local !alpha1 -197.53757_5.61906 'instrument back-to-back exponential ; refine with care only if necessary
local !beta0   63.52444_6.26024 'instrument back-to-back exponential ; refine with care only if necessary
local !beta1   2.96627_0.63835 'instrument back-to-back exponential ; refine with care only if necessary

local !dif_a  10.84004_0.29510 'will take out sample displacement - refine if needed
local !mu  0.07153_0.00720
local !two_theta 154

str
   phase_name ZnO
   r_bragg  2.41414787
   scale sc4  0.10876797`_0.000681
    peak_type pv
    TOF_PV(@, 199.29852`_6.99632, @, 0.0981806118`_0.0879028245, dif_c)
    TOF_CS_L(@, 198.24361`_52.63585, dif_c)
    TOF_CS_G(@, 134.94396`_30.35026, dif_c)
        'tof_sample_peakshape(lor_bank4, 0.448393811_0.0155393424,dsp_bank4, 1.00000_0.84756,dspsq_bank4,
20.04210_0.69958)

#endif
'}}}


'-------------------------------------------------------------

'{{ overall structural information here

'-------------------------------------------------------------
'Put overall structural and peak shape information here
'-------------------------------------------------------------


for xdds {


' for strs 1 to 1 {
str
space_group "P63cm"
   phase_name YMnO3
        a a_ymo  6.162388`_0.000036
        b =a_ymo;
        c c_ymo  11.392734`_0.000136
        al 90
        be 90
        ga 120
        site  Y1 x   0.0000     y 0.0000  z zy1  0.27113`_0.00048       occ Y 1.0       beq by1
0.63473`_0.03931
        site  Y2 x   =1/3;      y =2/3;  z zy2  0.23350`_0.00039       occ Y 1.0       beq by2
0.72040`_0.02658
        site  Mn x   xmn  0.32035`_0.00087      y 0.0000  z     0.0000  occ Mn 1.0      beq bmn
```

```
0.27360`_0.03216
        site  O1 x   xo1  0.31030`_0.00040      y 0.0000  z zo1  0.16239`_0.00046       occ O 1.0   beq
bo  0.70936`_0.01217
        site  O2 x   xo2  0.64140`_0.00034      y 0.0000  z zo2  0.33582`_0.00048       occ O 1.0   beq
bo  0.70936`_0.01217
        site  O3 x   0.0000     y 0.0000  z zo3  0.47400`_0.00055       occ O 1.000     beq bo
0.70936`_0.01217
        site  O4 x   =1/3;      y =2/3;  z zo4  0.01441`_0.00044        occ O 1.000     beq bo
0.70936`_0.01217

'}
}

'}}
```

Appendix C

Landau expansion and Mexican hat potential for hexagonal manganites

To derive the Landau free energy for the hexagonal manganites, we start from the *system independent* Taylor expanded Free energy G as a function of the order parameter φ is as follows:

$$G(\varphi) = a\varphi + b\varphi^2 + c\varphi^3 + d\varphi^4 + ... \tag{C.1}$$

Here, G_0 is the free energy for the high symmetry structure, while $a, b, c, d...$ are material dependent coefficients $(a, b, c, d...)$.

In the structural ground state, the Free energy of the structure is in a local minimum with respect to the order parameter: $\frac{\partial G}{\partial \varphi} = 0$, such that the odd order terms vanish:

$$G(\varphi) = b\varphi^2 + d\varphi^4 + f\varphi^6 + ... \tag{C.2}$$

For the next step, we need to know the nature of the continuous symmetry breaking in question. The free energy landscape should be able to describe the symmetry elements in both the high and low symmetry and the continuum between them. For the hexagonal manganites, the lowering of symmetry from $P6_3/mmc$ to $P6_3cm$ we need a two-dimensional order parameter, as both the amplitude and direction of the bipyramidal tilting are free to change. We name the order parameter Q, with components in the xy plane. When replacing φ

with Q_x and Q_y, the coupling between them needs to be considered in addition to the directly replaced terms, such that we obtain twice as many terms in the expansion:

$$\begin{aligned} G(Q) = &\underbrace{b(Q_\mathrm{x}^2+Q_\mathrm{y}^2)+d(Q_\mathrm{x}^4+Q_\mathrm{y}^4)+f(Q_\mathrm{x}^6+Q_\mathrm{y}^6)+...}_{\text{direct terms}} \\ &\underbrace{C_1(Q_\mathrm{x}Q_\mathrm{y})+C_2(Q_\mathrm{x}Q_\mathrm{y}^3)+C_3(Q_\mathrm{x}^2Q_\mathrm{y}^2)+C_4(Q_\mathrm{x}^3Q_\mathrm{y})+...}_{\text{coupling terms}} \end{aligned} \tag{C.3}$$

Since we know that the free energy landscape is dependent on tilting angles, it is practical to convert to spherical coordinates by replacing $Q_\mathrm{x} = Q\sin\Phi$ and $Q_\mathrm{y} = Q\cos\Phi$. The first coupling term becomes

$$Q_\mathrm{x}Q_\mathrm{y} = Q^2\cos\Phi\sin\Phi = \frac{Q^2}{2}\sin 2\Phi \tag{C.4}$$

where the second step follows from trigonometric rules found in a mathematical formula collection in a shelf near you. The term $\sin\Phi$ is not allowed in a hexagonal system, so it can be omitted. It is easy to see that similar derivation of the second, third and fourth coupling terms will yield the same result, so they can also be omitted. This means that all the coupling terms explicitly written in Eq. C.3 are omitted, and the next possible terms are of sixth order:

$$\begin{aligned} Q_\mathrm{x}^3Q_\mathrm{y}^3 = Q^6\cos^3\Phi\sin^3\Phi = \frac{1}{4}&\underbrace{(3\sin\Phi-\sin 3\Phi)\frac{1}{4}(3\cos\Phi-\cos 3\Phi)}_{\text{trigonometric identities}} \\ = \frac{Q^6}{16}(9\underbrace{c_0\sin\Phi\cos\Phi}_{c_0\sin 2\Phi=0}-3\underbrace{c_1\sin\Phi\cos 3\Phi}_{c_1\sin 4\Phi=0}&-3\underbrace{c_2\cos\Phi\sin 3\Phi}_{c_2\sin 4\Phi=0}+\underbrace{c_3\sin 3\Phi\cos 3\Phi}_{c_3\cos 6\Phi}) \\ &= C_6Q^6\sin 6\Phi \end{aligned} \tag{C.5}$$

The expansion now has the form

$$G(Q,\Phi) = bQ^2+dQ^4+fQ^6(C+C_6\cos 6\Phi) = G_0(Q,\Phi) \tag{C.6}$$

which describes the symmetry of Q and its coupling to the angle. Knowing that the hexagonal manganites become ferroelectric under an improper coupling between the Q, Φ and the polarization P, additional terms need to be included:

$$\begin{aligned} G(Q,\Phi,P) = G_0(Q,\Phi)+a_\mathrm{P}P^2+b_\mathrm{P}P^4+... \\ g_1PQ+g_2P^2Q^2-g_3PQ^3\cos 3\Phi-g_4P^3Q\cos 3\Phi... \end{aligned} \tag{C.7}$$

We neglect all terms from the sixth, as they become negligible. To investigate whether or not the coupling terms are allowed, we need to make sure that they conserve momentum. Thus we need to investigate the order dependence of the order parameters in reciprocal space. The Q and P in reciprocal space are

$$\begin{aligned} Q(r) &= \sum_q Q(q)\mathrm{e}^{i\mathbf{qr}} \\ P(r) &= \sum_q P(q)\mathrm{e}^{i\mathbf{qr}} \end{aligned} \tag{C.8}$$

The Γ_2^- causing the polarization P, carries a zone center reciprocal space vector $q = (0, 0, 0)$ by definition. The K_3 mode driving the distortion by Q, Φ has a reciprocal space vector $q = (1/3, 1/3, 0)$ Q^1 to the zone-boundary. The free energy should be independent on these vectors, such that all terms which change these vectors are not allowed. We can see that any power of P is thus allowed, as the Γ-point always sums to 0. For the K_3 mode, the summation over q vectors must sum to either 0 or 1. For the first order terms of Q, momentum is not conserved, and the term is not allowed. For second order powers of Q, momentum is conserved if one sums over one positive and one negative q, and for third order terms, the summation over three positive q conserves momentum:

$$\begin{aligned} Q^2(r) &= \sum_q Q^2(q)\mathrm{e}^{i\mathbf{r}(\mathbf{q}_1-\mathbf{q}_2)} \\ Q^3(r) &= \sum_q Q^3(q)\mathrm{e}^{i\mathbf{r}(\mathbf{q}_1+\mathbf{q}_2+\mathbf{q}_3)} \end{aligned} \tag{C.9}$$

By combining Eq. C.6 and the allowed terms from Eq. C.7 the final equation becomes:

$$\begin{aligned} G(Q, \Phi, P) = bQ^2 + dQ^4 + fQ^6(C + C_6 \cos 6\Phi) \\ + a_{\mathrm{P}}P^2 + b_{\mathrm{P}}P^4 + g_2 P^2 Q^2 - g_3 P Q^3 \cos 3\Phi \end{aligned} \tag{C.10}$$

Often, additional terms are included to account for energy cost of order parameter fluctuations, but the derivation of these are not addressed here. The constants in the equation can be obtained from Density Functional theory (DFT) calculations, by calculating how the energy changes with specific distortions. Due to the two-dimensional order parameter and 6-fold symmetry, the free energy for hexagonal manganites will resemble a Mexican hat, as shown in Fig. C.1.

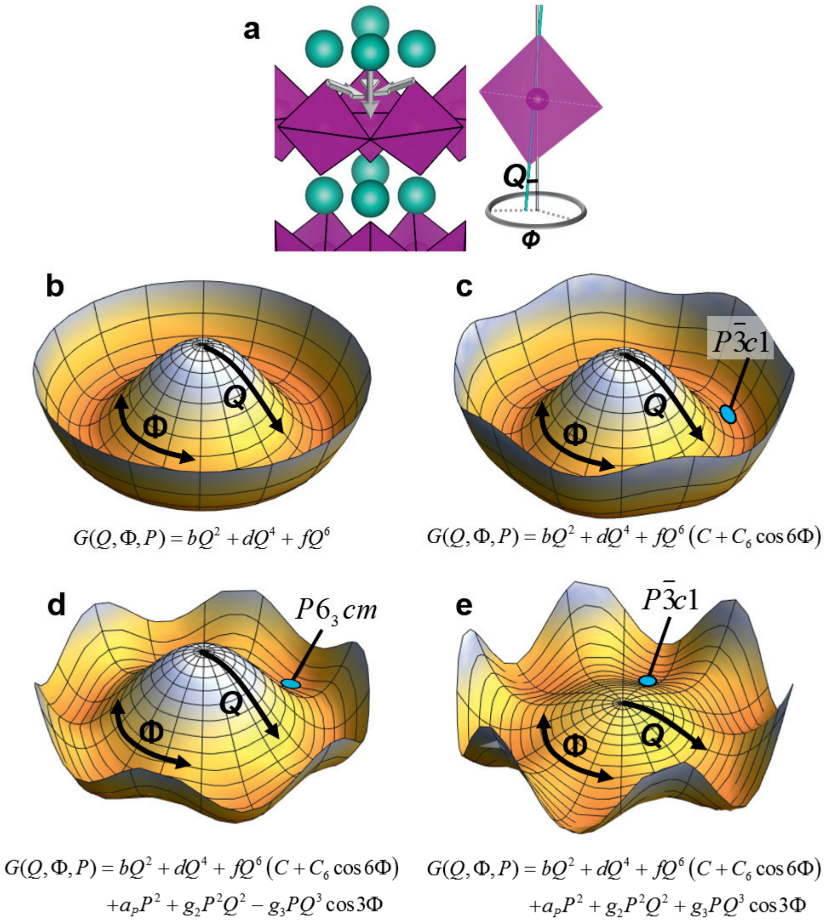

Figure C.1: **(a)** Excerpt of the polar $P6_3cm$ structure with arrows showing the tilting of the trigonal bipyramids and its relation to the order parameter amplitude Q and angle Φ. **(b)** The Landau free energy including only the Q terms giving the energy landscape the shape of a Mexican hat. **(c)** All terms including Q, Φ and their coupling terms breaking the symmetry towards antipolar $P\bar{3}c1$.**(d)** All terms including Q, Φ, P and a negative coupling term between P and Q, reversing the coupling between Q and Φ to give the polar hettotype $P6_3cm$. If the coupling term between P and Q is positive the symmetry stays antipolar $P\bar{3}c1$, panel **(e)**.